EXTERNAL STRENGTHENING

OF

REINFORCED CONCRETE PIER CAPS

A Dissertation
Presented to
The Academic Faculty

by

Andrew J. Bechtel

In Partial Fulfillment
of the Requirements for the Degree
Doctor of Philosophy in the
School of Civil and Environmental Engineering

Georgia Institute of Technology
December 2011

EXTERNAL STRENGTHENING

OF

REINFORCED CONCRETE PIER CAPS

Approved By:

Dr. Bruce R. Ellingwood, Advisor
School of Civil and Environmental Engineering
Georgia Institute of Technology

Dr. Abdul-Hamid Zureick, Advisor
School of Civil and Environmental Engineering
Georgia Institute of Technology

Dr. Lawrence F. Kahn
School of Civil and Environmental Engineering
Georgia Institute of Technology

Dr. Leroy Z. Emkin
School of Civil and Environmental Engineering
Georgia Institute of Technology

Dr. T. Russell Gentry
School of Architecture
Georgia Institute of Technology

Date Approved: October 4, 2011

ACKNOWLEDGMENTS

First, I would like to thank my advisors, Dr. Bruce Ellingwood and Dr Abdul-Hamid Zureick, for giving me this opportunity. They gave me the freedom to create on my own, while giving me the guidance I needed to keep on track. Without their time and input my work would not have been possible. Thank you to my defense committee members: Dr. Lawrence Kahn, Dr. Leroy Emkin, and Dr. T. Russell Gentry, for their time and input.

I would like to thank my wife, Anna, for her unconditional support. Without her motivation I may not have been able to finish this work. She was always there to pick me up when I was down, and give me confidence when mine was waning.

I would like to thank my family for believing in me, giving me the inspiration to work hard, and being there when I finally came home: My parents Ed and Louise Bechtel, my brothers Patrick and Thomas, my sister Colleen, and my grandparents Joseph and Mary Martignetti and Joseph and Elizabeth Bechtel. I could not have finished in the time that I did without help from my friends: Robert Moser, Amal Jayapalan, Jonathan Hurff, Curtis O'Malley, Guoqing Xu, Tim Wright, Sung-Hu Kim, Falak Shah, Nicholas Reynolds, Jeremy Mitchell, Benjamin Kosbab, Brett Holland, Daniel MacDonald, Jesse Hayden, and Dave Jaekel.

The research described in this dissertation was supported in part by the Georgia Department of Transportation, and the donation of the composite materials used in this study was generously arranged by Ron Thomas at Sika Corporation. This support is gratefully acknowledged.

TABLE OF CONTENTS

LIST OF TABLES

LIST OF FIGURES

SUMMARY

The shear capacity of reinforced concrete pier caps in bridge support systems can be a factor which limits the capacity of an existing bridge. Pier caps are loaded over a short shear span making them behave as deep beams. Reinforced concrete deep beams have the ability to carry load through tied arch action after the formation of diagonal cracks. Externally bonded fiber reinforced polymer (FRP) reinforcement has been shown to increase the shear capacity of reinforced concrete members in flexure. Unfortunately, there is insufficient research on the effect of externally bonded FRP reinforcement on strength of deep beams to make it a viable strengthening system for pier caps.

This research was aimed at investigating the behavior of reinforced concrete pier caps through a coordinated experimental and analytical program and using the knowledge gained from that investigation to recommend an external strengthening scheme. The experimental study was performed on laboratory specimens based on an existing bridge in Georgia with perceived shear deficiencies in its pier caps. A novel part of modeling the behavior of a pier cap was to include the effects of the column supporting the pier cap. This was accomplished by including a stub column in each of the specimens. The stub column induced a stress concentration at the reentrant corner between the column and pier cap, which dictated the failure mode in some of the specimens. Two failure modes were observed: yielding of the longitudinal tension

reinforcement, and splitting of the concrete in the arch. The effects of changes in longitudinal tension reinforcement ratio, beam depth, and crack control reinforcement were examined. The results showed that increasing the longitudinal tension reinforcement decreased the principal compression strut angle; this increased the capacity by changing the shape of the tied arch which forms, and reducing the stress concentration. The inclusion of crack control reinforcement did not change the point at which diagonal cracking occurred, but it did increase the ultimate capacity by reinforcing the splitting crack in the concrete. There was a significant size effect when splitting failure governed the ultimate limit state.

The results of the experimental study were used in conjunction with a larger database developed from the literature to examine different analytical methods for determining the ultimate capacity of reinforced concrete deep beams. A new method based on a modification of a previous approach suggested by Zararis was developed for use in the design of external strengthening schemes. Two specimens were tested with externally bonded FRP reinforcement applied longitudinally to increase the strength of the tension tie. The test results correlated well with the proposed method of analysis and showed that increasing the strength of the longitudinal tension tie is an effective way to increase the strength of a reinforced concrete deep beam.

CHAPTER 1

INTRODUCTION

1.1 Motivation

The infrastructure of the United States is aging; 12% of all the bridges in the United States are structurally deficient (ASCE 2009). A structurally deficient bridge is unable to carry the current required traffic loads safely. Structural deficiencies occur due to the historic increase in the required truck loads, improved understanding of bridge performance, and decay over time. Structural deficiencies lead to posting of the bridge structure. Posting limits the trucks which are permitted to cross the bridge and may have a significant economic impact on the transportation of goods and materials. One factor that contributes to the structural deficiency of a bridge is lack of shear capacity in their pier caps. A pier cap is a large reinforced concrete beam which transfers the loads from the bridge superstructure (girders) to its foundation. Figure 1.1 shows the pier caps of Bridge 085-0018 in Dawson County, GA.

Externally bonded reinforcement has been shown to improve the shear strength of reinforced concrete elements. The problem with implementing these strengthening schemes on pier caps is lack of research on their effectiveness when applied to reinforced concrete beams with similar geometry and loading as a pier cap. Pier caps are a unique type of structure mainly due to the short shear span over which load is applied. If it were possible to strengthen the existing pier caps, postings could be reduced or even removed, allowing the bridges to return to normal service.

Strengthening also would increase the length of the bridge's life and provide economic benefits.

Figure 1.1- Pier caps of Bridge 085-0018 in Dawson County, Georgia

1.2 Objectives and Scope

The objectives of this research were to study the behavior of reinforced concrete pier caps up to and at their ultimate limit state both experimentally and analytically. The results of this study were used to design an external strengthening scheme for reinforced concrete pier caps which was then be implemented and validated experimentally.

1.3 Thesis Outline

This dissertation is organized around the research objectives identified above. We emphasize the importance of understanding the behavior of the reinforced concrete pier cap itself before trying to understand the behavior of a reinforced concrete pier cap with external strengthening. We begin with an assessment of those factors that affect the ultimate capacity of existing reinforced concrete pier caps, followed by an examination of the most structurally efficient methods for external strengthening and the development of practical methods for achieving the necessary strengthening in service.

The remainder of this dissertation is organized as follows:

Chapter 2- Background on Reinforced Concrete Deep Beams is a literature review on the behavior of reinforced concrete deep beams. It begins with a review of factors shown to affect the ultimate beam capacity of reinforced concrete deep beams. This is followed by an in-depth review of different analytical methods used to calculate the ultimate shear capacity of reinforced concrete beams. A special emphasis is placed on the design methods included in the 2007 AASHTO LRFD Bridge Design Specifications. The shear capacity calculation methods appropriate for deep beams are determined.

Chapter 3- Specimen Design outlines the design of the laboratory specimens used throughout the experimental program to represent a pier cap. The design of the specimens are based on the dimensions and details of the pier caps supporting Bridge 085-0018 in Dawson County, Georgia, which carries SR 136 over the Etowah River. The chapter presents the instrumentation scheme for the experimental program.

Chapter 4- Ultimate Capacity of Reinforced Concrete Pier Caps follows the testing to of the laboratory specimens to their ultimate limit state. The variables investigated are the beam size, reinforcement ratio, and the effect of AASHTO crack control reinforcement. The results of each of the experimental tests are compared to one another, and conclusions on the behavior of reinforced concrete pier caps are made.

Chapter 5- Evaluation of Analytical Methods Used to Calculate Ultimate Capacity explores existing methods of calculating the ultimate capacity of reinforced concrete deep beams. A systematic way of creating strut and tie models is developed along with a new proposed method of determining ultimate capacity based on Zararis's Method. The analysis methods are compared to the experimental results from Chapter 4 and a larger database from the literature.

Chapter 6- Background on the Shear Strengthening of Reinforced Concrete Beams with Fiber Reinforced Polymers is a literature review on the behavior of reinforced concrete members strengthened externally with FRP. The background on the behavior of reinforced concrete beams strengthened with FRP is done by analyzing a database of test results. The effects of the shear span, beam depth, longitudinal tension reinforcement, transverse reinforcement, fiber angle, and relative fiber layers are investigated. This is followed by an evaluation of the different analytical methods used to calculate the ultimate capacity of reinforced concrete members strengthened externally with FRP.

Chapter 7- Strengthening of Reinforced Concrete Deep Beams with FRP- discusses the theory behind the design of external strengthening of reinforced concrete deep beams, and then supports the theory experimentally. The strengthening schemes are based on the proposed method of calculating ultimate capacity developed in Chapter 5. The development of the design strategy is followed by the experimental results from laboratory tests of specimens strengthened with FRP reinforcement.

Chapter 8- Summary, Conclusions, and Future Work- summarizes all of the findings and conclusions from the previous chapters. The future work section discusses some of the different research opportunities which presented themselves during the work.

1.4 Commonly Used Notation

a	=	shear span (in)
A_s	=	area of longitudinal tension reinforcement (in^2)
A_{sv}	=	area of transverse reinforcement within distance S (in)
b or b_w	=	beam width (in)
c	=	distance from extreme compression fiber to the neutral axis (in)
c_s	=	depth of compression zone above diagonal crack
d	=	effective depth, distance from extreme compression fiber to centroid of longitudinal tension reinforcement (in)
d_a	=	maximum aggregate size (in)
E_s	=	elastic modulus of steel (ksi)
f'_c	=	concrete compressive strength (psi)
f'_{ct}	=	concrete tensile splitting strength (psi)
f_{cu}	=	maximum allowable stress in principal compression strut (kai)
f_y	=	yield stress of longitudinal tension reinforcement (ksi)
f_{yv}	=	yield stress of transverse reinforcement (ksi)
h_a	=	vertical face of nodal zone on tension side of beam (in)
h_s	=	vertical face of nodal zone on compression side of the beam (in)
l_b	=	length of bearing (in)
$l_{b\ comp}$	=	length of bearing on compression side of beam (in)
S	=	spacing of transverse reinforcement (in)
V_c	=	shear contribution from concrete (kips)
V_n	=	nominal shear capacity (kips)
V_s	=	shear contribution from transverse steel (kips)
α	=	angle of transverse reinforcement from longitudinal (°)
α_s	=	angle of principal compression strut (°)

ε_s = strain in longitudinal tension reinforcement

ρ = longitudinal tension reinforcement ratio $A_s/(bd)$

ρ_v = transverse reinforcement ratio $A_{sv}/(bS)$

θ_s = compression strut angle (°)

CHAPTER 2

BACKGROUND ON REINFORCED CONCRETE DEEP BEAMS

Although shear resistance in reinforced concrete beams has been studied for well over 50 years, there still are many theories concerning the mechanisms of how the beams resist shear and prediction of their ultimate shear strength. This chapter discusses the main factors which influence the shear strength of reinforced concrete beams, and examines some of these theories. Particular attention is paid to the methods used in the AASHTO 2007 LRFD Bridge Design Specification.

2.1 Factors Contributing to Shear Resistance

The work of Kani in the 1960's brought to light many of the factors that influence the shear resistance of reinforced concrete beams. Kani performed a series of tests on beams where he varied the effective depth, width, shear span, and the longitudinal reinforcement ratio. In these tests, the effective depth (d) was defined as the vertical distance from the extreme compression fiber to the centroid of the tension reinforcement, and the shear span (a) was the longitudinal distance from the center of the support to the center of the nearest applied load. Effective depth, shear span and longitudinal reinforcement ratio influenced the shear capacity significantly (Kani, 1964), whereas beam width had little effect (Kani, 1967). The results of some of these tests are shown in Figure 2.1; the effects of the effective depth and the ratio of shear span to

effective depth, *a/d,* can be seen. Figure 2.2 shows that the shear capacity decreases in beams with a small amount of longitudinal reinforcement. In the figure V_c is the ultimate shear capacity, and it is normalized by the width (b_w), the effective depth, and the concrete compressive strength (f'_c). The x axis is the reinforcement ratio (ρ) which is calculated by dividing the area of the longitudinal tension steel (A_s) by the beam width and effective depth. Kani showed that if the *a/d* ratio was less than two and diagonal cracking occurred, the beam could form a tied arch (Kani, 1964). This is shown by the significant increase in ultimate shear stress seen in Figure 2.1 for the specimens with a/d ratios less than two.

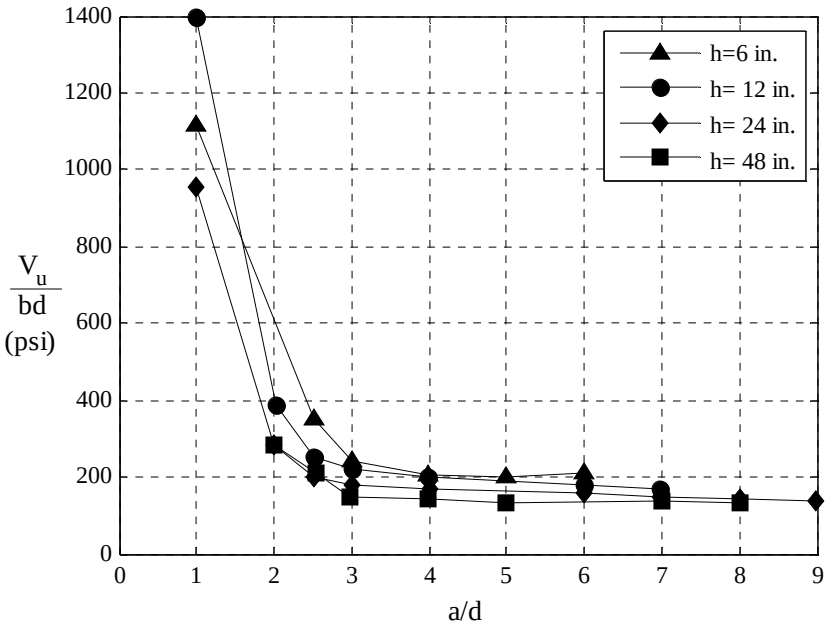

Figure 2.1- Shear stress vs. a/d for beams of increasing height (Kani, 1967)

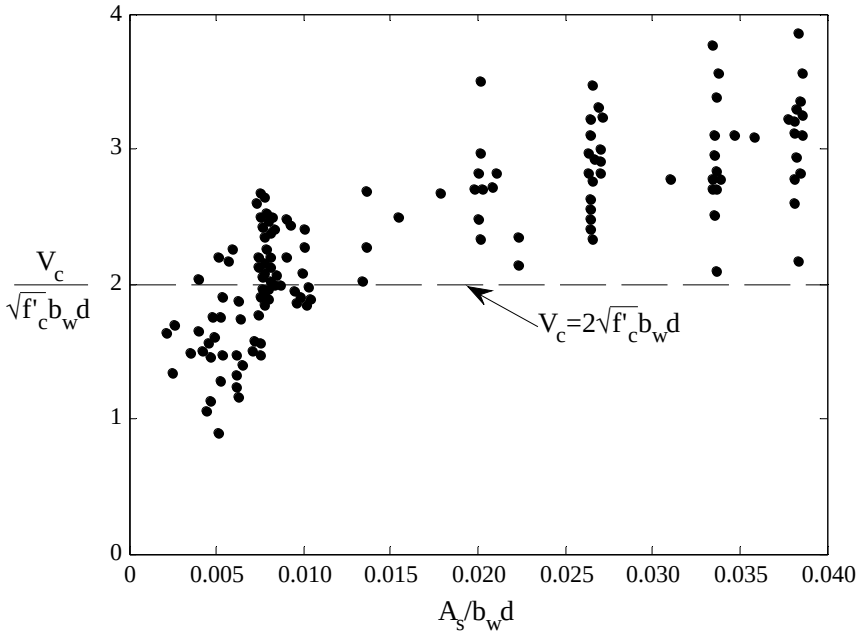

Figure 2.2- Relative shear strength vs. longitudinal reinforcement (MacGregor, 1997)

The work of Kani was expanded upon by Fenwick and Paulay (1968), who performed a series of tests that examined the principal mechanisms of shear resistance and the modes of shear failure. These authors found that factors contributing to shear resistance included aggregate interlock, dowel action of the longitudinal reinforcement, and tensile force in the transverse steel. The authors then derived Eq. 2.1 for the shear resistance of a reinforced concrete section (Fenwick and Paulay, 1968).

$$V = \frac{dM}{dx} = jd\,\frac{d(T)}{dx} + T\,\frac{d(jd)}{dx} \qquad (2.1)$$

in which T = tension force at the bottom of the beam in the longitudinal direction, and jd = length of the internal moment arm. If the moment arm remains constant, the second term in the equation drops out and the shear force is resisted entirely by the beam action.

The quantity $d(T)/dx$ is the shear flow; it exists due to the bond forces between the steel longitudinal reinforcement and the concrete. If the steel becomes debonded from the concrete or if a large diagonal crack forms between the load and the support, the shear flow becomes zero and the shear forces are carried entirely by arching action. In arch action, the tension force at the bottom of the beam remains constant and the moment arm changes to maintain moment equilibrium. The authors concluded that in order for arch action to occur, substantial translational displacements must occur along the longitudinal tension reinforcement. These displacements are confined to the regions of the beam where there is significant vertical and diagonal cracking. With the formation of wide diagonal cracks in the shear span, arch action can occur, but the formation of these large cracks prevents beam action. Due to this behavior, the authors concluded that the two forms of shear resistance, beam and arch, cannot occur simultaneously.

Fenwick and Paulay (1968) break down shear failure into three distinct mechanisms. A Type I failure involves the formation of a diagonal tension crack; no arch action can occur because the shear span is too large. This occurs at an $a/d > 3$. A Type II failure involves tension failure of the compression zone above diagonal cracking load at the point of transition to arch action after the failure of the beam mechanism. This occurs when $2 < a/d < 3$. A Type III failure occurs by crushing or splitting of the concrete in arch action. This occurs at an $a/d < 2$.

More recent research by Zararis (1997) questions the development of shear resistance due to aggregate interlock and dowel action in reinforced concrete. In a reinforced concrete beam, the compression zone acts as a buffer preventing any slip along a crack; this prevents shear friction and dowel action from contributing

significantly to shear resistance (Zararis, 1997). The shear forces are carried by shear in the reinforcing bars and in the compression zone. Aggregate interlock does not occur until either the steel yields or the compression zone fractures; only at that point does aggregate interlock serve to maintain equilibrium (Zararis, 2003).

2.1.1 Effect of Size on Strength of Reinforced Concrete Beams in Shear

Kani's work showed that the shear capacity of reinforced concrete beams depends on their size. Figure 2.1 shows how the ultimate shear stress of reinforced concrete beams decreases as the depth of the beam increases. In the figure V_u is the ultimate shear capacity, and it is normalized by the width, and the effective depth. This ratio gives the average shear stress, and these values are plotted vs. the ratio of the shear span to the effective depth. This size effect has caused many problems when developing shear provisions based on laboratory tests on beams with smaller depths, since such tests do not represent the behavior of larger beams accurately. Taylor (1974) and Bazant and Kim (1984) present two different theories on the cause of the size effect. Taylor (1974) bases his theory on shear friction, while Bazant and Kim (1984) base theirs on the release of energy as concrete crushes.

Size effect based on shear friction is presumed to be a function of the relationship between the maximum aggregate size and the crack width. As the crack width increases, the ability of the beam to transmit shear through shear friction is reduced; the same is true if the aggregate size is reduced (Sherwood et al. 2007). In contrast, Bazant and Kim (1984) have theorized that the size effect is caused by the amount of energy released as the concrete crushes at failure. Based on this concept and

a regression analysis, Bazant and Sun (1987) have proposed Eq. 2.2 for the ultimate shear capacity (V_u) of reinforced concrete beams:

$$V_u = [\sqrt{f'_c} + 3000\sqrt{\frac{\rho}{(a/d)^5}}] * \frac{6.5\rho^{(1/3)}(1+\sqrt{0.2/d_a})}{\sqrt{1+\frac{d}{25d_a(1+\frac{\rho_v}{\rho_0})}}}](b)(d) \qquad (2.2)$$

ρ_o=400{1+tanh[2(a/d-2.8)]}

(2.2b)

d_a= maximum aggregate size

ρ_v= shear reinforcement ratio A_{sv}/bS

A_{sv}= area of transverse reinforcement

S= spacing of transverse reinforcement

Walvern and Lehwalter (1994) performed a series of simple experiments with normal and light weight concretes to investigate Taylor (1974) and Bazant and Kim's (1984) theories for size effect. The concept of the experiments was that the weaker aggregate in the light-weight concrete would split and create a smooth crack surface eliminating the shear friction. The results of the experiment are shown in Figure 2.3. In the figure V_u is the ultimate shear capacity, and it is normalized by the width, the effective depth, and the concrete average tensile splitting strength (f'_{ct}). This ratio is plotted vs. the effective depth.

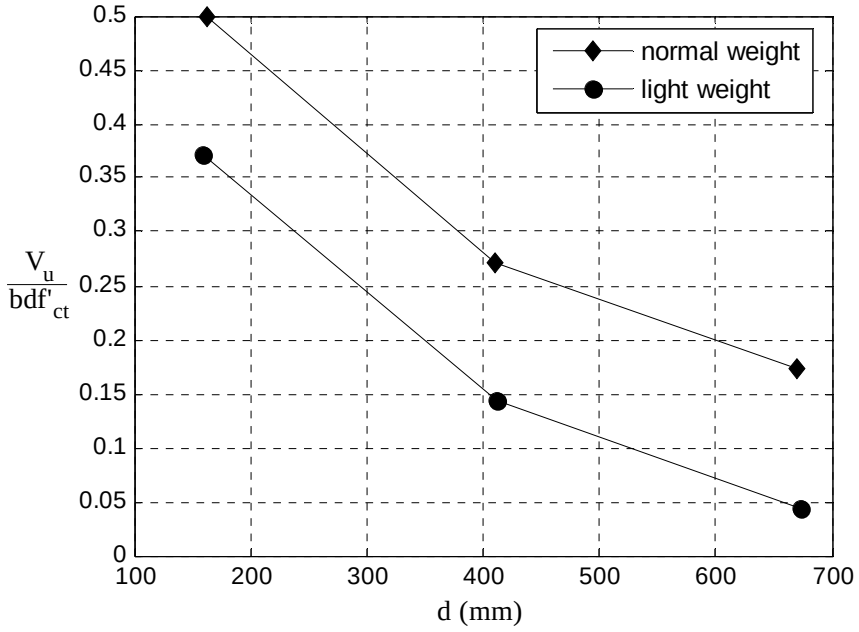

Figure 2.3- Ultimate shear capacity vs. beam depth with different aggregates *1 in. = 25.4 mm.* (Walraven and Lehwalter, 1994*)*.

Figure 2.3 reveals that the shear strength of the light-weight concrete was lower at each of the different beam depths, but it still experienced a noticeable size effect that was very similar to that of the normal-weight concrete. During the testing of the beams it was observed that the rate of crack formation was correlated to the beam depth. Cracks formed more rapidly in large beams than they did in smaller beams; this is a consequence of the energy release rate (Walraven and Lehwalter, 1994*)*. Walraven and Lehwalter concluded that the size effect was a function of the energy release rate and not the shear friction, thus supporting Bazant and Sun's (1987) theory.

2.2 AASHTO Shear Strength Models

The 2007 AASHTO LRFD Bridge Design Specifications provide four different methods for evaluating the nominal shear strength of a reinforced concrete beam:

1. the simplified procedure for nonprestressed sections (Section 5.8.3.4.1);
2. the general procedure (Section 5.8.3.4.2);
3. the simplified procedure for prestressed and nonprestressed sections (Section 5.8.3.4.3);
4, the strut and tie model (Section 5.6.3).

The simplified procedure for nonprestressed sections is a semi-empirical method for evaluating shear based on the truss model (Richart, 1927). The general procedure is the modified compression field theory (Vecchio and Collins, 1986). The simplified procedure for prestressed and nonprestressed sections is based on work by MacGregor et al. (1965) on shear strength of prestressed beams. The strut and tie model assumes arch action is carrying the load, and that the ultimate capacity of the arch governs the ultimate limit state. The methods permitted are highly dependent on the detailing of the reinforcing steel in each member.

2.2.1 Simplified Procedure for Nonprestressed Sections (Section 5.8.3.4.1)

The simplified procedure for nonprestressed sections is based on the truss model. The truss model, developed by Ritter in 1899 was the first model for the

prediction of shear resistance in reinforced concrete members, and was expanded on by Morsch in 1904 when he published the first design specification for reinforced concrete (MacGregor, 1997). In this model, an analogous Howe truss is superimposed on the concrete beam, with the compression members of the truss modeled with concrete, and its tension members modeled with steel. The angle of the compression struts is assumed to be 45°. This truss model does not account for forces transferred through shear friction or tension in the concrete and for these reasons tends to be conservative in its prediction of shear strength. To improve the truss model, Richart (1927) suggested that the shear resistance attributed to the concrete should be found empirically, while the shear resistance of the steel reinforcement is found through the truss model. This leads to the current simplified procedure for nonprestressed members found in the 2007 AASHTO LRFD Bridge Design Specifications and in the 2008 ACI 318 Building Code and Commentary. If the beam has at least the minimum amount of transverse steel reinforcement stipulated in the code, the nominal strength (in kips) can be found as:

$$V_n = V_c + V_s \tag{2.3a}$$

$$V_c = 2(0.0316)\sqrt{f'_c}\,bd \tag{2.3b}$$

$$V_s = \frac{A_{sv} f_{yv} d \ (\cos\alpha + \sin\alpha)}{S} \tag{2.3c}$$

V_n= nominal shear capacity (kips)

V_c= shear capacity from concrete (kips)

V_s= shear capacity from transverse steel (kips)

f_{yv}= yield stress of transverse reinforcement (ksi)

α= angle of transverse reinforcement from longitudinal (degrees)

The 0.0316 in the V_c is a result of f'_c being based in kips per square inch rather than pounds per square inch. The minimum required reinforcement (A_{sv}) is given by Eq. 2.4.

$$A_{sv} \geq 0.0316\sqrt{f'_c}\,\frac{bS}{f_{yv}} \qquad (2.4)$$

2.2.2 General Procedure (MCFT) (Section 5.8.3.4.2)

The general procedure is the modified compression field theory (MCFT) developed by Vecchio and Collins (1986). In the MCFT, cracked concrete is treated as a new material, and equilibrium, compatibility and stress-strain relationships are formulated in terms of average stresses and strains. To develop the MCFT, a series of tests were performed on square concrete elements subjected to shear and normal forces (Vecchio and Collins, 1986). Stresses were calculated based on the applied loads and Mohr's circle. The specimen is shown in Figure 2.4. In the tests, the calculated shear stresses were compared to the measured strains (Vecchio and Collins, 1986). Mohr's circle was generated for the average stresses and strains at different stages of loading. The MCFT is an excellent model for calculating the ultimate shear capacity of reinforced concrete members with small amounts of longitudinal reinforcement or high strains in the longitudinal reinforcement. Since the specimens used to develop the MCFT were simplified elements, not beams, they could not develop the tied arch mechanism of shear resistance; therefore, the MCFT is not a suitable model for shear resistance by arch action.

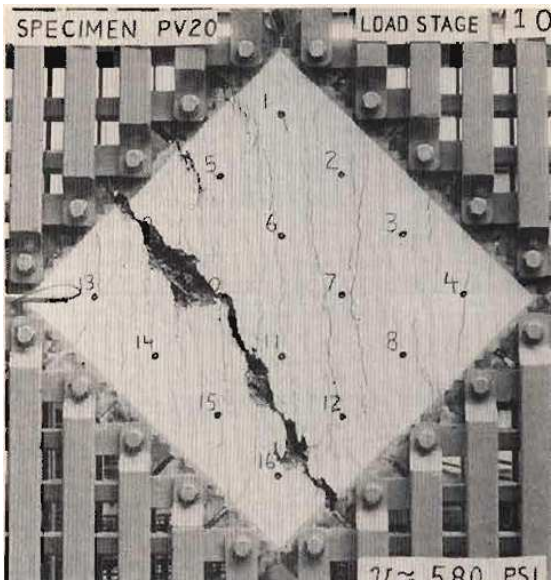

Figure 2.4- Specimen used to develop the MCFT (Vecchio, 1986)

The MCFT is the default shear analysis in AASHTO, and can be applied to any beam regardless of the reinforcement detail. The version of the MCFT that appears in the AASHTO 2007 LRFD Bridge Design Specifications is simplified through the use of tables. This reduces the number of steps required to calculate the shear resistance. The only equations that remain in AASHTO are three equations for calculating tensile strains under different conditions and one equation to calculate size effects due to beam depth and the maximum aggregate size. This size effect is based on shear friction which, as noted previously, is not supported by Walraven and Lehwalter's (1994) data. The equations for axial strain are:

- If the section contains greater than the minimum amount of transverse reinforcement (Eq 2.4):

$$\varepsilon_x = \frac{\left(\frac{M_u}{d_v} + 0.5N_u + 0.5(V_u - V_p)\cot\theta - A_{ps} f_{po}\right)}{2(E_S A_S + E_p A_{ps})} \qquad (2.5a)$$

- If an existing section contains less than the minimum transverse reinforcement (Eq. 2.4):

$$\varepsilon_x = \frac{\left(\frac{M_u}{d_v} + 0.5N_u + 0.5(V_u - V_p)\cot\theta - A_{ps} f_{po}\right)}{E_S A_S + E_p A_{ps}} \qquad (2.5b)$$

- If the initial value from the previous equations are negative due to the presence of prestressing forces:

$$\varepsilon_x = \frac{\left(\frac{M_u}{d_v} + 0.5N_u + 0.5(V_u - V_p)\cot\theta - A_{ps} f_{po}\right)}{2(E_S A_S + E_p A_{ps} + E_c A_c)} \qquad (2.5c)$$

ε_x= longitudinal strain

A_c= area of concrete on the flexural tension side of member (in^2)

A_{ps}= area of prestessed longitudinal tension steel (in^2)

E_p= elastic modulus of prestressing strand (ksi)

f_{po}= elastic modulus of prestressing tendon multiplied by locked in difference in strain between prestressing tendons and surrounding concrete (ksi)

N_u= factored axial force (kip)

M_u= factored moment (kip-in)

V_u= factored shear force (kip)

V_p= effective prestressing force in direction of shear (kip)

θ= angle of inclination of diagonal compressive stresses (degrees)

E_c= elastic modulus of concrete (ksi)

$A_c = bd$ (in^2)

- The size effect equation is:

$$s_{xe} = s_x \frac{1.38}{a_g + 0.63} \qquad (2.5d)$$

s_{xe} = crack spacing parameter
a_g = maximum aggregate size (in)
s_x = the lesser of either d or the maximum distance between crack control reinforcement (in)

Taking the results of these equations to the appropriate table yields a β and θ value which can be applied to Eq. 2.6 to calculate the nominal shear resistance of the member. The effects of the strains and size effect are taken into account in the computations performed by the tables.

$$V_n = V_c + V_s \qquad (2.6a)$$

$$V_c = \beta(0.0316)\sqrt{f'_c}\,bd \qquad (2.6b)$$

$$V_s = \frac{A_{sv} f_{yv} d \ (\cot\theta + \cot\alpha)\sin\alpha}{S} \qquad (2.6c)$$

α= angle of transverse reinforcement from longitudinal (degrees)
β= factor indicating ability of cracked concrete to transmit shear
θ= angle of inclination of diagonal compressive stresses (degrees)

2.2.3 Simplified Procedure for Prestressed and Nonprestressed Members (Section 5.8.3.4.3)

The simplified procedure for prestressed and nonprestressed members is based on theories developed for predicting the diagonal shear cracking of prestressed concrete members (MacGregor et al., 1965). This method limits the shear strength of the member based on the formation of these diagonal cracks. This limit is different and lower than the ultimate capacity of the member.

In prestressed concrete members, diagonal shear cracks form in two ways. The first is a flexure shear crack. The flexure shear crack forms from existing flexure cracks. Essentially, a vertical flexure crack changes its angle of inclination to become a diagonal shear crack. The shear capacity governed by the formation of a flexure shear crack is based on empirical observation and is calculated by:

$$V_{ci} = 0.02\sqrt{f'_c}\, b\ d + V_d + \frac{V_i M_{cr}}{M_{\max}} \geq 0.06\sqrt{f'_c}\, bd \qquad (2.7)$$

V_{ci}= nominal shear resistance of concrete when inclined cracking results from shear and moment (kip)

V_d= shear force at section due to unfactored dead load (kip)

V_i= factored shear force at section due to externally applied loads (kip)

M_{cr}= moment causing flexural cracking due to external loads (kip-in)

M_{max}= maximum factored moment (kip-in)

The second type of shear crack is the web shear crack. These cracks form in the web of a reinforced concrete member before flexural cracking of the member (MacGregor et al, 1965). This shear stress at which this type of crack forms is calculated theoretically from a Mohr's Circle analysis of the web. The shear capacity governed by the formation of a web shear crack is given by:

$$V_{cw} = (0.06\sqrt{f'_c} + 0.30\, f_{pc})bd\ + V_p \qquad (2.8)$$

V_{cw}= nominal shear resistance when inclined cracking results from excessive principal tension in web (kip)

f_{pc}= compressive stress in concrete (ksi)

V_p= effective prestressing force in direction of shear (kip)

The shear resistance of the concrete is taken as the lesser of V_{ci} and V_{cw}. The resistance of the transverse shear reinforcement is given by Eq. 2.6c. If $V_{ci} < V_{cw}$ then $\cot(\theta)=1$. If $V_{ci} > V_{cw}$ then:

$$\cot\theta = 1.0 + 3\left(\frac{f_{pc}}{\sqrt{f'_c}}\right) \leq 1.8 \qquad (2.9)$$

This method can only be implemented if the area of the transverse steel exceeds the minimum requirement.

2.2.4 Strut and Tie Model (Section 5.6.3)

The strut and tie model (STM) is a generalization of the truss model (Schlaich et al, 1987). It was developed to model the shear in any region even if it is discontinuous. Large cracks are assumed to be present and shear is no longer carried through beam action. The applied forces are in equilibrium with a system of forces existing in concrete compression struts and steel tension ties. It is based on the lower bound theorem of plasticity, which states that any system of forces in equilibrium with an applied load provides a lower bound of the strength of a structure provided that no element is overloaded, and deformation capacity is not exceeded (MacGregor, 1997). A strut and tie model is implemented by laying out a truss that carries the applied load to the supports. Struts and ties meet at nodal regions. The sizes of the struts, ties, and nodal regions are based on equilibrium with the applied loads and the size of the bearings at the nodal regions. The layout of the truss is subjective, and there can be more than one

effective model for a single beam. The way to find the most effective solution is to sum the strain energy in all the members (Schlaich et al, 1987); the strut and tie model which utilizes the smallest amount of strain energy is the most effective model. In the 2007 AASHTO LRFD Bridge Design Specifications, crack control reinforcement is required if a strut and tie model is used. The reinforcement ratio in both the longitudinal and transverse direction must be at least 0.003. These details are meant to improve the serviceability of members designed using a strut-and-tie analysis, and to prevent premature failure due to concrete splitting.

The specification for performing the strut and tie analysis in the AASHTO 2007 LRFD Bridge Design Specifications consists of limiting areas of struts and nodal areas as well as the crushing strength of the concrete. Figure 2.5 shows the AASHTO method for calculating the maximum size for struts and nodal areas. The size of the struts are a function of the bearing plates and either the longitudinal steel or the depth of the compression zone. The compressive strength of the concrete in the compression strut is limited by Eq. 2.10.

$$f_{cu} = \frac{f'_c}{0.8 + 170\varepsilon_1} \leq 0.85 f'_c \qquad (2.10a)$$

$$\varepsilon_1 = \varepsilon_s + (\varepsilon_s + 0.002)\cot^2(\alpha_s) \qquad (2.10b)$$

ε_s= strain in longitudinal reinforcement

α_s= angle of principal compression strut (degrees)

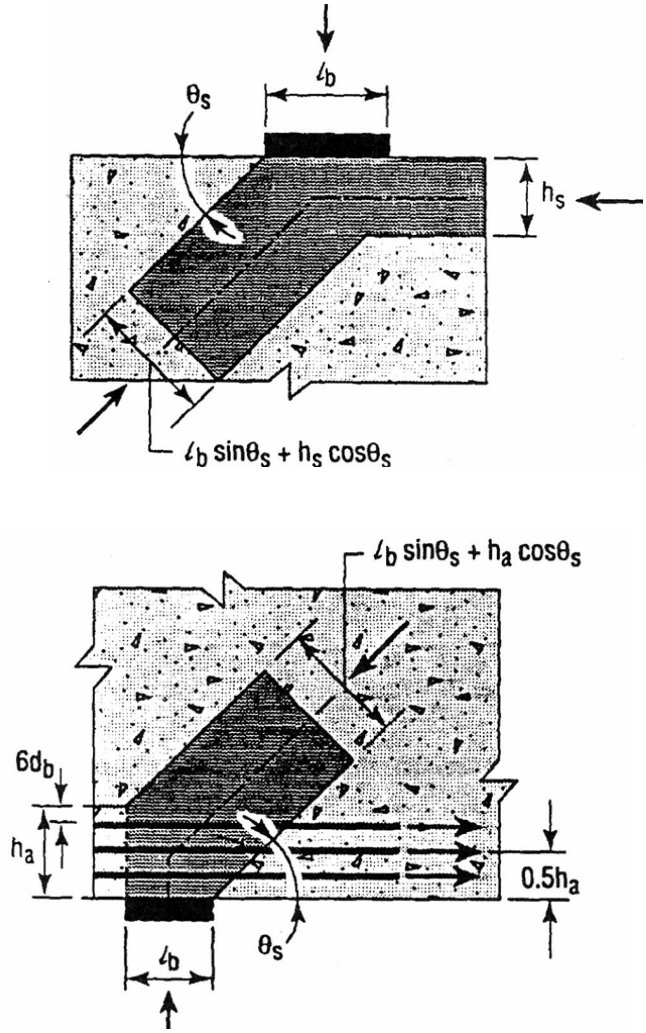

Figure 2.5- Limiting area for nodes and struts (AASHTO 2007)

The logic behind Eq.-2.10 is that if concrete is subject to a principal tensile strain it reduces its maximum compressive stress. The commentary of the AASHTO 2007 LRFD Specifications states, "If the reinforcing bars are to yield in tension, there should be significant tensile strains imposed on the concrete. As these tensile strains increase, f_{cu} decreases." The ultimate compressive strength for the strut is a function of strain ε_1. This strain is a function of the strain in the longitudinal bar (ε_s) and the angle

of the between the compression strut and the longitudinal steel (α_s). In most cases α_s is equal to the strut angle θ_s. The compression strength of the nodal zones is reduced by a factor based on the type of struts entering into the nodal zone. If only compression struts enter into the node the factor is 0.85. The compressive strength of the concrete is reduced by a factor of 0.75 if one tension tie passes through a node and by a factor of 0.65 if multiple tension ties pass through a node.

2.3 Other Shear Strength Models

The following models for shear strength have been proposed, but have not been incorporated into the AASHTO Specifications. Some expand on the models which have been incorporated.

2.3.1 Softened Truss Model

The softened truss model is an update of the truss model and was developed by Hsu (1988). It incorporates the plastic truss model of Lampert and Thurlimann (1968), uses the compatibility equations developed by Collins in the Diagonal Compression Field Theory (Collins, 1973) and also incorporates the softening effects of tensile strain on the compressive strength of the concrete found by Vecchio and Collins (1987). Using all these theories, Hsu developed three equations of equilibrium using Mohr's circle for stresses, three equations for compatibility using Mohr's circle for strains, and six equations based on constitutive relations. These 12 equations can be used to solve for shear resistance. To extend the softened truss model to deep beams, an effective transverse compressive stress due to the applied loads and supports was assumed, and a proportionality constant based on the *a/d* ratio was employed. The ratio

relates the transverse stress due to the applied shear force to the shear stress (Mau and Hsu, 1987). This approach requires that longitudinal and transverse steel be present in the web of the beam.

2.3.2 Shear Friction

The concept of shear friction is commonly used to design the interface along a possible slip plane. Loov (1998) extended this concept to beams. To evaluate the shear capacity of a beam using shear friction the shear resistance is calculated along a series of slip planes which include the effects of the longitudinal and transverse reinforcement. The plane with the lowest resistance is the governing failure plane giving the ultimate shear resistance for the section. This method depends on identifying all the failure planes, and is best performed using a computer analysis.

2.3.3 Punching Shear Failure

In his book *Innovative Shear Design* Stamenkovic (2002) disagrees with the assumptions made in developing the truss model for beams in flexure. His work is based on the theories of shear stress resisting horizontal slip in a flexed beam developed by Timoshenko and Young (1968). Stamenkovic believed that diagonal cracking is caused by punching shear from the supports and the applied loads. In this case the shear resistance of the member is based on the shear forces from the applied load, the supports, the horizontal tensile force, and the angle of cracking.

2.3.4 Zararis's Method

The Zararis method for determining failure of reinforced concrete deep beams is based on the assumption that a beam with an *a/d* ratio between 1 and 2.5 will fail as the result of a compression failure in the concrete above a critical diagonal crack in the compression zone (Zararis 2003). The method assumes that adequate bearing is provided at the supports, and that the beam is detailed correctly to prevent de-bonding of the longitudinal reinforcement. Zararis's Method is based on calculating the depth of the compression block in flexure and then reducing its depth due to diagonal cracking. This calculation is performed through 3 sets of equations. The first equation calculates the depth of the compression block for flexure based on equilibrium between the tension in the longitudinal steel and the compression block on the opposite side of the beam. These forces are calculated based on a linear strain with the concrete crushing strain assumed to be 0.002. The compression block is assumed to a simple parabolic shape with a maximum stress of f'_c. Equation 2.11 is Zararis's equation for the depth of the flexural compression block; it is a quadratic equation that can be solved by factorization or the quadratic formula. Equation 2.11 was converted from metric to imperial units, and the value of f'_c is in psi. The desired solution to Eq. 2.11 is the positive root.

$$\left(\frac{c}{d}\right)^2 + 87{,}000\frac{\rho}{f'_c}\left(\frac{c}{d}\right) - 87{,}000\frac{\rho}{f'_c} = 0 \qquad (2.11)$$

c= depth from extreme compression fiber to the neutral axis (in)

Once the depth of the flexural compression depth is calculated, it is used in Eq. 2.12 to calculate the reduced compression block.

$$\frac{c_s}{d} = \frac{1 + 0.27R(a/d)^2}{1 + R(a/d)^2}\frac{c}{d} \qquad (2.12a)$$

$$R = 1 + (\rho_v / \rho)(a/d)^2 \qquad (2.12b)$$

c_s= depth of compression zone above diagonal crack (in)

With the reduced depth c_s calculated the ultimate shear force the section can resist can then be calculated with Eq. 2.13. The ultimate shear force is calculated using moment equilibrium around the centroid of the compression zone. The method assumes that the cracks have formed and arch action is the load carrying mechanism.

$$V_u = \frac{bd}{a/d}\left[\frac{c_s}{d}\left(1 - 0.5\frac{c_s}{d}\right)f'_c + 0.5\rho_v f_{yv}\left(1 - \frac{c_s}{d}\right)^2\left(\frac{a}{d}\right)^2\right] \qquad (2.13)$$

2.4 Critical Review

The evaluation of existing reinforced concrete bridge structures is done in accordance with the AASHTO Manual for Bridge Evaluation (2008). For the evaluation of the nominal shear strength of reinforced concrete members, the manual directs the user to the 2007 AASHTO LRFD Bridge Design Specifications. Pier caps are deep beams with shear spans less than two; this allows them to carry load through arch action. The appropriate model in the AASHTO specification for use with deep beams is the strut and tie model. The simplified method for nonprestressed sections is a semi-empirical approach based on the traditional truss model. It only incorporates the effects of the concrete strength and the transverse reinforcement; it does not account for the effects of depth or longitudinal reinforcement. The limit state for this model is set to the

formation of diagonal cracks. In order for arch action to occur diagonal cracks must be present (Fenwick and Paulay, 1968), and arch action allows deep beams to carry load in excess of the diagonal cracking load when the *a/d* is less than two. The simplified method for prestressed and nonprestressed sections is another semi-empirical method based on the loads required to cause a diagonal crack to form. Again, arch action allows deep beams to carry loads in excess of the diagonal cracking load. The general procedure does not account for arch action, and therefore does not model the mechanics correctly.

The commentary to the 2007 AASHTO LRFD Design Specifications states that the required crack control reinforcement for beams designed with the strut-and-tie model is intended to control the width of cracks and ensure a minimum ductility (C5.6.3.6). Research comparing the ultimate strength of deep beams with properly detailed steel reinforcement to those without such reinforcement has shown that the ultimate strengths are within 5% of each other (Aguilar et al, 2002). This small difference indicates that the addition of transverse reinforcement has very little effect on the ultimate strength of deep beams. The transverse steel reinforcement in Aguilar et al's specimens was instrumented with strain gages. The data collected showed that in many cases the transverse reinforcement did not yield (Aguilar et al, 2002). Both Bazant and Sun (1987) and Zsutty (1971) concluded that transverse reinforcement did not achieve its full yield capacity based on the evaluation of data sets on shear failure of reinforced concrete beams. It should be noted that all methods for evaluating the nominal shear strength of reinforced concrete members, except the strut-and-tie model, assume that all of the transverse reinforcement yields.

One major point distinguishing the different methods of shear strength evaluation is the incorporation of shear friction. The MCFT and the shear friction models both attribute a portion of the shear resistance of the beam to shear friction along the crack. In contrast, Zararis theorized that the compression zone of the beam acts as a buffer preventing slip along the cracks and thus preventing shear friction from contributing to the shear resistance until a failure in the compression zone. Vecchio and Collins (1987) also suggested that shear friction was the cause of the size effect on the shear resistance of reinforced concrete beams, but the findings of Bazant and Sun (1987) and Walraven and Lehwalter (1994) indicated that shear friction is not a major contributor to the shear resistance of a concrete beam.

Based on the literature review, three methods for predicting the ultimate capacity of reinforced concrete deep beams were chosen based on their formulations and their practical application. These methods were the Strut and Tie Model, Zararis's Method, and Bazant's Equation. The strut and tie model and Zararis's Method are based on the assumption that arch action is the main form of shear resistance. Bazant's equation was derived from empirical fitting which incorporated data on deep beams. Hsu's softened truss model was omitted because a proportionality factor was used to account for deep beam behavior, and transverse steel reinforcement is required in the section. Also, solving 12 equations simultaneously is too cumbersome for practical applications. The selected methods will be evaluated through experimental testing described in the following sections.

CHAPTER 3

EXPERIMENTAL SPECIMEN DESIGN

The reinforced concrete specimens tested in this experimental program are based on the pier caps supporting Bridge 085-0018 in Dawson County, Georgia, which carries SR 136 over the Etowah River. The bridge carries two lanes of traffic. Currently the bridge is posted due to shear deficiencies in the pier cap. The pier cap is a 36 inch. reinforced concrete beam spanning between two 36 inch. square reinforced concrete columns, as illustrated in Figure 3.1. The superstructure consists of four steel girders carrying a non-composite concrete deck with sidewalk and parapets. The interior girders are W33x130 steel shapes, and the exterior girders are W33x118 steel shapes. The girders are spaced at 8 ft on center. This makes the shear span 4 ft and the *a/d* ratio 1.43 based on an effective depth of 33.4 inch.

3.1 Critical Section of Reinforced Concrete Pier Caps

To determine the critical components of the reinforced concrete pier cap in terms of maximum stresses and geometric effects, a finite element (FE) model of the bridge superstructure was developed using shell elements in ABAQUS. All materials in the bridge were modeled as linear-elastic. A linear elastic model cannot account for the effects of cracking, but under the applied loads the stresses should be well below the level which would cause cracking. The model was created to determine the distribution of loads from the superstructure to the substructure. The modulus of elasticity for steel was 29,000 ksi, and the modulus of elasticity for concrete was 3605 ksi based on an assumed concrete compressive strength of 4000 psi. 4000 psi was assumed to be a representative concrete strength for a bridge designed in 1964. Load was applied to the

bridge in the form of two AASHTO HS-20 trucks (AASHTO, 2007). To maximize the reaction forces at the supports of each girder, the back axles of the HS-20 trucks were placed on the supports at one edge of the bridge. This was based on the influence line for the reaction forces of a simple span beam. Multiple analyses were performed with the trucks at different transverse positions on the bridge, as shown in Figs. 3.2 (a), (b), (c), and (d). The reaction forces at the end of each girder where the trucks were located are shown in Table 3.1. The girders are labeled G-1 to G-4 in Figs. 3.1 and 3.2, and these labels correspond to the column headings in Table 3.1. The goal of this exercise was to find the largest reactions which, in turn, would cause the greatest shear in the pier cap. From the results in Table 3.1, it can be seen that truck position 4 (Figure 3.2 (d)) causes the greatest force in the outside girder (G1).

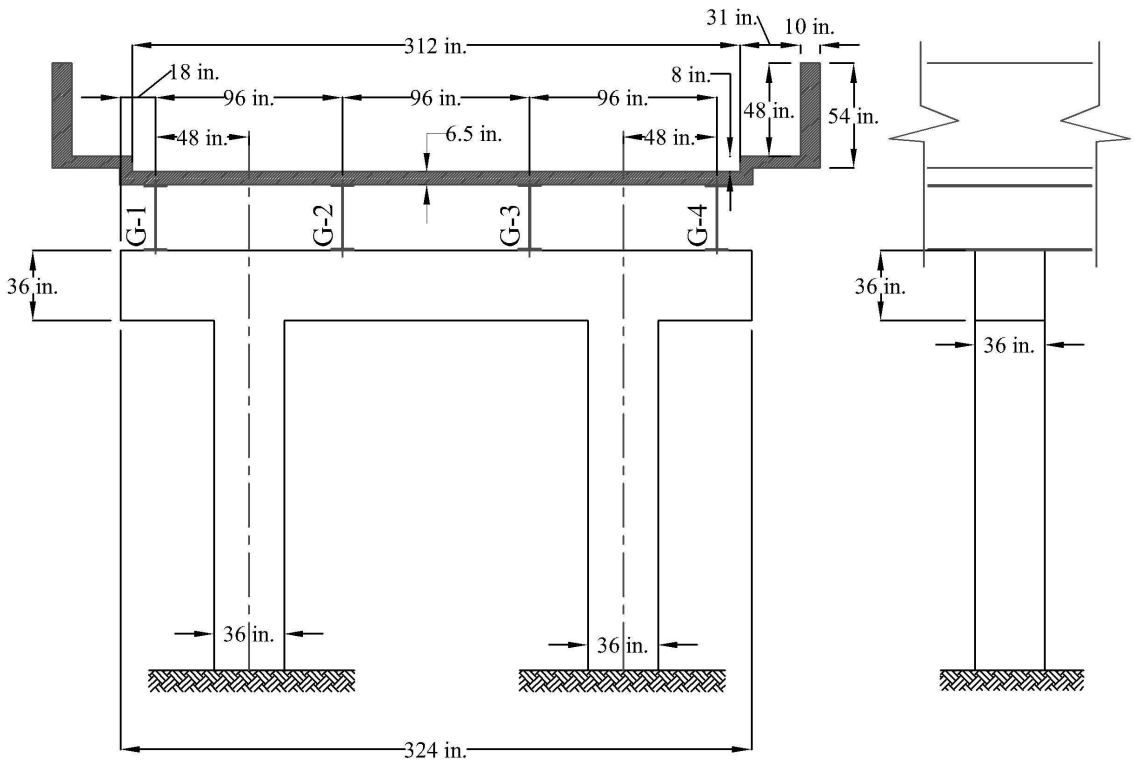

Figure 3.1 Pier and bridge geometry

Table 3.1- Reaction forces at girder support for different truck locations

	Reaction Force (kips)			
Truck Position	G-1	G-2	G-3	G-4
Dead Load	40	12	12	40
1	65	52	52	65
2	75	34	34	75
3	48	61	61	48
4	76	52	47	44

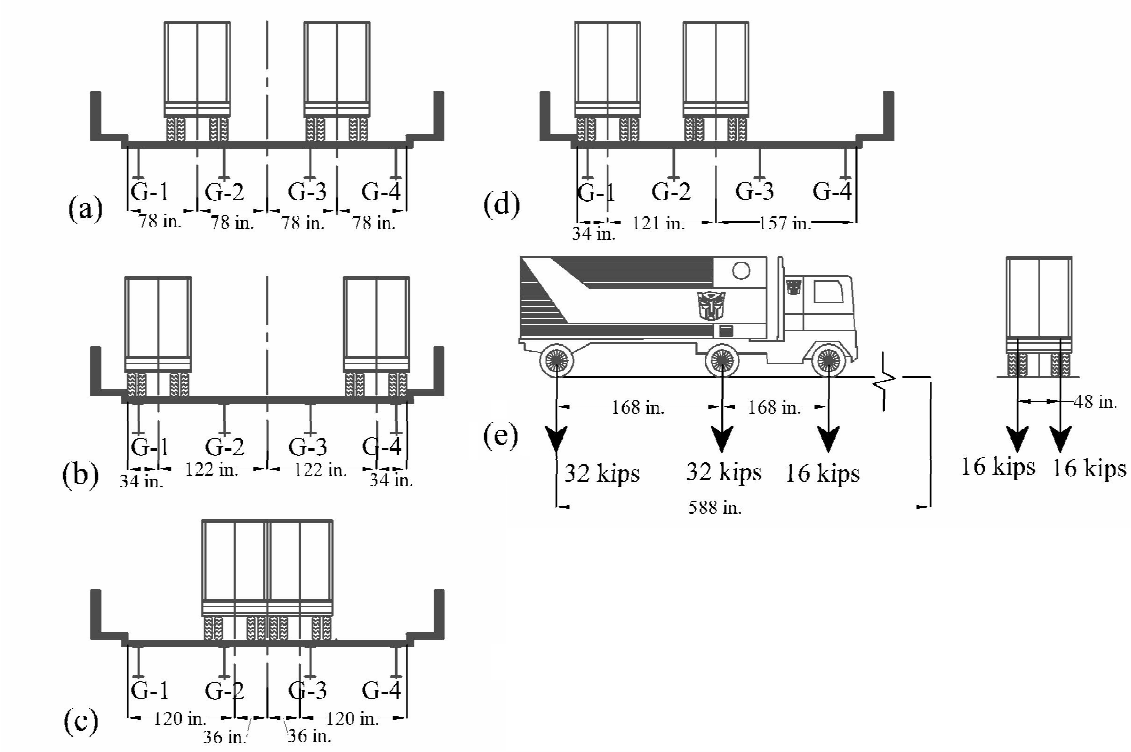

Figure 3.2- (a) Truck position 1, (b) Truck position 2, (c) Truck position 3, (d) Truck position 4, (e) HS-20 truck location on bridge span

With these forces calculated, a FE model of the bridge substructure was developed using three dimensional (Type C3D8R) elements. These are ABAQUS eight-node linear brick elements with hourglass control. These elements use reduced

integration and therefore require hourglass control to prevent modes other than rigid body modes from occuring. The loads for truck position 4 in Table 3.1 were applied as pressures over the girder bearing area (11.5 in. x 36 in.). Figure 3.3 shows the stress contours resulting from this analysis. Stress contours are shown for both the longitudinal stress (S11) and the shear stress (S12). The figure shows that both the longitudinal and shear stresses are larger over the left column between the 76 and 52 kip loads. The greatest shear force occurs between the application of the 76 kip load and the left column; the critical shear occurs at an angle of 51° extending from the edge of the column to the edge of the support.

In testing of deep beams, it is common (e.g., Clark 1951, Moodey et al. 1954, Aguilar et al. 2002) to simulate columns and other bearing areas with steel plates. This is done so that the specimen can be cast as a simple rectangular beam rather than a beam with a stub column. To investigate the effects of using either steel plates or shortened columns, two additional FE analyses were performed. In the first, the column length was reduced to 18 inches, while in the second, the column was replaced with a 2 inch. thick steel plate.

Figure 3.4 shows the results when the column length is reduced to 18 inches. The results are very similar to those of the entire pier. The critical shear area is still in the same location, and the shear stress forms at the same 51° angle. The magnitudes of the shear and longitudinal stress are very similar in both the full pier and the pier with 18 inch columns. The pier with 18 inch columns replicates the entire pier well.

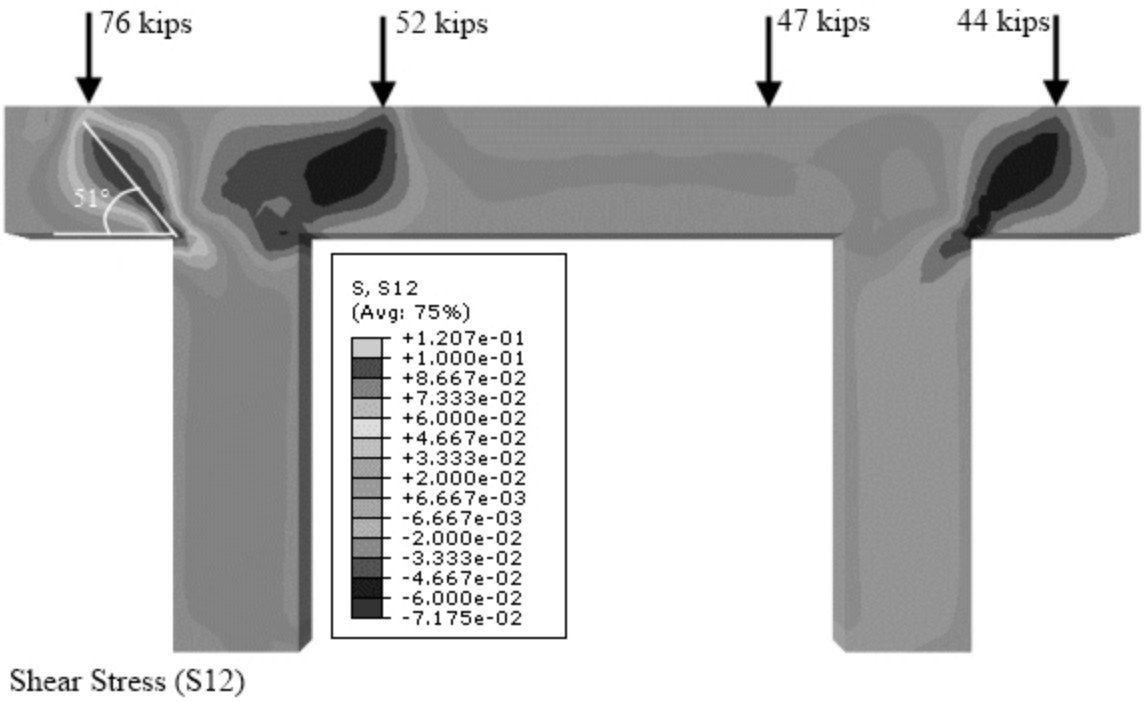

Shear Stress (S12)

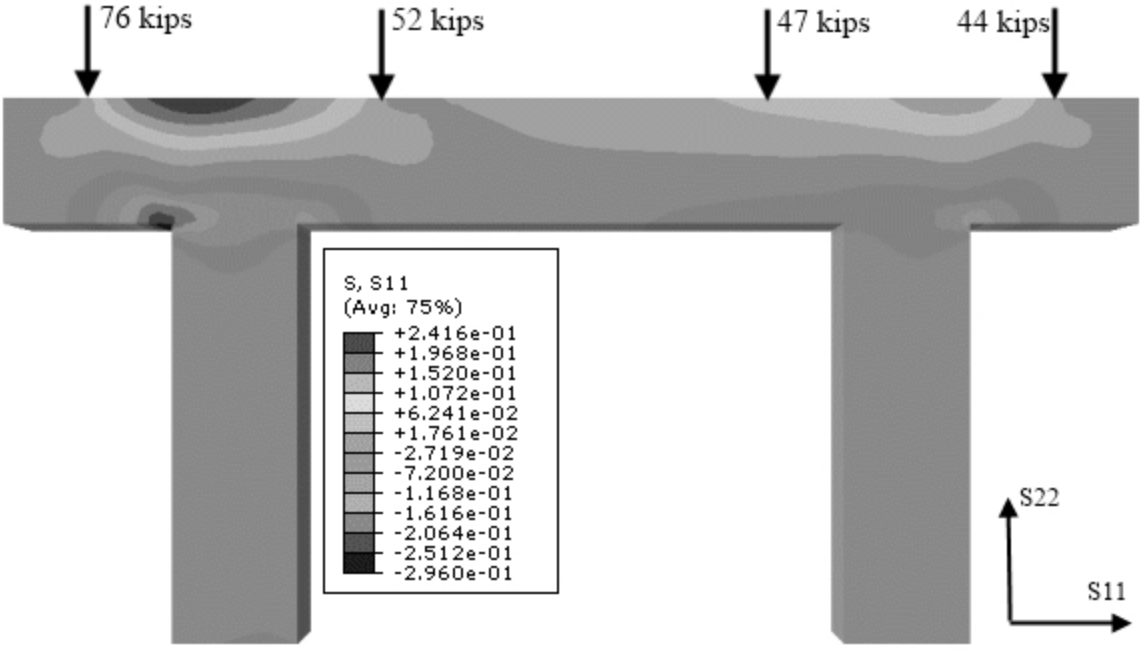

Longitudinal Stress (S11)

Figure 3.3- Longitudinal (S11) and shear stress (S12) for entire pier cap

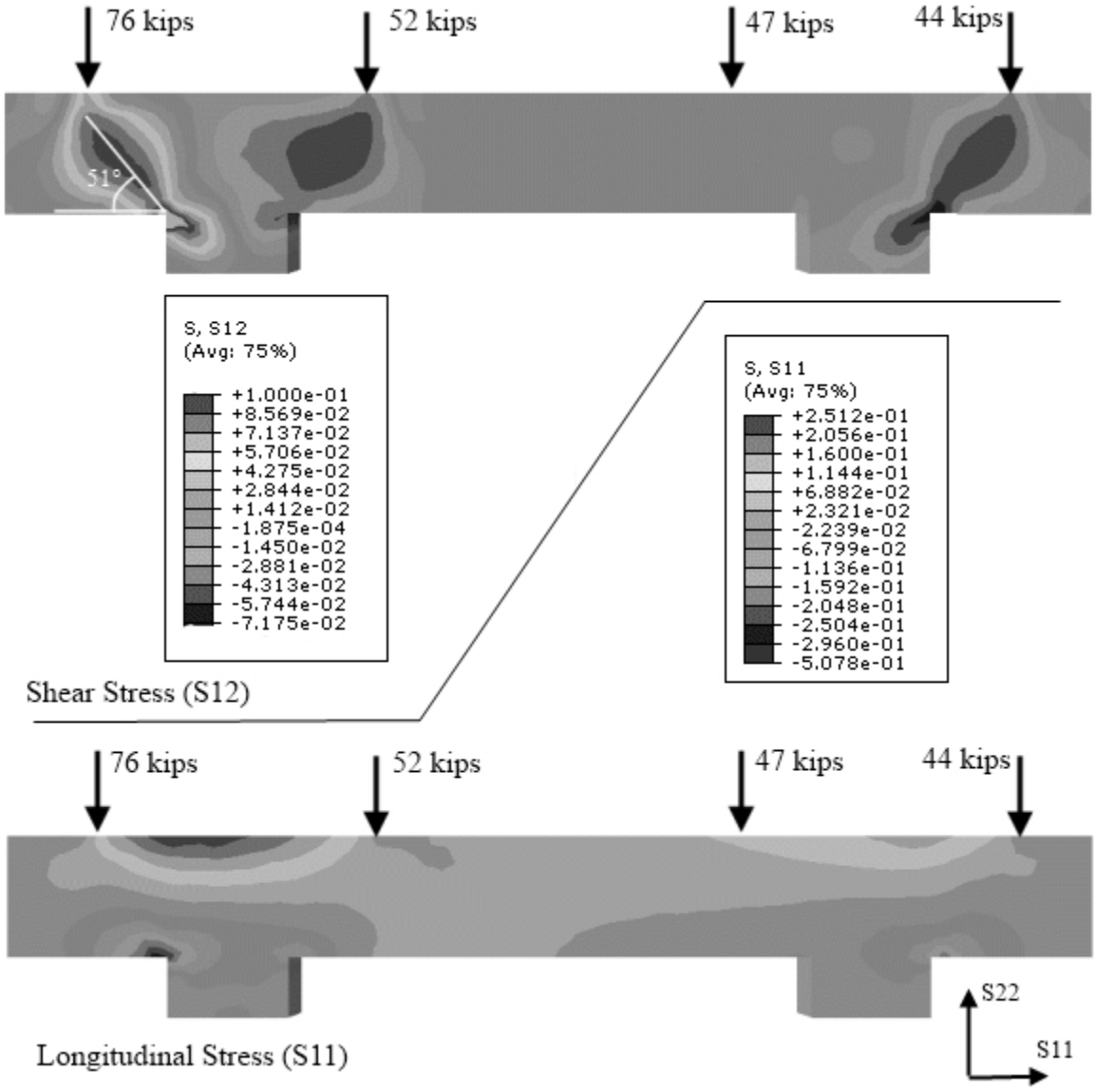

Figure 3.4- Longitudinal (S11) and shear stress (S12) for pier cap with 18 inch. column

Figure 3.5 shows the stresses developed when the column is replaced with a 2 inch. thick steel plate. Two-dimensional shell elements were used to model the steel plates. The plates were connected to the concrete pier using ABAQUS multi-point constraint (MPC) beam elements. These elements link together two nodes and make the rotations and displacements identical; they are infinitely stiff beam elements. While the

stresses in the longitudinal direction remained similar to those of the pier; there is a change in the shear stresses. The magnitudes of the stresses are similar, but the shear stress occurs at an angle of 46° and is wider. The change in the angle is due to the difference in stiffness between the 2 inch. steel plate and the concrete stub column at the point of applied load. The steel plate is less stiff and can bend; this causes a reduction in the angle of the compression strut. Also, it can be seen that stress concentrations which form at the corners of the column are not present when the steel plate is used.

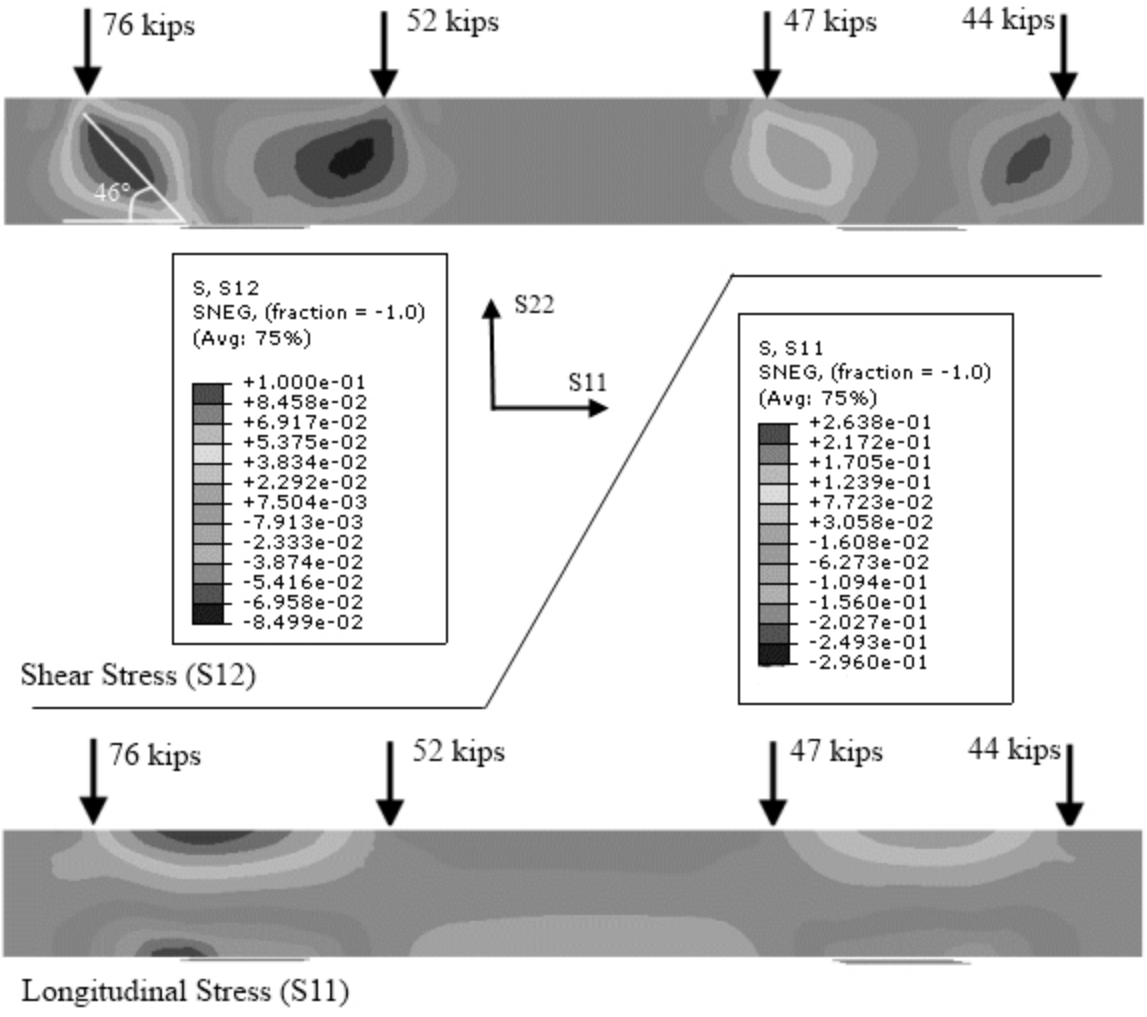

Figure 3.5- Longitudinal (S11) and shear stress (S12) for pier cap with 2 inch. steel plate

These analyses show that using a steel plate at the point of application of the concentrated load in the test alters the distribution of stresses in the pier cap. A concrete stub column is necessary to ensure that the response of the laboratory specimen is as close as possible to that in the existing structure. To simplify laboratory testing, symmetric loading was used. One final FE model was created of the critical section of the pier, consisting of one 18 inch. column with two 76 kip loads applied symmetrically around it; the stress contours from this model are shown if Figure 3.6. A schematic of the critical pier section and corresponding test specimen are shown in Figure 3.7.

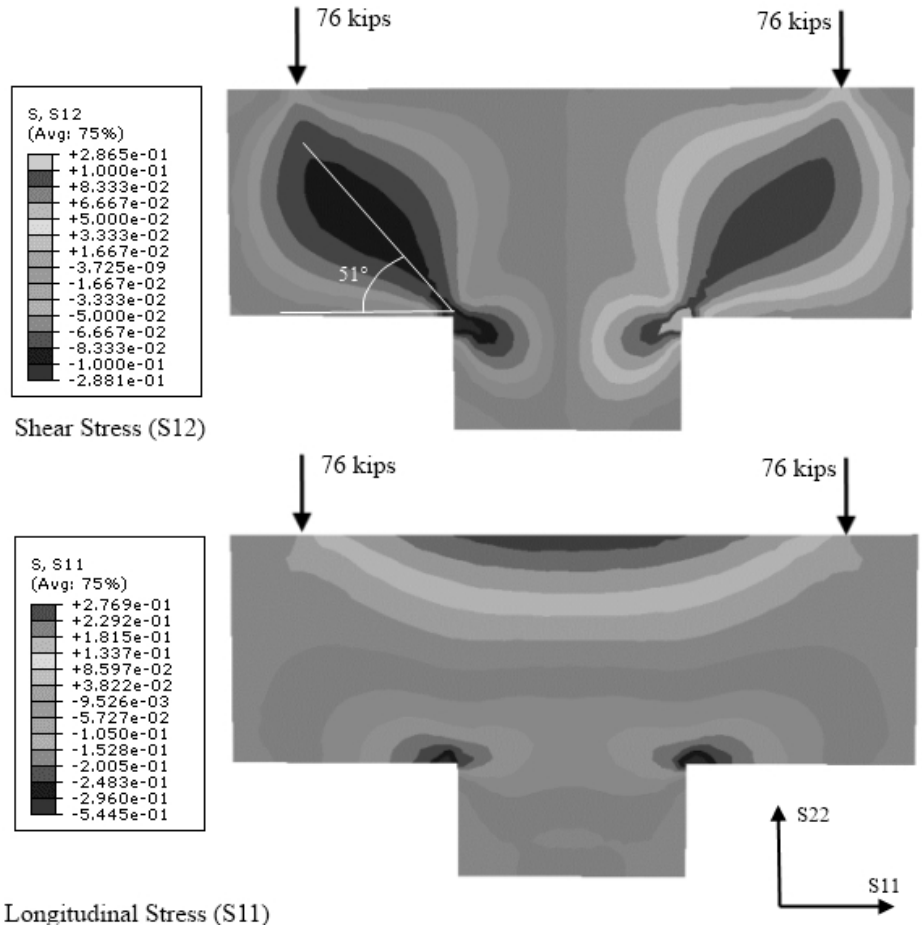

Figure 3.6- Symmetric loading of critical pier section with 18 inch column

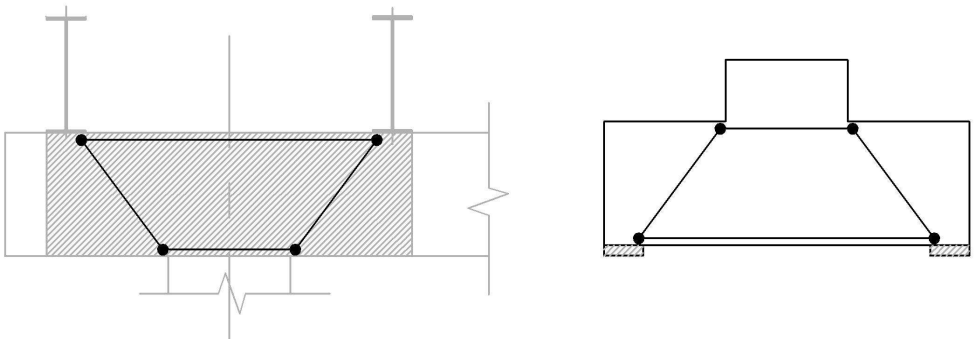

Figure 3.7- Critical pier section and test specimen

3.2 Large Specimen Design

Experimentation on pier cap specimens of prototypical size (36 in. by 36 in.) is difficult because of their weight and large ultimate capacity. By creating scaled specimens, experimentation becomes less difficult, provided that the size effects (if any) can be treated properly. It is possible to use what is known about the size effect in shear along with the laws of similitude to design appropriately scaled specimens.

The first step in scaling the reinforced concrete specimen is to reduce the width. It has been shown that there is no size effect associated with scaling beam width (Kani, 1967). Reducing the width of a 36 inch deep specimen to 18 inches makes it possible to decrease the shear and moment capacity by a factor of two. The longitudinal reinforcement ratio for a typical 36 inch by 36 inch pier cap in the State of Georgia ranges from a minimum of around 0.5% to approximately 1.5%. The pier cap in Bridge 085-0018 in Dawson County has a 36 inch width and an effective depth of 33.4 inches. The main longitudinal reinforcement consists of six #10 bars, making the reinforcement ratio in the pier cap approximately 0.65%. This reinforcement ratio and a ratio of 1.3% were chosen for two different 36 inch deep specimens. Having two different reinforcement ratios allows the effects of the longitudinal reinforcement to be observed.

These large specimens are shown in Figure 3.8. The beam with 1.3% longitudinal reinforcement contains six #10 bars with a combined area of 7.62 in^2, and the beam with 0.65% longitudinal reinforcement contains half the reinforcement or 3 #10 bars with an area of 3.81 in^2.

The development for the longitudinal bars is provided externally with steel plates and ERICO bolt couplers. These couplers allow a bolted connection to be attached to the end of the reinforcing bars. Development of the reinforcement is provided in this manner so that the force in each bar can be monitored using a load cell, as shown in Figure 3.9. The load cell fits over the coupler and the whole assembly is bolted into place. The force in the bar is transferred through the coupler into the bolt. The bolt bears on the washer plate which transfers the load through the load cell to the bearing plate and back into the concrete specimen, thus developing the strength of the bar. The length of the bearing plate is determined by taking six times the bar diameter, which is the value used in the 2007 AASHTO LRFD Bridge Design Specifications when determining the bearing area of longitudinal bars in a strut and tie analysis

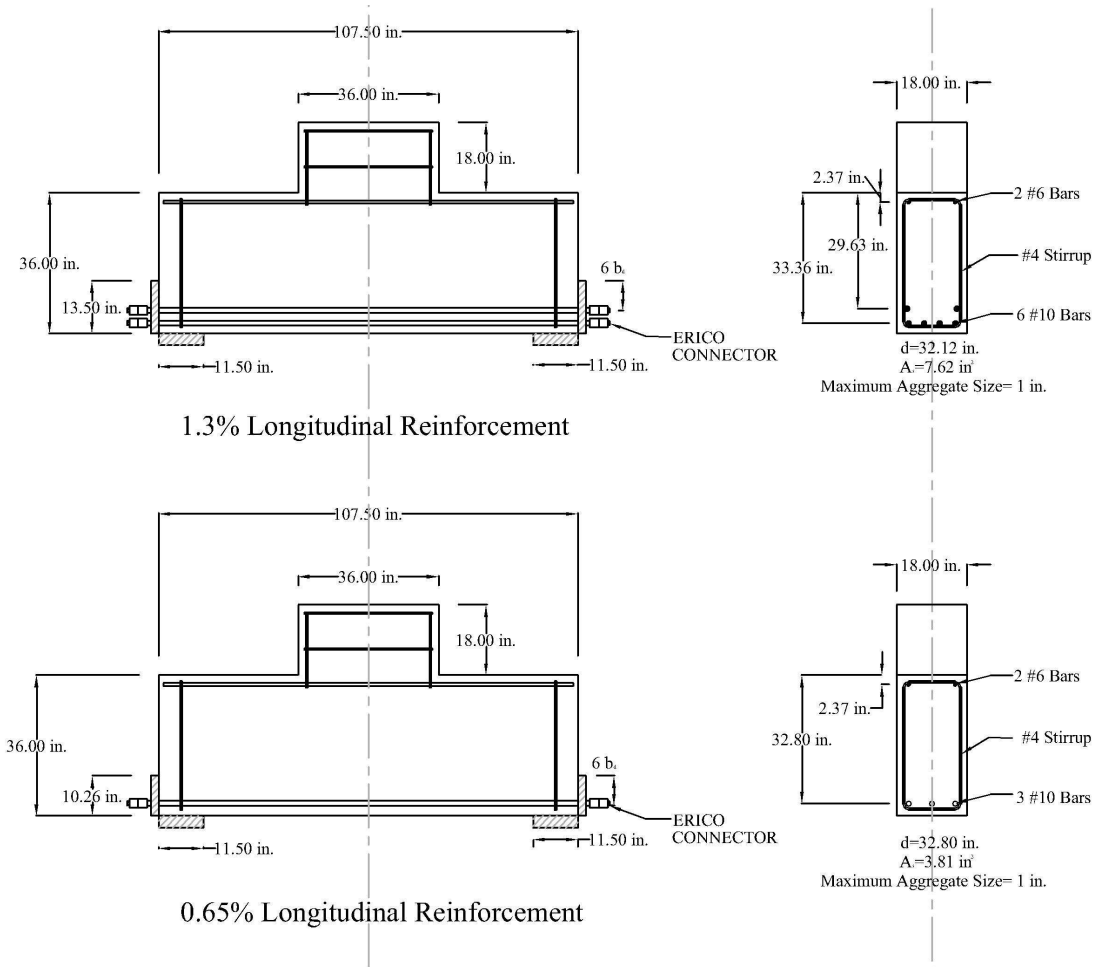

Figure 3.8- Large beam specimens

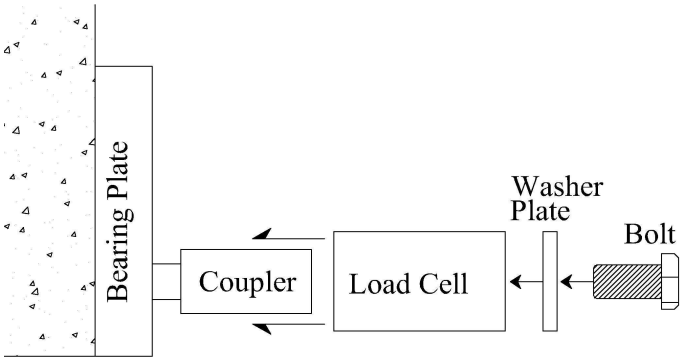

Figure 3.9- Bar development detail

3.3 Small Specimen Design

To achieve further reduction in test specimen size, a dimensional analysis was performed using Eq. 2.2, and the equations governing moment equilibrium of reinforced concrete beams in flexure. Dimensional analysis is a tool that makes it is possible to deduce how certain variables affect a specific response variable without knowing the actual mathematical relation between the variables. The basis of this analysis is the Buckingham Pi Theorem which states: "If there is an independent function that is made up of physical variables, it can be transformed into another function made up of dimensionless Pi terms (Sabnis and Harris, 1983)." The number of Pi terms is dictated by both the number of physical variables and independent physical units. Independent physical units are dimensions such as length, force (or mass), temperature, electric charge, and time. With the resulting Pi terms from the dimensional analysis it is possible to show similitude of specimens at different scales. If the dimensionless Pi terms are equal for specimens at different scales, there is similitude between the specimens.

The dimensional analysis of the reinforced concrete specimen with Eq. 2.2 is complicated by the term $(1+\sqrt{(0.2/d_a)})$, which accounts for the influence of aggregate size. In this term, 0.2 is a constant which represents characteristic length. Characteristic length is a material constant with units of inches. This value depends on sand grain size and the difference between the elastic moduli of the aggregate and the mortar. It governs the minimum possible width of a zone of strain-softening damage in non-local continuum formulations or the minimum possible spacing of cracks in discrete fracture models. This length must be determined experimentally (Bazant and Pijaudier-Cabot, 1989). The effectiveness of the dimensional analysis relies on being able to scale each element of the equation which has physical units. In most cases this applies only to physical variables, but in this case a constant has physical units. For this reason it is not

possible to directly scale the specimen using Eqs. 2.2 and have models with perfect similitude, but the difference in the model scales can be accounted taken into account.

The physical variables for the dimensional analysis are given in Table 3.2. Note that the dimensions of the areas of the supports (j) and the point at which the load is applied (k) are included and that ρ_v can be simplified into A_{sv}/bd. The independent physical units for this analysis are force and length. By placing the physical units into Table 3.3 along with the identity matrix the Pi analysis can be performed using Eq. 3.3 to calculate Matrix C. With Matrix C, the Pi terms can be assembled by reading Table 3.3 from left to right. The dimensionless Pi terms produced by this analysis, shown in Figure 3.10, can be used to scale the reinforced concrete pier specimens illustrated in Figure 3.11. It is important to note that the maximum aggregate size is scaled in each specimen. The large specimen has a maximum aggregate size of one inch, while the small specimen has a maximum aggregate size of ½ -inch. As before, the longitudinal reinforcement will be provided by normal deformed bar reinforcement bonded to the concrete, and development will be provided in the same manner as the large specimen.

Table 3.2- Physical variables

Physical Variables	Physical Units	Description
A_s	in^2	area of longitudinal steel reinforcement
b	in	beam width
d	in	depth to longitudinal steel reinforcement
a	in	shear span
d_a	in	maximum aggregate size
f'_c	lb/in^2	concrete compressive cylinder strength
f_y	lb/in^2	yield stress of longitudinal steel
A_{sv}	in^2	area of transverse steel
f_{yv}	lb/in^2	yield stress of transverse steel
S	in	transverse steel spacing
j	in	length of support area
k	in	length of applied load area

Table 3.3- Pi analysis

	A_s	B	j	a	d_a	k	f_y	A_{sv}	f_{yv}	D	f'_c
Length	2	1	1	1	1	1	-2	2	-2	1	-2
Force	0	0	0	0	0	0	1	0	1	0	1
π_1	1	0	0	0	0	0	0	0	0	-2	0
π_2	0	1	0	0	0	0	0	0	0	-1	0
π_3	0	0	1	0	0	0	0	0	0	-1	0
π_4	0	0	0	1	0	0	0	0	0	-1	0
π_5	0	0	0	0	1	0	0	0	0	-1	0
π_6	0	0	0	0	0	1	0	0	0	-1	0
π_7	0	0	0	0	0	0	1	0	0	0	-1
π_8	0	0	0	0	0	0	0	1	0	-2	0
π_9	0	0	0	0	0	0	0	0	1	0	-1

Matrix B

Matrix A

Identity Matrix

Matrix C

$$[C] = -([A]^{-1} * [B])^T \qquad (3.3)$$

$$\pi_1 = \frac{A_s}{d^2} \qquad \pi_2 = \frac{b}{d} \qquad \pi_3 = \frac{j}{d}$$

$$\pi_4 = \frac{a}{d} \qquad \pi_5 = \frac{d_a}{d} \qquad \pi_6 = \frac{k}{d}$$

$$\pi_7 = \frac{f_y}{f'_c} \qquad \pi_8 = \frac{A_{sv}}{d^2} \qquad \pi_9 = \frac{f_{yv}}{f'_c}$$

Figure 3.10- Pi terms

Table 3.4 compares the Pi values for the scaled specimens at the two different reinforcement ratios along with the loads to cause the nominal shear, calculated by Eq. 2.2, and moment. In these specimens, no shear reinforcement is provided in the span so π_8, which is the scaling factor for shear reinforcement, is not required. Term π_8 is included for use in the design of later specimens. There is good agreement with all of the Pi terms. The only term which shows any difference is π_1; this term scales the longitudinal reinforcement ratios. The exact area of steel is not scaled perfectly because it is linked to available bar sizes. Equation 2.2 is used to calculate the nominal shear strength of the specimen. Since the specimens are loaded in three-point bending and are symmetric, the load to cause shear failure (P_v) is calculated by multiplying the nominal shear strength by two. The load to cause moment failure is calculated by multiplying the nominal moment capacity by 4 and dividing by the span length. The nominal moment capacity is calculated using a rectangular stress block as in Eqs. 3.1 and 3.2. If the specimens were perfectly scaled the ratio of P_v/P_m would be the same for both the large and small specimens. As discussed earlier the characteristic length constant in Eq. 2.2 makes this almost impossible, and the P_v/P_m ratios for the specimens with 1.31% and 0.655% longitudinal reinforcement ratios differ by 10.5%

and 12%, respectively. With this difference known, however, it is possible to account for it when examining the experimental results.

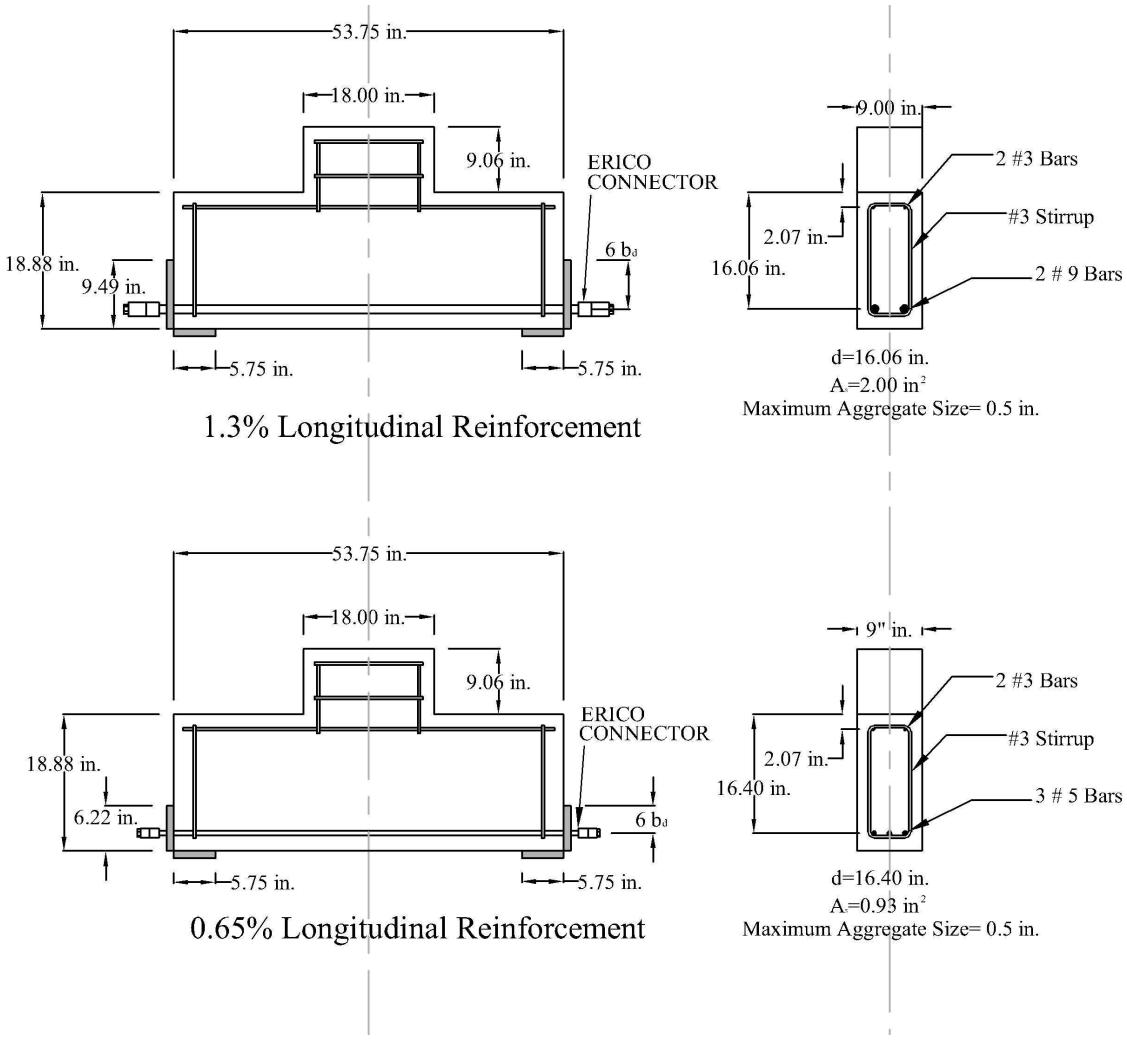

Figure 3.11- Small beam specimens

Table 3.4- Comparison of Pi terms

	ρ = 1.3 %			ρ = 0.65 %		
	Large	Small	% Difference	Large	Small	% Difference
π_1	0.00739	0.00775	4.8%	0.00354	0.00346	2.4%
π_2	0.56040	0.56040	0.0%	0.54878	0.54878	0.0%
π_3	0.35803	0.35803	0.0%	0.35061	0.35061	0.0%
π_4	1.49440	1.49440	0.0%	1.46341	1.46341	0.0%
π_5	0.03113	0.03113	0.0%	0.03049	0.03049	0.0%
π_6	1.12080	1.12080	0.0%	1.09756	1.09756	0.0%
π_7	15	15	0.0%	15	15	0.0%
π_8	0	0	0.0%	0	0	0.0%
π_9	15	15	0.0%	15	15	0.0%
Pv (kips)	321.9	93.8		212.5	59.0	
Pm (kips)	540.7	141.0		294.6	72.0	
Pv/Pm	0.59540	0.66520	10.5%	0.72136	0.81974	12.0%

3.4 Design of Instrumentation

The instrumentation was designed to monitor several aspects of the performance of the specimens. These are:

- the applied load
- deflection at midspan
- principal compression strut angle
- strains in the longitudinal tension reinforcement
- longitudinal strains in the compression zone
- transverse stains in the shear span
- force in the longitudinal tension steel anchorage

Achieving each of these goals required different instrumentation, and in some cases multiple instrumentation schemes were used to look at the same phenomena. Figure 3.12 shows the location of all of the instrumentation.

The applied load was monitored using a single load cell under the hydraulic ram. The applied load is the metric for the entire test. All of the significant occurrences such as cracking and failure will be distinguished by the applied loads at which they occur. The mid-span deflection of the beam was monitored with a single string potentiometer. The deflection was monitored because, in conjunction with the applied load, it is a good indicator of ductility.

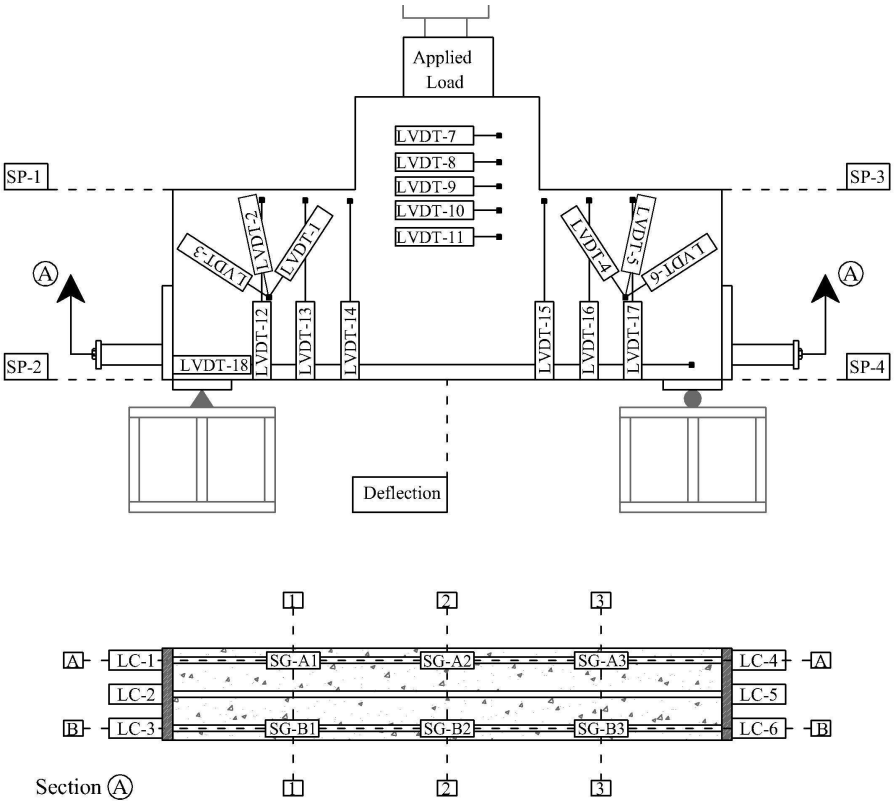

Figure 3.12- Instrumentation diagram

The main phenomenon that distinguishes the behavior of deep beams from ordinary beams is their ability to carry load through arch action. Fenwick and Paulay (1968) concluded that arch action and beam action were incompatible because arch action cannot occur to any appreciable extent until after the breakdown of beam action.

For this reason it is important to have a good understanding of when arch action is initiated, and several different instrumentation methods were used to capture the initiation of arch action. The first is the strain gages bonded to the reinforcing bars. Theoretically, once the arch action is initiated, the strain in the longitudinal reinforcement should become constant over its length. Linear variable differential transformer (LVDT) 18 (Figure 3.12) spans the entire length of the beam. This effectively gives the longitudinal strain at the bottom of the beam averaged over its length, including all of the cracks. It was thought that this strain data might give insight into when arch action occurs. In conjunction with this idea, the end rotations of the beam were monitored using string potentiometers 1 – 4. The string potentiometers were used to monitor displacements; rotation angles at the ends of the beam were calculated from the relative displacements. The data collected from this instrumentation as well as the calculated compression strut angle were used to determine the point at which arch action becomes the effective load carrying method.

One of the main factors that governs the performance of deep beam behavior is the angle at which the primary compression strut forms. For this reason, several instrumentation schemes were used to identify this angle. Two rosettes of LVDTs (LVDTs 1,2,3 and LVDTs 4,5,6) were used to compute the principal stresses using a mechanics of materials approach. Longitudinal forces produced by the reinforcement were calculated using constitutive relations and strains from the strain gages on the reinforcing bars and from LVDT 18. , Using these longitudinal forces and vertical reactions calculated from static equilibrium, an effective strut angle was calculated. Once the bars completely debonded, the force from the load cells at the anchorage could be used for the longitudinal force and the strut angle could again be calculated. The load cells mounted on the ends of the longitudinal reinforcement also served to measure the amount of force needed to develop the longitudinal reinforcement.

Finally, LVDTs were positioned vertically within the shear span of the beam (Figure 3.12) to capture the transverse strains.

CHAPTER 4

ULTIMATE CAPACITY OF REINFORCED CONCRETE PIER CAPS

The first part of the experimental plan was an investigation into the behavior of the reinforced concrete specimens leading up to and at their ultimate state. The effects of the amount of longitudinal and crack control reinforcement were of particular interest. The longitudinal tension reinforcement is one of the more variable parameters in reinforced concrete pier caps. The amount of the crack control reinforcement is a requirement which has changed over time. Understanding how it influences the behavior is important in understanding older pier caps. Scaled specimens were also tested to observe the size effect.

4.1 Specimen Construction

Figure 4.1 shows the formwork for one of the large specimens. Special attention was paid in the formwork design to remove inclusions in the concrete which serve as crack initiators. For this reason, buttresses were used for the large specimen formwork instead of the more common ties. Before the reinforcing bars were placed into the formwork, they were instrumented with strain gages. The bars were smoothed using a grinding wheel, and then the strain gages were epoxy bonded to the bars. Lead wires were then soldered to their terminals. All gages were sealed with silicone for protection. Figure 4.2 shows the strain gages installed on the reinforcing bars. Before the bars were placed in the formwork, the strain gages were tested by placing the bar in three point bending, applying a known load and comparing the theoretically calculated strains under the load to the measured strains. The wires for the strain gages were run along the

longitudinal tension reinforcement and out of the top of the beam as shown in Figure 4.3.

Figure 4.1- Large specimen formwork

Figure 4.2- Rebar with strain gages installed

Figure 4.3- Strain gage wires and coil bolt anchor detail

To allow for the installation of the Erico bolt couplers and the monitoring of the forces in the bar anchorage, the ends of the reinforcement projected from the formwork, as shown in Figure 4.4. The rebar spanned from one end of the formwork to the other. This allowed the rebar to be placed at the proper height without the use of rebar chairs, further reducing the amount of crack initiators in the specimen.

Two different concrete mixes were needed to cast the large and small specimens. The mix for the large specimens required a maximum aggregate size of one inch while the mix for the small specimens required a maximum aggregate size of one-half inch. The desired concrete strength for both of the mixes was between 3500 and 4500 psi. The mixes were chosen by looking at recent 28 day cylinder strengths. The mix for the large specimen had a designation of RMXBJASAAND and an average 28 day cylinder strength of 3,735 psi plus or minus one standard deviation of 331 psi (3735± 331 psi) based on 39 samples. The mix for the small specimen had a designation

of RMXBJAGEAUE and an average 28 day cylinder strength of 3685 psi based on two samples.

Figure 4.4- Longitudinal reinforcement extended outside of formwork

All specimens were cast in two stages. On the first day, all of the beams were cast. Figure 4.5 shows the beams after the placement of the concrete. The concrete was then allowed to cure for 48 hours, and then the column stubs were cast on top. This created a cold joint between the beam and the column stub in the same location as there would be in a common pier cap. The concrete in the area of the column was roughened to improve friction between the column and the beam; this is shown in Figure 4.6. The concrete used in all of the columns for all of the beams (large and small) had a maximum one inch aggregate size. Since cracking and failure were expected to occur in the beam not in the column, the difference in the aggregate size was inconsequential. For curing, after each pour the beams were covered with wetted burlap and plastic; this

is shown in Figure 4.7. The finished specimens are shown in Figure 4.8 after removal from the formwork.

Figure 4.5- Specimens after first casting

Figure 4.6- Concrete roughened in column area

Figure 4.7- Specimen covered for curing

Figure 4.8- Completed specimens

4.2 Experimental Set-up

Preparation for the test of each specimen consisted of positioning specimen in the test frame with the proper alignment and span and installing the external instrumentation. Table 4.1 gives the designations of the Phase I specimens as well the depth (d) reinforcement ratio (ρ) and the shear span to depth (a/d) ratio. The shear span (a) is the distance from the center of the column to the center of the support.

The specimens were cast at two separate times. The first casting involved three 36 inch specimens and three 18 inch specimens. These specimens were cast on the same time period from ready mix concrete trucks and are designated as the A series. An additional small specimen (AS4) was cast later with concrete mixed in house and was included with the A series specimen. The second casting was of seven 36 inch specimens. These specimens are designated as B Series specimen. In Table 4.1 the specimens are designated A and B according to their series. The 36 inch deep specimens are labeled with an L, and the 18 inch deep specimens are labeled with an S.

Table 4.1- Phase I specimen designations and parameters

Specimen Designation	Height (in)	d (in)	ρ (%)	Span (in)	a (in)	a/d
AL1	36	32.8	0.65	96	48	1.46
AL2	36	32.1	1.3	96	48	1.49
AS1	18.88	16.4	0.65	48	24	1.46
AS2	18.88	16.4	0.65	48	24	1.46
AS3	18.88	16.1	1.3	48	24	1.49
AS4	18.88	16.1	1.3	48	24	1.49
BL1	36	32.8	0.65	96	48	1.46
BL2	36	32.1	1.3	96	48	1.49
BL3	36	32.1	1.3	96	48	1.49
BL4	36	32.1	1.3	96	48	1.49
BL5	36	32.1	1.3	96	48	1.49

Figure 4.9 shows a small specimen loaded into the testing frame. Load was applied to the specimen using a hydraulic ram; the force applied by the ram was measured using a load cell. A ball and socket joint was placed in between the beam and the ram to prevent the transfer of moment into the ram. The ball and socket arrangement does not prevent the ram from applying lateral load resistance. Pin and roller supports were used. The supports were spaced to give the small specimens a total span of 48 inches. Figure 4.10 shows a small specimen with the external instrumentation installed.

Figure 4.11 shows a large specimen in the load frame. For the large specimens a tapered stack of steel plates was used to distribute the force from the ball and socket joint into the column stub. The same pin and roller supports were used, and they were spaced to give the large specimens a 96 inch span. Figure 4.12 shows a large specimen with external instrumentation.

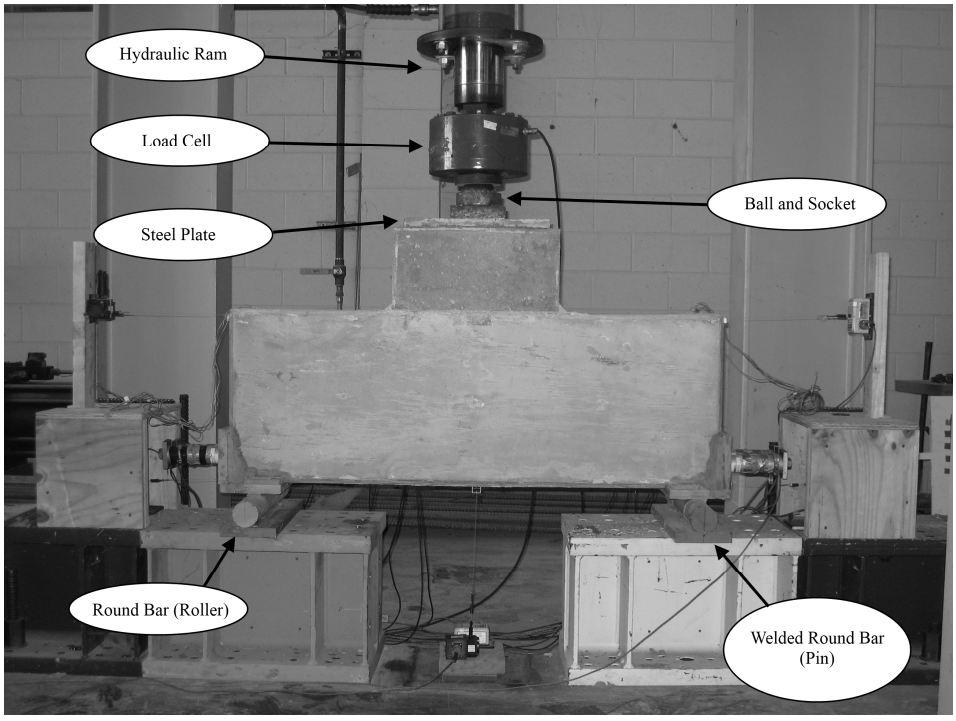

Figure 4.9- Small specimen in test frame

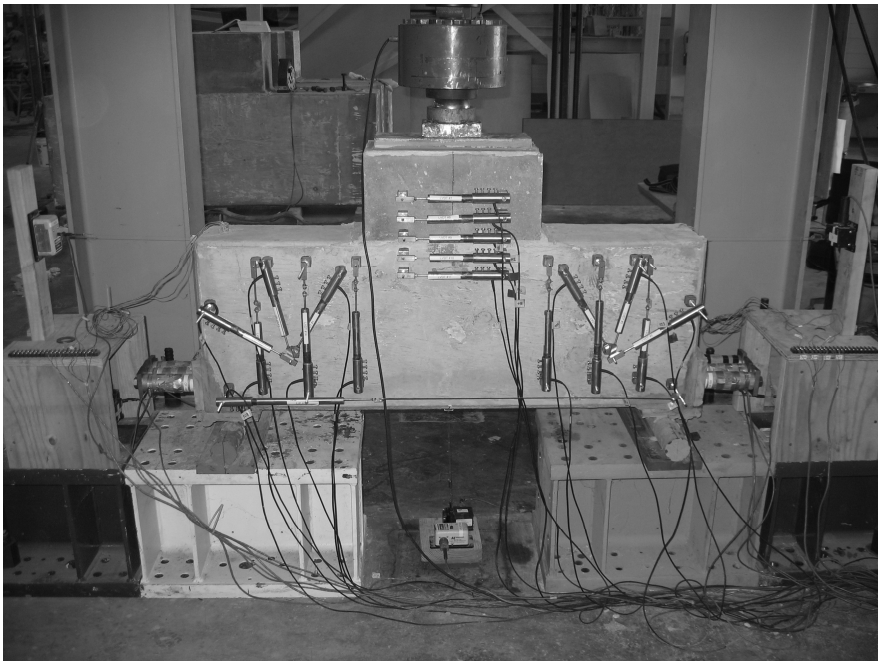

Figure 4.10- Small specimen with external instrumentation

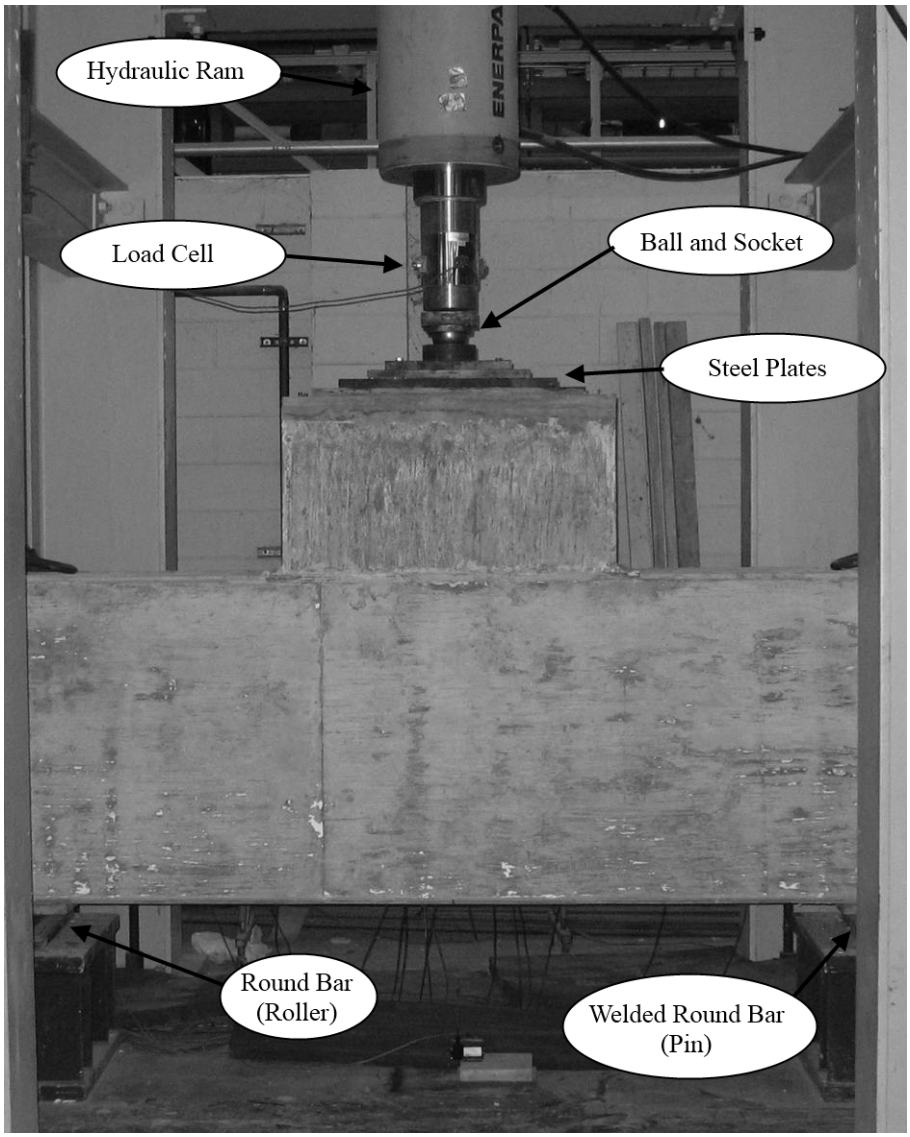

Figure 4.11- Large specimen in test frame

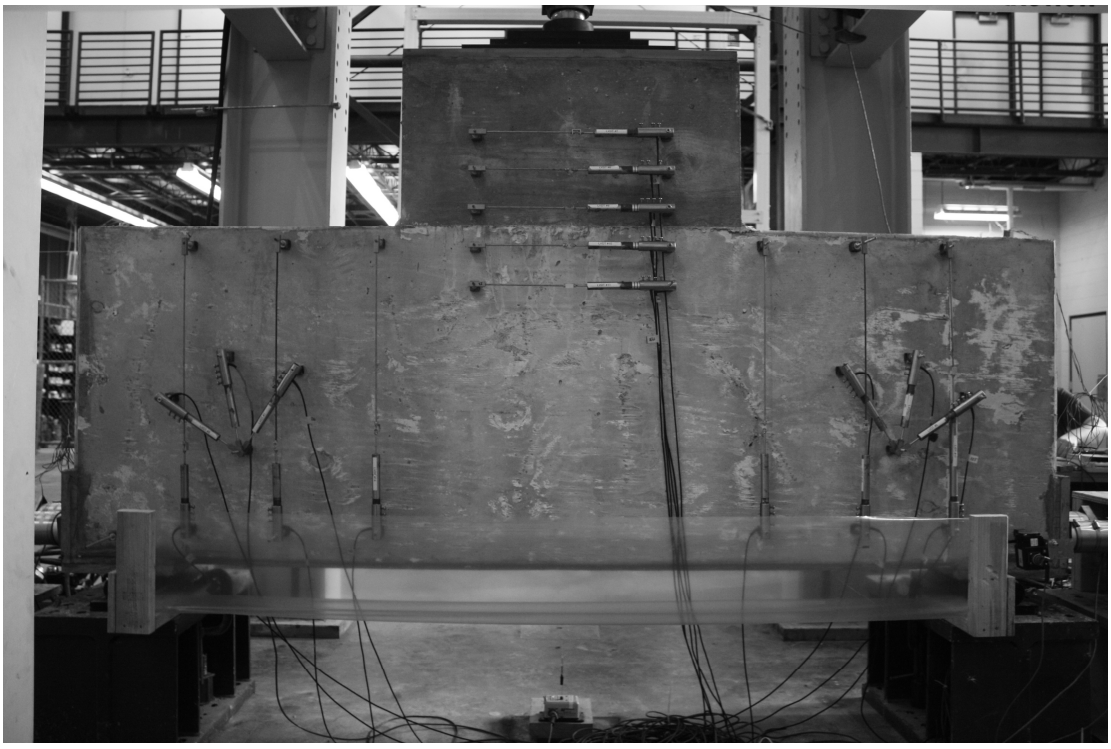

Figure 4.12- Large specimen with external instrumentation

4.3 Tests of Small Scale Specimens

The tests of the small scale specimens follow. These tests were performed first. The tests were easier to set up and perform due to the specimen size.

4.3.1 Test of Specimen AS1

On the day of the beam test, companion concrete cylinders that had been cast along with the beam were tested for compression strength (ASTM C-39, 2010), tensile strength (ASTM C-496, 2004), and elastic modulus (ASTM C-469, 2002). Based on these companion cylinder tests, the concrete in the beam had an average compressive strength of 4,123± 168 psi based on three samples, an average tensile strength of 421± 43 psi based on three samples, and an average elastic modulus of 3,177± 348 ksi based on three samples. Only compression tests were performed on the concrete in the

column; the concrete in the column had an average compressive strength of 3,046± 293 psi based on three samples. The average yield strength of the longitudinal steel was 79± 1.7 ksi based on three samples.

Load was applied to the specimen using a hydraulic jack. Data were recorded from all channels of instrumentation at a rate of 1Hz. The load was applied slowly to achieve a quasistatic response, and at several points during the test, loading was stopped, allowing time to observe, mark, and measure crack sizes. The crack sizes were only marked and measured up until a load of 120 kips; this was the estimated capacity of the specimen.

The first cracks to form in the specimen were flexural cracks directly below the edges of the stub column on the tension face of the beam at a load of 60 kips. These cracks are labeled *B* and *C* in Figure 4.13. Diagonal shear cracks did not form until a load of 90 kips when crack *D* formed. Crack *A* formed at a load of 110 kips. The ultimate strength of the specimen was governed by yielding of the longitudinal reinforcement at an applied load of 165 kips. Once the longitudinal reinforcement yielded, the specimen deformed with little increase in applied load. At an applied load of 172 kips, the concrete at the tip of Crack *A* crushed. The crushing of the concrete in the beam also caused damage to the column; in Figure 4.13 the column steel can be seen where the concrete in the column has spalled.

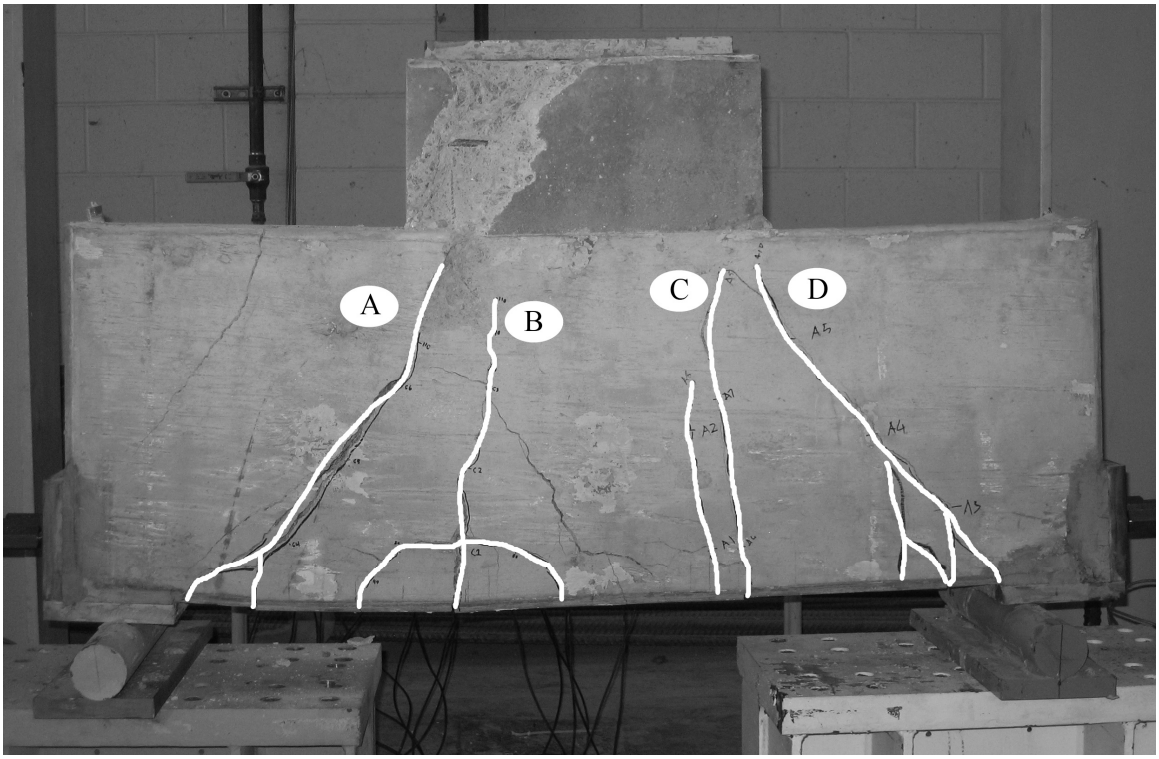

Figure 4.13- Cracks in specimen AS1

Following an analysis of the test results, it was determined that the behavior of each test could be best described by the plot of load vs. deflection and the plot of strut angle vs. load. The strut angle was calculated using equilibrium and the strain in the longitudinal tension reinforcement. Of the longitudinal strain measurements, LVDT 18 (shown in Figure 4.14) provided an average strain for the longitudinal tension reinforcement. The strains recorded by the strain gages attached to the longitudinal reinforcement were affected by cracking in the specimen. Gages located closer to the cracks showed higher strains than those farther away. The LVDT spanning from one support to the other effectively averaged out the localized effects of the cracks. Strain gages bonded to the longitudinal tension reinforcement provided a back-up measurement of the longitudinal strain. When multiple layers of bars were used (Specimens AL2, BL2, BL3, BL4 , and BL5), the externally bonded LVDT also had the

advantage of being placed at the centroid of the longitudinal tension force even when it did not correspond with the centroid of the bars themselves. Only qualitative conclusions can be made from the load cells anchoring the longitudinal reinforcement, and the results are shown in Appedix A. The gage length of the LVDT's in the compression zone was too large to obtain useful measurements on their own (LVDT's 7, 8, 9, 10, and 11), but their measurements were used to calibrate an elastic finite element model. The other instrumentation did not provide any additional insight and will not be discussed.

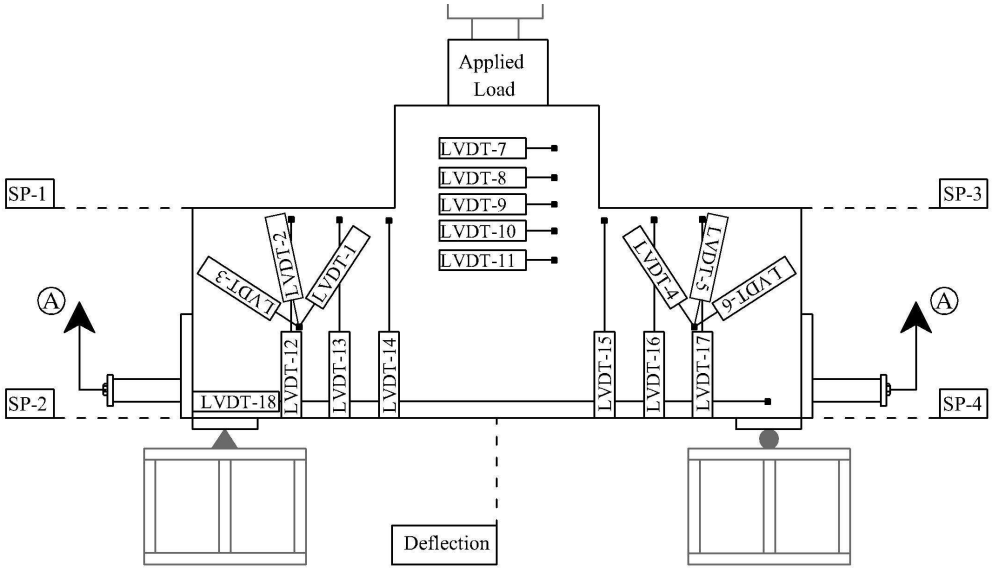

Figure 4.14- External instrumentation diagram

Figure 4.15 shows the load vs. deflection plot for Specimen AS1. Labeled on the figure are the loads at which cracks formed and the load at which the longitudinal reinforcement yielded. The crack labels correspond to the cracks shown in Figure 4.13. The load deflection plot shows that the specimen's failure was ductile; the beam underwent deformations after reaching its ultimate limit state of yielding of the

longitudinal tension reinforcement. After the steel yielded at an applied load of 165 kips and a deflection of 0.15 inches, there was only a small increase in load before the ultimate capacity of 172 kips was reached.

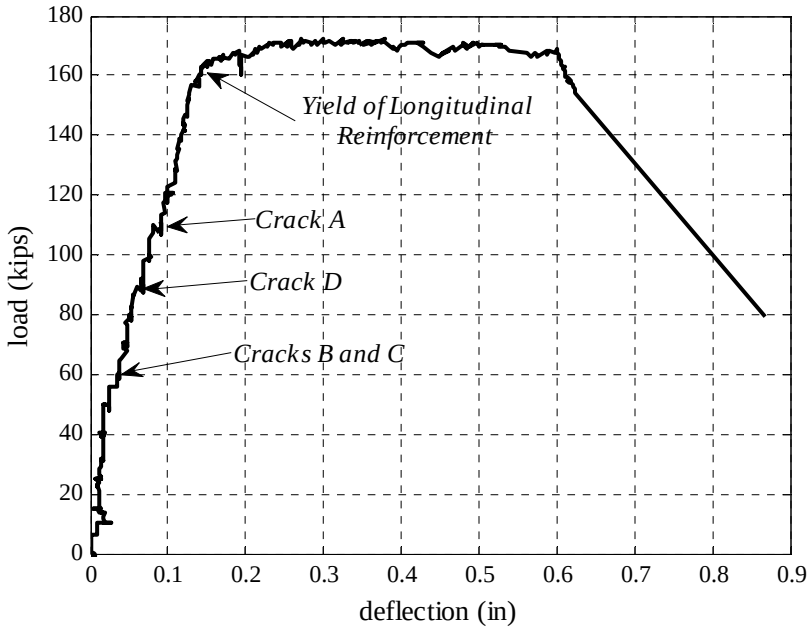

Figure 4.15- Load vs. deflection plot for Specimen AS1

Calculating the principal compression strut angle from equilibrium requires the use of constitutive relations to convert the strains in the longitudinal bar into stresses and then forces. A MATLAB program was written to analyze the data. This program required a stress-strain curve for the longitudinal reinforcement along with a yield value. The stress-strain curve was then broken down into four distinct segments based on the following strain regions:

$$\varepsilon \le f_y / 29{,}000 \qquad \text{(a)}$$

$$f_y / 29{,}000 < \varepsilon \le 1.2(f_y / 29{,}000) \qquad \text{(b)}$$

$$1.2(f_y / 29{,}000) < \varepsilon \le 0.05 \qquad \text{(c)}$$

$$0.05 < \varepsilon \le 0.1 \qquad \text{(d)}$$

With the stress-strain curve broken down in this manor, it was then possible to fit a third order polynomial to each of the four regions. Figure 4.16 shows plots of the stress strain curve created from materials testing data and the four curves fit to the four strain regions. The curves represent the stress strain properties of the steel well; they have a coefficient of variation of 0.999 with the measured steel behavior. Table 4.2 gives the constants for the polynomials fit to each region for each of the different types of longitudinal tension reinforcement used in the experimental program.

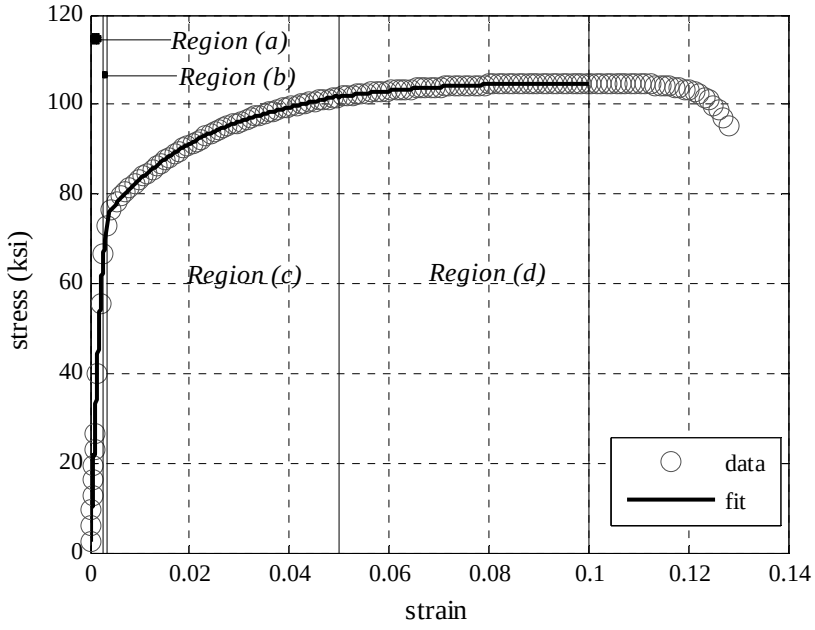

Figure 4.16- Steel stress- strain curve fit

Table 4.2- Polynomial constants fit to stress strain curves for longitudinal tension reinforcement

		3rd Order Polynomial				
Series	Bar	x^3	x^2	x	1	Region
A	#5	-2.234E+09	6.192E+06	2.373E+04	-1.528E-01	(a)
		-9.634E+09	8.060E+07	-2.133E+05	2.436E+02	(b)
		2.208E+05	-2.886E+04	1.521E+03	7.052E+01	(c)
		1.471E+04	-4.888E+03	5.379E+02	8.516E+01	(d)
A	#9 (AS3)	1.295E+09	-5.977E+06	3.544E+04	-5.299E-01	(a)
		8.735E+09	-7.822E+07	2.415E+05	-1.823E+02	(b)
		-6.897E+05	5.386E+04	-6.309E+02	7.799E+01	(c)
		6.255E+04	-1.426E+04	1.137E+03	6.414E+01	(d)
A	#9 (AS4)	-9.044E+08	3.015E+06	2.611E+04	-7.063E-02	(a)
		-6.731E+09	6.085E+07	-1.697E+05	2.229E+02	(b)
		-1.734E+06	9.130E+04	-9.103E+02	9.008E+01	(c)
		1.393E+05	-2.414E+04	1.524E+03	7.229E+01	(d)
A	#10	-1.979E+09	7.400E+06	2.139E+04	-9.745E-02	(a)
		1.406E+09	-3.870E+07	1.720E+05	-1.445E+02	(b)
		-2.668E+06	1.209E+05	-6.502E+02	6.583E+01	(c)
		-4.761E+05	3.095E+04	1.266E+02	6.900E+01	(d)
B	#10	-1.056E+09	2.440E+06	2.947E+04	5.180E-02	(a)
		-9.573E+10	9.040E+08	-2.831E+06	3.017E+03	(b)
		-1.999E+06	1.036E+05	-9.751E+02	8.223E+01	(c)
		1.294E+05	-2.276E+04	1.520E+03	6.571E+01	(d)

The strut angle in specimen AS1 was calculated by taking the inverse tangent of the vertical reaction force divided by the horizontal force in the longitudinal tension reinforcement. Figure 4.17 shows a plot of the strut angle in degrees vs. the applied load in kips. This plot was generated using the data obtained from LVDT 18, and the crack labels correspond to the cracks shown in Figure 4.13. Once the diagonal cracks formed at loads of 90 and 110 kips, the strut angle held at a constant value of approximately 50° and arch action became the primary load carrying mechanism. The strut angle then decreased again to a value of 45.9° at the ultimate load. The transition from beam action to arch action occured as the all of the cracks, both flexural and shear, cracks formed between applied loads of 50 and 110 kips.

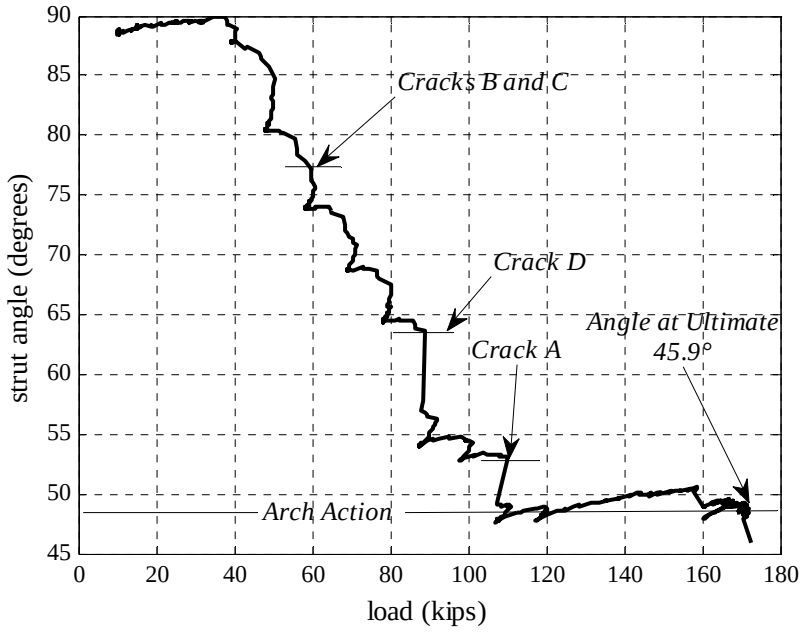

Figure 4.17- Strut angle vs. applied load for Specimen AS1

4.3.2 Test of Specimen AS2

Specimen AS2 was similar to AS1, and was tested to investigate the repeatability of not only the specimen's ultimate strength, but also the repeatability of the data collected by the instrumentation scheme.

Materials tests on companion concrete cylinders were performed on the same day as the specimen test. Based on these tests, the concrete in the beam had an average compressive strength of 4,226± 97 psi based on three samples, an average tensile strength of 400± 28 psi based on three samples, and an average elastic modulus of 3,235± 94 ksi based on three samples. As in the previous beam test, only compression tests were performed on the concrete in the column; the concrete in the column had an average compressive strength of 3,186± 111 psi based on three samples. The longitudinal steel was from the same batch as specimen AS1; it had a yield stress of 79± 1.7 ksi based on three samples.

The load was applied in the same manor as described in the previous test. The first flexural cracks formed at a load of 50 kips. These cracks are labeled *B* and *C* in Figure 4.18. The first diagonal crack *D* formed at a load of 60 kips and was followed by crack *A* at a load of 75 kips. These cracking loads were less than those of the identical specimen AS1. Again, the longitudinal reinforcement governed the ultimate capacity. The bars yielded at a load of 160 kip, but large deformations did not occur. Soon after yield, the concrete crushed at the tip of Crack *A* in the same manor as Specimen AS1.

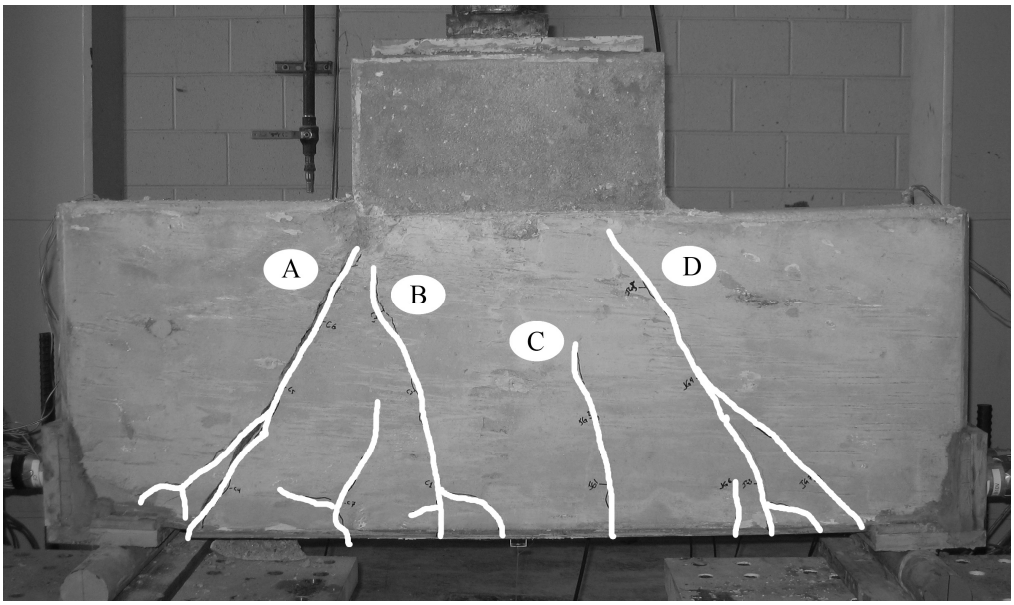

Figure 4.18- Cracks in Specimen AS2

Specimen AS2 had similar behavior to Specimen AS1. The main difference between the two specimens was the deflection sustained prior to failure. Figure 4.19 shows the load vs. deflection plot for specimen AS2. The longitudinal bars in the specimen reached yield, but this did not allow Specimen AS2 to undergo the large deflection seen for Specimen AS1. Both beams had their bars yield at a deflection of

0.15 inches. and a load of about 160 kips. The crack labels in Figure 4.19 and 4.20 correspond to those in Figure 4.18

Figure 4.20 shows the strut angle vs. applied load plot for Specimen AS2. The strut angle behaves in much the same manor as Specimen AS1. In both specimens, the formation of cracks led to the development of arch action at a load of approximately 110 kips. At ultimate load, Specimen AS2 had a strut angle of 46.2°.

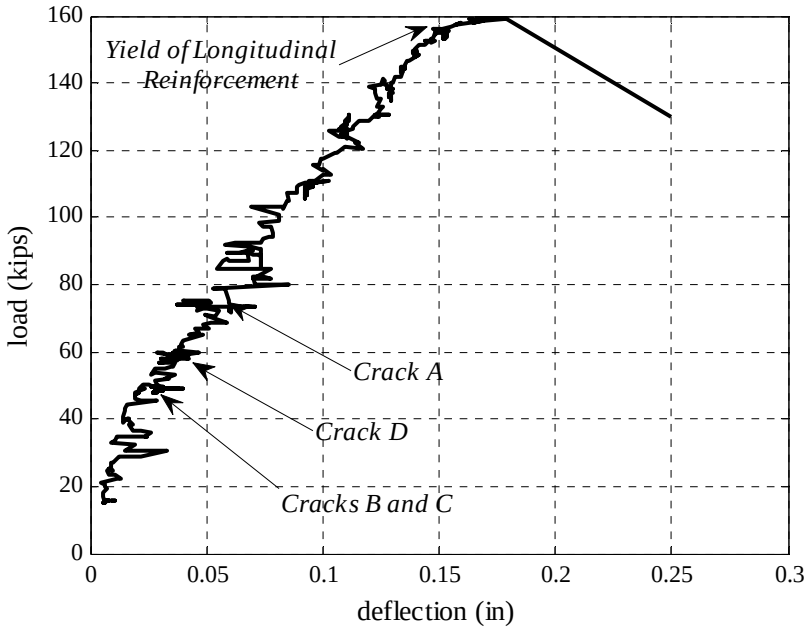

Figure 4.19- Load vs. deflection for Specimen AS2

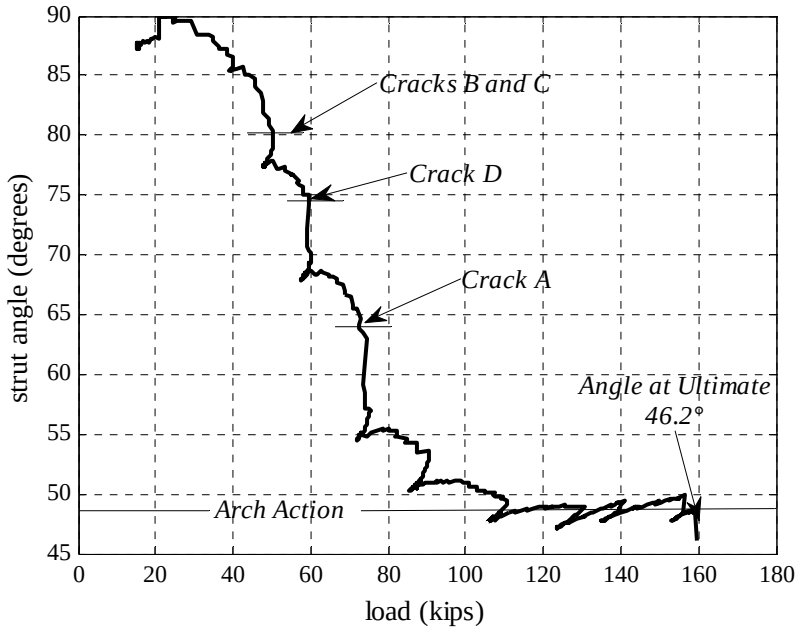

Figure 4.20- Strut angle vs. applied load for Specimen AS2

4.3.3 Test of Specimen AS3

Specimen AS3 was a small specimen with a longitudinal tension reinforcement ratio of 1.3%. This is double the amount of longitudinal tension steel in Specimens AS1 and AS2. Based on companion cylinder tests, the concrete compressive stress on the day of testing was 4037± 5.8 psi based on three samples, and the split tension strength was 458± 37 psi based on three samples. The average elastic modulus of the concrete was 2,971 based on two samples, The compression strength of the concrete in the column was 3121± 61 psi based on three samples. The longitudinal reinforcing steel had an average yield strength of 76 ksi based on two samples.

The first flexural cracks formed in Specimen AS3 at an applied load of 75 kips. These cracks are labeled *B* and *C* in Figure 4.21. Crack *C* began as a flexural crack, and then, later in the testing, a diagonal crack grew and merged into it. Diagonal crack *A* formed at a load of 125 kips while crack *D* formed at a load of 170 kips. Failure

of the specimen occurred at a load of 260 kips when a large splitting crack instantaneously formed and propagated from the corner of the column to the center of the support, causing the longitudinal reinforcement to debond. The splitting of the concrete is labeled in Figure 4.21. This splitting occurred due to stress concentrations induced by the column and the supports.

The increase in the amount of longitudinal reinforcement caused a significant change in the performance of the specimen. The specimen failed in a non-ductile manor. Figure 4.22 shows the load vs. deflection plot for Specimen AS3. The specimen reached its ultimate capacity at a load of 260 kips. At this load the longitudinal steel had reached a strain of 0.0041 this is above its yield strain of 0.0029. The crack labels in Figure 4.22 and 4.23 refer to the crack labeled in Figure 4.21.

The increase in the longitudinal reinforcement caused a decrease in the angle of the principal compression strut. When the strut angle was calculated from equilibrium, the strut angle decreased from 50° to 40°. Figure 4.23 shows the strut angle vs. the applied load. Again, the formation of the diagonal strut is a function of crack formation. For specimen AS3 the strut angle approaches approximately 40°. The angle at ultimate was 43.5°.

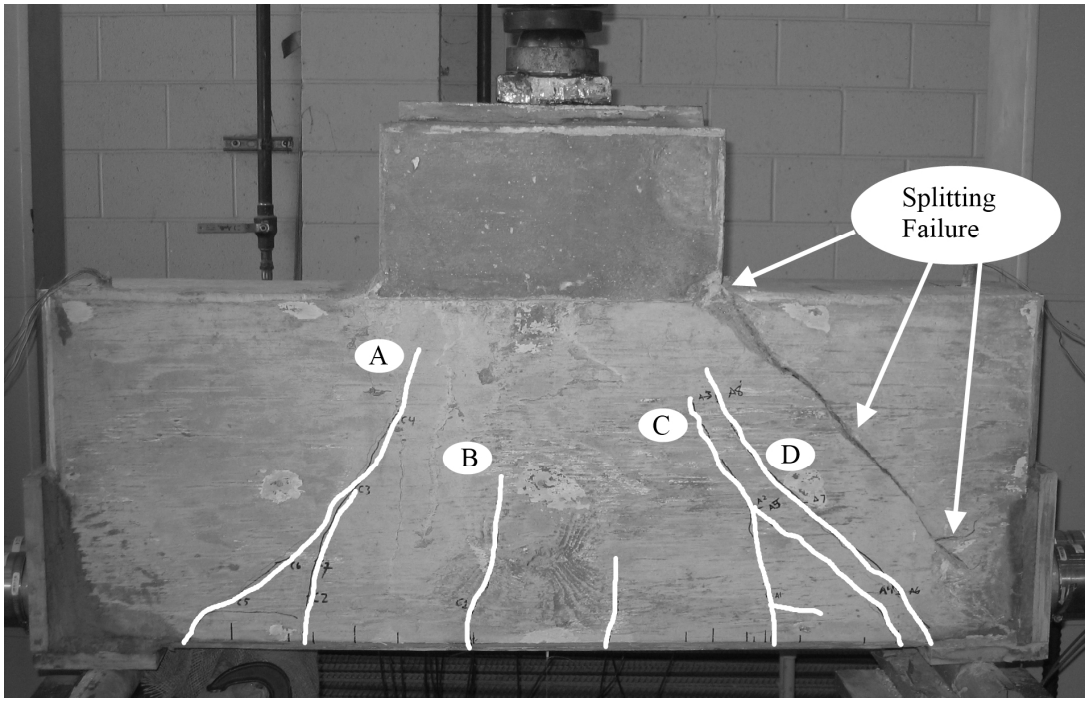

Figure 4.21- Cracks in Specimen AS3

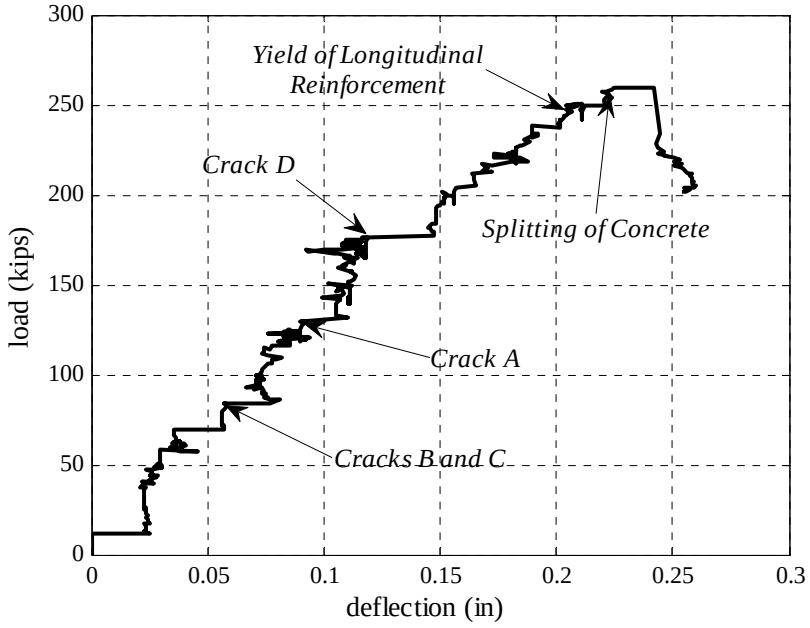

Figure 4.22- Load vs. deflection for Specimen AS3

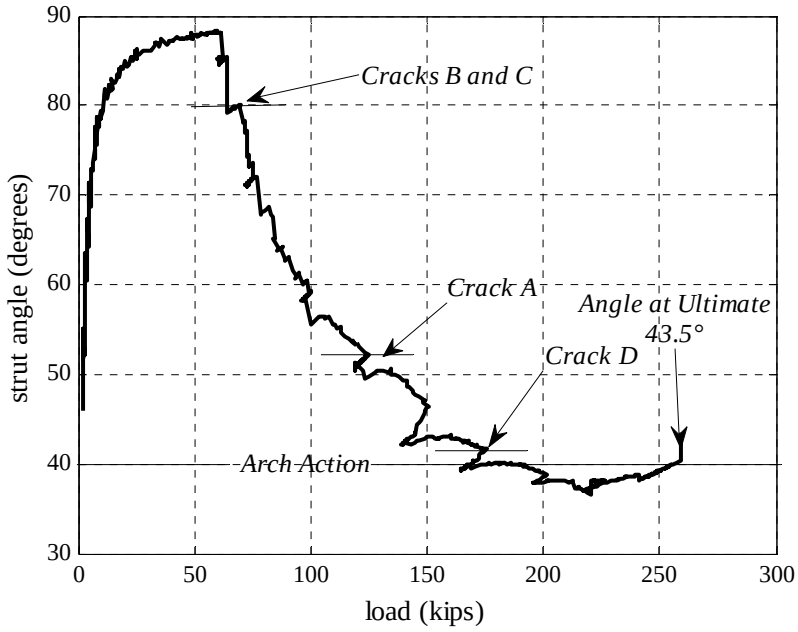

Figure 4.23- Strut angle vs. applied load for Specimen AS3

4.3.4 Test of Specimen AS4

After observing the difference in failure modes between the small specimens with 0.63% and 1.3% longitudinal tension reinforcement, an additional small specimen was fabricated with 1.3% longitudinal tension reinforcement. In contrast to the mixes for the other specimens, which were procured from a local supplier, the concrete for Specimen AS4 was mixed in the Structures Laboratory at the Georgia Institute of Technology. This limited the amount of concrete available for companion cylinder testing, and only compression strength tests were performed. The compression strength of the concrete in the beam was 4,650± 843 psi based on three samples, and the compression strength of the concrete in the column was 3,975± 78 psi based on three samples. The longitudinal reinforcement had a yield strength of 88± 1.7 ksi based on three samples.

The first cracks to form in Specimen AS4 were flexural cracks, labeled as *B* and *C* in Figure 4.24, appearing at an applied load of 75 kips. Crack *A* formed at a load of 100 kips, and was followed by crack *D* at a load of 110 kips. Failure of Specimen AS4 occurred when a diagonal splitting crack formed between the edge of the column and the support at an applied load of 267 kips. The failure mechanism was the same as in Specimen AS3, but unlike specimen AS3, the longitudinal steel did not reach yield before the failure. This was due to the difference in yield strengths between the two different longitudinal reinforcements (79 vs 88 ksi).Figure 4.25 shows the load vs. deflection plot for Specimen AS4. The crack labels in both Figs. 4.25 and 4.26 correspond to the labels in Figure 4.24. Figure 4.26 shows the plot of strut angle vs. load for Specimen AS4. The strut angle again approaches approximately 40°. The formation of arch action for this specimen was less distinct than in any of the previous tests; the calculated arch angle varies from 50° to 40°.

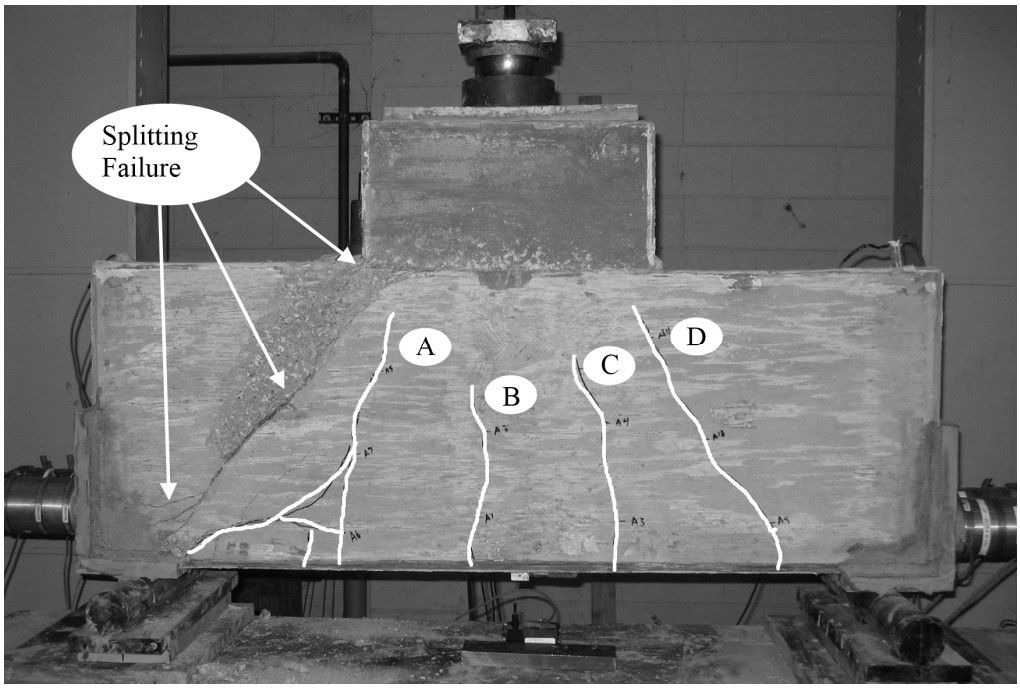

Figure 4.24- Cracks in Specimen AS4

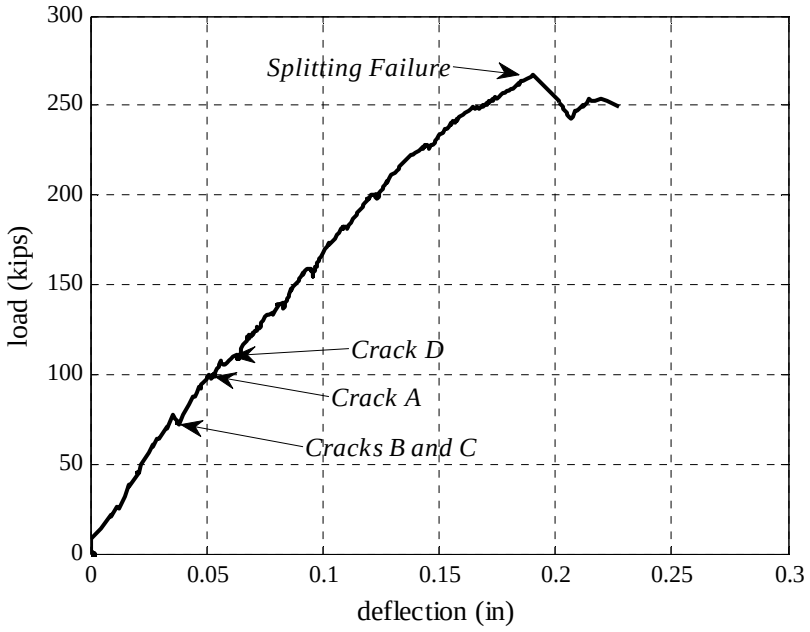

Figure 4.25- Load vs. deflection for Specimen AS4

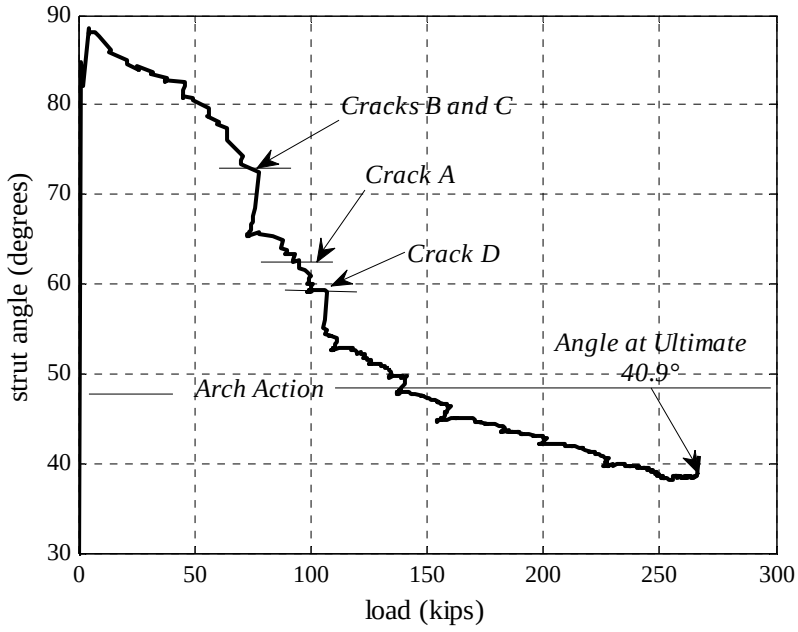

Figure 4.26- Strut angle vs. applied load for Specimen AS4

4.4 Tests of Full Scale Specimens

The results for the full scale specimens were separated from the small scale specimens due to the size effect. The behavior of these specimens replicates the behavior of a full scale pier cap.

4.4.1 Test of Specimen AL1

Specimen AL1 was the first of the 36 inch deep specimens tested. It contained 0.65% longitudinal tension reinforcement; this makes it the companion to Specimens AS1 and AS2. On the day of beam testing, companion cylinder testing indicated that the compressive strength of the concrete in the beam was 3,473± 142 psi based on three samples with an elastic modulus of 3,298± 8 ksi based on three samples. The split tension strength of the concrete was 384± 26 psi based on three samples. The compressive strength of the concrete in the column was 3,066± 165 psi based on three samples, and the longitudinal steel had a yield stress of 65± 8 ksi based on three samples.

Figure 4.27 highlights the cracks that formed during the testing of Specimen AL1. In comparison with specimens AS1 and AS2, a larger number of individual cracks formed during the testing of the large specimen. The highlighted cracks represent the larger and more critical cracks which formed during testing. The flexural cracks *C* and *D* formed first at a load of 150 kips. The diagonal shear cracks *B* and *E* formed at a load of 200 kips followed by crack *A*, which formed at 250 kips. At an applied load of 505 kips, the longitudinal reinforcement reached its yield point. The specimen reached its ultimate capacity at an applied load of 545 kips. At this point the steel had yielded and the concrete crushed at the corner of the stub column above the merger of cracks *D* and *E*. The failure mode and even the crack patterns agreed well with those observed in Specimen AS1.

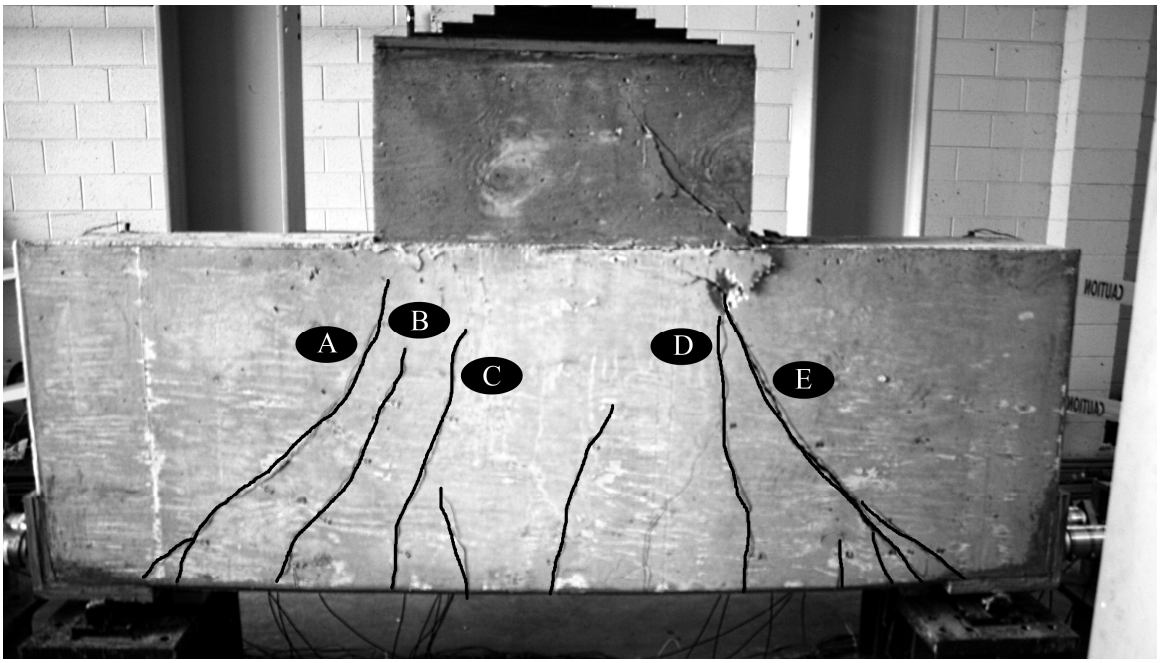

Figure 4.27- Cracks in Specimen AL1

Overall, the results of the testing of Specimen AL1 agreed well with that of Specimen AS1 and AS2. Figure 4.28 shows the load vs. deflection plot for the Specimen AL1. Like Specimen AS1, Specimen AL1 was able to double its total deflection after yielding of the longitudinal reinforcement and failed in a ductile manor. The cracks denoted in Figs. 4.28 and 4.29 reference the cracks in Figure 4.27.

The strut angles calculated through equilibrium also were similar in the small and large specimens. Specimens AS1 and AS2 had approximate strut angles of 50°, while Specimen AL1 had an approximate strut angle of 46°. Figure 4.29 shows the strut angle vs. load plot for specimen AL1. This plot was created using the strain data from a strain gage at midspan of the specimen. This gage was used because when the span was doubled from 48 to 96 inches it became harder to install the longitudinal LVDT along the reinforcement. A string potentiometer was used in place of the LVDT because it was simpler to mount on the specimen. This string potentiometer was not as precise as the LVDT and was unable to measure the small displacements early in the

test. It could not capture the small strains. The strain gage is localized at midspan so it could not capture the effects of cracking in other parts of the specimen; this can clearly be seen in the way arch behavior begins before any of the major cracks become visible (see Figure 4.29). Avoiding this localization is one of the main advantages of using the LVDT to measure longitudinal strains in the reinforcement, and an LVDT was used for all of the following tests.

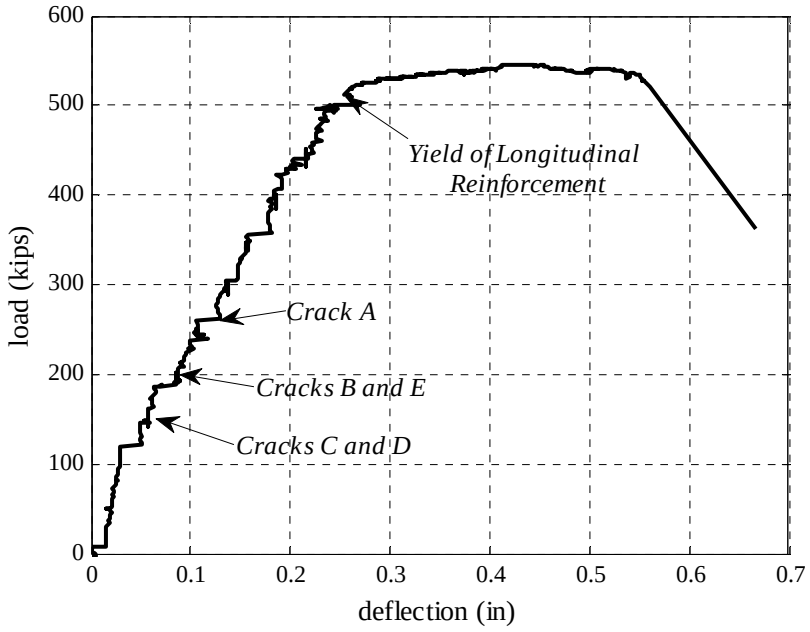

Figure 4.28- Load vs. deflection for Specimen AL1

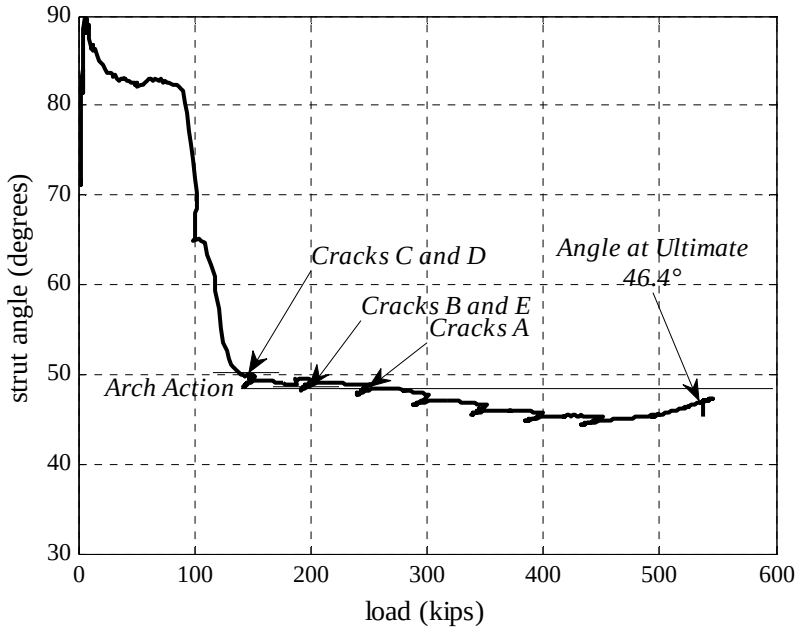

Figure 4.29- Strut angle vs. applied load for Specimen AL1

4.4.2 Test of Specimen AL2

Specimen AL2 was 36 inches. deep with a longitudinal tension reinforcement of 1.3%. It was the large-scale companion to Specimen AS3 and AS4. On the day of testing, the concrete that made up the beam had a compressive strength of 3,651± 218 psi based on three companion cylinder samples, an average elastic modulus of 3,298 ksi based on two samples, and a split tension strength of 394± 37 psi based on three samples. The concrete in the column had a compressive strength of 3,338± 243 psi based on three samples. The longitudinal steel was from the same batch as that for Specimen AL1. It again, had a yield stress of 65± 8 ksi based on three samples.

Figure 4.30 is a photograph of Specimen AL2 with the cracks highlighted. The first flexural crack *B* became visible at a load of 200 kips. Crack *C* formed at a load of 250 kips and was followed by crack *A* at a load of 300 kips. Shear crack *D* formed around an applied load of 400 kips. The beam failed rapidly when a splitting crack

formed, running from the corner to the support, at a load of 660 kips, as illustrated in Figure 4.31.

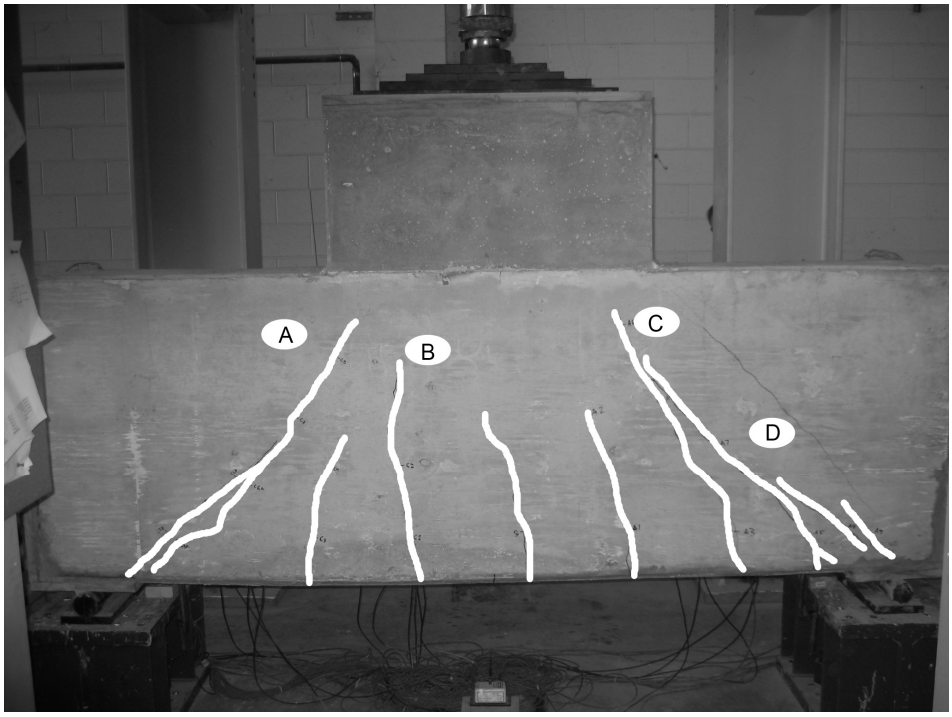

Figure 4.30- Cracks in Specimen AL2

Specimen AL2 performed similarly to its small-scale counterparts, Specimen AS3 and AS4. The splitting of the concrete occurred before the longitudinal reinforcement could yield. Figure 4.32 shows a plot of the applied load vs. the deflection for Specimen AL2, and Figure 4.33 shows the angle of the principal compression strut at approximately 40° which coincides with that of Specimen AS3. The strut angle at ultimate was 34.2°. The specimen exhibited brittle behavior. The cracks denoted in Figs. 4.32 and 4.33 correspond to those labeled in Figure 4.30.

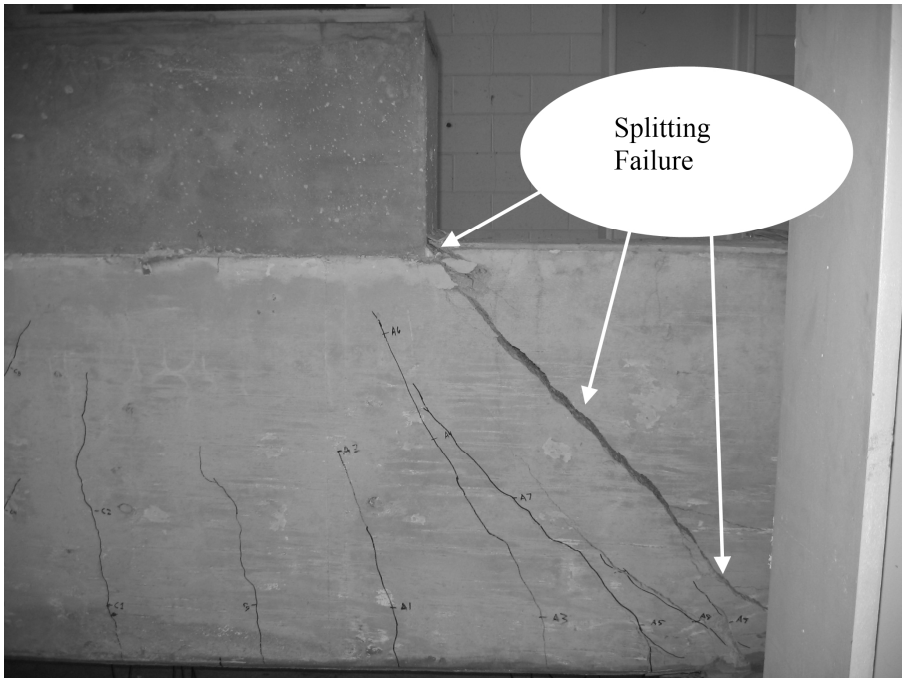

Figure 4.31- Splitting crack in Specimen AL2

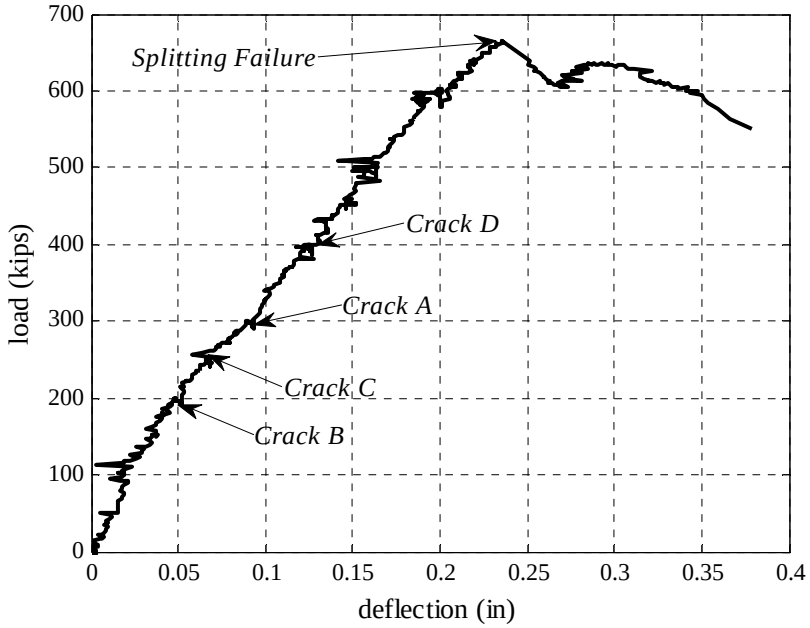

Figure 4.32- Load vs. deflection for Specimen AL2

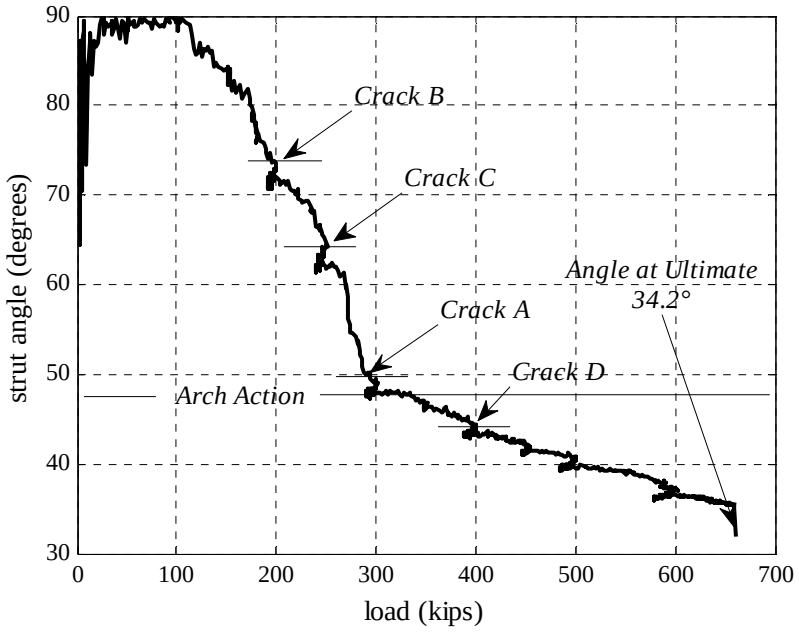

Figure 4.33- Strut angle vs. applied load for Specimen AL2

4.4.3 Test of Specimen BL1

Specimen BL1 was part of a second set of specimens, intended to investigate the effect of including AASHTO's crack control reinforcement for deep beams and to serve as controls for the strengthening schemes. Specimen BL1 was constructed similarly to Specimen AL1.

On the day of testing, the concrete that made up the beam had a compressive strength of 3,352± 226 psi based on six samples, a split tension strength of 377± 43 psi based on three samples, and an elastic modulus of 3051± 42 ksi based on three samples. The concrete in the column had a compressive strength of 3,263± 253 psi based on three samples. The longitudinal steel had a yield stress of 80± 1.22 ksi based on three samples. This is significantly higher than for specimen AL1 whose longitudinal reinforcement had a yield stress of 65 ksi.

As load was applied to specimen BL1, the first flexural cracks formed at a load of 175 kips. The cracks are labeled *C* and *D* in Figure 4.34. The cracks were then followed promptly by *A, B, E,* and *F* at an applied load of 225 kips. Specimen BL1 failed when a splitting crack formed running from the column to the support at an applied load of 500 kips. At this load the longitudinal reinforcement had not yielded. This failure mode is not consistent with the other specimens with 0.65% longitudinal tension reinforcement in which the longitudinal reinforcement yielded. The failure mode of Specimen BL1 was more like the brittle failure mode of the specimens with 1.3% longitudinal tension reinforcement.

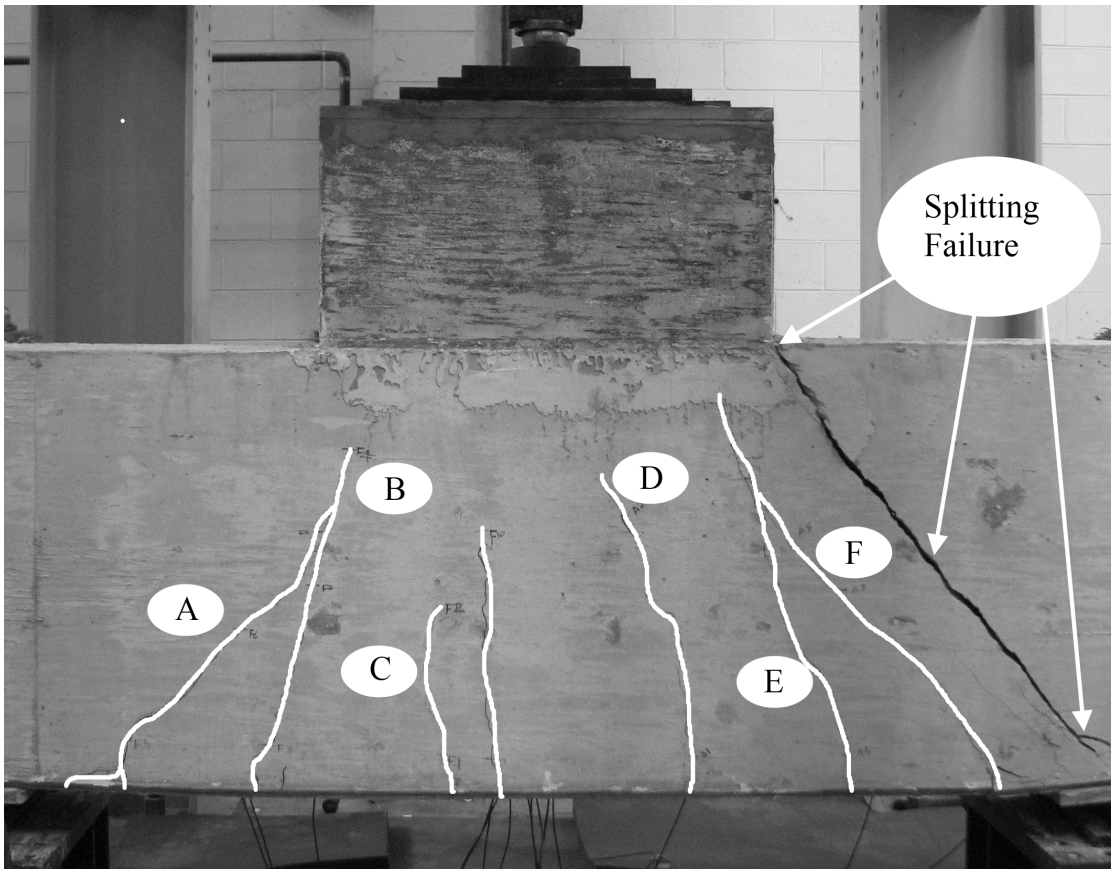

Figure 4.34- Cracks in Specimen BL1

Figure 4.35 shows the load vs. deflection plot for Specimen BL1. Despite having the same longitudinal reinforcement as Specimen AL1, the load deflection curve for Specimen BL1 resembles that of Specimen AL2 more closely. The crack labels in Figs. 4.35 and 4.36 refer to the cracks shown in Figure 4.34. Despite the difference in failure mode, the strut angle vs. applied load plot for Specimen BL1 agrees well with that of Specimen AL1. The strut angle approaches an approximate value of 46°, and is 43.4° at ultimate.

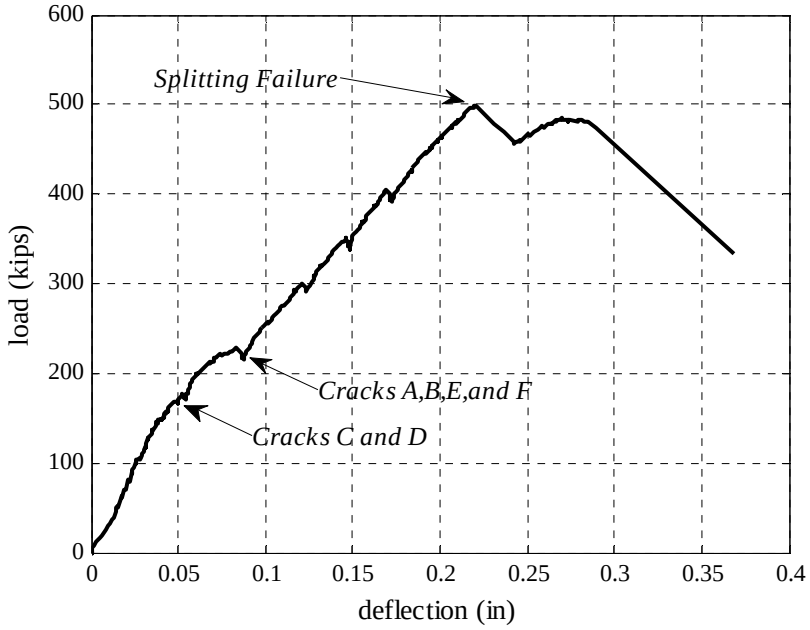

Figure 4.35- Load vs. deflection for Specimen BL1

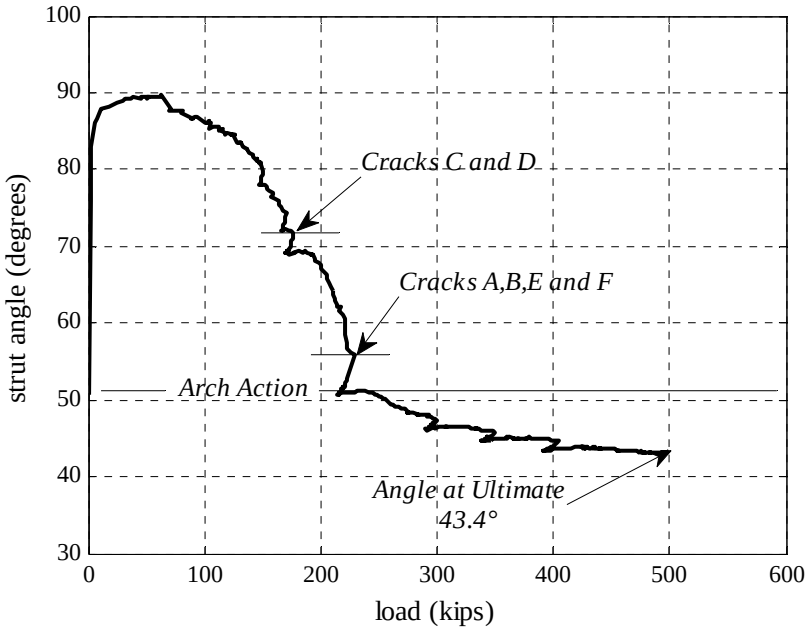

Figure 4.36- Strut angle vs. applied load for Specimen BL1

4.4.4 Test of Specimen BL2

Specimen BL2 was built similarly to Specimen AL2. It has 1.3% longitudinal tension reinforcement, and it is the control for the specimens which include AASHTO crack control reinforcement. The concrete in the beam section of Specimen BL2 had a compressive strength of 3,353± 226 psi based on six companion cylinder samples, a split tension strength of 370± 45 psi based on three samples, and an elastic modulus of 3,338 ± 158 ksi based on three samples. The concrete in the column had a compressive strength of 3,082± 142 psi based on three samples. Again the longitudinal reinforcement had a yield strength of 80± 1.22 ksi based on three samples.

Figure 4.37 shows the crack pattern and failure of Specimen BL2. Minor flexural cracking began at an applied load of 200 kips. Cracks *B C D* and *E* appeared at a load of 250 kips. Crack *F* presented itself at a load of 350 kips, and Crack *A* formed at a load of 400 kips. Specimen BL2 reached its ultimate capacity at a load of 631 kips,

when, a splitting crack formed suddenly between the corner of the column and the support before the steel could yield. This failure mode agreed well with Specimen AL2 which failed at an applied load of 660 kips. The results from the testing of Specimen BL2 agree well with Specimen AL2. Both the plots of load vs. deflection (Figure 4.38) and strut angle vs. load (Figure 4.39) match closely those for Specimen AL2. The crack labels in the figures refer back to Figure 4.37

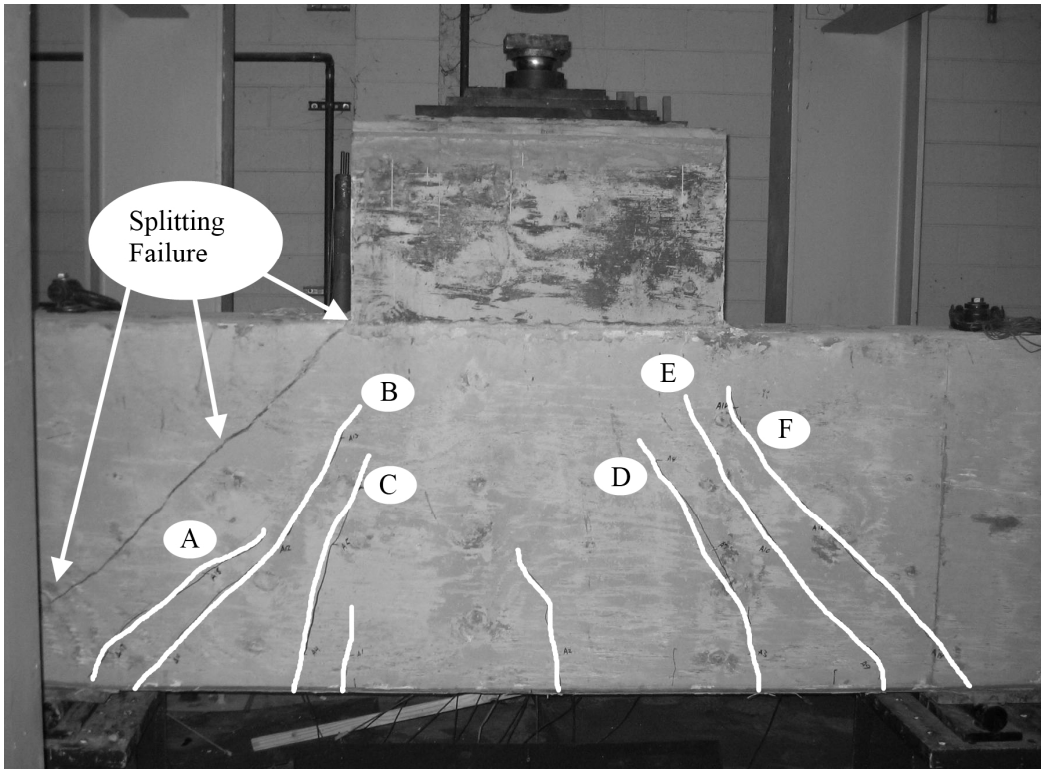

Figure 4.37- Cracks in Specimen BL2

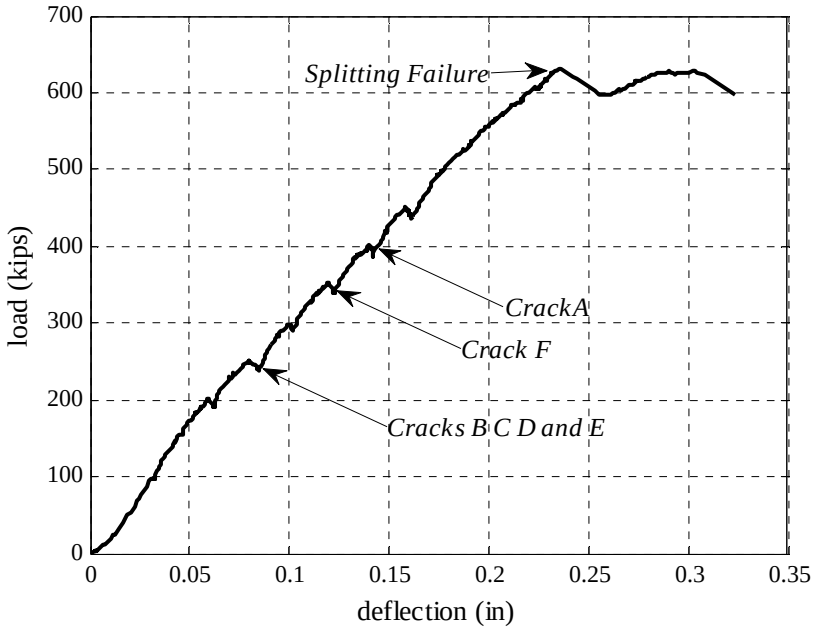

Figure 4.38- Load vs. deflection for Specimen BL2

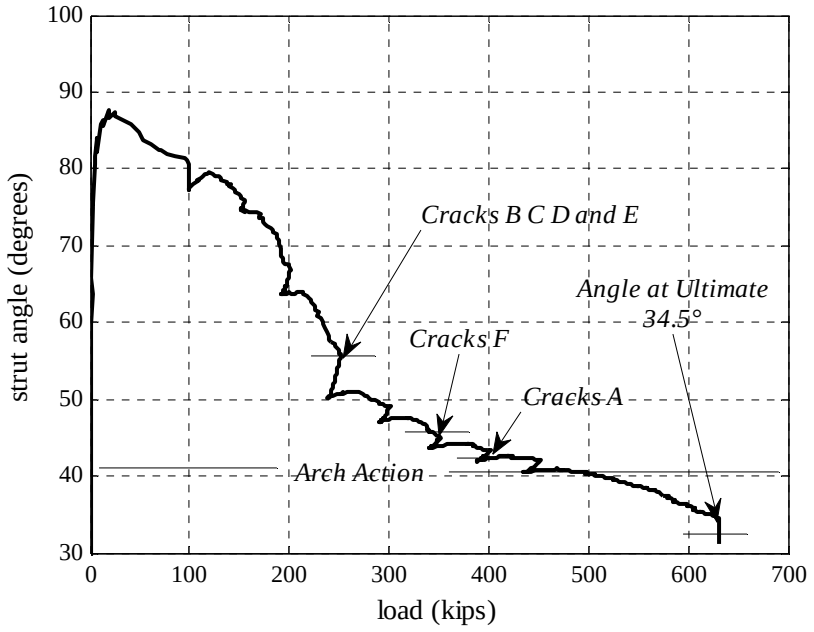

Figure 4.39- Strut angle vs. applied load for Specimen BL2

4.4.5 Test of Specimen BL3

In order to investigate the effects of the crack control reinforcement required by the AASHTO 2007 LRFD Specification for deep beams, additional transverse and longitudinal reinforcement was added to the specimens. The Specification requires that there be no less than a 0.003 reinforcement ratio (0.3%) in both the transverse and longitudinal directions and that the spacing between these reinforcing bars be no greater than 10 inches (AASHTO Section 5.6.3.6). To accomplish this #4 bars and stirrups were added to a typical specimen with 1.3% longitudinal reinforcement. The #4 bars in the longitudinal direction were required to meet the minimum spacing requirements. The specimen with 1.3% longitudinal reinforcement was chosen because of the brittle nature of its failure; if the stirrups had an effect it would be more pronounced in this type of specimen. Figure 4.40 shows the additional crack control reinforcement. Specimen BL3 was the first specimen tested with crack control reinforcement.

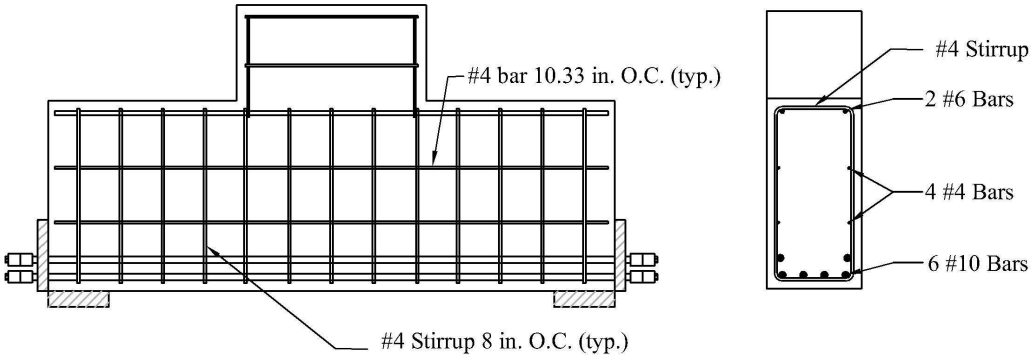

Figure 4.40- Specimen with 1.3% longitudinal and crack control reinforcement

On the day of testing, the concrete in the beam had a compressive strength of 3,966± 185 psi based on three samples, a split tension strength of 429± 23 psi based

on three samples, and an elastic modulus of 3,067± 165 ksi based on three samples. The concrete in the column had a compressive strength of 2,920± 324 psi based on three samples. The #10 bars in main longitudinal reinforcement had yield strength of 80± 1.22 ksi based on three samples. The #4 bars in the crack control reinforcement had a yield stress of 85± 2.3 ksi based on three samples.

The first flexural crack in Specimen BL3, Crack *D*, appeared at an applied load of 250 kips as shown in Figure 4.41. Then at a load of 300 kips Cracks *C* and *E* formed. Crack *C* was a common flexural crack, but Crack *E* was a diagonal tension crack running from the support to just below the edge of the column. This type of crack had instantaneously caused failure in Specimens AL2, BL1, and BL2; the specimens could not sustain load after the formation of this crack. Loading was continued, and at a load of 350 kips Cracks *A* and *B* formed. The loading continued to an applied load of 739 kips, at which point Crack *E* finally propagated all the way to the edge of the column causing failure. The longitudinal reinforcement had yet to yield, making the splitting tension the crack the failure mode.

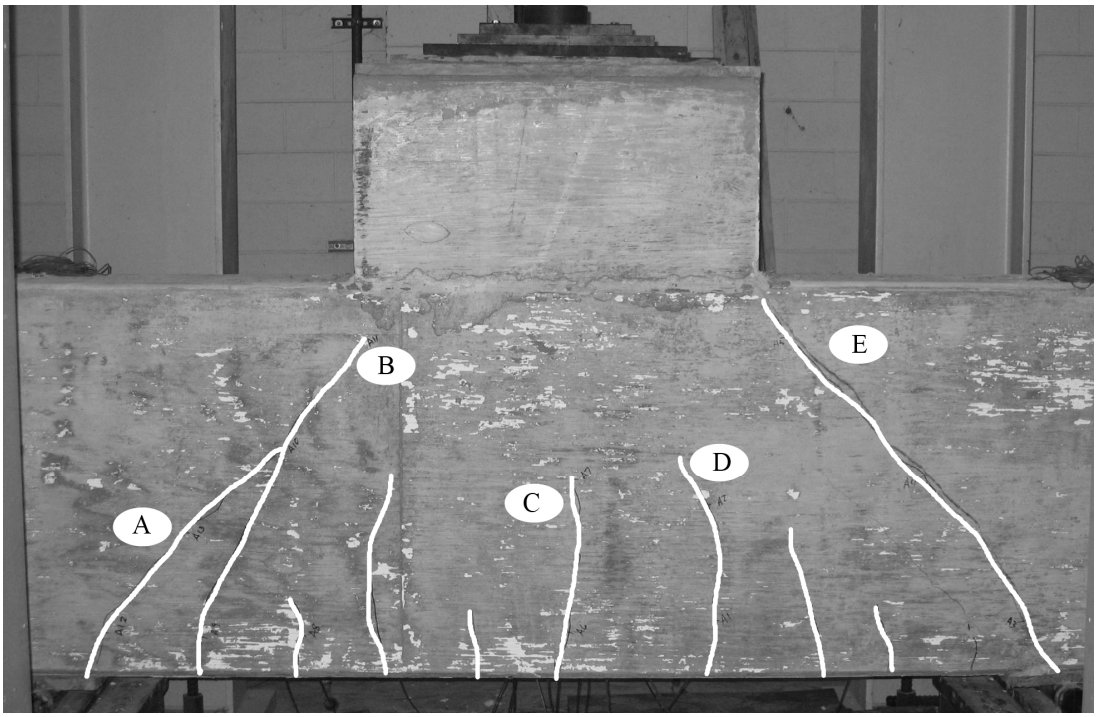

Figure 4.41- Cracks in Specimen BL3

The load vs. deflection plot shown in Figure 4.42 for Specimen BL3 agrees well with similar plots from tests of Specimen AL2 and BL2 despite the early formation of the splitting crack. One main difference can be seen: after reaching the ultimate load, the curve in Figure 4.42 decreases slowly, in contrast to the sharp decrease shown in Figs. 4.32 and 4.38 for Specimens AL2 and BL2, respectively. The crack labels in Figs. 4.42 and 4.43 correspond to the labels in Figure 4.41. The plot of strut angle vs. applied load shown in Figure4.43 does show some differences from that of Specimens AL2 and BL2 (Figs. 4.33 and 4.39). While arch action does initiate at about the same point (about 400 kips) the approximate strut angle is slightly higher at about 45°. The calculated strut angle at ultimate is also higher; 39.3° as apposed to 34.4° and 34.2° for Specimens AL2 and BL2 respectively. The inclusion of the crack control reinforcement did not have a large effect on when cracks formed and arch action began, but it did slightly increase the strut angle and allow the beam to carry load after the formation of the splitting crack

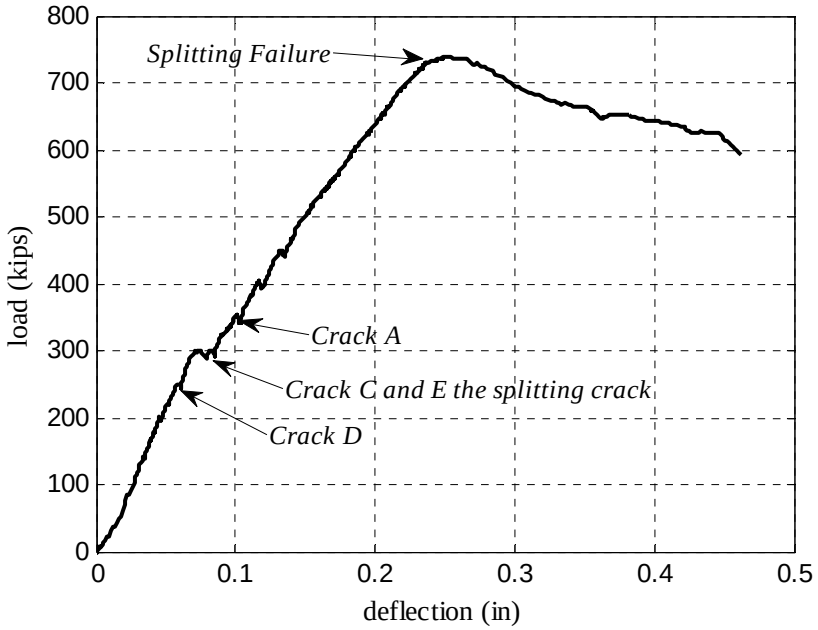

Figure 4.42 Load vs. deflection for Specimen BL3

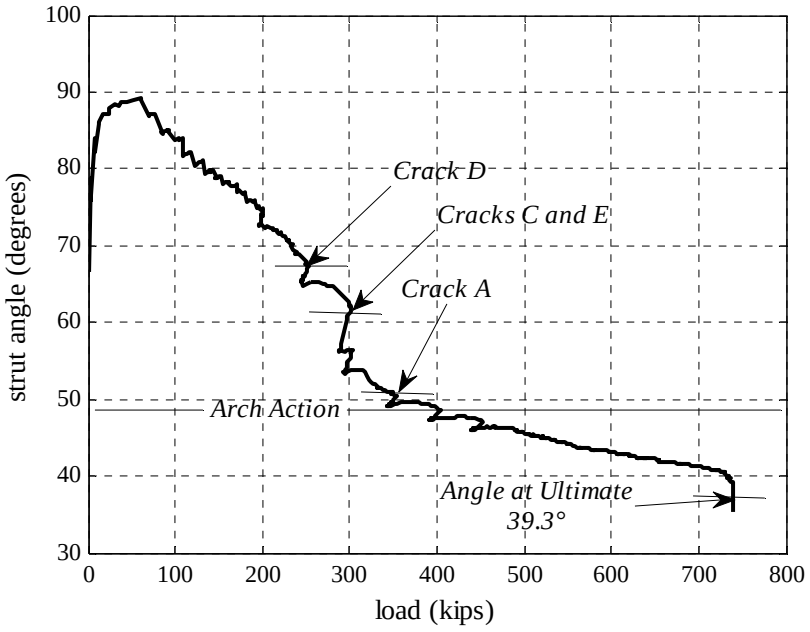

Figure 4.43- Strut angle vs. applied load for Specimen BL3

4.4.6 Test of Specimen BL4

Specimen BL4 was similar to Specimen BL3. On the day of testing, the strength in the beam was of 3,874± 159 psi in compression based on three samples, of 448± 40 psi in tension based on three samples, and the elastic modulus of 3,482± 110 ksi based on three samples. The concrete in the column had a compressive strength of 3,041± 434 psi based on three samples. The #10 bars which constituted the main longitudinal reinforcement had a yield stress of 80± 1.22 ksi based on three samples, and the #4 bars used for crack control reinforcement had a yield stress of 85± 2.3 ksi based on three samples.

The first flexural cracks formed at a load of 250 kips; these cracks are labeled *B* and *C* in Figure 4.44. These cracks were followed by *A* and *D* at an applied load of 300 kips. Crack *E* formed at a load of 450 kips. Failure occurred when a diagonal splitting crack formed between the corner of the column and the center of the support at a load of 859 kips. At this point the steel had not reached yield, and the splitting crack did not appear prior to failure as it did for Specimen BL3.

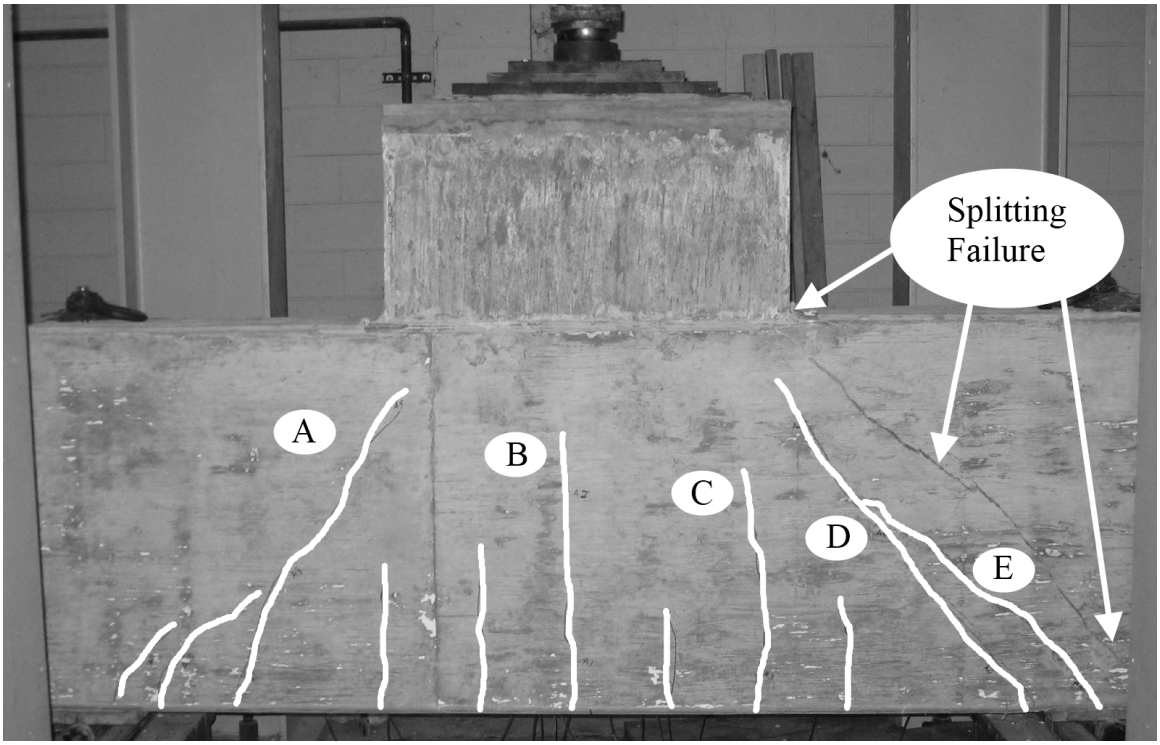

Figure 4.44 Cracks in Specimen BL4

Figures 4.45 and 4.46 show the load vs. deflection and the strut angle vs. applied load plots for Specimen BL4. Specimen BL4 behaved in the same manner as Specimen BL3. The main difference was that the splitting crack did not appear until the ultimate load has been reached; this allowed Specimen BL4 to achieve an ultimate load 120 kips (16%) higher than Specimen BL3. The strut angle at ultimate for Specimen BL4 was 38.6°.

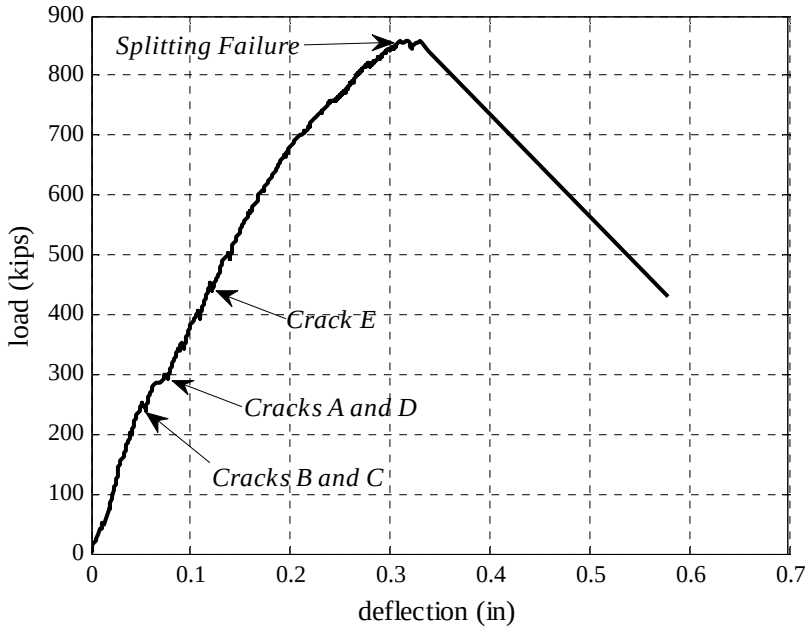

Figure 4.45- Load vs. deflection for Specimen BL4

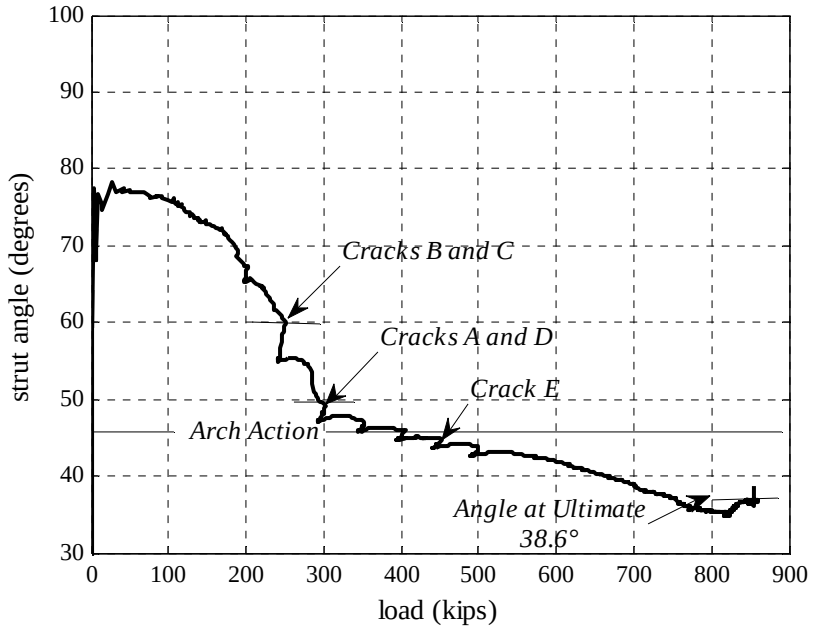

Figure 4.46- Strut angle vs. applied load for Specimen BL4

4.4.7 Test of Specimen BL5

Specimen BL5 was similar to both Specimens BL3 and BL4. This test was performed due to the large discrepancies in ultimate capacity between Specimens BL3 and BL4. The concrete in the beam portion of Specimen BL5 had a compressive strength of 3,998± 87 psi based on three samples, a split tension strength of 426± 40 psi based on three samples, and an elastic modulus of 3,232± 439 ksi based on three samples. The concrete in the column section of Specimen BL5 had an average compressive strength of 3,163 psi based on two samples. The steel reinforcement in the specimen had the same reinforcement as Specimens BL3 and BL4. The longitudinal steel had a yield stress of 80± 1.22 ksi based on three samples, and the crack control reinforcement had a yield stress of 85± 2.3 ksi based on three samples.

Figure 4.47 shows the major cracks which formed during the testing of Specimen BL5. The first Cracks *D* and *E* formed at an applied load of 250 kips. Cracks *B*, *C*, and *F* formed at a load of 300 kips, and Crack *G* formed at a load of 450 kips. Then, at a load of 750 kips, a diagonal splitting crack formed at a point just below the corner of the column and the support. Failure did not occur immediately following the formation of this crack; rather, loading increased to 871 kips, at which point the splitting crack penetrated all the way to the corner of the stub column.

The crack labels in both Figs. 4.48 and 4.49 refer to the labels in Figure 4.47. Figure 4.48 shows that the load-deflection relationship for Specimen BL5 was similar to that of Specimen BL4. The ultimate load was 871 kips which is close to Specimen BL4's ultimate capacity of 859 kips. Figure 4.49 shows the strut angle vs. applied load for specimen BL5, which agrees well with that of Specimen BL4.

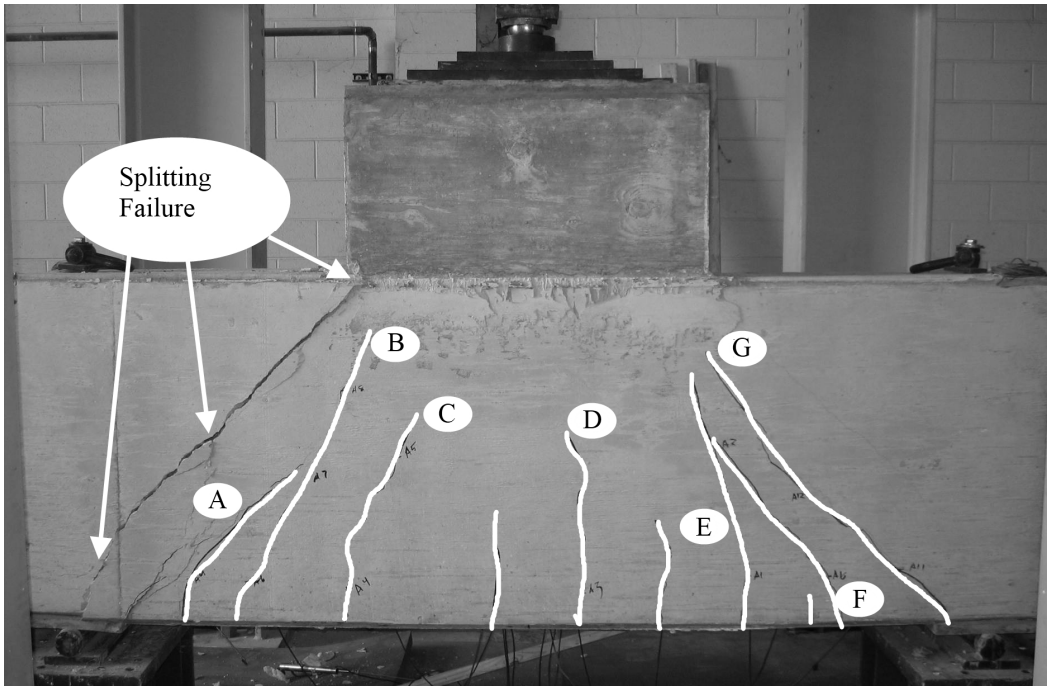

Figure 4.47- Cracks in Specimen BL5

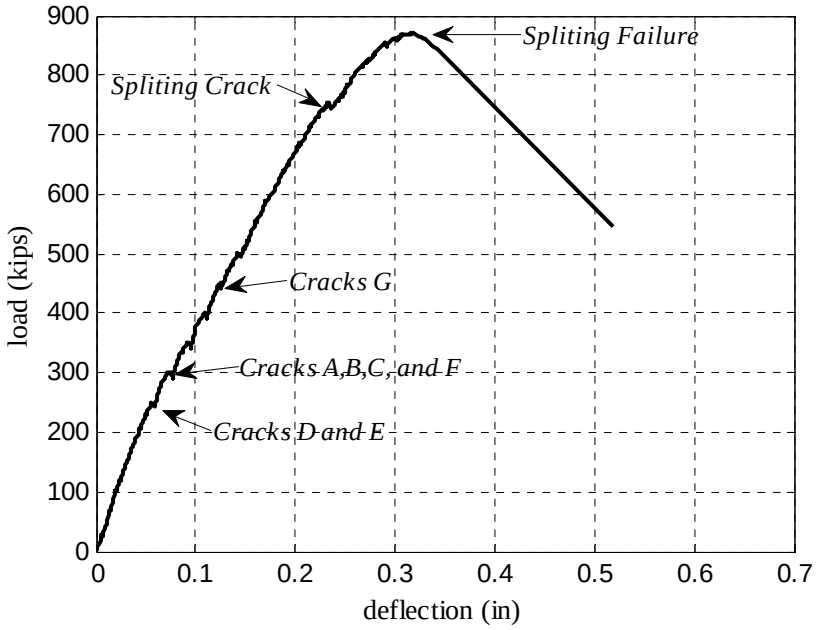

Figure 4.48-Load vs. deflection for Specimen BL5

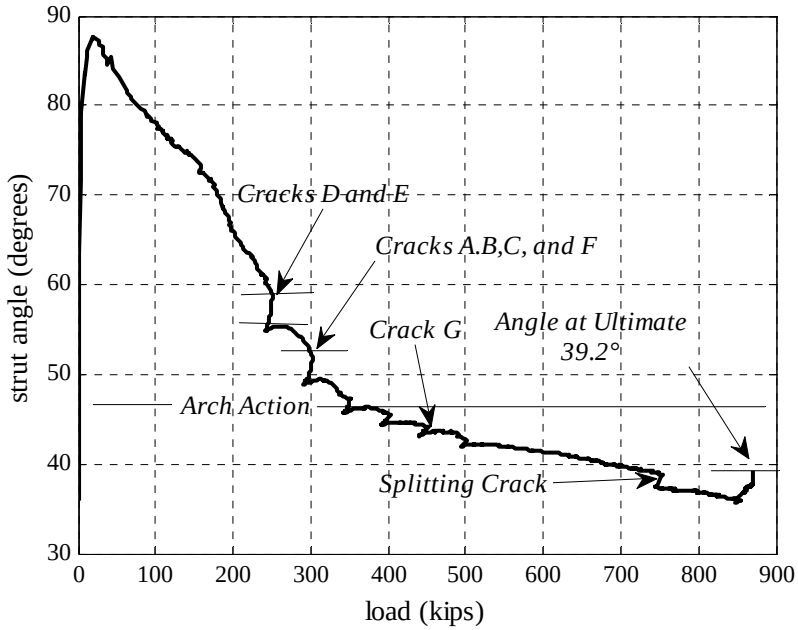

Figure 4.49- Strut angle vs. applied load for Specimen BL5

4.5 Conclusions

The results of the experimental tests showed the influence of the longitudinal tension reinforcement, the inclusion of crack control reinforcement, and the effect of size. The inclusion of the column was important in modeling the behavior of a pier cap. These results can be used to develop a rational for the strengthening of existing pier caps.

4.5.1 Effect of the Column Stub

The effect of applying load through the column stub was very important in achieving the proper boundary conditions to capture the behavior of the pier caps. This detail has been excluded from many different experimental programs in the past. Often the column was omitted and replaced with a steel plate to simplify specimen construction, but removing the column also removed stress concentrations.

The longitudinal strains measured in the column and the bars were used to calibrate an elastic finite element model. Figure 4.50 shows the strains through the depth predicted by the finite element model and measured during the testing of Specimen AL1. There is good agreement at 50 kips of applied load, but the strains in the bar diverge at an applied load of 100 kips. This difference is due to the influence of cracking in the beam. Figure 4.51 shows the loads plotted vs. the strain in the longitudinal reinforcement. Linear behavior can be seen before an applied load of approximately 90 kips. After that the influence of cracking changes the behavior of the strains. The linear elastic finite element model is on applicable at a load of 50 kips.

Figure 4.52 shows the strains in the longitudinal direction. Depicted on the Figure is the location of the LVDT's and strain gage used to compare longitudinal strains. The strain/stress concentrations can be seen at the corners of the column. Figure 4.53 shows the maximum principal compression stress. A set of compression struts can be seen running from the corner of supports to the corner of the column; another set can be seen running from the corner of the column to the applied load. The stress concentrations can clearly be seen at the corners of the column. These stress concentrations contributed to the splitting cracks which lead to failure in each of the specimens whose ultimate capacity was not governed by yielding of the longitudinal reinforcement. The difference between column loading and loading through a steel plate can be seen very clearly in the crack patterns reported by Foster and Gilbert (1998), which are shown in Figure 4.54. The failure at the edge of the column can clearly be seen as opposed to the entire area under the load plate. For this reason it is important for researchers to include the proper boundary details when working with deep beams.

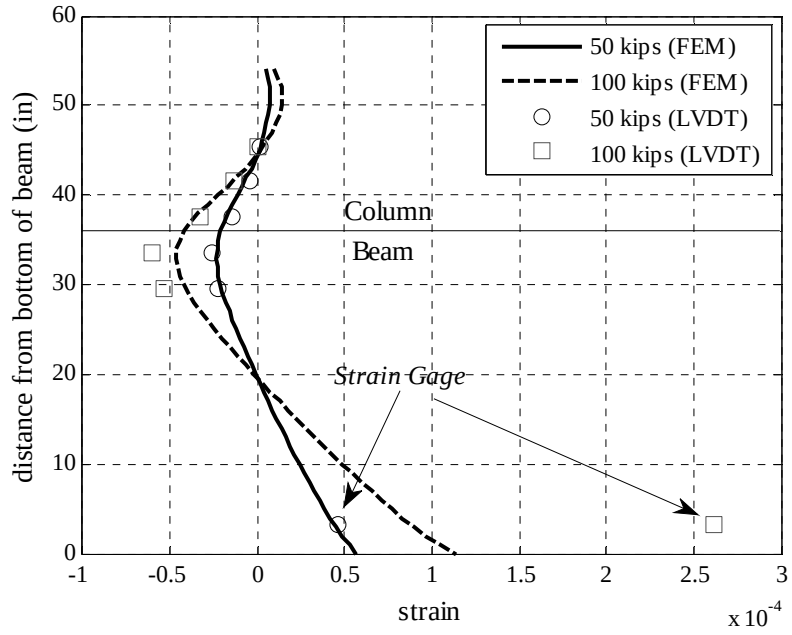

Figure 4.50- Strains through the depth of the specimen at midspan

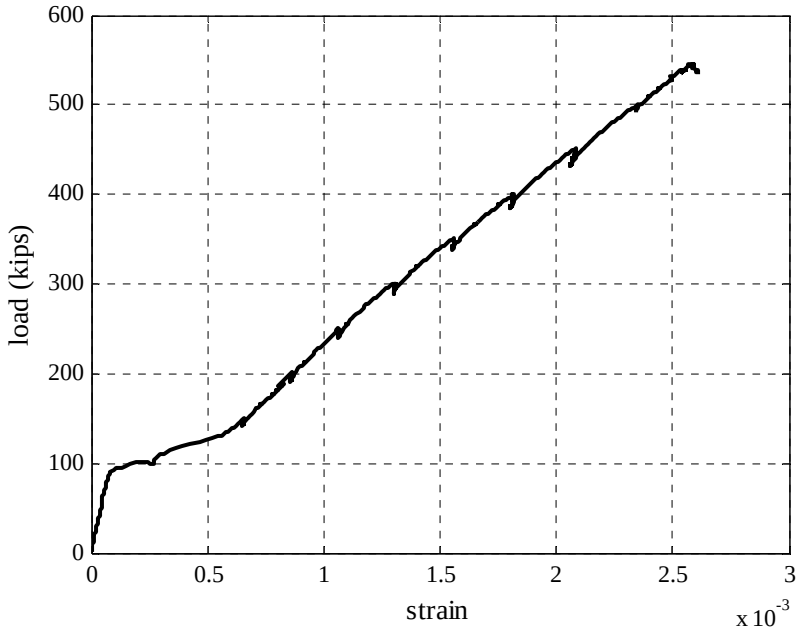

Figure 4.51- Load vs. strain in the longitudinal reinforcement

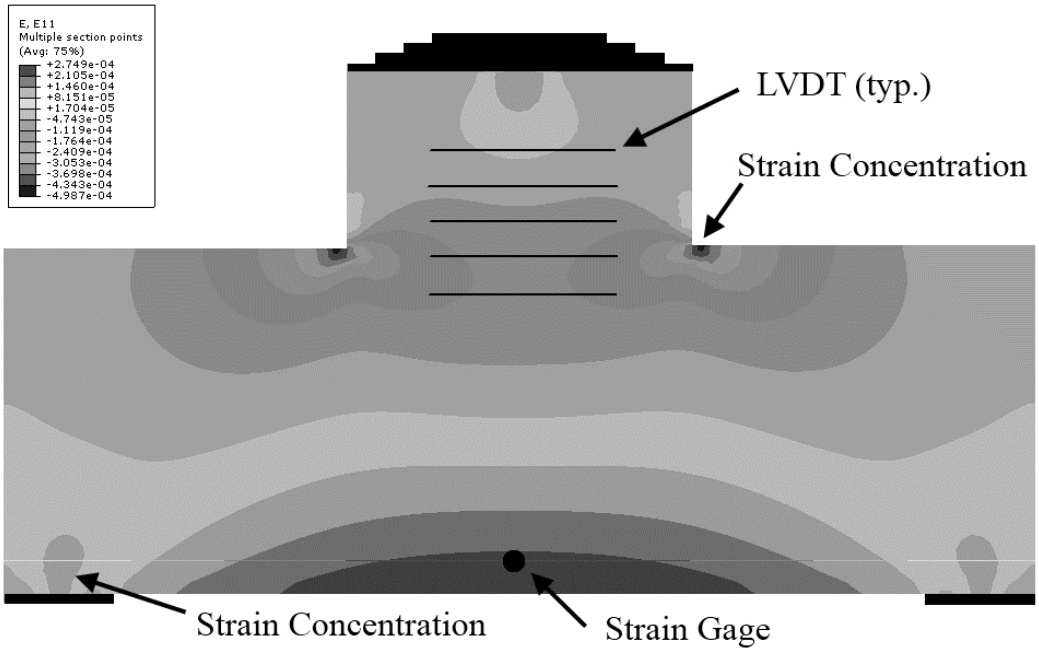

Figure 4.52- Strain contours in the longitudinal (E11) direction for Specimen AL1 at 50 kips

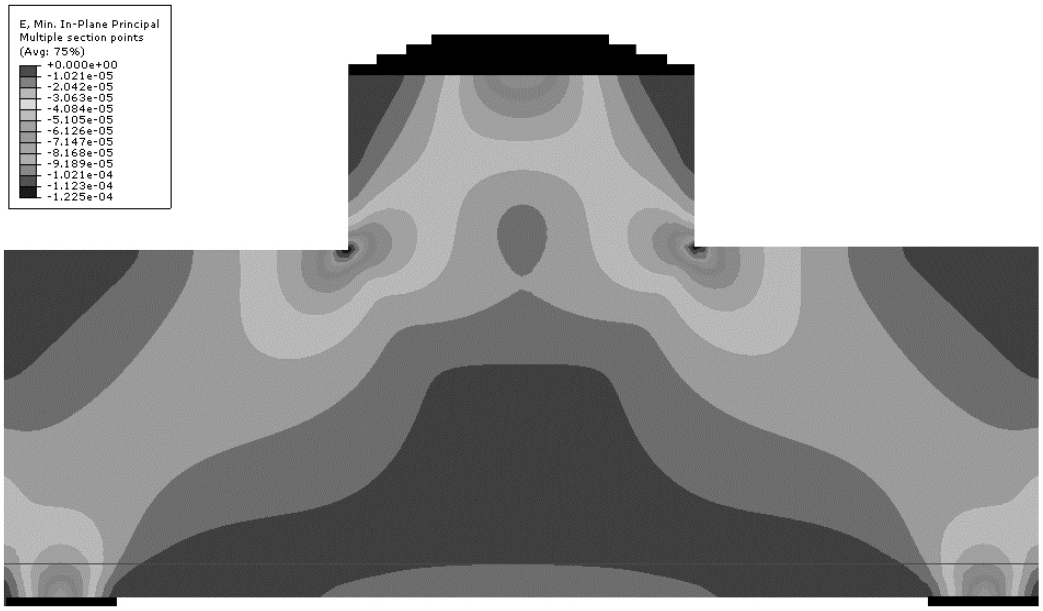

Figure 4.53- Maximum in-plane principal compressive strain for Specimen AL1 at 50 kips

The diagonal splitting failure of the concrete seen in the specimens is a function of the stress concentration introduced by the column and the supports. This phenomenon has been observed before, and it has been interpreted as a bottle strut. The Commentary to Appendix A in the ACI 318-08 Building Code notes that a bottle shaped strut is one that is wider at mid-length than it is at its ends, but no insight into when this type of struts forms is given. When a bottle strut forms the capacity of the strut is reduced and special reinforcement is required (ACI 318 Section A.3.3). The AASHTO 2007 LRFD Bridge Design Specifications do not include any mention of a bottle strut, but the AASHTO crack control reinforcement meets the requirements of the reinforcement required for a bottle strut in ACI 318. Figure 4.55 shows a bottle-shaped strut superimposed on a specimen that underwent diagonal splitting failure of the concrete in a test conducted at the University of Texas-Austin (Brown and Bayrak, 2005). In this case, a steel plate with enough stiffness to introduce the stress concentration was used to apply the load. When the bottle strut was drawn onto the photograph, the stress concentration was not considered; however, there is a clear difference between the centerline of the splitting crack and the strut. The failure of a bottle strut is assumed to be governed by the shape of the strut, which is a function of the stress concentrations introduced by the loading and the supports. This failure mode should always be assumed when the boundaries of the beam are stiff enough (columns) to induce stress concentrations. In general, this is all deep beams.

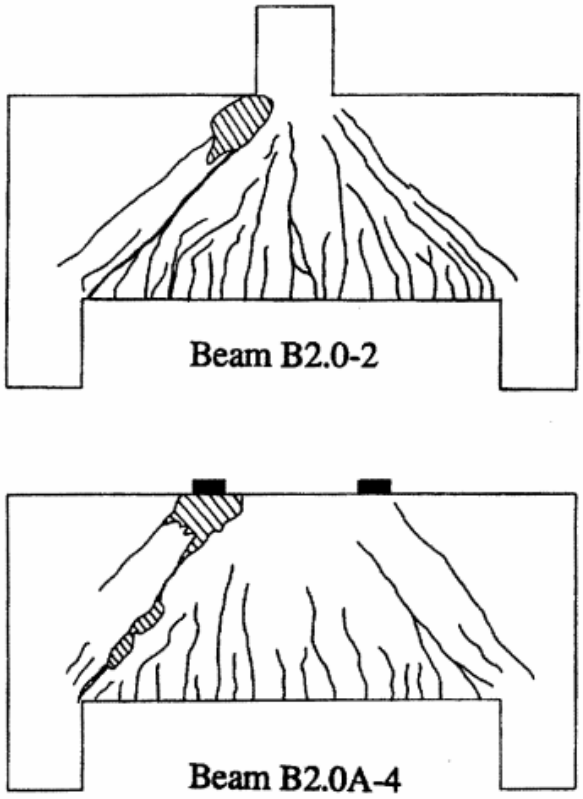

Figure 4.54- Difference in column and plate loading (Foster and Gilbert, 1998)

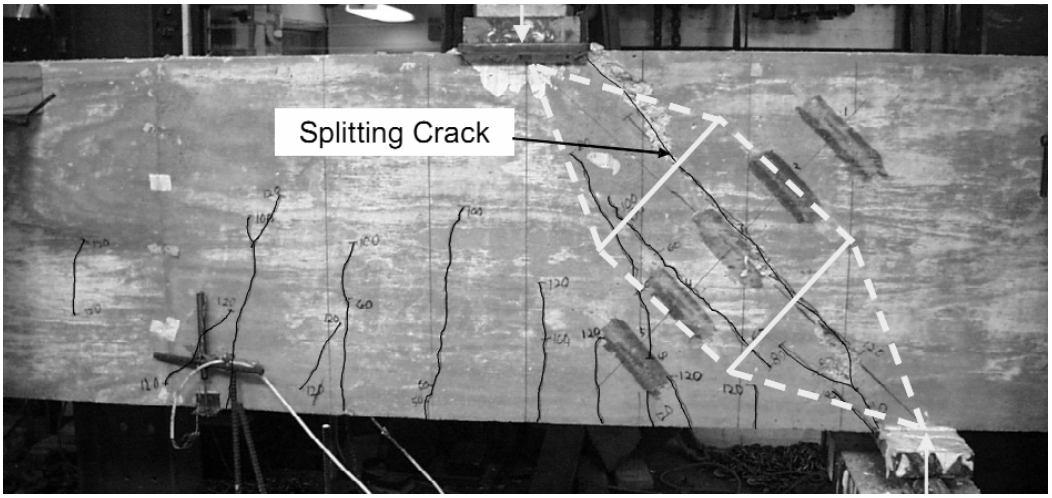

Figure 4.55- Bottle strut and splitting failure crack (Brown and Bayrak, 2005)

While introducing the stress concentration which defines the failure mode, the column also decreases the stresses in the beam portion of the specimen by allowing them to distribute into the column as well as shortening the effective span. These two factors tend to increase the ultimate capacity of the specimen with a stub column. The distribution of stresses into the column can clearly be seen in the results of the FE model shown in Figs. 4.52 and 4.53. The effective shortening of the span can be seen in the strut angles seen at ultimate in Table 4.2. The inclusion of the column effects the strut angle. In table 4.2 a is the distance between the center of the support to the center of the applied load, and d is the distance from the top of the beam to the centroid of the longitudinal reinforcement. It is common to approximate a strut angle by taking the inverse tangent of d/a. When compared to the strut angles calculated using equilibrium, applied load, and strain data in the longitudinal reinforcement, the measured strut angle is larger in every case. The differences in the values of a and a_{eff} ranges from 1.7%-33.7% depending on the reinforcement details. The assumption that the strut angle can be approximated using the d/a ratio is reasonable when the longitudinal tension reinforcement ratio is high.

Table 4.3- Summary of experimental results

Specimen	ρ	ρ_v	a (in)	d (in)	$\theta_{d/a}$ (degrees)	θ_{ult} (degrees)	P_{crack} (kips)	P_{ult} (kips)
AS1	0.65%	0.0%	24	16.4	34.35	45.86	90	172
AS2	0.65%	0.0%	24	16.4	34.35	46.16	60	160
AS3	1.30%	0.0%	24	16.06	33.79	43.52	125	259
AS4	1.30%	0.0%	24	16.06	33.79	40.90	100	267
AL1	0.65%	0.0%	48	32.8	34.35	46.38	200	546
AL2	1.30%	0.0%	48	32.12	33.79	34.24	300	661
BL1	0.65%	0.0%	48	32.8	34.35	43.40	225	499
BL2	1.30%	0.0%	48	32.12	33.79	34.46	200	631
BL3	1.30%	0.3%	48	32.12	33.79	39.30	300	739
BL4	1.30%	0.3%	48	32.12	33.79	38.61	300	858
BL5	1.30%	0.3%	48	32.12	33.79	39.20	300	871

4.5.2 Longitudinal Reinforcement

The amount of longitudinal reinforcement impacts the behavior and the failure mode of the pier cap specimen. The addition of longitudinal reinforcement caused a reduction in the angle of the compression strut and an increase in capacity. Only the large specimens presented in Section 4.4 are discussed to avoid including size effect. Figure 4.56 shows the load vs. deflection plots for Specimens AL1, AL2, BL1, and BL2 up to ultimate load. The specimens with 0.65% longitudinal reinforcement (AL1 and BL1) failed at an average load of 522 kips, while the specimens with 1.3% longitudinal reinforcement (AL2 and BL2) failed at an average load of 646 kips.

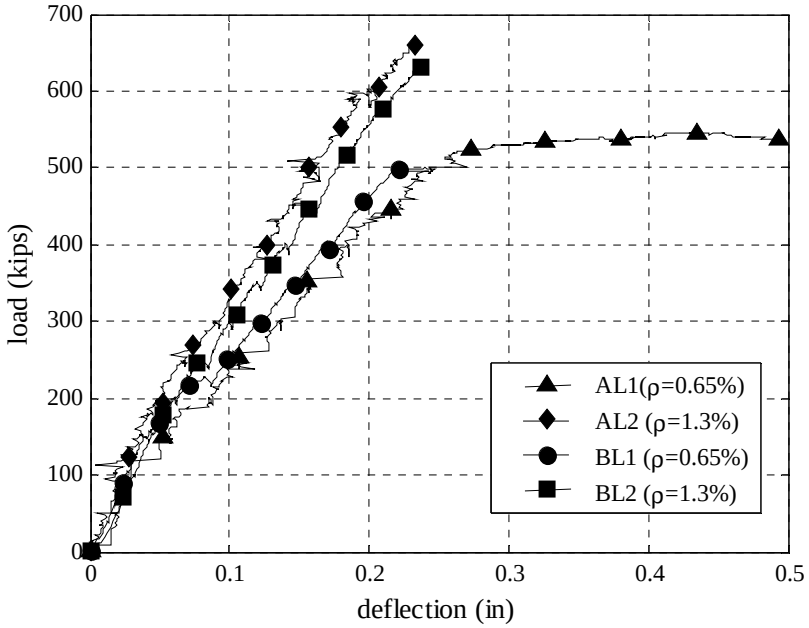

Figure 4.56- Load vs. deflection plot for Specimens AL1, AL2, BL1, and BL2

The ultimate capacity of Specimen AL1 was governed by yielding of the longitudinal reinforcement. Despite being constructed in the same manner, Specimen BL1 failed due to tension splitting. The reason for this was the difference in the yield

stress of the longitudinal reinforcement. The longitudinal steel in Specimen AL1 had a yield stress of 65 ksi while the longitudinal reinforcement of BL1 had a yield stress of 80 ksi. The lower yield stress of the longitudinal steel gave Specimen AL1 its ductile behavior. The ductile failure mode will govern for specimens with smaller reinforcement ratios and lower yield stresses. Figure 4.57 shows the applied load vs. the strain in the longitudinal reinforcement for specimens AL1, AL2, BL1, and BL2. The strains were calculated for all specimens using the LVDT 18 except for Specimen AL1 where a strain gage mounted on the longitudinal reinforcement at midspan was used. Also depicted in the figure are the yield strains for their respective longitudinal reinforcement. Specimen BL1 failed at a strain very close to the point where specimen AL1's reinforcement yielded. If specimens AL1's longitudinal reinforcement had a slightly higher yield point it can be presumed a splitting failure of the concrete like specimen BL1's would have occurred. The strains in both Specimens AL2 and BL2 did not reach yield.

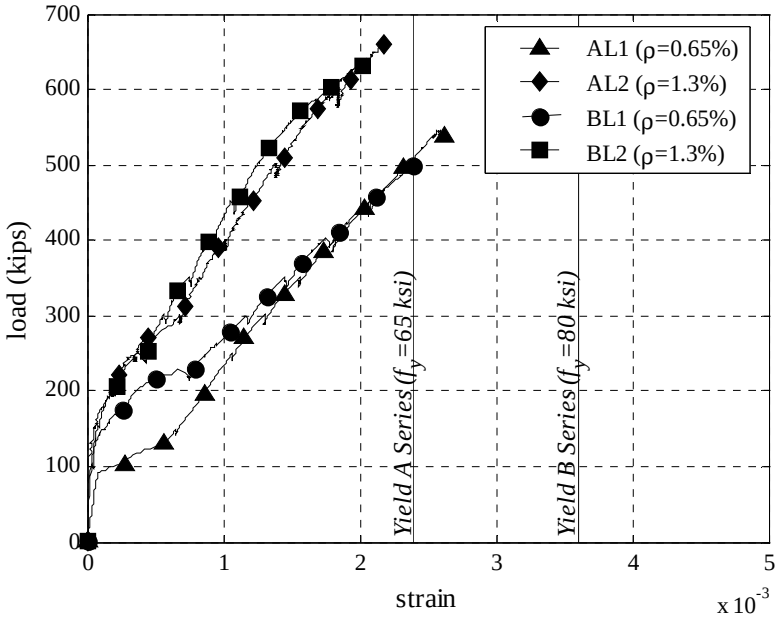

Figure 4.57-Load vs. strain for Specimens AL1, AL2, BL1, and BL2

Doubling the longitudinal reinforcement increased the average capacity of the specimen by 23%. Changing the longitudinal reinforcement ratio changed the shape of the tied arch which formed increasing its size and allowing greater loads to be reached. This is shown by the change in the angle of the principal compression strut when the reinforcement ratio is increased, as shown in Figure 4.58 for Specimens AL1, AL2, BL1, and BL2. Again, the principal compression strut angle is calculated using equilibrium, the applied load and the strains in the longitudinal reinforcement.

Arch action for the full scale specimens began between 200 and 300 kips of applied load. Specimen AL1 appears to be an outlier, but this is because a strain gage at midspan of the bar of the bar was used to calculate the strut angle. The localized strain gage was not as sensitive to cracking across the entire span as the LVDT; this is why the plot for AL1 shows a truncated transition into arch action. The cracking loads for Specimen AL1 agree well with results for the other specimens; since arch action is initiated by cracking; this indicates that arch action begins at the same time.

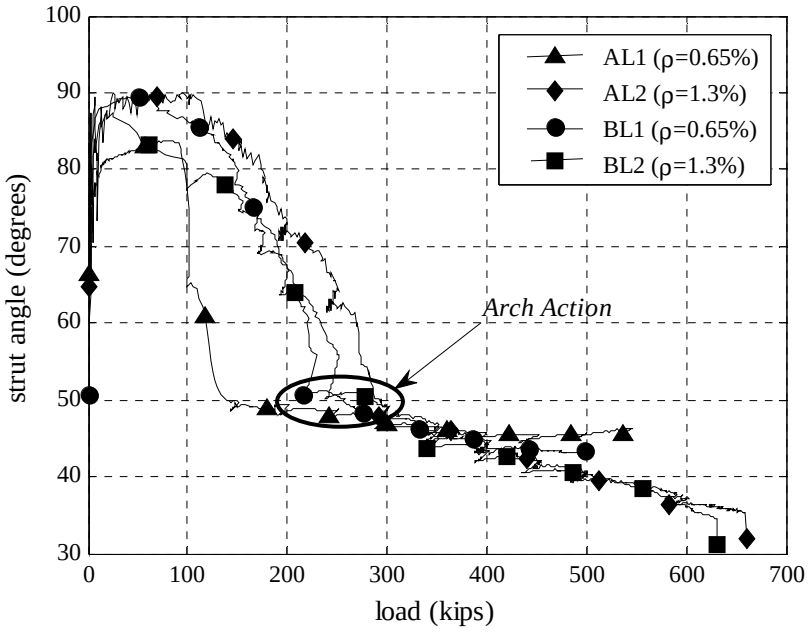

Figure 4.58- Strut angle vs. load for Specimens AL1, AL2, BL1, and BL2

The specimens with 1.3% longitudinal reinforcement (AL2, and BL2) had a smaller strut angle than the specimens with 0.65% longitudinal reinforcement (AL1, and BL1). At ultimate, the strut angle for the specimens with 1.3% longitudinal reinforcement had an average value of 34.4°, and the specimens with 0.65% longitudinal reinforcement had an average value of 45°. There is a difference of 11° between these values. By reducing the strut angle the trajectory of the strut is moved away from the corner of the column to the center of the column. This reduces the influence of the stress concentration. If no change in the shape of the tied arch occurred with the increase of longitudinal reinforcement; the stress concentration would have had the same influence and failure would have occurred at the same loads despite the difference in longitudinal reinforcement.

4.5.3 Size Effect

The effect of depth (or size) on the ultimate shear capacity of reinforced concrete beams is well documented. Bazant and Sun (1987) included size effect into their equation for shear capacity. They postulated that the size effect was due to a difference in the energy release rate at the different beam sizes, and the energy release rate is governed by the size of the aggregate and the characteristic length of the concrete. Of all the analysis methods investigated, Bazant's equation is the only one which considers the effect of size. Since this is the case, the small specimens were scaled using Bazant's equation and the flexural moment capacity. Scaling the specimens for size effect included reducing the maximum aggregate size from one inch to a half an inch for the small scale specimens.

Figures 4.59, 4.60, 4.61, and 4.62 show the normalized load vs. deflection and strut angle vs. applied load for the comparable large and small specimens. The plots are normalized to remove the effects of the different scales and concrete strengths; the specimens are separated by reinforcement ratio to improve clarity. The performances of the large and small specimens agree reasonably well; they even had similar crack patterns which are shown in Figs. 4.63 and 4.64. The small-scale specimens tended to develop arch action at a higher normalized load, and the strut angle tended to be greater than the large specimens. For specimens with 0.65% longitudinal reinforcement the average strut angles for large and small specimens were 45° and 46° respectively; there is only about a one degree difference between the two. For specimens with 1.3% longitudinal reinforcement the average strut angle was 42° for small specimens and 34° for large. There is 8° degree difference between the two.

Figure 4.59 shows that all of the specimens with 0.65% longitudinal reinforcement reached similar normalized ultimate capacities. The ultimate capacities of all of these specimens were governed by yielding of the longitudinal reinforcement except for Specimen BL1 which failed by splitting of the concrete. Despite this there is

no distinguishable size effect on ultimate capacity for specimens with 0.65% longitudinal reinforcement. This is not the case for specimens with 1.3% longitudinal reinforcement. In figure 4.60 the average normalized loads at which the small specimens fail is greater than that of the larger specimens by 32%. In Chapter 3 when the small scale specimens were designed it was discussed how the characteristic length of the concrete could not be scaled, and the area of reinforcement that could be provided was limited to common bar sizes. This created an error in the scaling. These errors were 10.5% for specimens with 0.65% longitudinal reinforcement and 12% for specimens with 1.3% longitudinal reinforcement. Despite the scaling error, the percent difference between the normalized ultimate capacity between the large and small specimens with 0.65% longitudinal reinforcement was 3%; well within the experimental error. This low error can be attributed to the fact that the ultimate capacity of three out of the four specimens was governed by yielding of the longitudinal reinforcement; and there should be no size effect for the yielding of steel. On the other hand, the 32% difference for the specimens with 1.3% longitudinal reinforcement is over two and a half times greater than the expected error. This shows that there is a size effect when splitting failure of the concrete governs the ultimate capacity, and that the provisions for size effect in Bazant's equation (aggregate size and effective length) do not properly account for it. This means that full depth specimens will be required to get accurate results applicable to existing pier caps This study has shown that size does have an effect on when arch action begins, and it causes an increase in the angle of the principal compression strut.

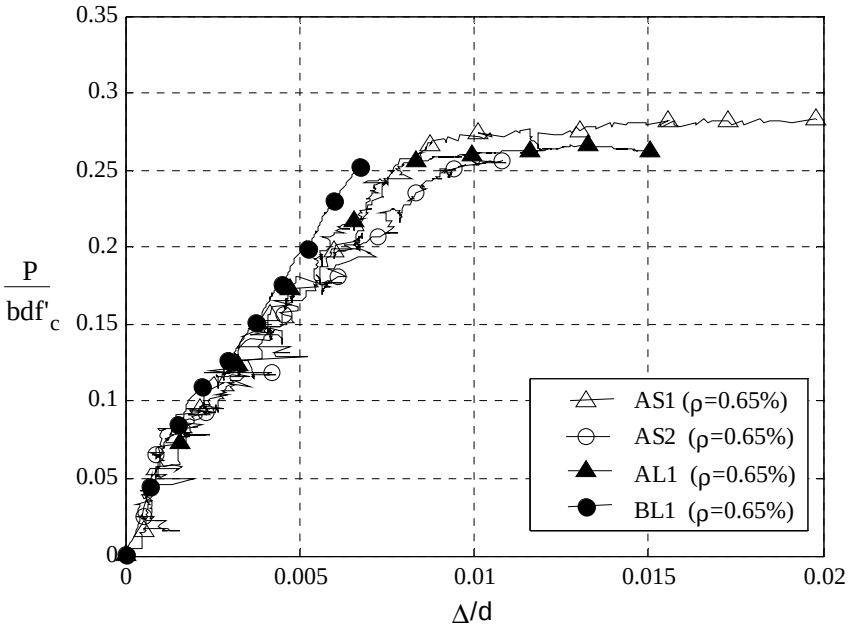

Figure 4.59- Normalized load vs. deflection plots for specimens with ρ=0.0065

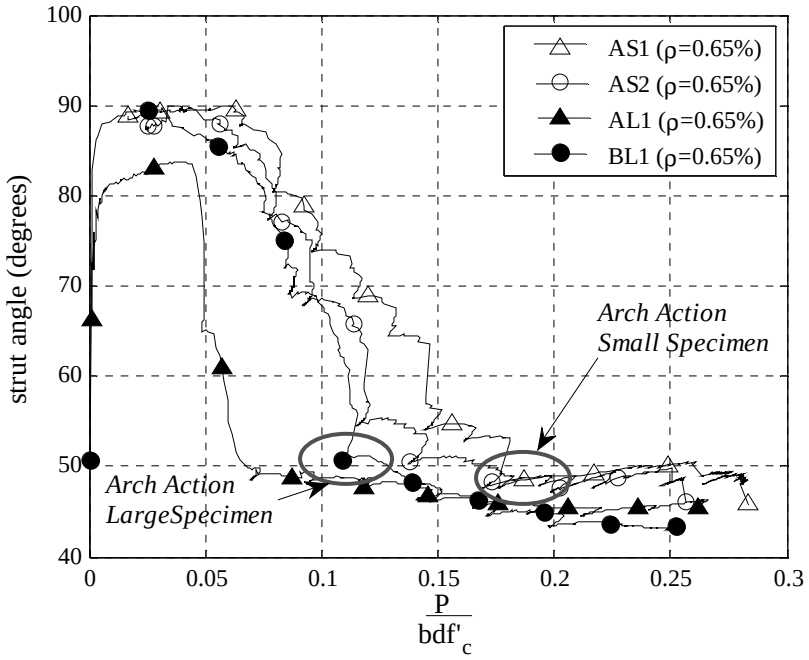

Figure 4.60-Normalized strut angle vs. load for specimens with ρ=0.0065

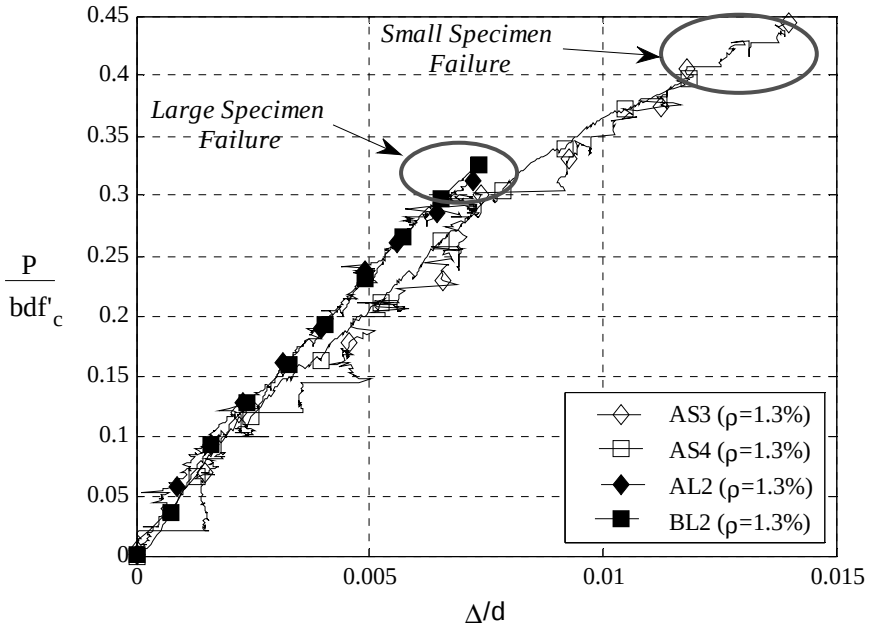

Figure 4.61- Normalized load vs. deflection plots for specimens with ρ=0.013

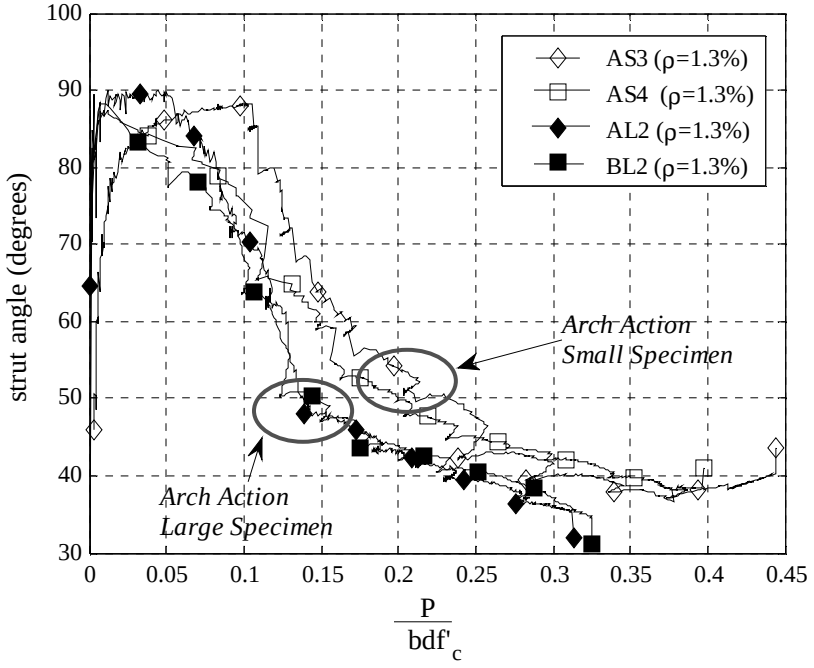

Figure 4.62- Normalized strut angle vs. load for specimens with ρ=0.013

Figure 4.63- Specimens with ρ=0.0065

Figure 4.64- Specimens with ρ=0.013

4.5.4 Effect of Crack Control Reinforcement

The most important effect that the crack control reinforcement had was that it allowed load to be carried after the formation of the splitting crack. The splitting crack caused failure immediately in the specimens that did not contain crack control reinforcement. The splitting failure mode was the failure mode in all of the specimens shown in Figure 4.65, but the addition of the reinforcement confined the crack and allowed the specimens to achieve much greater capacities. The open markers represent specimens with crack control reinforcement while the filled markers represent beams without crack control reinforcement. The addition of the crack control reinforcement increased the average ultimate capacity by 27%.

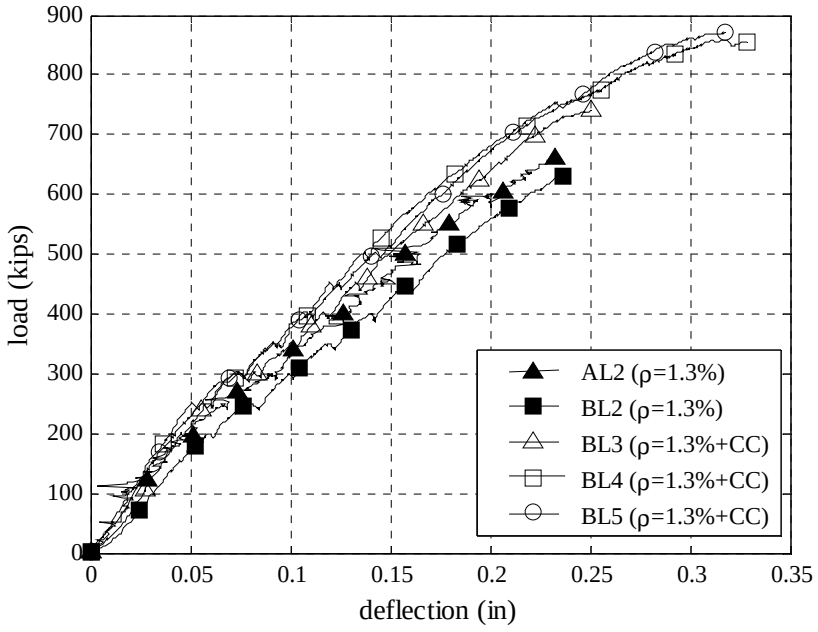

Figure 4.65- Load deflection plot comparing the effect of control reinforcement

The crack control reinforcement did not affect the formation of any crack other than the splitting crack. Figure 4.66 shows a plot of strut angle vs. load comparing

the effects of crack control reinforcement. Despite the inclusion of the reinforcement, the diagonal cracks formed at close to the same loads as the specimens without reinforcement. This is shown by the way that arch action begins in the same area, between 200 and 300 kips. Figure 4.71 shows that the inclusion of the crack control reinforcement did increase the angle of the principal compression strut. At ultimate, the specimens with crack control reinforcement had an average strut angle of 40° as compared to 34° for beams without reinforcement. The experiments have shown that the angle of the principal compression strut is a function of the loading and supports, the longitudinal reinforcement ratio, the depth of the beam, and the crack control reinforcement. With the loading and supports being held constant, the amount of the longitudinal reinforcement had the greatest effect on the strut angle.

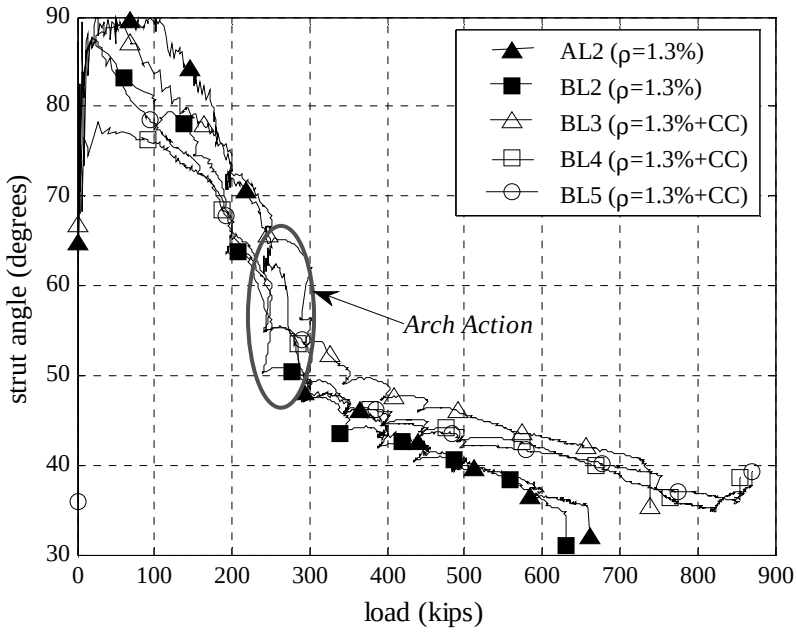

Figure 4.66- Strut angle vs. load plot comparing effect of crack control reinforcement

Chapter 5

CALCULATION OF ULTIMATE CAPACITY

With the experimental data presented in Chapter 4 representing the behavior of a common pier cap, the effectiveness of different methods for analyzing the behavior and strength of pier caps *in situ* can be evaluated. At the end of Chapter 2 the Strut and Tie Model, the Zararis Method, and Bazant's equation were selected as candidates for the analysis of deep beams. Of these methods, the Strut and Tie model and Zararis's Method can be considered mechanical models, while Bazant's equation is based on empirical fitting. Bazant's equation is the only one of the three that incorporates size effect. In this chapter, some modifications are made to the general procedures of strut and tie modeling so that they more closely represent the behavior seen in the experimental testing. Modifications are also made to Zararis's method. Along with these methods, the AASHTO Simplified Model for Non-prestressed beams will be compared. Sample calculations using each of these methods are presented in Appendix B.

5.1 Proposed Modifications to Strut and Tie Model

The strut and tie procedures in the AASHTO Specifications are specifically oriented toward the design of new structures, not the evaluation of existing structures. A set of procedures were developed to construct strut and tie models for the assessment of existing structures which satisfy the AASHTO requirements while being simple, repeatable, programmable, and representative of what was observed in the experimental program. In the design of new structures the load requirements of the pier cap are known, and the applied loads drive the analysis. In contrast, in order to calculate the

ultimate capacity of an existing structure the strain in the bar must be used as a variable to determine the ultimate applied load.

Figure 5.1 defines the geometric parameters needed to develop a strut and tie model according to the AASHTO 2007 LRFD Bridge Design Specifications. In the analysis of an existing structure, the bearing width (l_b) and the amount and location of longitudinal reinforcement are known. The depth of the nodal zones (h_a and h_s) and the strut angle (θ_s) need to be determined. With these variables, the width of the strut (w_s) can be determined.

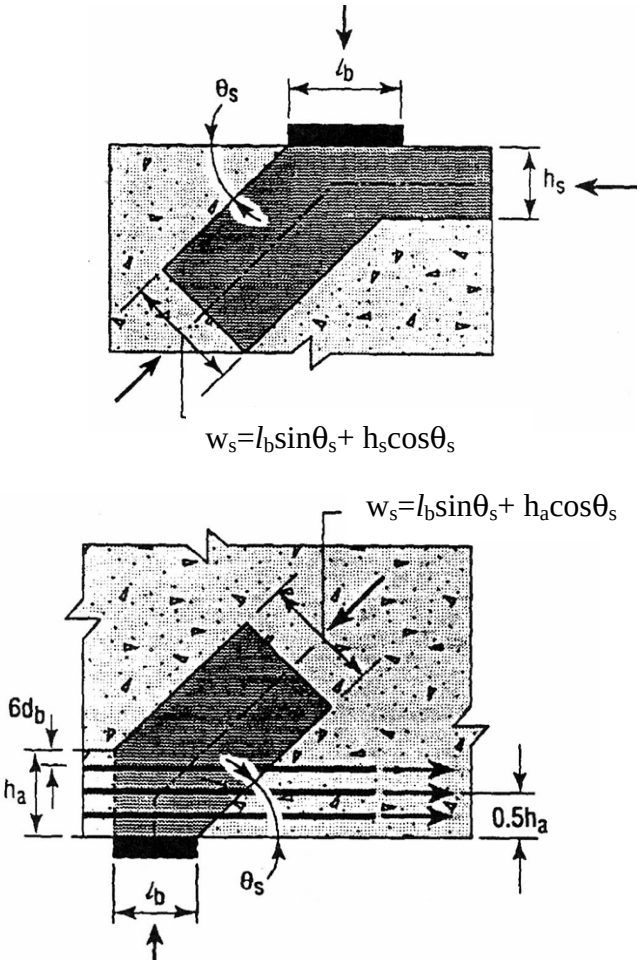

Figure 5.1- Limiting area for nodes and struts (AASHTO 2007)

To simplify the procedure, a strut with a constant width will be used; this means that l_b will be the same at either end of the compression strut, and that h_a and h_s, shown in Figure 5.1, also will be equal. Figure 5.2 shows the proposed strut and tie model superimposed on a specimen with 1.3% longitudinal reinforcement from the experimental program. The first step in creating the strut and tie model is to determine the smallest bearing length; this bearing length will govern for the strut and tie model. In the case of Figure 5.2 (which is representative of most pier caps in the State of Georgia), the bearing at the bottom of the beam is the smallest. For a typical pier cap the l_b on the tension face of the beam is approximately the girder flange width while the l_b on the compression face is the width of the column. Next, the vertical projection of the nodal zone (h_a) is calculated using Eq. 5.1, which is based on equilibrium of forces in the horizontal direction. The terms A_s, E_s, and ε_s represent the force provided by the longitudinal reinforcement in tension. A_s is the area of the longitudinal tension reinforcement, ε_s is the strain in the longitudinal tension reinforcement, and E_s is the elastic modulus of steel. The terms $0.75f'_c$, and b represent the equilibrating compressive force. The reduction factor of 0.75 is specified in the AASHTO 2007 LRFD Specifications for when a tension tie is present in a nodal zone. This factor reduces the compressive strength of the concrete (f'_c). The variable b represents the width of the beam.

$$h_a = \frac{A_s E_S \varepsilon_s}{0.75 f'_c b} \qquad (5.1)$$

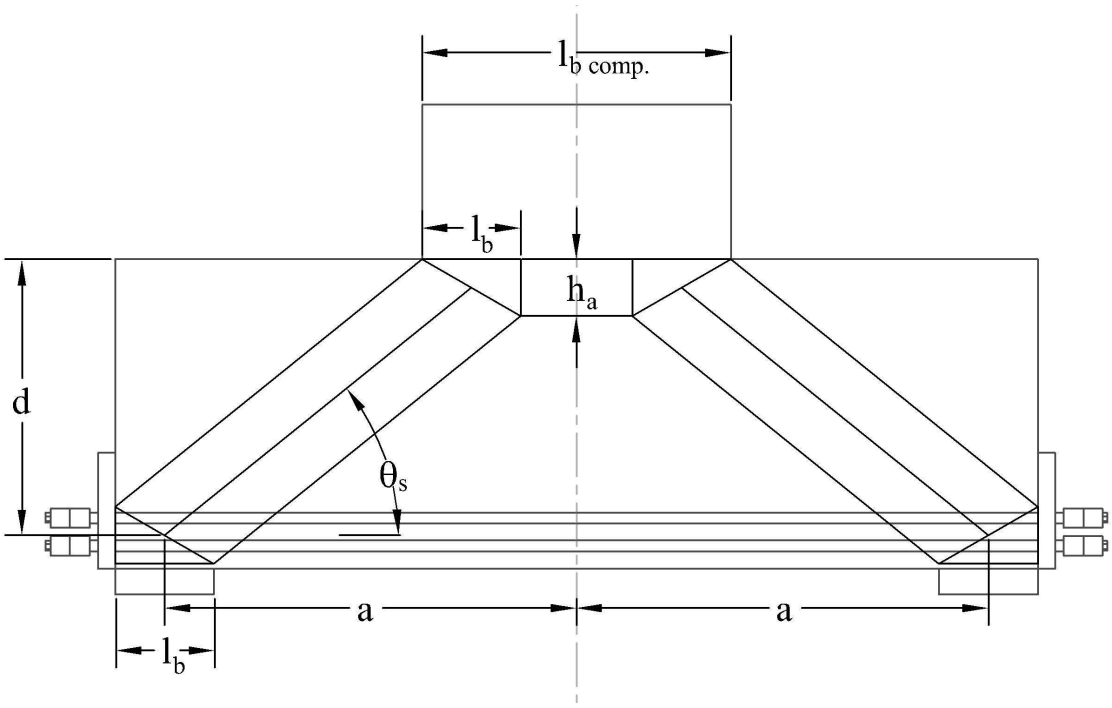

Figure 5.2- Geometry of a compression strut

In order to calculate the angle of the compression strut (θ_s), the location of the node located on the tension side of the beam must be assumed. The limit for the depth of the nodal zone anchored by the tension tie is a function of the bar diameter which can be seen in Figure 5.1. Figure 5.1 is an idealization; in general, the main longitudinal reinforcement is not spaced conveniently at 6 bar diameters from the bottom of the beam and in perfect symmetry, allowing the nodal area to be centered at the effective depth of (d). The tension force in the longitudinal reinforcement is not resisted by a compressive stress along the vertical face of the nodal zone on the tension side of the beam as implied by Figure 5.1. It is developed through shear forces between the bar and the concrete, in addition to any anchorage provided. As long as the bar has proper development length or anchorage, the vertical part of the node will not fail. Moodey et al. (1956) tested details with and without hooked bars, and concluded that the hook had no effect on the development of the bar. Due to the compression forces

induced by the supports on the tension side of the beam the development length of the longitudinal tension reinforcement became so short the hook was not needed to anchor the bar. This agrees well with the small anchorage forces measured during the current experimental program; these forces are discussed in Appendix A. The formation of the tied arch decreases the development length required for the longitudinal reinforcement. With proper anchorage, debonding is not an issue. Therefore in practice, if a check of the details reveals that proper anchorage for the longitudinal reinforcement is provided, the location of the center of the nodal zone can be assumed to be at the intersection of the centroid of the longitudinal tension reinforcement and the center of the vertical bearing.

With the center of the tension nodal zone located, the strut angle can be calculated from the known geometry of the structure and the vertical face of the nodal zone. Figure 5.2 shows the geometry of a compression strut. The shear span (*a*), is defined as the distance between the center of the applied load and its reaction, while *d* is the distance from the extreme compression edge of the beam to the centroid of the longitudinal reinforcement. $l_{b\,comp.}$ is the width of the bearing on the compression side of the beam. In the case of different specimens and loading schemes it is possible for l_b to be equal to $l_{b\,comp.}$ The nodal area at the compression side of the beam is located near the edge of the column as depicted in Figure 5.2; this replicates what was seen in the experimental program. This allows the node on the compression side of the beam to be located using both *a* and *d*. Equation 5.2 gives the angle of the compression strut. With the strut angle (θ_s) and the width and depth of the nodal zone (h_a and l_b), the width of the strut can be calculated using the equation listed in Figure 5.1 and shown as Eq. 5.3.

$$\theta_s = \tan^{-1}\left(\frac{d - \frac{1}{2}\frac{A_s E_s \varepsilon_s}{0.75 f'_c b}}{a - \frac{l_{b\,comp.}}{2} + \frac{l_b}{2}}\right) \tag{5.2}$$

$$w_s = l_b \sin(\theta_s) + h_a \cos(\theta_s) \tag{5.3}$$

The stress in the strut can be calculated as a function of the force in the longitudinal reinforcement and the width of the strut. Equation 5.4 gives the nominal stress (f_n) in the compression strut.

$$f_n = \frac{A_s E_s \varepsilon_s}{w_s b_v \cos(\theta_s)} \tag{5.4}$$

This nominal stress must be less than the maximum allowable stress (f_{cu}) set by AASHTO and represented in Eq. 5.5.

$$f_{cu} = \frac{f'_c}{0.8 + 170\varepsilon_1} \leq 0.85 f'_c \tag{5.5a}$$

$$\varepsilon_1 = \varepsilon_s + (\varepsilon_s + 0.002)\cot^2(\alpha_s) \tag{5.5b}$$

Each equation involved in the analysis is a function of the strain in the longitudinal reinforcement ε_s. The set of equations can be solved iteratively be changing the longitudinal strain and checking if the stress in the compression strut (Eq. 5.4) is less than or equal to the allowable value (Eq. 5.5), and the nodal areas are within the geometric boundaries. The longitudinal strains used must be less than or equal to the yield strain.

Procedures for the development of strut and tie models in ACI 318 are very similar to those seen in the AASHTO Specifications. The main difference is that the allowable stress in the concrete strut is not a function of the strain in the longitudinal reinforcement. The allowable stress in the concrete compression strut is limited by Eq. 5.6.

$$f_{ce} = 0.85\beta_s f'_c \tag{5.6}$$

$\beta s=0.6$ no crack control reinforcement

$\beta_s=0.75$ crack control reinforcement

Other than this, the modified procedures developed in this section for performing an AASHTO strut and tie calculation are appropriate for performing an ACI strut and tie calculation also.

5.2 Proposed Modifications to Zararis's Method

The concept behind Zararis's method is that diagonal cracking reduces the depth of the flexural compression block, and by calculating the crushing capacity of the reduced block, the ultimate capacity of a deep beam can be determined. Therefore, Zararis's Method begins with the calculation of the flexural compression block. In this calculation, the longitudinal tension steel is modeled as linear elastic. This works for beams reinforced above the balanced point where the concrete crushes before the longitudinal tension steel yields, but does not work for beams reinforced below the balanced point where the longitudinal tension steel can yield before the concrete crushes as noted by Senturk and Higgins (2010). They concluded that for their specimens the compression force from the restricted compression block calculated with Zararis's method was greater than what the tension steel could provide. They developed a method where equilibrium was checked at the end of the analysis and, it was not satisfied, an alternate method of calculating the restricted compression block was used. This accounts for yielding of the longitudinal tension reinforcement at the end of the analysis rather than at the beginning.

The method proposed herein takes into account the effects of yielding of the longitudinal tension reinforcement by calculating the flexural compression block using an equation which models the tension reinforcement with an elastic perfectly plastic behavior. Furthermore, in order to make the calculation of the flexural compression block consistent with flexural design in the U.S., the crushing strain of the concrete is

assumed to be 0.003 and the ratio of the maximum flexural compressive stress to the compressive stress is assumed to be 0.85 (Mattock et al. 1961). With these concepts and the elastic-perfectly plastic model for the longitudinal tension reinforcement, Zararis's equation for the normalized depth of the flexural compression block, *c/d*, was re-derived, as shown in Eq. 5.7. The compression force was assumed to be $C=(2/3)bc(0.85)f'_c$ and the tension force was assumed to be $T=\rho bdE_s\varepsilon_c(d-c)/c$ if the longitudinal reinforcement does not yield. If the longitudinal reinforcement yields, then $T=A_sf_y$. The stress and strain diagrams for these force formulations are shown in Figure 5.3. This type of parabolic stress block was used by Zararis when developing his original model. The rest of Zararis's method remains unchanged.

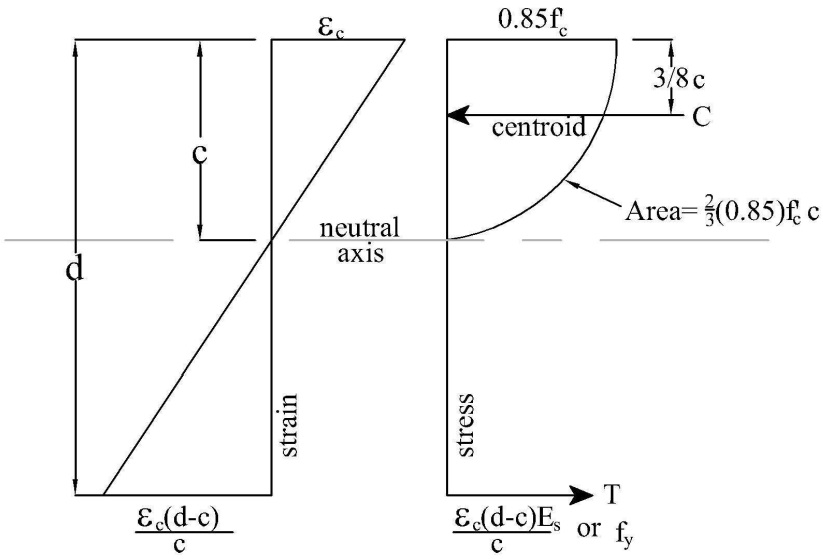

Figure 5.3- Strain and parabolic stress diagrams for flexural compression block calculation

$$\left(\frac{c}{d}\right)^2+153{,}520\frac{\rho}{f'_c}\left(\frac{c}{d}\right)-153{,}520\frac{\rho}{f'_c}=0 \quad \text{if } \varepsilon_s \le \varepsilon_y \qquad (5.7a)$$

$$\frac{c}{d} = \frac{3A_s f_y}{2(0.85) f'_c b_v d} \qquad \text{if } \varepsilon_s > \varepsilon_y \qquad (5.7b)$$

5.2.1 Evaluation of Proposed Model

To determine how the proposed changes to Zararis's model affect the calculation of the ultimate capacity the results of the experimental program were used to calculate the ratio of the experimental ultimate capacity over the calculated ultimate capacity. With known values for the material properties and the principal compression strut angle at ultimate, this shows how accurately the models can predict the ultimate capacity of the specimen with reference to the experimentally determined capacity. In order to incorporate the known strut angle, an effective shear span was calculated by $a_{eff}=d/\tan(\theta_{test})$, where θ_{test} was the strut angle at ultimate calculated from equilibrium for each test. In the experimental program θ_{test} was measured from the horizontal axis, and in this case $\tan(\theta_{test})= d/a$. Zararis measured his strut angle from the vertical axis. By calculating a_{eff} the measured strut angle can be incorporated and, Zararis's assumption that $\tan(\theta_s) \approx a/d$ is maintained. The measured strut angle could also have been converted to Zararis angle by subtracting it from 90°.

Table 5.1 shows the P_{calc}/P_{exp} for Zararis's Method and the Proposed Modifications to Zararis's Method in the last two columns of the table. Zararis's Method has an average P_{calc}/P_{exp} of 0.96 plus or minus one standard deviation of 0.21 (0.96±0.21). The average P_{calc}/P_{exp} for the Proposed Modifications to the Zararis's method has an average of 0.99 ±0.11. The modifications had little impact on the mean bias, but reduced its coefficient of variation by a factor of two.

While good agreement is seen between the models and the test results, it is not possible to replicate this analysis for an existing structure. The main problem is in determining the strut angle. In this case it was determined experimentally; the experimental program has shown that the strut angle is affected by loading geometry,

reinforcement ratio (both longitudinal and transverse), and the beam depth. Figure 5.4 shows the geometry used to formulate the effective *a/d* ratio. It mimics the calculation of the strut angle in Eq. 5.2 and shown in Figure 5.2. The main difference is that h_a is replaced with three eighths c, the distance of the centroid of the parabolic compression block from the compression face of the pier cap. The effective shear span (a_{eff}) is taken horizontally from the middle of the compression bearing to the middle of the bearing at the edge of the column It is calculated by subtracting half of the bearing on the compression side from the shear span. Half of the smallest bearing is then added to the value. The effective depth is taken vertically from centroid of the longitudinal tension reinforcement to the centroid of the flexural compression zone. The centoid of the assumed parabola is calculated as three eighths c as shown in Figure 5.3. It is calculated by subtracting three eighths c from the effective depth. These formulations resulted in Eq. 5.8. Equation 5.8 gives the approximate strut angle in the form of an effective *a/d* ratio. The effective shear span to depth ratio cannot be greater than the actual shear span to depth ratio.

$$a/d_{effective} \approx \frac{a - \frac{l_{b\,comp}}{2} + \frac{l_b}{2}}{d\left(1 - \frac{3}{8}\left(\frac{c}{d}\right)\right)} \leq a/d \qquad (5.8)$$

Table 5.1- Calculation of specimens ultimate capacity

Specimen	θ_{test} (°)	a_{eff} (in)	b (in)	d (in)	a_{eff} /d	A_s (in^2)	f_y (ksi)	ρ	A_{sv} (in^2)	f_{yv} (ksi)	ρ_v	f'_c (psi)	$P_{Prop.}$ (kips)	$P_{zararis}$ (kips)	P_{exp} (kips)	P_{exp} /P_{prop}	P_{exp} /$P_{Zararis}$
AS1	45.9	15.91	9	16.40	0.97	0.93	79	0.0063	0	0	0.0000	4123	160.7	222.2	172.4	1.07	0.78
AS2	46.2	15.75	9	16.40	0.96	0.93	79	0.0063	0	0	0.0000	4226	163.6	229.3	159.9	0.98	0.70
AS3	43.5	16.91	9	16.06	1.05	2.00	76	0.0138	0	0	0.0000	4036	269.4	248.1	258.9	0.96	1.04
AS4	40.9	18.54	9	16.06	1.15	2.00	85	0.0138	0	0	0.0000	4650	263.6	237.5	267.2	1.01	1.12
AL1	46.4	31.25	18	32.80	0.95	3.81	65	0.0065	0	0	0.0000	3473	557.0	825.5	545.8	0.98	0.66
AL2	34.2	47.19	18	32.12	1.47	7.62	65	0.0132	0	0	0.0000	3651	534.4	546.7	660.7	1.24	1.21
BL1	43.4	34.69	18	32.80	1.06	3.81	80	0.0065	0	0	0.0000	3352	573.0	689.5	498.8	0.87	0.72
BL2	34.5	46.80	18	32.12	1.46	7.62	80	0.0132	0	0	0.0000	3352	617.0	522.5	630.8	1.02	1.21
BL3	39.3	39.24	18	32.12	1.22	7.62	80	0.0132	2.4	85	0.0034	3966	906.3	831.3	739.5	0.82	0.89
BL4	38.6	40.22	18	32.12	1.25	7.62	80	0.0132	2.4	85	0.0033	3873	872.6	793.4	859.0	0.98	1.08
BL5	39.2	39.48	18	32.20	1.23	7.62	80	0.0131	2.4	85	0.0034	3672	888.2	791.1	871.0	0.98	1.10
															Mean	0.99	0.96
															Std	0.11	0.21
															C_v	0.11	0.22

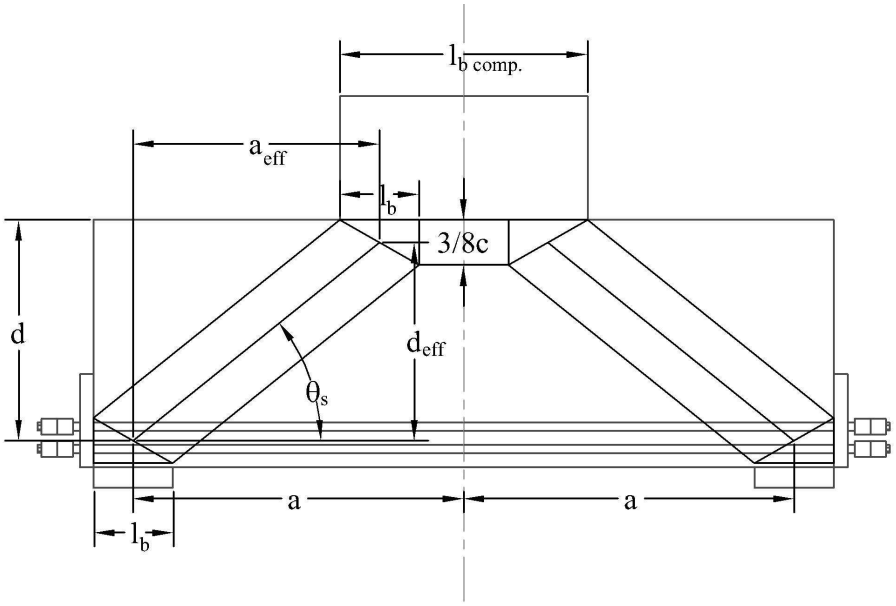

Figure 5.4- Geometry for effective a/d ratio

Table 5.2 compares strut angles calculated with Eq. 5.8 ($\theta_{a/d\ eff.}$) to strut angles calculated by assuming tan(θ_s) ≈d/a ($\theta_{a/d}$). The angles are measured from the horizontal axis. The ratio of $\theta_{test}/\theta_{calc}$ was calculated. It is clear that the mean for Eq. 5.8 is closer to one, making it a better estimate.

The calculation of the ultimate capacity of a reinforced concrete deep beam using the proposed modifications to the Zararis Method is a straight forward procedure. The depth of the flexural tension block is calculated using Eq. 5.7a. The results are then checked using Eqs. 5.9 and 5.10. If the compression force (C) is greater than the tension force (T), Eq. 5.7b must be used to define the flexural compression block.

$$C = \frac{2}{3} bc(0.85) f'_c \tag{5.9}$$

$$T = A_s f_y \tag{5.10}$$

Table 5.2- Comparison of strut angles

Specimen	$\theta_{a/d\ eff}$ (°)	$\theta_{a/d}$ (°)	θ_{test} (°)	θ_{test} / $\theta_{a/d\ eff}$	θ_{test} / $\theta_{a/d}$
AL1	40.2	34.3	46.4	1.15	1.35
AS1	40.2	34.3	45.9	1.14	1.34
AS2	40.2	33.8	46.2	1.15	1.37
AL2	37.2	33.8	34.2	0.92	1.01
AS3	36.6	34.3	43.5	1.19	1.27
AS4	36.8	33.8	40.9	1.11	1.21
BL1	39.5	34.3	43.4	1.10	1.26
BL2	35.7	33.8	34.5	0.96	1.02
BL3	36.5	33.8	39.3	1.08	1.16
BL4	36.4	33.8	38.6	1.06	1.14
BL5	36.0	33.8	39.2	1.09	1.16
			Mean	1.09	1.21
			Std	0.08	0.12
			C_v	0.07	0.10

The effective *a/d* ratio is then calculated using Eq. 5.8. The reduced compression block due to diagonal cracking is calculated using Eq. 5.11. Finally, the nominal strength is computed using Eq. 5.12.

$$\frac{c_s}{d} = \frac{1 + 0.27R(a/d_{effective})^2}{1 + R(a/d_{effective})^2} \frac{c}{d} \tag{5.11a}$$

$$R = 1 + (\rho_v / \rho)(a / d_{effective})^2 \quad (5.11b)$$

$$V_u = \frac{bd}{a / d_{effective}} \left[\frac{c_s}{d} \left(1 - 0.5 \frac{c_s}{d} \right) f'_c + 0.5 \rho_v f_{yv} \left(1 - \frac{c_s}{d} \right)^2 \left(\frac{a}{d_{effective}} \right)^2 \right] \quad (5.12)$$

5.3 Comparison of Analysis Methods

The objective of this section is to determine which of the analysis models best represents the behavior of the reinforced concrete deep beams when compared to the experimental results and, more importantly, the laboratory tests of the pier cap specimens. To compare the different analysis methods, a larger sample of tests is required than those tested herein and reported in Chapter 4. To supplement the present experimental program, a database of symmetrically loaded reinforced concrete beams tested at *a/d* ratios between 1 and 2 was assembled. Tests were only included if the material properties were characterized properly and the dimensions of the bearing and loading points were reported. Appendix C gives the details of the specimens considered. Table 5.6 gives the calculated ultimate capacity of each of the specimens using the six different methods, and the ratio of the experimental ultimate capacity to the calculated ultimate capacity. The material properties used to calculate the ultimate capacity were those reported from material characterization, not nominal design values. Including the results from the current experimental program, 92 individual tests are listed in the database.

The average reinforcement ratio for this database is 2.2% and the average beam height is 20 inches. These values differ from the standard pier cap used to design the experimental program which had a reinforcement ratio of 0.65% and a height of 36 inches. Since this was the case, both the entire database and just the results of the experimental program were used when making conclusions about analysis methods.

Table 5.3 summarizes this analysis, giving the mean, standard deviation and coefficient of variation for the ratio of P_{exp}/P_{calc} for each of the different analysis methods.

Table 5.3- Ratio of experimental to calculated ultimate capacity for entire database and Phase I specimens

	$P_{exp.}/P_{Zararis}$	$P_{exp.}/P_{Mod.\ Zararis}$	$P_{exp.}/P_{AASHTO}$	$P_{exp.}/P_{ACI}$	$P_{exp.}/P_{Simplified}$	$P_{exp.}/P_{Bazant}$
Entire Database n=92						
Mean	0.98	1.06	2.22	1.74	2.48	1.54
Std.	0.21	0.19	0.91	0.51	1.55	0.62
C_v	0.21	0.18	0.41	0.29	0.63	0.40
Current Experimental Program n=11						
Mean	1.37	1.18	1.48	1.40	3.97	2.53
Std.	0.19	0.18	0.17	0.22	1.89	0.28
C_v	0.14	0.15	0.11	0.16	0.48	0.11

Looking at the entire database and presuming that a ratio as close to 1.0 is desirable; Zararis's method has the ratio closest to one followed by the Modified Zararis Method. Bazant's equation had a ratio closer to one than both the ACI and AASHTO strut and tie models. The ACI strut and tie model was less conservative and had a bias closer to 1.0 than the AASHTO strut and tie model. Since the geometries of the models were constructed in the same manner, the difference between the two models is entirely a function of how the allowable stresses in the struts are calculated. The AASHTO simplified model did the poorest job in this regard.

Regarding the specimens in the current experimental program reported in Chapter 4, the results are slightly different. The correlation between the calculated and experimental ultimate capacity improved for both the AASHTO and ACI strut and tie models, while the correlation worsened for Zararis's Method, the Modified Zararis Method, Bazant's Equation, and the AASHTO Simplifed method. The change in results for Zararis's Method is due to the smaller reinforcement ratio. Zararis's method could not account for the yield of the longitudinal tension steel. Also, by approximating the

principal compression strut angle as a/d it does not account for the effects of the stub column. The change for the Modified Zararis Method is strictly caused by the effect of the stub column on the strut angle. Bazant's equation is based on a regression analysis, and it is possible that some of the same tests in the database were used in the development of his equation. This is why Bazant's equation does not perform as well when applied to the experimental program as it did when applied to the larger database. Any regression equation will work well for the test results used in its derivation. Finally, the larger ratio shown by the AASHTO Simplified method for both the database and the current experimental program indicates that it is much less applicable to deep beams than any of the other methods.

Taking into account the results presented in Table 5.3, the Modified Zararis Method appears to be the most suitable model for calculating the ultimate capacity of reinforced concrete deep beams similar in configuration to the pier caps considered in this study. It performs well when compared to both the database and the results from the experimental program. When the exact strut angle is known, it can predict the ultimate capacity with a ratio of P_{exp}/P_{calc} of 0.99 and a standard deviation of 0.11 as shown in Table 5.1. When the strut angle is unknown and must be calculated, the average of P_{exp}/P_{calc} increases to 1.18, as shown in Table 5.3. With further investigation of the parameters that affect the strut angle, further improvements in the Modified Zararis method might be possible. .

Both the AASHTO and ACI strut and tie models could be improved through better handling of the allowable stress as well as improved methods of determining the truss geometry. The best indicator of the truss geometry in a deep beam is provided by the cracks, which show the boundaries of the compressive struts. Figure 5.5 shows the strut and tie configuration formulated for Specimen AL2. ; The observed cracks are superimposed onto the beam, and indicate that the strut and tie model is generating compression struts which encroach into the cracked area of the beam and are

too large. When the ratio of P_{exp}/P_{calc} is examined, the AASHTO and ACI strut and tie models have ratios above one. This indicates that they are conservative. Since the arches are modeled as larger than is appropriate as shown by Figure 5.5 the allowable stress in the struts must be underestimated to make the calculations conservative.

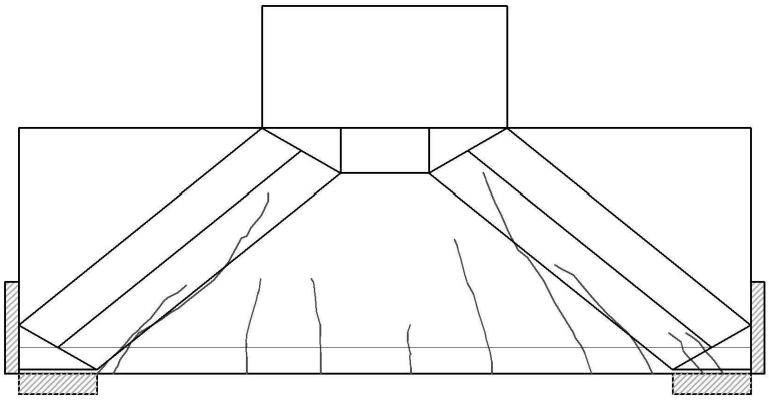

Figure 5.5- Strut and tie model with observed cracks for Specimen AL2

5.3.1 Effect of Stub Column

The specimens designed for this experimental program included a stub column to distribute the applied load. Other experimental tests with columns cast along with beams were found and added to the database. With this data, it is possible to use hypothesis testing to determine if the column has a statistically significant effect on the ultimate capacity of the specimens. Before performing a hypothesis test, a probability distribution to describe the data needed to be determined. Three distributions were compared using probability plots: the normal, log normal, and Weibull distributions. When the data are plotted vs. the matching theoretical distribution, the plot should be linear. Table 5.4 gives the coefficient of determination (R^2 value) for a line fit to the data in the probability plots; the closer the value is to one the more linear the fit. The

entire database of 92 samples was used to determine the distribution. From the table, it can be seen that the Log-Normal distribution provides the best fit to the data of the three distributions tested.

Table 5.4- R^2 values for linear fits to probability plots

	Normal	Log-Normal	Weibull
Zararis	0.93	0.96	0.90
Mod Zararis	0.89	0.95	0.86
AASHTO	0.84	0.96	0.80
ACI	0.89	0.93	0.88
Simplified	0.88	0.94	0.84
Bazant	0.99	0.98	0.97

The Kolmogorov-Smirnov test (K-S Test) was used to determine if the data for specimens with and without columns originated from the same distribution, at the 5% significance level (Georgakakos, 2009). The results of the K-S Test for the six methods indicated that specimens which included stub columns came from a different statistical population than those which did not. Table 5.5 summarizes the means, standard deviations, and coefficients of variation of the ratio of ultimate experimental capacity to calculated ultimate capacity for beams with and without stub columns. The presence of the column does clearly have an effect, making the ultimate capacities predicted by the Zararis Method, the proposed Modified Zararis Method, the AASHTO simplified method, and Bazant's equation more conservative. This agrees with the conclusion from chapter four that despite adding a stress concentration the presense of the column tends to increase the ultimate capacity of the specimen by distributing stresses into the column and shortening the shear span. The means and coefficients of variation are reduced for all of these models. The column has the opposite effect on the strut and tie models. The correlation between the calculated ultimate capacity and the

experimental ultimate capacity improves with the inclusion of the stub column for the strut and tie models.

Table 5.5- Ratio of ultimate experimental capacity to calculated ultimate capacity for beams with and without columns

	$P_{exp.}/P_{Zararis}$	$P_{exp.}/P_{Mod.\ Zararis}$	$P_{exp.}/P_{AASHTO}$	$P_{exp.}/P_{ACI}$	$P_{exp.}/P_{Simplified}$	$P_{exp.}/P_{Bazant}$
Without Columns n=64						
Mean	0.94	0.99	2.45	1.86	2.16	1.21
Std.	0.30	0.15	0.43	0.38	1.53	0.42
C_v	0.32	0.15	0.18	0.20	0.71	0.35
With Column n=28						
Mean	1.06	1.23	1.72	1.48	3.19	2.29
Std.	0.14	0.19	0.98	0.52	1.46	0.34
C_v	0.13	0.15	0.57	0.35	0.46	0.15

Table 5.6- Ultimate capacity calculations

Specimen	$P_{exp.}$ (kips)	$P_{Zararis}$ (kips)	$P_{Mod. Zararis}$ (kips)	P_{AASHTO} (kips)	P_{ACI} (kips)	$P_{Simplified}$ (kips)	P_{Bazant} (kips)	$P_{exp.}/P_{Zararis}$	$P_{exp.}/P_{Mod. Zararis}$	$P_{exp.}/P_{AASHTO}$	$P_{exp.}/P_{ACI}$	$P_{exp.}/P_{Simplified}$	$P_{exp.}/P_{Bazant}$
Bechtel 2011													
AL1	545.0	425.2	397.4	422.1	422.1	139.1	206.7	1.28	1.37	1.29	1.29	3.92	2.64
AS1	170.0	117.4	117.9	118.4	125.2	37.9	59.4	1.45	1.44	1.44	1.36	4.49	2.86
AS2	160.0	119.2	118.5	120.3	125.5	38.4	59.7	1.34	1.35	1.33	1.28	4.17	2.68
AL2	660.0	532.5	633.0	532.4	521.8	139.6	317.2	1.24	1.04	1.24	1.26	4.73	2.08
AS3	260.0	144.7	185.6	144.9	144.2	36.7	93.9	1.80	1.40	1.79	1.80	7.08	2.77
AS4	252.0	159.1	210.4	159.8	166.1	39.4	96.2	1.58	1.20	1.58	1.52	6.40	2.62
BL1	498.8	415.7	462.5	344.5	486.3	136.6	205.3	1.20	1.08	1.45	1.03	3.65	2.43
BL2	630.8	502.4	663.1	436.9	479.0	133.8	312.9	1.26	0.95	1.44	1.32	4.71	2.02
BL3	739.5	643.2	786.0	516.4	566.8	553.5	321.5	1.15	0.94	1.43	1.30	1.34	2.30
BL4	859.0	634.7	777.4	527.7	553.5	551.8	320.3	1.35	1.10	1.63	1.55	1.56	2.68
BL5	871.0	616.0	757.7	524.3	524.8	548.0	317.5	1.41	1.15	1.66	1.66	1.59	2.74

Table 5.6- Ultimate capacity calculations continued

Specimen	$P_{exp.}$ (kips)	$P_{Zararis}$ (kips)	$P_{Mod. Zararis}$ (kips)	P_{AASHTO} (kips)	P_{ACI} (kips)	$P_{Simplified}$ (kips)	P_{Bazant} (kips)	$P_{exp.}/P_{Zararis}$	$P_{exp.}/P_{Mod. Zararis}$	$P_{exp.}/P_{AASHTO}$	$P_{exp.}/P_{ACI}$	$P_{exp.}/P_{Simplified}$	$P_{exp.}/P_{Bazant}$
Clark 1951													
B1-1	125.4	110.2	119.8	27.6	70.5	114.1	90.3	1.14	1.05	4.55	1.78	1.10	1.39
B1-2	115.4	115.8	126.6	29.6	76.5	115.3	91.7	1.00	0.91	3.89	1.51	1.00	1.26
B1-3	128.1	111.1	120.9	27.9	71.5	114.3	90.6	1.15	1.06	4.59	1.79	1.12	1.41
B1-4	120.6	110.0	119.6	27.5	70.3	114.1	90.3	1.10	1.01	4.38	1.72	1.06	1.34
B1-5	108.6	113.7	124.0	28.9	74.3	114.9	91.2	0.96	0.88	3.76	1.46	0.95	1.19
B2-1	135.4	133.0	139.8	27.4	70.1	199.5	90.2	1.02	0.97	4.93	1.93	0.68	1.50
B2-2	144.9	141.7	150.2	30.6	79.5	201.3	92.4	1.02	0.97	4.73	1.82	0.72	1.57
B2-3	150.6	137.8	145.5	29.2	75.2	200.5	91.4	1.09	1.04	5.16	2.00	0.75	1.65
B6-1	170.6	157.0	143.1	45.6	127.1	123.9	101.7	1.09	1.19	3.74	1.34	1.38	1.68
C1-1	124.9	130.9	124.3	49.9	56.1	93.8	100.3	0.95	1.01	2.50	2.22	1.33	1.25
C1-2	139.9	133.1	124.8	51.0	57.7	94.2	100.7	1.05	1.12	2.74	2.43	1.49	1.39
C1-3	110.6	125.4	122.7	47.3	52.5	92.8	99.3	0.88	0.90	2.34	2.11	1.19	1.11
C1-4	128.6	141.4	126.8	55.0	63.5	95.7	102.2	0.91	1.01	2.34	2.02	1.34	1.26
C2-1	130.4	138.8	137.3	46.8	84.0	156.3	99.1	0.94	0.95	2.79	1.55	0.83	1.32
C2-2	135.4	143.1	138.9	48.9	88.7	157.1	99.9	0.95	0.97	2.77	1.53	0.86	1.36
C2-3	145.6	140.4	137.9	47.6	85.7	156.6	99.4	1.04	1.06	3.06	1.70	0.93	1.46
C2-4	129.6	149.2	141.1	51.9	95.7	158.3	101.1	0.87	0.92	2.50	1.35	0.82	1.28
C3-1	100.5	89.3	96.9	30.5	30.8	86.0	92.4	1.13	1.04	3.29	3.26	1.17	1.09
C3-2	90.1	88.1	95.5	30.0	30.2	85.8	92.2	1.02	0.94	3.00	2.98	1.05	0.98
C3-3	84.6	88.7	96.2	30.3	30.5	85.9	92.3	0.95	0.88	2.79	2.77	0.98	0.92
C4-1	139.0	142.9	158.5	52.8	53.9	93.3	133.7	0.97	0.88	2.63	2.58	1.49	1.04
C6-2	190.6	214.6	186.2	86.4	99.7	103.8	146.0	0.89	1.02	2.21	1.91	1.84	1.31
C6-3	195.6	212.9	185.9	85.6	98.4	103.6	145.7	0.92	1.05	2.29	1.99	1.89	1.34
C6-4	192.7	221.7	187.4	89.8	104.8	104.8	147.1	0.87	1.03	2.15	1.84	1.84	1.31
D1-1	135.4	188.4	162.5	89.4	109.2	94.5	151.4	0.72	0.83	1.52	1.24	1.43	0.89
D1-2	160.4	188.1	162.5	89.2	108.9	94.4	151.4	0.85	0.99	1.80	1.47	1.70	1.06
D1-3	115.4	180.6	160.9	85.2	102.3	93.5	150.5	0.64	0.72	1.35	1.13	1.23	0.77
D2-1	130.4	180.7	163.9	83.8	100.0	114.5	150.2	0.72	0.80	1.56	1.30	1.14	0.87
D2-2	140.4	189.5	166.0	88.6	107.9	115.6	151.3	0.74	0.85	1.58	1.30	1.21	0.93

Table 5.6- Ultimate capacity calculations continued

Specimen	$P_{exp.}$ (kips)	$P_{Zararis}$ (kips)	$P_{Mod. Zararis}$ (kips)	P_{AASHTO} (kips)	P_{ACI} (kips)	$P_{Simplified}$ (kips)	P_{Bazant} (kips)	$P_{exp.}/P_{Zararis}$	$P_{exp.}/P_{Mod. Zararis}$	$P_{exp.}/P_{AASHTO}$	$P_{exp.}/P_{ACI}$	$P_{exp.}/P_{Simplified}$	$P_{exp.}/P_{Bazant}$
Clark 1951 Continued													
D2-3	150.4	184.4	164.8	85.8	103.3	115.0	150.7	0.82	0.91	1.75	1.46	1.31	1.00
D2-4	150.6	183.0	164.4	85.0	102.0	114.8	150.5	0.82	0.92	1.77	1.48	1.31	1.00
D3-1	177.6	231.9	233.7	104.6	117.5	159.6	206.3	0.77	0.76	1.70	1.51	1.11	0.86
D4-1	140.4	192.1	181.0	81.4	96.3	199.2	149.8	0.73	0.78	1.72	1.46	0.70	0.94
D1-6	78.6	78.9	85.8	23.3	61.3	82.8	63.0	1.00	0.92	3.37	1.28	0.95	1.25
D1-7	80.6	79.5	86.5	23.6	62.1	82.9	63.1	1.01	0.93	3.42	1.30	0.97	1.28
D1-8	83.6	79.1	86.1	23.4	61.6	82.8	63.1	1.06	0.97	3.57	1.36	1.01	1.33
B0-1	54.4	64.3	45.9	22.3	40.8	28.6	44.1	0.85	1.18	2.44	1.33	1.90	1.23
B0-2	42.4	64.9	46.0	22.5	41.4	28.8	44.2	0.65	0.92	1.88	1.02	1.47	0.96
B0-3	57.6	64.2	45.9	22.2	40.7	28.6	44.0	0.90	1.25	2.59	1.41	2.02	1.31
C0-1	78.4	93.4	65.3	40.4	54.0	29.3	60.6	0.84	1.20	1.94	1.45	2.68	1.29
C0-2	79.9	90.4	65.1	38.9	51.4	28.5	60.0	0.88	1.23	2.05	1.55	2.80	1.33
C0-3	75.1	90.7	65.1	39.1	51.6	28.6	60.1	0.83	1.15	1.92	1.45	2.62	1.25
D0-1	99.6	150.9	103.3	74.3	71.5	30.0	100.5	0.66	0.96	1.34	1.39	3.32	0.99
D0-2	116.9	152.2	103.4	75.0	72.4	30.2	100.6	0.77	1.13	1.56	1.61	3.88	1.16
D0-3	100.4	151.3	103.3	74.5	71.8	30.0	100.5	0.66	0.97	1.35	1.40	3.34	1.00
Moody et al. 1954													
24 a	133.0	125.4	141.2	69.4	76.8	29.8	137.0	1.06	0.94	1.92	1.73	4.46	0.97
24 b	136.0	140.2	159.1	78.3	89.0	32.1	139.4	0.97	0.85	1.74	1.53	4.23	0.98
25 a	120.0	168.6	190.6	93.7	105.1	34.9	168.9	0.71	0.63	1.28	1.14	3.44	0.71
25 b	130.0	129.1	143.3	70.3	74.4	29.4	162.7	1.01	0.91	1.85	1.75	4.42	0.80
26 a	189.0	161.3	179.4	88.0	93.5	32.9	193.4	1.17	1.05	2.15	2.02	5.74	0.98
26 b	178.0	155.2	172.2	84.4	89.0	32.1	192.5	1.15	1.03	2.11	2.00	5.54	0.92
27 a	156.0	144.0	163.7	80.6	92.3	32.7	140.0	1.08	0.95	1.94	1.69	4.77	1.11
27 b	160.0	151.6	172.9	85.1	98.8	33.9	141.2	1.06	0.93	1.88	1.62	4.73	1.13
28 a	136.0	163.1	184.0	90.4	100.6	34.2	168.1	0.83	0.74	1.50	1.35	3.98	0.81
28 b	153.0	158.3	178.2	87.6	96.7	33.5	167.3	0.97	0.86	1.75	1.58	4.57	0.91
29 a	175.0	161.7	179.9	88.2	93.8	33.0	193.5	1.08	0.97	1.98	1.87	5.31	0.90
29 b	196.0	180.3	201.9	99.2	107.7	35.4	196.4	1.09	0.97	1.98	1.82	5.54	1.00

Table 5.6- Ultimate capacity calculations continued

Specimen	$P_{exp.}$ (kips)	$P_{Zararis}$ (kips)	$P_{Mod. Zararis}$ (kips)	P_{AASHTO} (kips)	P_{ACI} (kips)	$P_{Simplified}$ (kips)	P_{Bazant} (kips)	$P_{exp.}/P_{Zararis}$	$P_{exp.}/P_{Mod. Zararis}$	$P_{exp.}/P_{AASHTO}$	$P_{exp.}/P_{ACI}$	$P_{exp.}/P_{Simplified}$	$P_{exp.}/P_{Bazant}$
Moody et al. 1954 Continued													
30	215.0	193.0	212.3	100.5	109.5	107.5	196.8	1.11	1.01	2.14	1.96	2.00	1.09
31	228.0	185.2	199.7	90.6	153.6	156.7	194.2	1.23	1.14	2.52	1.48	1.46	1.17
Rogowsky 1984													
BM1/1.0 T1	270.7	425.1	293.9	190.6	135.2	86.9	201.9	0.64	0.92	1.42	2.00	3.12	1.34
BM1/1.0 T2	314.3	427.5	293.5	190.6	135.2	72.4	201.9	0.74	1.07	1.65	2.32	4.34	1.56
BM2/1.0 T1	337.2	432.5	294.5	194.2	138.8	87.8	202.5	0.78	1.14	1.74	2.43	3.84	1.67
BM1/1.5 T1	136.2	143.1	95.5	75.2	131.8	51.9	67.7	0.95	1.43	1.81	1.03	2.62	2.01
BM1/1.5 T2	159.2	142.8	98.2	75.2	131.8	70.1	67.7	1.11	1.62	2.12	1.21	2.27	2.35
BM2/1.5 T1	101.6	142.8	98.2	75.2	131.8	70.1	67.7	0.71	1.03	1.35	0.77	1.45	1.50
BM2/1.5 T2	156.5	142.8	98.2	75.2	131.8	70.1	67.7	1.10	1.59	2.08	1.19	2.23	2.31
Foster and Gilbert 1998													
B2.0-1	357.5	373.3	266.6	189.3	194.9	120.2	143.7	0.96	1.34	1.89	1.83	2.97	2.49
B2.0-2	370.9	466.2	273.2	241.9	281.8	131.0	153.0	0.80	1.36	1.53	1.32	2.83	2.43
B2.0-3	314.7	359.4	265.2	181.4	183.1	118.6	142.3	0.88	1.19	1.73	1.72	2.65	2.21
B2.0B-5	263.0	383.8	253.2	198.4	209.0	55.0	145.3	0.69	1.04	1.33	1.26	4.78	1.81
B2.0C-6	328.2	403.2	275.2	204.4	218.4	148.5	146.4	0.81	1.19	1.61	1.50	2.21	2.24
B2.0D-7	323.7	428.0	270.9	220.2	244.2	126.6	149.2	0.76	1.19	1.47	1.33	2.56	2.17
B3.0-1	229.3	228.8	175.6	81.3	134.4	160.9	85.0	1.00	1.31	2.82	1.71	1.43	2.70
B3.0-2	236.1	284.6	180.8	108.5	198.4	172.6	95.1	0.83	1.31	2.17	1.19	1.37	2.48
B3.0-3	236.1	224.1	175.0	79.1	129.4	159.9	84.2	1.05	1.35	2.99	1.82	1.48	2.80
B3.0A-4	348.5	330.8	235.6	155.2	187.9	155.4	120.3	1.05	1.48	2.24	1.85	2.24	2.90
B3.0B-5	195.6	219.6	143.8	87.9	149.5	55.0	87.5	0.89	1.36	2.23	1.31	3.56	2.24
Aguilar et al. 2002													
ACI-I	610.0	613.2	496.2	397.9	452.0	274.5	332.6	0.99	1.23	1.53	1.35	2.22	1.83
STM-I	510.0	502.7	428.3	330.1	405.9	265.0	276.4	1.01	1.19	1.55	1.26	1.92	1.85
STM-H	578.0	576.1	496.6	369.6	401.5	268.7	335.3	1.00	1.16	1.56	1.44	2.15	1.72
STM-M	574.0	566.1	479.5	369.6	401.5	154.3	335.1	1.01	1.20	1.55	1.43	3.72	1.71

CHAPTER 6

SHEAR STRENGTHENING OF REINFORCED CONCRETE BEAMS WITH FIBER REINFORCED POLYMERS

Strengthening by externally bonded fiber reinforced polymer (FRP) composites has been viewed as an effective method for improving the performance of existing structures for many years. What makes them particularly desirable is their high strength to weight ratio.

6.1 Existing Experimental Research on the External Shear Strengthening Using FRP

Existing research into rehabilitation with externally bonded FRP composites to enhance shear strength was reviewed to determine how different parameters affect the strengthening of reinforced concrete beams in shear with FRP. In this review, a database of 139 experimental specimens was compiled from 17 different publications and 14 different research groups. The data collected on the concrete specimens focused on the parameters which affect shear resistance (beam height, ratio of shear span/depth, and longitudinal reinforcement ratio) as well as the overall beam geometry and transverse reinforcement ratio. It was also noted if the concrete specimen was cracked before retrofit. The data collected on the FRP rehabilitation included the fiber type, the orientation of the fiber to the longitudinal axis, the type of wrap, if an ASTM standard was used to evaluate the composite tensile properties.

The ultimate shear capacities of the rehabilitated specimens were then compared to the control specimens included in each of the individual studies to evaluate the percent increase in shear capacity. Studies were only incorporated into the database

if they included tests on specimens with no external rehabilitation for comparison. The entire database is presented in tabular form in Appendix D Using the database the following sections explore the effects that the different reinforced concrete and FRP parameters have on the increase in shear strength. This type of study was first performed by Triantafillou in 2000. Bouselham and Challal revisited it in 2004 expanding on the database which Tiantafillou (2000) had collected. This work again expands the database incorporating tests which were performed to fill out areas Bouselham and Challal (2004) had identified as needing further research; most notably beams with greater heights.

To improve the shear strength of an existing reinforced concrete beam FRP reinforcement is bonded to the beam's exterior surface. Load is transferred by shear from the concrete through the bond into the FRP reinforcement. If epoxy is used to bond the composite there must be a nominal amount of FRP bonded to the concrete to develop load in the FRP reinforcement (Chajes, 1995). This is the effective development length. The effective development length is a function of the axial stiffness of the FRP, longer development lengths being required for larger FRP stiffness (Pellegrino et al, 2008). Development of load in the FRP composite can greatly be improved by using different shaped wraps. Figure 6.1 shows the three most common wrap types, the side bond, the u-wrap, and the full wrap.

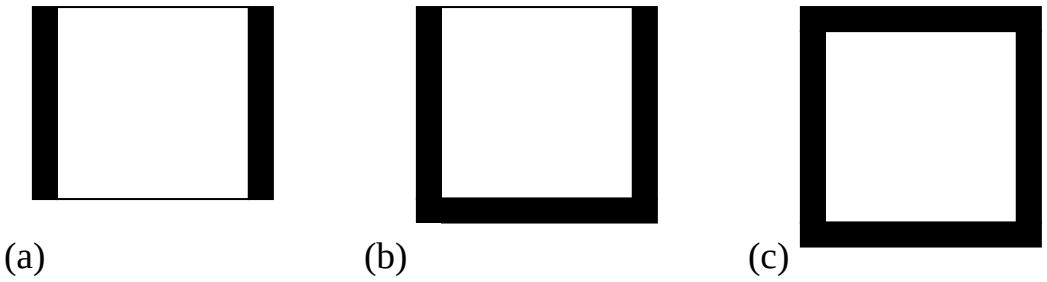

Figure 6.1- FRP wrap configurations (a) side (b) U-wrap (c) full wrap

The FRP reinforcement can be bonded as individual strips, much like steel stirrups, or it can be bonded continuously. Figure 6.2 shows examples of beams with FRP applied continuously (a) and as strips (b).

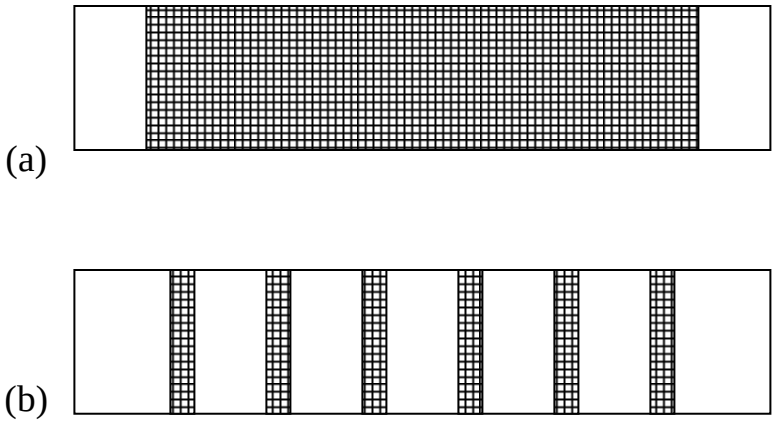

Figure 6.2- Longitudinal application of FRP (a) continuous wrap (b) wrap as strips

The main advantage of using strips is that most of the concrete beam remains exposed, making inspection easy. However, the continuous wrap involves the application of more FRP, allowing a stronger retrofit and improved development length in the longitudinal direction.

6.1.1 Shear Span to Depth Ratio

Chapter 2 showed that the ratio of the shear span to the effective depth of the beam, *a/d*, has been shown to affect the shear resistance of reinforced concrete members significantly. Depending on the *a/d* ratio, different failure modes can be expected. Figure 6.3 shows the ratio of the increase of the shear strength due to the external application of FRP vs. the *a/d* ratio. This ratio of shear strength increase is defined by Eq. 6.1.

$$R_{inc.} = \frac{V_{frp} - V_{control}}{V_{control}} \qquad (6.1)$$

R_{inc}=ratio of increase in ultimate shear due to application of FRP

V_{frp}=experimental shear capacity of specimen strengthened with FRP

$V_{control}$=experimental shear capacity of specimen with no FRP strengthening

There is a large scatter in the data points. While the FRP reinforcement appears to be more effective at higher *a/d* ratios, the data are inconclusive on this point because very few tests were performed at an *a/d* less than two. At an *a/d* less than 2, arch action is the main load carrying mechanism. Bousselham and Challal (2004) also concluded that the externally bonded shear FRP reinforcement was more effective at higher *a/d* ratios.

The *a/d* ratio has been used as a control variable in two studies. In the first, Zhang et al. (2004) tested rectangular beams and found that a decrease in *a/d* caused a decrease in the effectiveness of the FRP strengthening schemes. The strengthening of

these beams included both side bonded and U-wrapped configurations, with fiber angles ranging from 0 to 90 degrees from the longitudinal axis. Zhang et al. (2004) concluded that as *a/d* decreased in deep beams, strengthening with fibers at 90° to the longitudinal axis became less effective while strengthening with fibers at 45° became more effective. In addition, as *a/d* decreased the effectiveness of employing U-wrap decreased. This could be due to the increase of the angle of the compression strut as *a/d* decreases. In the second study, Bousselham and Chaallal (2006) tested T-beams, and observed the opposite behavior from the rectangular beams; as *a/d* decreased the effectiveness of the FRP strengthening increased. The strengthening on these beams were U-wraps made of 0°/90° woven fibers.

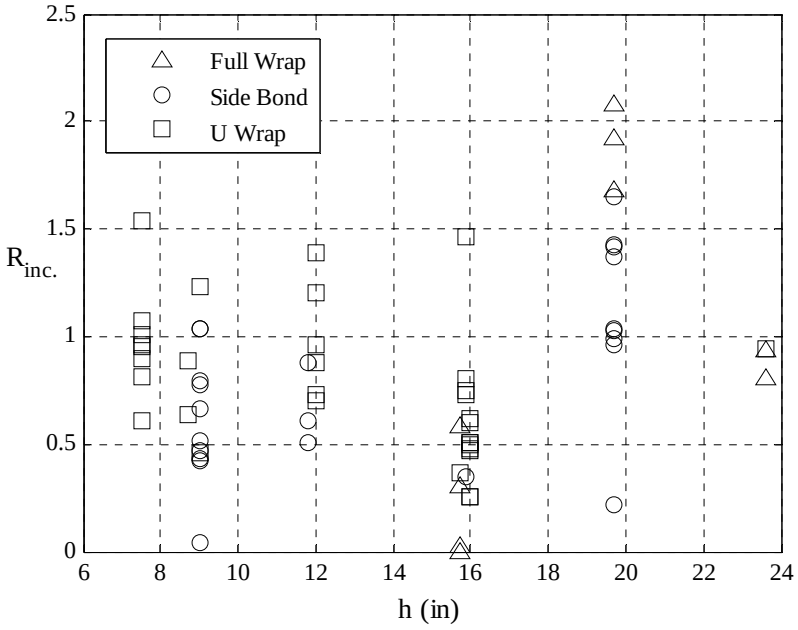

Figure 6.3- Ratio of shear strength increase vs. *a/d* ratio

6.1.2 Beam Depth

Chapter 2 showed that there is a size effect for the shear resistance of reinforced concrete beams. Figure 6.4 shows the shear force increase plotted against the beam depth in beams that had been strengthened with externally bonded FRP composites. The experimental data presented in this figure was taken for beams which had no transverse steel reinforcement because such reinforcement can mask size effect. Since there is no detectable pattern in the data presented in Figure 6.4, it can be concluded that the effectiveness of externally bonded FRP rehabilitations does not depend on the size of the beam. This conclusion is different from that of Bousselham and Challal (2004), who concluded that there was a size effect. It should be noted, however, that the data set explored by Bousselham and Challal was limited because it had only a few tests with specimen depths greater than 12 inches. The data that they had made it appear that there was a possible size effect. Beam depth was used as a control variable in two later studies by Bousselham and Challal (2008) and Leung et al. (2007). The results of those reports also conflict with the overall data shown in Figure 6.4, finding a size effect for both side-bonded and U-wrapped rehabilitations but no size effect for full-wrap rehabilitations. Both studies found that as the beam depth increased, the effectiveness of the FRP reinforcement decreased.

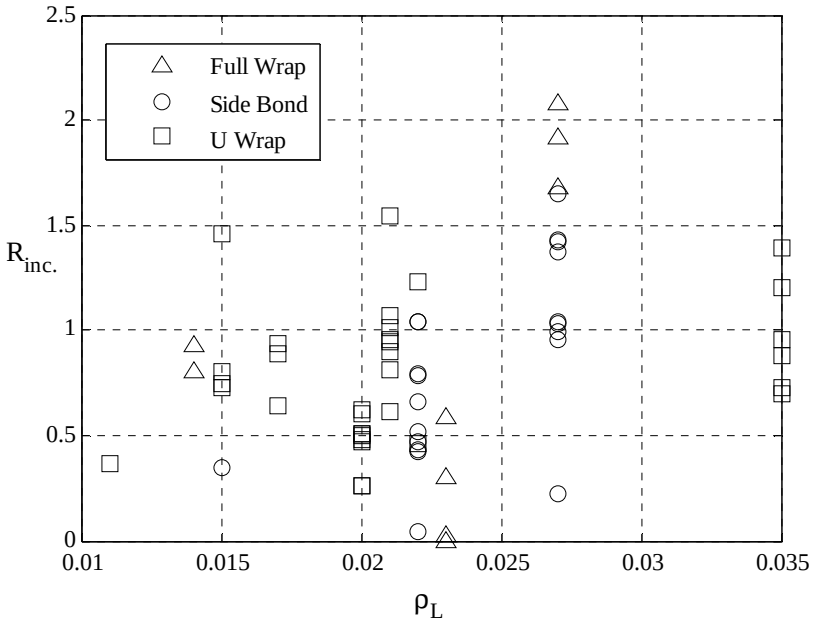

Figure 6.4- Ratio of shear strength increase vs. beam depth

6.1.3 Longitudinal Reinforcement

Kani (1967) asserted that a reduction in the amount of longitudinal steel causes a reduction in the shear capacity of a reinforced concrete beam. Figure 6.5 shows the ratio of shear strength increase vs. the longitudinal reinforcement ratio in beams that had been strengthened with FRP reinforcement. This figure was again developed for test specimens with no transverse steel reinforcement.

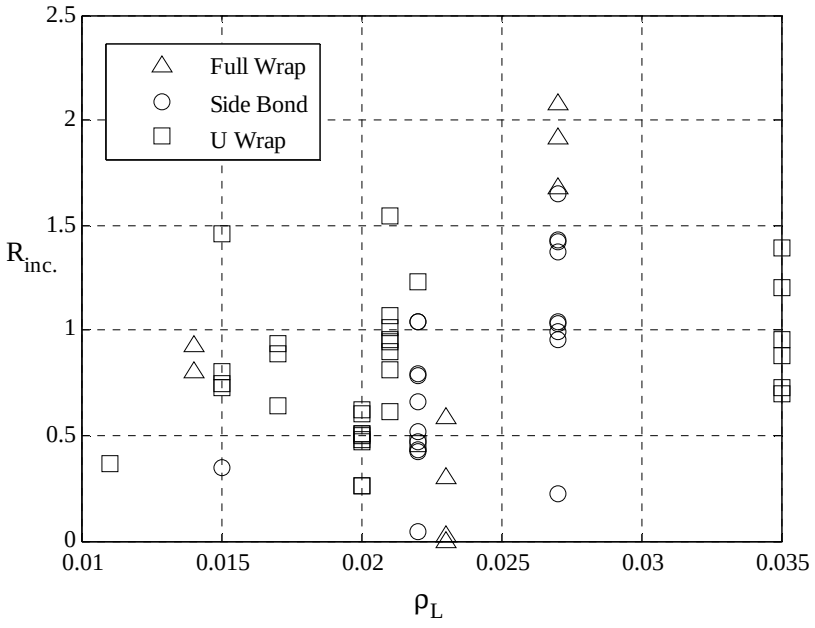

Figure 6.5- Ratio of shear strength increase vs. longitudinal reinforcement ratio

Longitudinal reinforcement does not appear to have an effect on beams strengthened with externally bonded FRP reinforcement, but no controlled study on the effect of longitudinal reinforcement has been performed to date. Moreover, all of the beams in the database have reinforcement ratios greater than 1%. Bousselham and Challal (2004) concluded from their data that there was a relation between longitudinal reinforcement and the effectiveness of the rehabilitation. They based their conclusions on a study of the shear strength vs the ratio of longitudinal reinforcement to the amount of applied FRP reinforcement; unfortunately, this study shows the effect of applying more or less FRP reinforcement; not the effect of longitudinal reinforcement.

6.1.4 Transverse Reinforcement

Transverse steel reinforcement is thought to be the most common way of increasing the shear capacity of a reinforced concrete beam. Figure 6.6 shows the ratio

of shear strength increase vs. transverse reinforcement ratio. It shows that the effectiveness of the FRP strengthening decreases as the web reinforcement ratio increase. Bousselham and Challal (2004) also concluded that the effectiveness of FRP strengthening decreases as web reinforcement increases. To investigate the effect of the *a/d* ratio and the effect of the web reinforcement together, an axis was added to Figure 6.6 resulting in Figure 6.7. From Figure 6.7 it can be seen that the effectiveness of the FRP strengthening is decreased by both the addition of web reinforcement and a decrease in *a/d*.

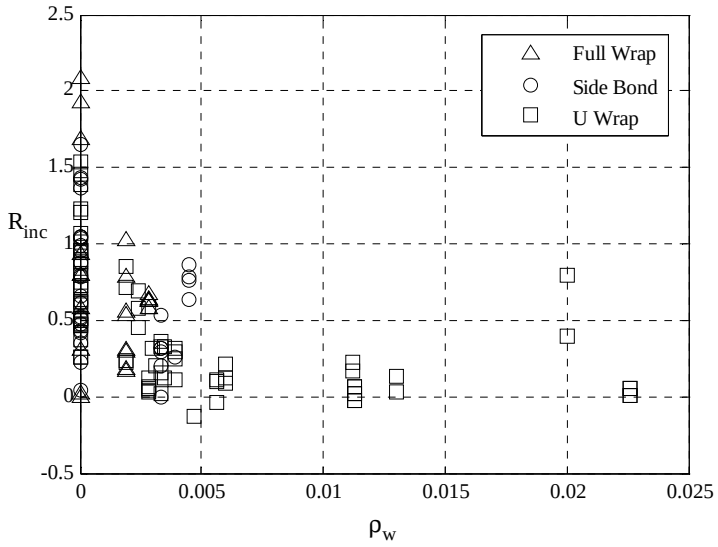

Figure 6.6- Ratio of shear strength increase vs. web reinforcement ratio

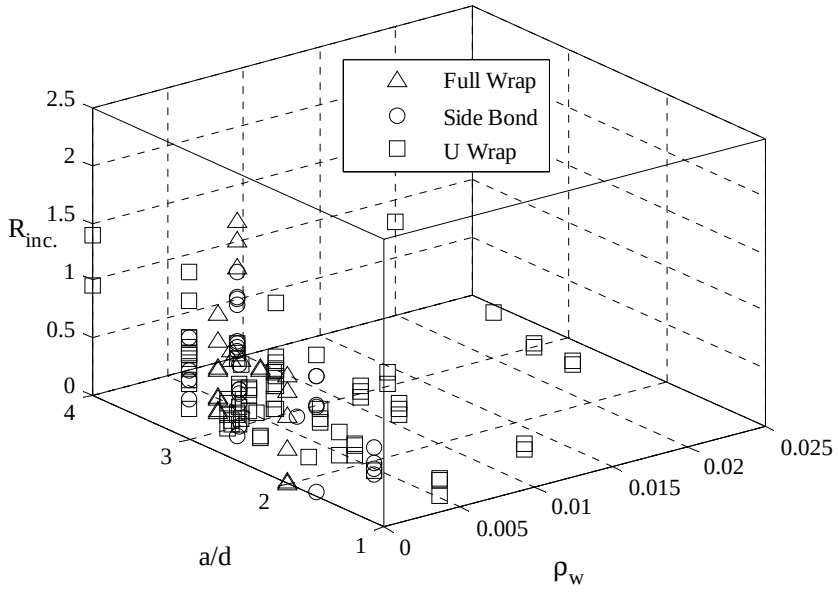

Figure 6.7- Ratio of shear strength increase vs. a/d vs. web reinforcement ratio

The transverse steel reinforcement ratio was used as a control variable in eight publications: Bousselham and Chaallal (2006, 2008), Denaud and Cheng (2001, 2003), Taerwe et al. (1997), Pellegrino and Modenia (2002, 2006), and Khalifa and Nanni (2002). The results of these studies showed that applying FRP reinforcement is a much more effective method of strengthening a reinforced concrete member when there is no transverse steel reinforcement present than when such reinforcement is already present. In some cases, if enough transverse steel reinforcement is already present, the FRP reinforcement provides essentially no increase in shear strength. However, Bousselham and Chaallal (2006, 2008) observed that the strain in the transverse steel was less in beams where FRP reinforcement was applied. Pellegrino and Modenia (2002, 2006) observed that the relative stiffness of the transverse steel to the FRP reinforcement controls the effectiveness of the FRP strengthening scheme. In particular, if the FRP reinforcement is much stiffer than the transverse steel, the FRP will carry the

majority of the load while the steel carries almost nothing. Conversely, if the FRP reinforcement is less stiff then the steel, the steel will carry the majority of the load.

6.1.5 Fiber Angle

The relation of the load relative to the fiber angle greatly affects the strength and stiffness of a unidirectional fiber reinforced composite. For this reason the orientation of fibers relative to principal tensile force is of great interest. Applying the fibers parallel to the primary tension force gives the greatest composite stiffness and strength. The fiber angle has been a control variable in three publications: Chajes et al. (1995), Challal et al. (1998), and Carolin and Taljsten (2005). The results of these tests show that applying FRP reinforcement in which the fibers are aligned with the longitudinal axis of the beam are not beneficial in enhancing shear capacity. All of the specimens tested by each or the researchers had a/d ratios in excess of 2, and could not carry load through arch action. Applying fibers at 90 and 45 degrees to the longitudinal axis is more effective.

6.1.6 Strength of Composite

Increases in the strength and stiffness of the composite do not always increase the shear resistance of the beam. There appears to be a maximum level of strength and stiffness (Khalifa and Nanni, 2000). Since the FRP reinforcement is externally bonded, the load is transferred from the concrete to the FRP reinforcement through shear. The contribution of the FRP is limited by the shear strength of the concrete substrate.

6.2 Existing Mechanical Models and Design Methods

There exist several models for the strengthening of reinforced concrete members for shear with FRP reinforcement. NCHRP Report 655 (Zureick et al. 2010) is a guide specification on the strengthening of reinforced concrete members with FRP which has been published for use with the AASHTO Specifications. It includes provisions for shear strengthening with FRP reinforcement. Report 655 is discussed first and is followed by other methods for predicting the strengths of concrete members strengthened with FRP reinforcement.

6.2.1 NCHRP Report 655

NCHRP Report 655 (Zureick et al. 2010) presents provisional guidelines for the strengthening of bridge components using fiber reinforced polymers. Chapter 4 of the report deals with shear strengthening. The nominal shear strength of the unreinforced member is calculated in accordance with the 2007 AASHTO LRFD Bridge Design Specifications. The shear resistance contribution from the FRP is calculated through the truss model and is dependent on the type of reinforcement. FRP can be applied in strips, or as a continuous sheet. These two reinforcement types are shown in Figure 6.2. The shear resistances of the FRP strengthening are given as:

- For continuous reinforcement

$$V_{frp} = N^{e}_{frp}(\sin\alpha + \cos\alpha)d_{frp} \qquad (6.2)$$

V_{frp}= nominal shear strength provided by FRP

N^{e}_{frp}= effective strength per unit width of FRP

α= angle between FRP principal direction and longitudinal axis

d_{frp}=effective FRP reinforcement depth

- For intermittent reinforcement

$$V_{frp} = \frac{N^{e}_{frp} w_{frp} (\sin\alpha + \cos\alpha) d_{frp}}{S_v} \quad (6.3)$$

w_{frp}= width of FRP reinforcement

S_v= spacing FRP reinforcement

The FRP reinforcement can be bonded to two (side bond), three (U-wrap) or four (full wrap) sides of the member. Figure 6.1 shows examples of the three wrap types. The side bond is not considered to be an effective strengthening method because it is so dependent on the bond between the FRP and concrete, so no value for N^{e}_{frp} is given for the side bond case. The values of N^{e}_{frp} for the cases of the u-wrap and full-wrap are:

- For the U-wrap

$$N^{e}_{frp} = N_{0.004} \quad (6.4)$$

$N_{0.004}$= tensile strength per inch width at a strain of 0.004

- For the full wrap

$$N^{e}_{frp} = N_{0.004} + \frac{1}{2}\left[0.5N_{frp\,ult} - N_{0.004}\right] \quad (6.5)$$

$N_{frp,w}$= $0.5N_{ut} \geq N_{0.004}$

N_{ut}=nominal tensile strength of FRP

The value of $N_{0.004}$ is the force in the FRP reinforcement at debonding, which occurs at an FRP reinforcement strain of 0.004. This means that the strength of the FRP in a U-wrap is invariably governed by debonding. The ultimate strength of the FRP is incorporated into the full wrap because full wraps may fail by fracture of the FRP. The ultimate strength is reduced due to stress concentrations where the FRP is wrapped around corners.

6.2.2 Other Models

There are many methods for design of shear strengthening using FRP reinforcement, including models developed by Triantafillou (1998), Khalifa et al (1998), Chen and Teng (2003), Carolin and Taljsten (2005), and more recently Monti and Liotta (2007). All of the methods take the same general approach, in that they assign a shear contribution to the concrete, the transverse steel reinforcement, and the applied FRP separately.

Triantafillou (1998) and Kahlifa et al. (1998) employed an equation for the shear contribution of externally bonded FRP reinforcement which is a function of the elastic modulus of the FRP reinforcement, FRP reinforcement ratio, and the strain in the FRP reinforcement. The strains in the FRP reinforcement are found through the use of empirical equations based on strain measurements taken during the testing of reinforced concrete members strengthened in shear with FRP reinforcement. The method proposed by Carolin and Taljsten (2005) takes a similar approach, but instead of using empirical data, they use an assumed stress profile and relative stiffnesses to convert the stresses to strains for the strengthened member. Monti and Liotta (2007) developed closed-form solutions for the FRP stress using a stress slip constitutive law, compatibility with the width of the opening shear crack, and boundary conditions based on available bond. These methods are all intended to work with the truss model of shear behavior, discussed in Chapter 2.

Chen and Teng's model, known as the strip method, breaks the FRP reinforcement into strips and uses normalized strains, based on experimental measurements in FRP reinforcement crossing a shear crack, to calculate the development length, the bond strength, and the ultimate strain in the FRP reinforcement

(Deniaud, 2004). This method was developed for use with the truss model, but was later expanded for use with the shear friction model.

Park and Aboutaha (2009) developed a design procedure which incorporated FRP reinforcement into the strut and tie model. Their method simply used the resultant of forces in the transverse reinforcement (both steel and FRP) to locate transverse tension ties horizontally, and they used transformed sections to locate longitudinal the tension ties which are made up of both internal steel reinforcement and externally bonded FRP. The locations of transverse and longitudinal tension ties are given by Eqs. 6.6 and 6.7 respectively.

$$a = \frac{\sum f_{fi} A_{fi} a_{fi} + \sum f_{yi} A_{si} a_{si}}{\sum f_{fi} A_{fi} + \sum f_{yi} A_{si}} \tag{6.6}$$

$$d_{tie} = d + \frac{A_f E_f}{A_f E_f + A_s E_s} d_f \tag{6.7}$$

a= horizontal distance to direction of loading between two nodes

f_{fi} and f_{yi}= allowable stress in FRP and in steel respectively

A_{ft} and A_{si}= areas of transverse steel and FRP respectively

a_{ft} and a_{si}= horizontal distance of FRP and steel stirrups from support

d_{tie}= effective depth of longitudinal reinforcement FRP and steel

d= effective depth of longitudinal reinforcement steel

A_f and A_s= areas of longitudinal steel and FRP respectively

E_f and E_s= modulus of elasticity of FRP and steel respectively

d_f= distance between center of longitudinal steel and FRP reinforcement

This model was then checked against a finite element analysis.

6.3 Critical Review

To properly design a strengthening scheme using FRP reinforcement, the properties of the FRP reinforcement must be understood and considered. The tensile properties of the entire composite, both fibers and matrix, must be tested and documented according to ASTM standards (ASTM D-3039 or D638). The strength of the fibers alone or the data provided by the manufacturer is not sufficient. Of the 139 tests in the database only 13 reported material properties according to an ASTM standard.

The behavior of members strengthened with FRP reinforcement is highly dependent on the member itself. A decrease in the *a/d* ratio appears to decrease the effectiveness of the strengthening, but the experimental results reviewed are in conflict on this point. The addition of transverse steel reinforcement has been shown to decreases the effectiveness of strengthening with FRP reinforcement. This means it may not be possible to apply an FRP strengthening scheme to an existing beam with significant transverse reinforcement and see any increase in strength. The amount of longitudinal reinforcement affects the shear capacity of a reinforced concrete member, but no study on how it influences the effectiveness of shear strengthening with FRP reinforcement has been performed, and there appears to be no trend in the compiled experimental data. The stiffness and orientation of the FRP clearly influences the effectiveness of the retrofit. Aligning the fibers with the direction of principal tension increases the effectiveness of the FRP. Increasing the strength and stiffness of the FRP only improves the retrofit to a point, beyond which there is no benefit. One obvious conclusion from examining the database is that there is a large amount of variation in the increase in strength provided by implementing FRP strengthening schemes. This can be seen in the large scatter in all of the plots. From an experimental point of view, this makes it important to repeat tests to get an idea of this distribution. Previous research on shear strengthening with FRP reinforcements has largely neglected the special case of

larger (h > 20in) deep beams (a/d < 2). The benefits, if any, of FRP reinforcement in a beam which supports load mainly through arch action remains an open question.

Of the available design methods, only the method proposed by Park and Aboutaha (2009) addresses the arch action seen in deep beam behavior. All of the other models are only applicable to beams which fail at the formation of diagonal cracks; they do not account for arch action. Failure due to the formation of diagonal cracks occurs when a/d is greater than 2. The addition of FRP and steel reinforcement is considered to restrict the growth of shear cracks preventing it from causing failure. The crack in most cases is assumed to grow at an angle of 45°; these assumptions are the basis for the Simplified Method for Nonprestressed beams given in the 2007 AASHTO LRFD Bridge Design Specifications. In the previous chapter it was shown that this model was very inaccurate when compared to the experimental data for deep beams. The main reason for this is that the formation of diagonal cracks does not limit the shear strength of a beam with an a/d ratio less than 2. Rather, the diagonal cracks simply form and allow arch action to develop. Failure of the beam occurs with failure of the arch, which is caused by either failure of the compression strut or yielding of the longitudinal steel tie. The addition of longitudinal and transverse crack control steel did not affect the formation of diagonal shear cracks, but they did provide confinement for the compression strut, which delayed splitting failure of the concrete.

Park and Aboutaha's model does account for arch action because it is based on the strut and tie model, but their assumptions regarding the effects of the inclusion of transverse steel and FRP reinforcements are inaccurate. Equation 6.7 for the location of the longitudinal tension tie is reasonable, but Eq. 6.6 can lead to an inaccurate representation of strut and tie action. As an example, Specimen BL3 included AASHTO crack control reinforcement. According to Park and Aboutaha the inclusion

of the transverse steel reinforcement should cause the formation of a transverse tension tie which is located using Eq. 6.6:

$$a = \frac{(0.4)(80)(8+16+24+32+40)}{(5)(0.4)(80)} = 19.2 \text{ in.}$$

Figure 6.8 compares the simple representation of the strut and tie action proposed by Park and Aboutaha to that which actually occurred in the specimen. The model by Park and Aboutaha suggests that the inclusion of the transverse steel reinforcement should increase the angle of the principal compression strut up to 59°. This is an increase in strut angle of 71% over the control specimen BL1 (34.5°). The angle measured at ultimate for Specimen BL3 was 39°; this was an increase over the control specimen of 4.5°. At the high strut angle proposed by Park and Aboutaha the limit state of the strut and tie model would be yielding of the transverse reinforcement at an applied load of 384 kips. Specimen BL3 failed at an applied load of 739.5 kips. An AASHTO strut and tie model which entirely neglects the inclusion of the transverse reinforcement predicted the capacity to be 516 kips. Clearly the model for strengthening does not represent the effects of the inclusion of transverse reinforcement well.

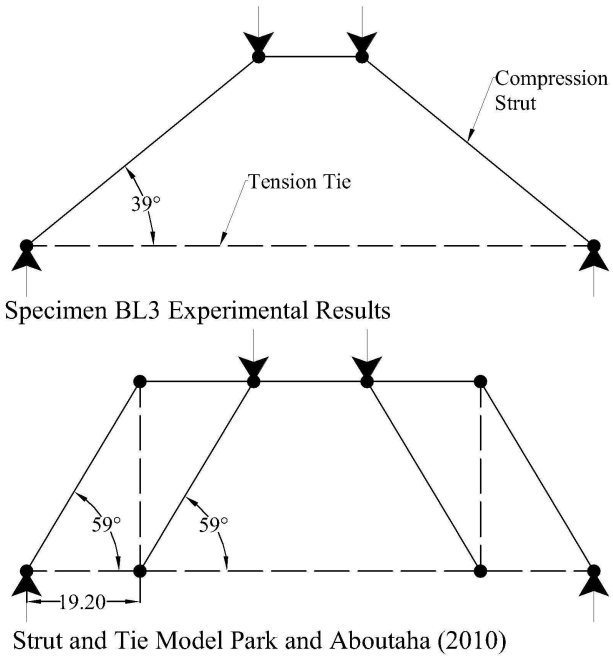

Figure 6.8- Comparison of strut and tie model per Park and Aboutaha (2010) to experimental results

The model by Park and Aboutaha not only predicts a much greater strut angle than that seen in the beam tests, it also results in more truss members and more steel. This means that the truss will develop higher strain energy of deformation under load. Due to the principle of minimum potential energy, the truss which has the smallest strain energy will be the one that forms. Changing the angle of the principal compression strut using external reinforcement is a very difficult task. An example where the required size of a transverse tension tie large enough to change the principal compression angle from 40° to 57° follows.

The elastic strain energy for truss members, given in Eq. 6.8, can be used to calculate the size of a transverse steel tension tie required to change the angle of the principal compression strut.

$$U = \frac{P^2 L}{2EA} \tag{6.8}$$

The first step to designing the tension tie is to calculate the elastic strain energy for the existing structure. We consider the elastic strain energy at the ultimate load for Specimen AL2 as an example. Specimen AL2 had a reinforcement ratio of 1.3% and had an ultimate capacity of 660 kips. It has a similar reinforcement ratio and geometry to Specimen BL3, but did not contain crack control reinforcement. It had an approximate strut angle of 40°. On the day of testing the concrete strength for Specimens AL2 was 3651 psi with an elastic modulus of approximately 3300 ksi.

A strut and tie model for Specimen AL2 was created using the strut angle calculated from equilibrium and using the cracks in the specimen as a guide. This was done to create a strut and tie model to as close to the experimental specimen as possible. The strut and tie model is shown in Figure 6.9. Calculating the strain energy using Eq. 6.12, we have:

$$U = \frac{(1.6P)^2 (45.37)}{(3300)(150.84)} + \frac{(1.23P)^2 (24.63)}{2(3300)(115.56)} + \frac{(1.23P)^2 (99.52)}{2(29000)(7.62)}$$

$$U = 2.33P^2 x10^{-4} + 4.88P^2 x10^{-5} + 3.41P^2 x10^{-4}$$

$$U = 6.23P^2 x10^{-4}$$

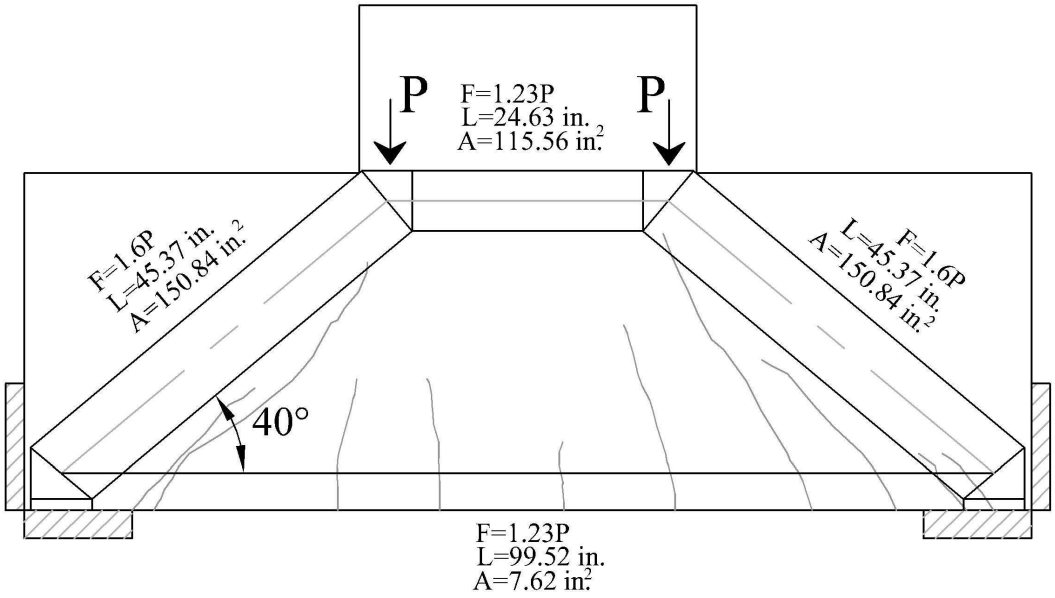

Figure 6.9- Strut and tie model for strain energy calculation for Specimen AL2

With the strain energy calculated for the original strut and tie model, a new strut and tie model for including a transverse tension tie can be created. The strengthening would increase the angle of the principal compression strut to 57°. The strut and tie model for the rehabilitation scheme is shown in Figure 6.10. The calculation of strain energy is done keeping the area (A_{rehab}) and elastic modulus (E_{rehab}) of the tension tie as variables.

$$U = \frac{(1.19P)^2(35.97)}{(3300)(133.2)} + \frac{(1.19P)^2(31.21)}{(3300)(133.2)} + \frac{(0.648P)^2(17.05)}{(3300)(71.82)} + \frac{(1.29P)^2(19.88)}{2(3300)(143.64)}$$

$$+ \frac{(0.648P)^2(19.66)}{(29000)(7.62)} + \frac{(1.29P)^2(60.19)}{2(29000)(7.62)} + \frac{(P)^2(30.14)}{E_{rehab}A_{rehab}}$$

$$U = 1.16P^2x10^{-4} + 1.01P^2x10^{-4} + 3.02P^2x10^{-5} + 3.49P^2x10^{-5}$$

$$+ 3.74P^2x10^{-5} + 2.27P^2x10^{-4} + \frac{(P)^2(30.14)}{E_{rehab}A_{rehab}}$$

$$U = 5.47P^2x10^{-4} + \frac{(P)^2(30.14)}{E_{rehab}A_{rehab}}$$

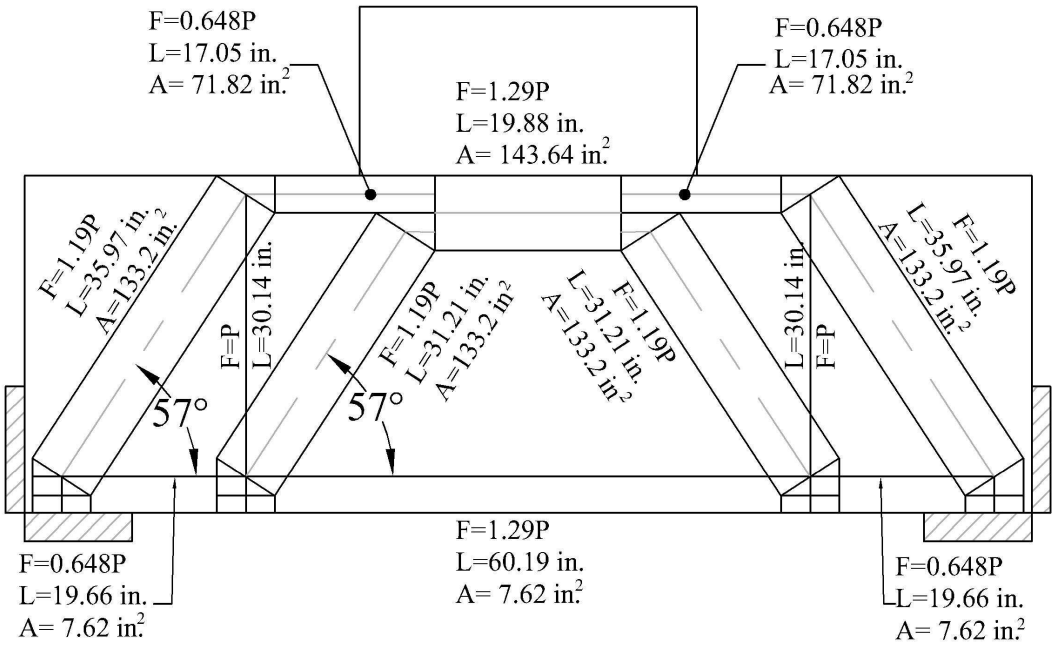

Figure 6.10- Strut and tie model for strain energy calculation for the rehabilitation of Specimen AL2

With the total strain energy for both of the strut and tie models, the area of the transverse tension tie can be can be calculated based on assumed moduli. The strut and tie action shown for the rehabilitation scheme will not form until it has a total strain energy less then that in the original strut and tie model.

$$6.23P^2x10^{-4} = 5.47P^2x10^{-4} + \frac{(P)^2(30.14)}{E_{rehab}A_{rehab}}$$

$$E_{rehab}A_{rehab} = 396{,}579$$

Figure 6.11 shows the required area of the tension tie vs. the elastic modulus of the tie. As the modulus decreases so does the required area. If the modulus is assumed to be 29,000, as for carbon steel, the area of the tension tie would need to be 13.7 in^2. This is a very large amount of steel, and is much larger than the 2 in^2 seen in Specimen BL3. This shows how the addition of an external strengthening large and stiff enough to change the angle of the principal compression strut is a difficult task.

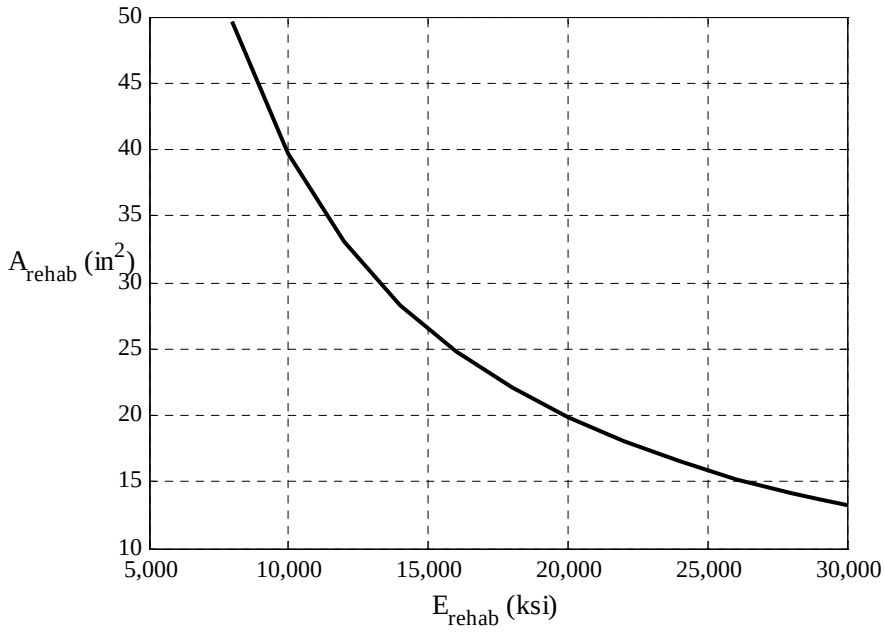

Figure 6.11- Plot of required transverse tension tie area vs. elastic modulus

CHAPTER 7

STRENGTHENING OF REINFORCED CONCRETE DEEP BEAMS WITH EXTERNALLY BONDED FRP REINFORCEMENT

The previous chapters have established a basis for developing practical methods for strengthening reinforced concrete pier caps using external reinforcement. The experimental program described in Chapter 4 showed that an increase in longitudinal reinforcement increased the capacity of the specimens by strengthening the tension tie and changing the geometry of the tied arch which forms. The change of geometry was the result of the change in the principal compression strut angle computed using equilibrium and measured strains in the longitudinal tension reinforcement. The addition of the crack control reinforcement increased the capacity by reinforcing the splitting crack which caused failure of the concrete arch but did not have a large effect on the geometry of the tied arch which formed. It also was found that it is necessary to include the effects of the column to obtain the proper boundary conditions in the test. With the experimental observations in hand, several different analysis methods were examined in Chapter 5, and it was determined that the Modified Zararis Method best captured the phenomena seen in the experiments. Previous research into the shear strengthening of reinforced concrete beams with FRP was reviewed and appraised in Chapter 6.

In this chapter, a method for designing strengthening schemes with the proposed Modified Zararis Method for pier caps deemed to be deficient is developed. This method is then validated experimentally through tests of strengthened specimens. The strengthening focused on specimens with 0.65% longitudinal reinforcement because this type of specimen represents an existing pier cap with shear deficiencies.

7.1 Design Strategy

The rehabilitation of an existing structure is very different from the design of a new one. In many ways, design of a new structure is much simpler because there is more freedom to change different parameters. In contrast, with a reinforced concrete pier cap, many parameters are fixed. The strength of the concrete and the internal reinforcement cannot be changed; nor can the girder and column spacing be adjusted.

To examine the effectiveness of various methods to externally strengthen a beam, a parametric study was performed on Specimen BL1 using the proposed Modified Zararis Method (summarized in Eq. 5.7 to 5.12). In the parametric study, the yield value of the transverse reinforcement was assumed to be 80 ksi; this is the same yield strength as the longitudinal tension reinforcement. Figure 7.1 shows the calculated effect of independently increasing the amount of longitudinal and transverse reinforcement in Specimen BL1. The x axis of the figure represents increases in both the longitudinal and transverse reinforcement, and the y axis depicts the calculated increase in ultimate capacity over the calculated capacity of Specimen BL1.

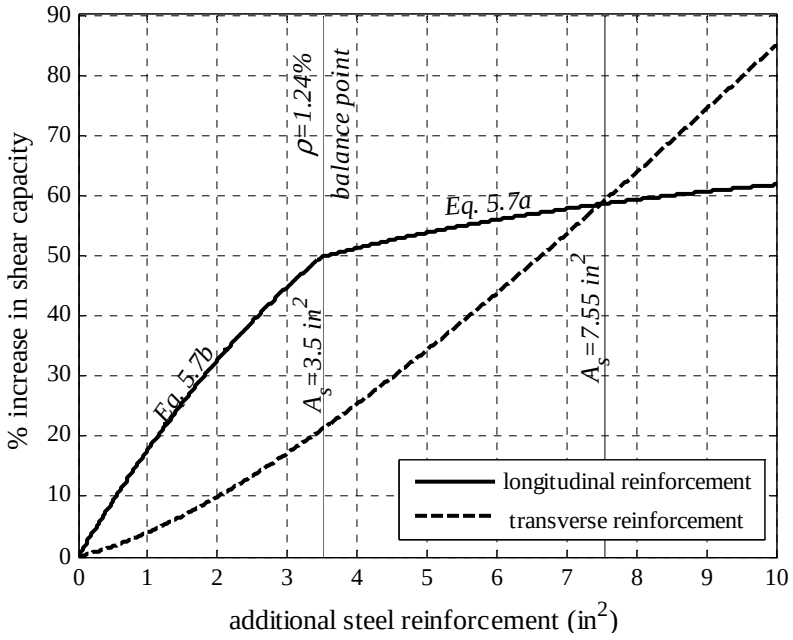

Figure 7.1- Percent increase in ultimate capacity calculated using the Modified Zararis Method for specimen BL1 due to increases in longitudinal and transverse reinforcement

Figure 7.1 shows that increasing the longitudinal reinforcement has a greater benefit until an additional 7.55 in^2 of steel longitudinal tension reinforcement has been added. The piece-wise nature of Eq. 5.7 can be seen in the figure. With the addition of 3.5 in^2 of longitudinal tension reinforcement the equation used to calculate the flexural compression block transitions from Eq. 5.7b to 5.7a. This transition occurs at a longitudinal tension reinforcement ratio of 1.24%, which is indicated in the figure. This is considered the balanced point, or the point where the flexural calculation in the proposed Modified Zararis Method predicts that the concrete will crush at the same load at which the longitudinal tension steel yields. Since the focus of the strengthening program is the specimens with 0.65% longitudinal tension reinforcement, the addition of externally bonded longitudinal tension reinforcement apparently is the simplest way of increasing the ultimate capacity.

7.2 Specimen RB1

Specimen RB1 was strengthened using a unidirectional carbon composite in the longitudinal direction. The specimen contained 0.65% longitudinal reinforcement tension reinforcement. It was cast at the same time as Specimen BL1, making it a B Series specimen; the geometry of Specimen BL1 and RB1 is shown in Figure 3.8. The carbon composite was applied using hand layup. The fibers were Sikawrap 117c, and the matrix was Sikadur 301. One layer of fabric was impregnated and made into panels which were then fabricated into coupons for tension testing. The coupons were created and tested in accordance with ASTM D-3039. A photograph of one of the coupons is shown in Figure 7.2. The results of the ten coupon tests are given in Table 7.1, which gives the width, maximum force per inch width, strain to failure, and the tensile stiffness of each coupon. The width of the specimen was measured in the middle and 3-5/8 inches from the end of each of the 10-inch coupons. The tensile stiffness was calculated by fitting a line to a plot of the force per inch width vs. strain. The slope of the best fit line was taken as the tensile stiffness for the coupon. In two of the coupons, the tabs debonded and no useful measurements were obtained. The thickness of a field-manufactured composite can vary greatly. To obtain a measure of the variability in thickness of the composite, 32 measurements were made over the two inch gage length of two different coupons. These measurements are shown in Figure 7.3. The mean from these 64 measurements was 0.0247 inches with a standard deviation of 0.0014 inches and coefficient of variation 0.057. This mean thickness was used along with the average tensile stiffness reported in Table 7.1 to approximate the elastic modulus of the composite. The elastic modulus was calculated by dividing the average tensile stiffness by the average thickness, resulting in an approximate elastic modulus of 9,510 ksi.

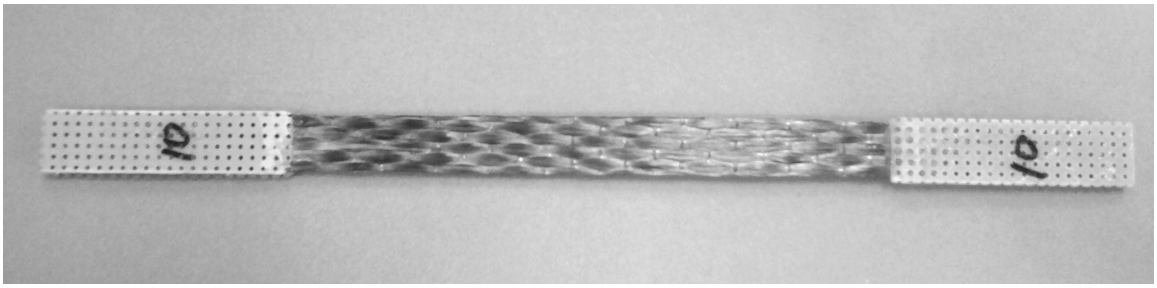

Figure 7.2- FRP coupon created according to ASTM D3039

Table 7.1- FRP properties for Specimen RB1

Coupon	Width[a] (in)	F_{max}/ in_{width} (kip/in)	Max Strain (%)	Tensile Stiffness (kip/in)
1	0.54	3.0	1.36	215.8
2	0.56	2.1	1.08	198.8
3	0.50		Tabs Debonded	
4	0.54	2.4	1.01	239.7
5	0.51		Tabs Debonded	
6	0.52	2.5	1.01	248.8
7	0.50	2.3	0.91	262.6
8	0.52	3.00	1.32	228.5
9	0.52	2.90	1.12	260.4
10	0.56	2.70	1.22	224.6
Mean	0.53	2.61	1.13	234.9

[a] The reported value is the average of three measurements

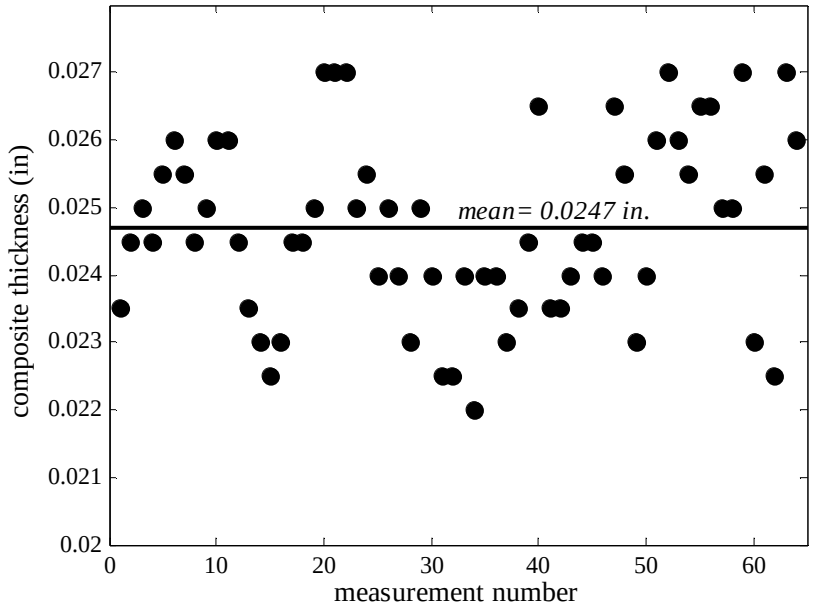

Figure 7.3- Measured thickness of composite coupons for Specimen RB1

7.2.1 Design of Strengthening for Specimen RB1

Let us assume that the desired increase in strength is set at 20%. This is a reasonable increase in capacity when looking at existing pier caps. When looking at Figure 7.1 an increase of approximately 20% can be gained by the addition of 1 in^2 of steel longitudinal tension reinforcement. If the externally bonded FRP is assumed to maintain compatibility of deformations with the beam and the internal reinforcement it is possible to use a modular ratio to determine the area of FRP required. The modular ratio of the FRP to the steel is 9,510 ksi/29,000 ksi or 0.32. This means that 3.125 in^2 of FRP are required. Using the width of the fiber fabric (12 in.) and the average thickness of the composite (0.0247 in.), the required number of layers of composite is 10.41. To have an equal number of layers of FRP strengthening on both sides of the specimen, it was wrapped six times on each side for a total of 12 layers. Figure 7.4 shows the strengthening scheme for Specimen RB1. The layers of the composite were wrapped

over themselves so that only one free end was exposed. The fiber fabric was cut into three lengths which were wrapped completely around the beam twice. The beam was wrapped in this manner to prevent global debonding of the FRP. The centroid of the composite is not located at the same depth as the longitudinal reinforcement in this particular beam. This is shown by the difference in d and d_{frp} in Figure 7.4. The strengthened specimen is shown in Figure 7.5.

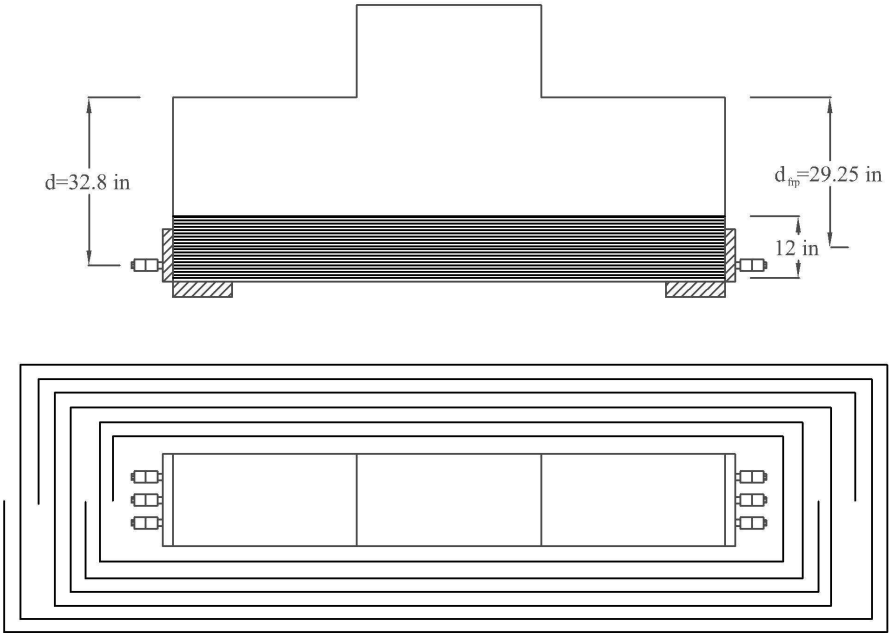

Figure 7.4- Strengthening scheme for Specimen RB1

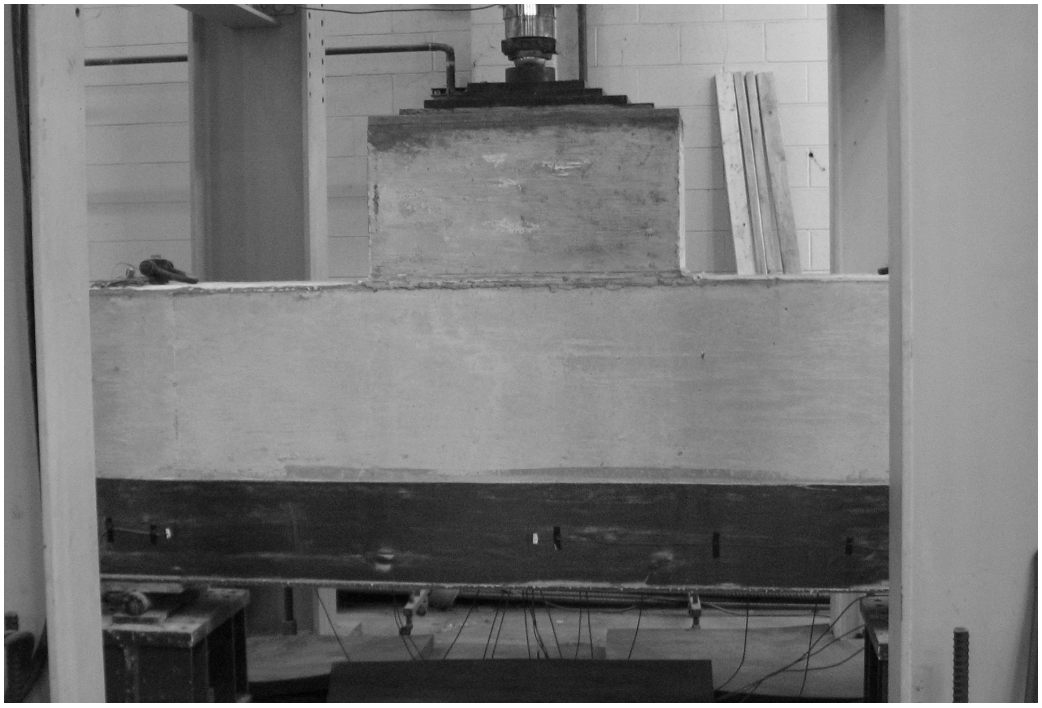

Figure 7.5- Specimen RB1

To calculate the capacity of the strengthened specimen, the material properties from Specimen BL1 were used because both specimens were cast at the same time. The first step is to recalculate the distance to the centroid of the longitudinal tension reinforcement (*d*). The modular ratio is used to transform the FRP into steel.

$$d = \frac{(3.81)(32.8) + (12)(0.0247)(12)(29.25)(0.32)}{3.81 + (12)(0.0247)(12)(0.32)} = 31.98\,\text{in}$$

With the new value of *d*, the Modified Zararis Method can be used to calculate the ultimate capacity of the specimen. Since the centroid of the FRP is above the centroid of the steel longitudinal reinforcement, the average strain in the FRP will be less than the strain in the steel. Furthermore, by wrapping the FRP completely around the end of the beam, global debonding of the FRP should be prevented, forcing failure of the FRP

reinforcement to occur by fracture rather than debonding. Fracture of the FRP occurred at an average strain of 1.3%, as shown in Table 7.1. The longitudinal tension steel will yield before the FRP fractures, making yield of the longitudinal reinforcement the governing factor for the strength of the tension tie. Since the steel will yield before the FRP reinforcement fractures the calculation of the ultimate capacity can be performed using the Modified Zararis Method and the transformed section of the FRP reinforcement.

$$\frac{c}{d} = \frac{3(4.962)(80{,}000)}{2(0.85)(3352)(18)(31.98)} = 0.363 \qquad (5.7b)$$

$$a / d_{effective} \approx \frac{48 - \frac{36}{2} + \frac{11.5}{2}}{31.98\left(1 - \frac{3}{8}(0.363)\right)} = 1.29 \qquad (5.8)$$

$$R = 1 \qquad (5.11b)$$

$$\frac{c_s}{d} = \frac{1 + 0.27(1.29)^2}{1 + (1.29)^2}(0.363) = 0.197 \qquad (5.11a)$$

$$V_u = \frac{(18)(31.98)}{1.29}\left[0.197\left(1 - 0.5(0.197)\right)(3352)\right] = 264{,}942 \text{ lbs} \qquad (5.12)$$

$$P = 2V_u = 530 \text{ kips}$$

The ultimate capacity of Specimen RB1 is calculated using eq (5.12) to be 530 kips. This is an increase of 15% over the calculated ultimate capacity of Specimen BL1 (462 kips). The difference between the original estimate of 20% and the new estimate of 15% is attributable to the reduction in *d*.

7.2.2 Testing of Specimen RB1

Specimen RB1 was cast at the same time as the other B-Series specimens. After strengthening using CFRP, it was tested to ultimate capacity. Companion

cylinders were tested on the same day as the beam test to determine its material properties. The concrete which made up the beam had an average ultimate compressive strength of 3,671 psi plus or minus one standard deviation of 115 psi (3,671± 115 psi) based on three samples, split tension strength of 457± 43 psi based on three samples, and an elastic modulus of 3,298± 96 ksi based on three samples. The compressive strength of the concrete which made up the column had a compressive strength of 3,297± 52 psi based on three samples, and the longitudinal reinforcing steel had yield strength of 80± 1.22 ksi based on three samples.

Specimen RB1 was tested in the same manner as the other specimen. Load was applied in a quasi-static manner, and pauses were taken to locate and measure cracks. Figure 7.6 highlights the cracks which formed in Specimen RB1. Cracks *B*, *C*, *E* and *F* were the first cracks to form at an applied load of 250 kips. These cracks were followed by Cracks *A* and *D* at an applied load of 300 kips. At a load of 350 kips, localized debonding of the FRP was observed at the location of Crack *F*; Figure 7.7 shows the FRP pulling away from the beam at the crack. At a load of 594 kips, a splitting crack between the corner of the column and the support formed, causing failure. The ultimate capacity of 594 kips was an increase of 19% over its control Specimen BL1 (500 kips).

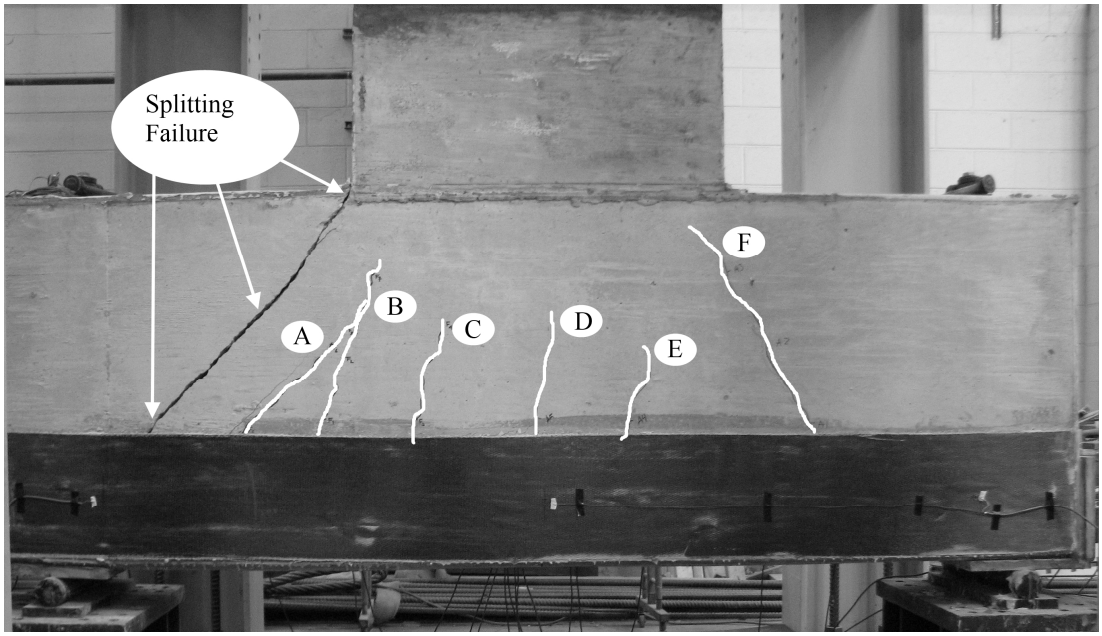

Figure 7.6- Cracks in Specimen RB1

Figure 7.7- Localized debonding of FRP at crack location for Specimen RB1

Figure 7.8 shows the load vs. deflection plots for Specimen RB1and for the control specimen, Specimen BL1. These specimens were cast at the same time with the same geometry and reinforcement. The addition of the FRP strengthening allowed Specimen BL1 to achieve a higher capacity. The increase in capacity of 19% was greater than the calculated 15%. This difference can be attributed to differences in the strength of the concrete between the two specimens. Specimen BL1 had a compressive strength of 3,352 psi while Specimen RB1 had a compressive strength of 3,671 psi. If the calculation of the increase in capacity is redone using the measured concrete strength of Specimen RB1 (3,671 psi) the capacity is 546 kips. This gives a calculated increase in capacity of 18% over the control beam, BL1, which correlates well with the experimentally observed 19% increase.

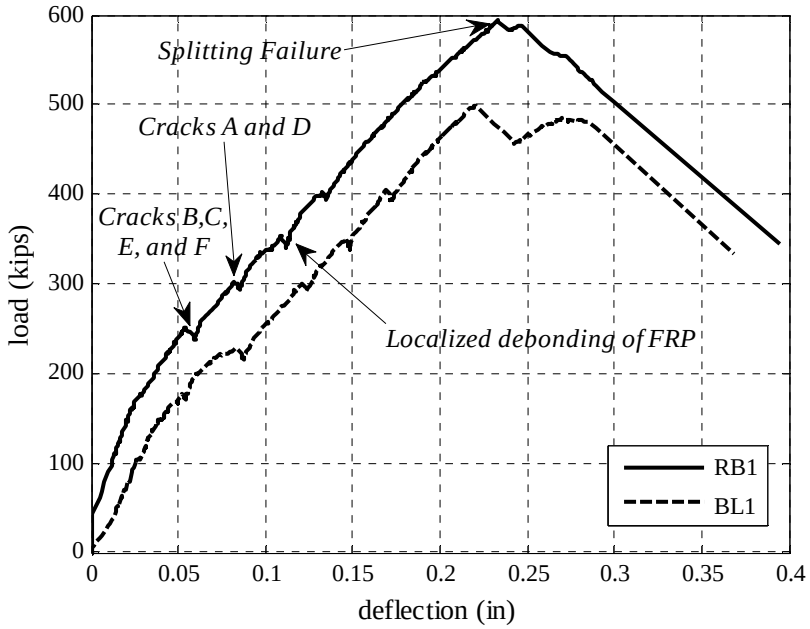

Figure 7.8- Load deflection plot for Specimen RB1

To investigate the compatibility of deformations between the FRP and the longitudinal reinforcement, strain gages were installed on the FRP. Figure 7.9 shows the location on the strain gages on both the bars and the FRP. The strain gages on the bars are located at the effective depth *d*, and the strain gages on the FRP are located at the effective depth of the FRP (d_{frp}). There is a difference of 3.55 in between the depths of the strain gages. Also, the strain gages on the FRP are located 12 inches from the end of the beam. The gages were located on the portion of the FRP crossing the anticipated cracks which grow from the supports. The gages on the longitudinal tension steel were located at mid shear span.

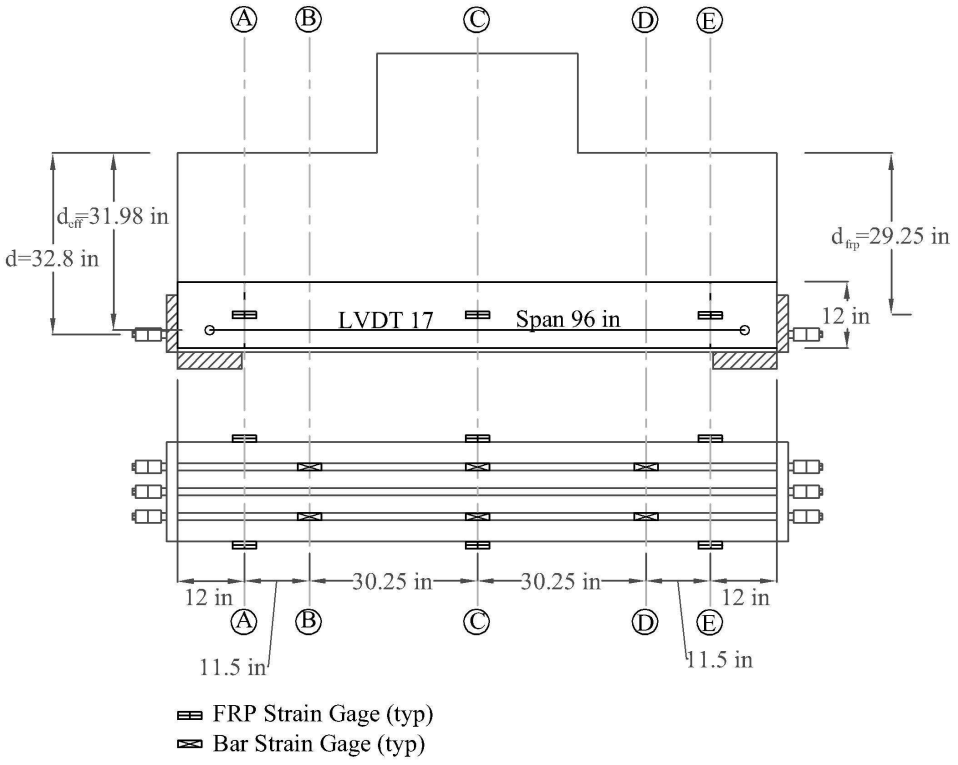

Figure 7.9- Strain gage locations on Specimen RB1

The relation between applied load vs. the strains measured at each of the longitudinal strain gage locations is illustrated in Figure 7.10 (Positions *A* to *E* in Figure 7.9). The strains shown in Figure 7.10 are averages from the sets of strain gages on the bar and the FRP respectively at the location. Early in the testing of Specimen RB1 the strain in the FRP reinforcement was smaller than the strain in the steel reinforcement. This could be due to the vertical and horizontal locations of the gages, and also the fact that the strain gages are located on the outside of the FRP. The difference is most prominent between the gages located in the spans, and is the largest at the point where cracks became visible in the span (250-300 kips). After the formation of the cracks, the strains in the bar and FRP begin to converge. Cracking appears to affect the strain gages attached to the bars before the gages attached to the FRP. At ultimate load, the strains converge and there is compatibility of deformations between the longitudinal reinforcing steel and the externally bonded FRP reinforcement.

Figure 7.11 shows the plot of strut angle vs. applied load for Specimen RB1. The strut angle was calculated using equilibrium and the longitudinal strains from LVDT 17. LVDT 17 was located at the effective depth, which was calculated for both the longitudinal steel reinforcement and the FRP reinforcement (31.98 in.); it spanned longitudinally from the center of the supports. Also shown in Figure 7.11 is the strut angle vs. applied load for the control Specimen BL1. The formation of cracks and arch action is similar between RB1 and BL1.

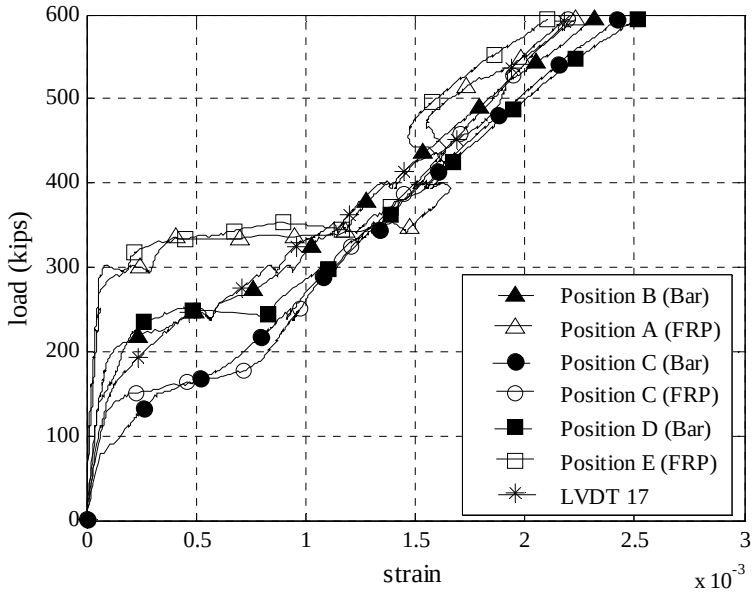

Figure 7.10- Strains in FRP and longitudinal bars for Specimen RB1

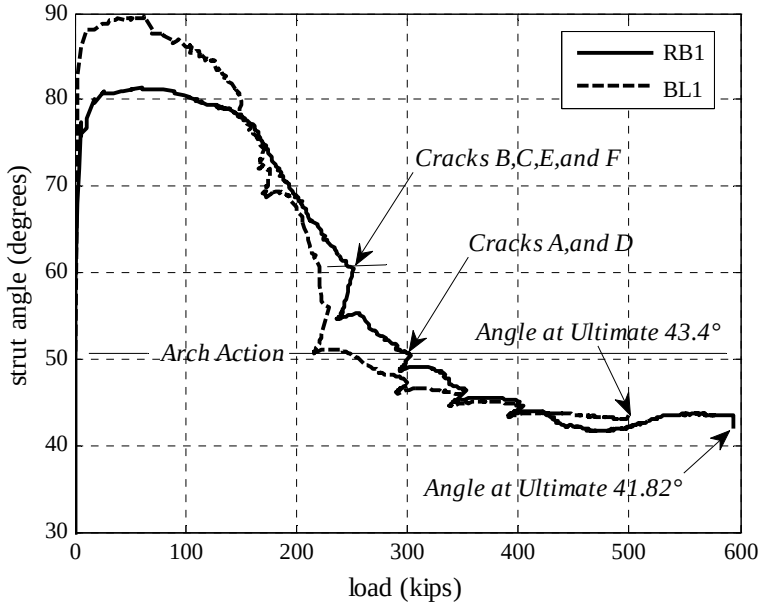

Figure 7.11- Strut angle vs. applied load for Specimen RB1

7.3 Specimen RA1

Specimen RA1 was an A series specimen; it was cast at the same time as Specimen AL1 (see Figure 3.8), contained the same amount of longitudinal tension reinforcement, and the reinforcement came from the same batch. The limit state of the A series specimens with 0.65% longitudinal tension reinforcement differed from that of the comparable B series specimens. Yield of the longitudinal tension reinforcement governed the limit state for the A Series specimens while splitting of the concrete governed for the B Series specimens. By strengthening the A Series specimen it is possible to determine the effect of increasing the longitudinal tension reinforcement of a specimen whose limit state is governed by yielding of the longitudinal tension reinforcement. Specimen RA1 was strengthened with unidirectional carbon fiber reinforced polymer. Sikawrap 117c and Sikadur 301 were again used to fabricate the composite. Ten coupons were made and tested in accordance with ASTM D3039; the results are shown in Table 7.2. The width and the elastic modulus were determined in the same manner as for Specimen RB1. The thickness measurements are shown in Figure 7.12; the mean thickness of the 64 samples was 0.0238 with a standard deviation of 0.0018 and coefficient of variation 0.076. The resulting approximate elastic modulus was 9,937 ksi.

Table 7.2- FRP properties for Specimen RA1

Coupon	Width[a] (in)	Force per Width (kip/in)	Max Strain (%)	Tensile Stiffness (kip/in)
1	0.56	2.3	1.05	237.7
2	0.49	2.0	0.74	271.3
3	0.48	2.7	1.14	225.1
4	0.56	2.6	1.16	222.1
5	0.51	3.0	1.25	224.0
6	0.50	1.8	0.83	254.1
7	0.54	2.5	1.12	238.8
8	0.54	1.9	1.06	219.4
9	0.51	1.7	0.90	223.6
10	0.55	2.4	0.95	248.9
Mean	0.52	2.3	1.02	236.5

[a]The reported value is the average of three measurements

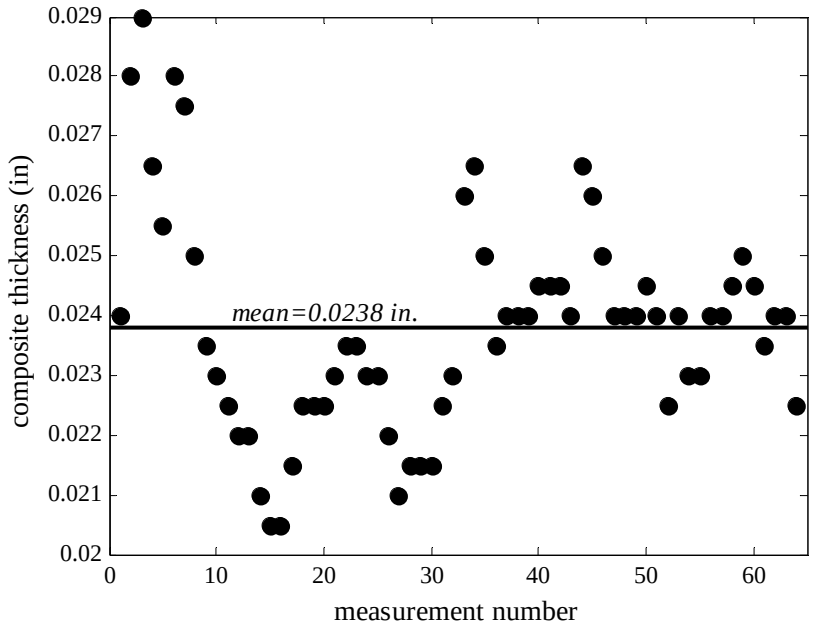

Figure 7.12- Measured thickness of composite coupons for Specimen RA1

7.3.1 Design of Strengthening for Specimen RA1

The strengthening for Specimen RA1 was designed to provide a greater increase in capacity than Specimen RB1, and the number of layers of FRP was increased to 16. Figure 7.13 shows the strengthening for specimen RA1. The calculation for the increase in capacity is the same as for Specimen RB1. The modular ratio of FRP to longitudinal tension steel is 9,937/29,000 or 0.34. The calculation of the increase in capacity is based on the geometry and material properties of Specimen AL1.

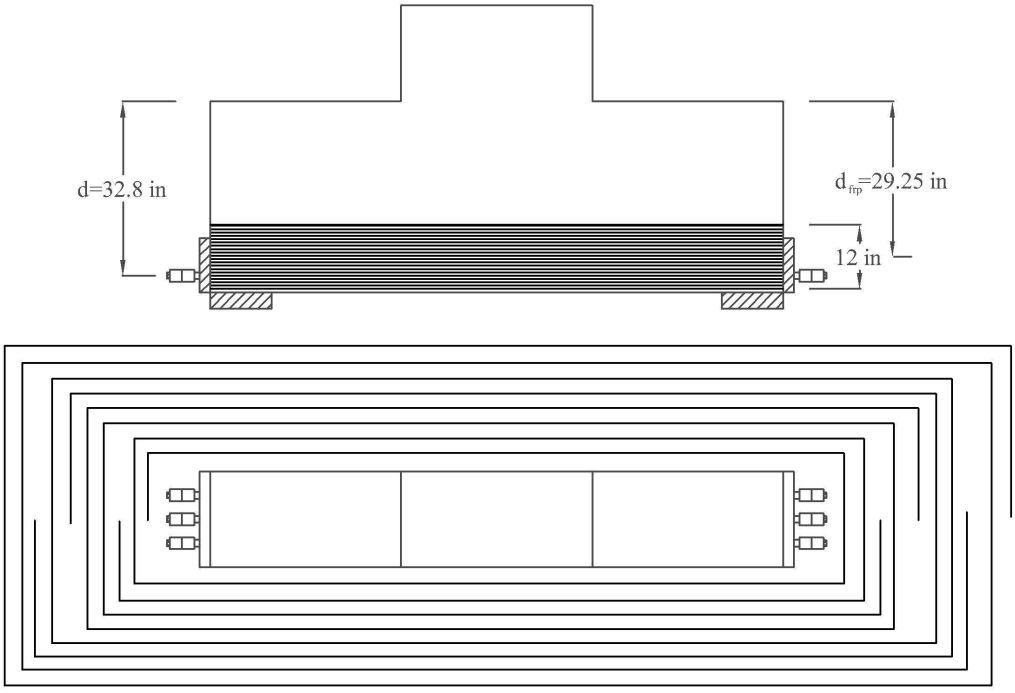

Figure 7.13- Strengthening scheme for Specimen RA1

The same steps used to calculate the ultimate capacity of Specimen RB1 were used to calculate the capacity of Specimen RA1. The FRP is transformed into steel

using the modular ratio, and then a new effective depth is calculated. The Modified Zararis Method is then used to calculate the ultimate capacity as follows.

$$d = \frac{(3.81)(32.8) + (12)(0.0238)(16)(29.25)(0.34)}{3.81 + (12)(0.0238)(16)(0.34)} = 31.77 \text{ in}$$

$$\frac{c}{d} = \frac{3(5.364)(65{,}000)}{2(0.85)(3473)(18)(31.77)} = 0.31 \qquad (5.7b)$$

$$a / d_{effective} \approx \frac{48 - \frac{36}{2} + \frac{11.5}{2}}{31.77\left(1 - \frac{3}{8}(0.31)\right)} = 1.27 \qquad (5.8)$$

$$R = 1 \qquad (5.11b)$$

$$\frac{c_s}{d} = \frac{1 + 0.27(1.27)^2}{1 + (1.27)^2}(0.31) = 0.17 \qquad (5.11a)$$

$$V_u = \frac{(18)(31.77)}{1.27}\left[0.17\left(1 - 0.5(0.17)\right)(3473)\right] = 243{,}254 \text{ lbs} \qquad (5.12)$$

$$P = 2V_u = 487 \text{ kips}$$

This is a calculated 22% increase over Specimen AL1 (397 kips).

7.3.2 Testing of Specimen RA1

Companion cylinder tests were performed on the same day as beam testing. The concrete in the beam had a compressive strength of 4,682± 124 psi based on three samples, a split tension strength of 473± 21 psi based on three samples, and an elastic modus of 4,120± 252 ksi based on three samples. The compressive strength of the concrete in the column was 4,389± 60 psi based on three samples, and the longitudinal steel had a yield stress of 65± 8 ksi based on three samples.

Figure 7.14 shows the cracks which formed in Specimen RA1. Cracks *B* and *C* formed at an applied load of 200 kips. Crack *A* formed at a load of 300 kips, and

Cracks *D* and *E* formed at 350 kips. At an applied load of 600 kips, the longitudinal tension reinforcement reached its yield point. The specimen continued to carry increasing loads up until a load of 702 kips when a splitting crack formed.

Figure 7.15 compares the load vs deflection for Specimen AL1 and RA1. The crack labels correspond to those shown in Figure 7.14. The addition of the FRP greatly changed the behavior of the specimen. The limit state was governed by splitting failure of the concrete rather than yield of the longitudinal steel reinforcement. The longitudinal tension reinforcement in Specimen RA1 reached the yield point at an applied load of 600 kips; this was 100 kips higher than in Specimen AL1 (500 kips). The yield of the longitudinal reinforcement did not cause the large change in the load-deflection behavior which was observed for Specimen AL1, where yielding of the longitudinal tension reinforcement led to a relatively large increase in deflection without an increase in applied load. Specimen RA1 reached an ultimate capacity of 702 kips; this was a 29% increase over Specimen AL1 (545 kips). The difference in concrete strengths between the two specimens (3,473 psi vs. 4,682 psi) accounted for an estimated[1] 6% increase in capacity. The addition of the external FRP reinforcement accounted for an estimated[1] 26% increase in capacity; this is a total calculated increase in capacity of 32% which agrees well with the observed 29% increase.

[1] Estimated using the Modified Zararis Method

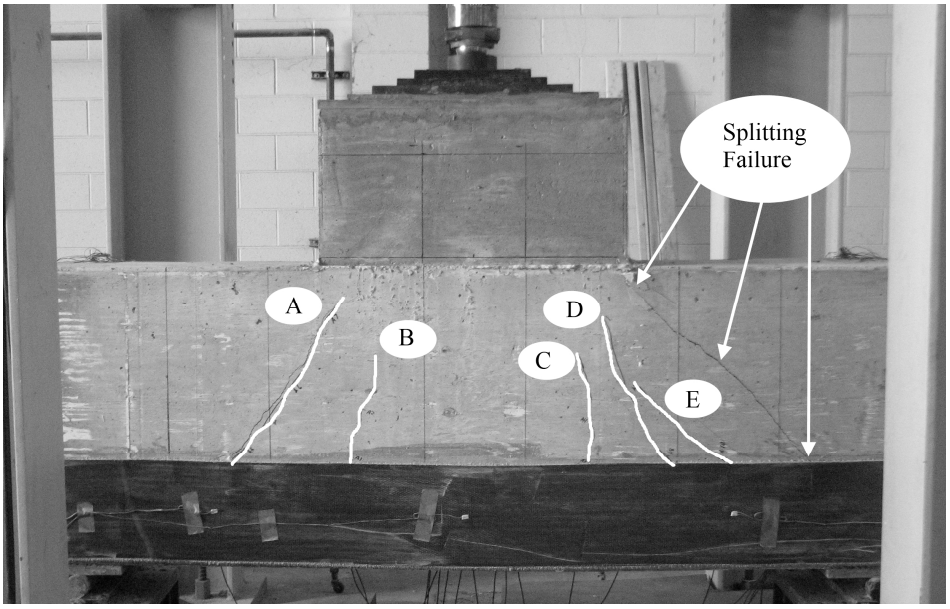

Figure 7.14- Cracks in Specimen RA1

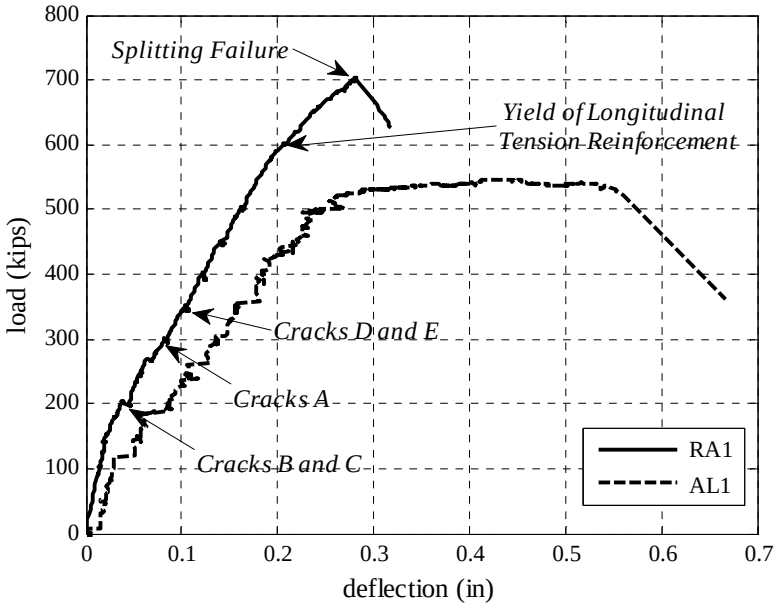

Figure 7.15- Load vs. deflection plot for Specimen RA1

Strain gages were installed on the FRP to compliment the gages installed on the longitudinal tension reinforcement. Figure 7.16 shows the locations of the strain gages and the longitudinal LVDT 17. The strain gages on the FRP were placed at the same longitudinal locations as the gages on the bars. This was done to determine if the longitudinal location of the gages was the cause for the lag between the strain measured during the testing of Specimen RB1. For independent verification, LVDT 17 was located at the effective depth of 31.76 inches, and was mounted on the exterior of the beam over the FRP spanning from the center of the supports. It had a total length of 96 inches. The strains measured are shown in Figure 7.17. Moving the strain gages to the same longitudinal location did reduce the lag shown in the strains for Specimen RB1 significantly, but the gages on the FRP did not measure as much strain as the gages on the bar at ultimate. This could have been due to the distance of the FRP gages from the location of the cracks. Also there was not the large amount of debonding seen in Specimen RB1. After the debonding of the FRP, compatibility of strains was maintained in Specimen RB1. The strains calculated from LVDT 17 show strain compatibility with the gages installed on the longitudinal tension reinforcement. The difference in the strain gage measurements can be attributed to localized effects.

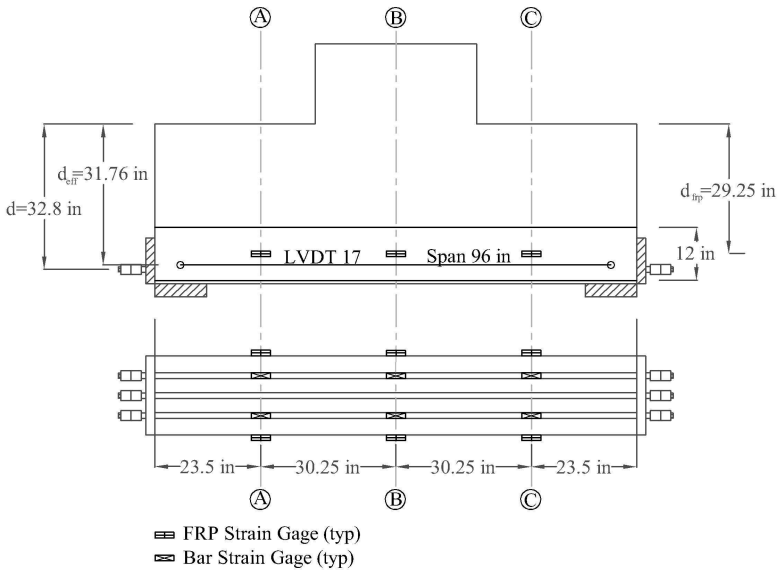

Figure 7.16- Strain gage locations for Specimen RA1

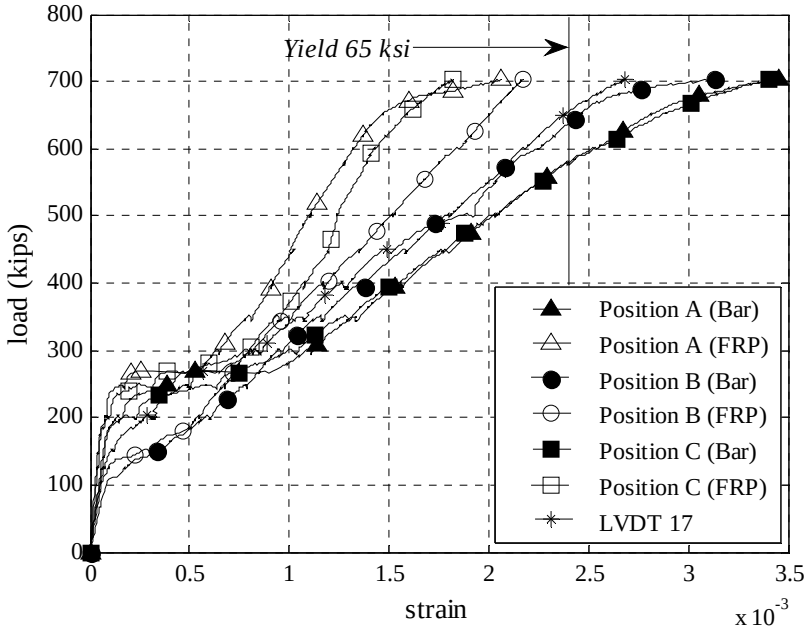

Figure 7.17- Strains for Specimen RA1

Figure 7.18 shows the strut angle calculated from the strains in LVDT 17 vs. the applied load. For comparison, the strut angle vs. load for Specimen AL1 is also shown in the figure. The strut angle for Specimen AL1 is calculated using a strain gage at midspan instead of an LVDT. That strain gage was susceptible to localized effects which causes some variation in the results. From the plots it can be seen that Specimen RA1 achieves a lower strut angle, which is consistent with the addition of longitudinal tension reinforcement. Arch action is achieved at later point than for Specimen AL1.

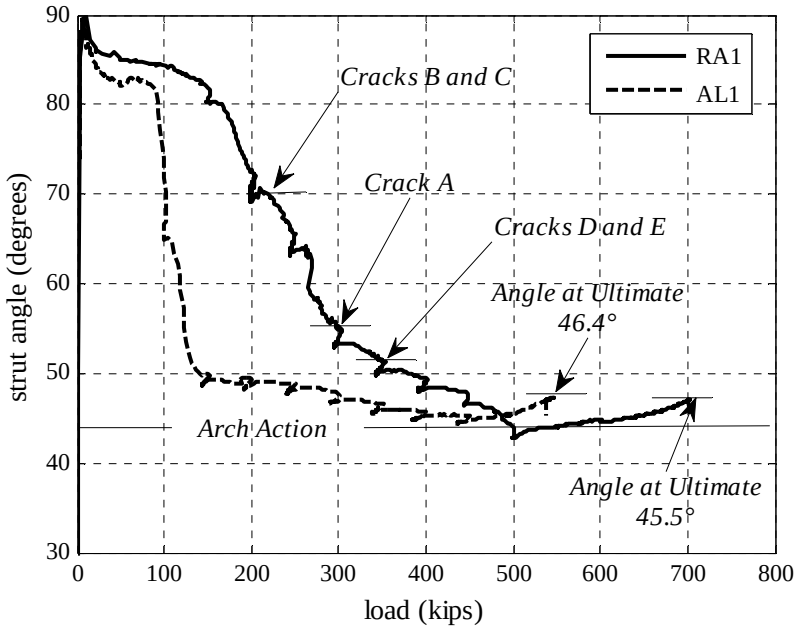

Figure 7.18- Strut angle vs. applied load for Specimen RA1

7.4 Conclusions

This chapter has presented a simple approach to strengthening reinforced concrete beams with externally bonded FRP reinforcement, using transformed sections

and the Modified Zararis Method for reinforced concrete deep beams with a longitudinal reinforcement ratio less than the balanced point. The FRP reinforcement provides additional longitudinal tension reinforcement, increasing the strength of the longitudinal tension tie which, in turn, changed the shape of the concrete arch which formed. This led to an increase in ultimate capacity.

Table 7.3 summarizes the results of the tests conducted in support of the proposed strengthening method. It gives the ultimate capacity of the experimental specimen (P_{ult}) and the calculated ultimate capacity based on the Modified Zararis Method (P_{calc}). The experimental ($P_{control\ ult}$) and calculated ($P_{control\ calc}$) ultimate capacities for the corresponding control specimens are also tabulated. With these values, the percent increase in ultimate capacity was calculated based on both the experimental (Δ_{exp}) and calculated (Δ_{calc}) ultimate capacities. The ratios of P_{ult}/P_{calc}, and $\Delta_{exp}/\Delta_{calc}$ were then calculated. The results show that the calculated increase in capacity represents the observed experimental increase in capacity well. The average ratio for $\Delta_{exp}/\Delta_{calc}$ is 0.971. The ratio of P_{ult}/P_{calc} was 1.21.

Table 7.3- Results of strengthening experiments

Specimen	P_{exp} (kips)	P_{calc} (kips)	Control	$P_{control\ exp}$ (kips)	$P_{control\ calc}$ (kips)	Δ_{exp}	Δ_{calc}	$\Delta_{exp}/\Delta_{calc}$	P_{exp}/P_{calc}
RB1	594	546	BL1	500	463	19%	18%	1.049	1.088
RA1	702	525	AL1	545	397	29%	32%	0.893	1.337
							Mean	0.971	1.213

Chapter 8

SUMMARY, CONCLUSIONS, AND RECOMMENDATIONS

This Chapter summarizes the major accomplishments in this dissertation, while highlighting its important conclusions. The summary and conclusions are followed by ideas for possible future work which have been identified during the research.

8.1 Summary of research

Reinforced concrete pier caps in aging bridges may suffer from deterioration, leading to deficiencies in their shear capacity that may prompt posting. This limits the travel of goods and services, and may lead to costly repair or to replacement. If the deficiencies in the pier caps can be addressed through economical strengthening or rehabilitation, the postings can reduced or lifted and the bridge can be returned to normal use.

A pier cap is a large deep reinforced concrete beam in which the shear spans are short (typically less than twice the effective depth of the beam). Due to their size and loading, they have the ability to carry load through arch action. Externally bonded reinforcement has been successfully used to strengthen reinforced concrete members, but there is little existing research to shed light on how it might be used to strengthen a beam similar to a pier cap.

It is essential to understand the behavior of reinforced concrete pier caps before attempting to address the merits of various strengthening methods. Accordingly, the research was conducted in two distinct parts. The first was an experimental study on

the behavior of reinforced concrete pier caps without externally bonded reinforcement. This work involved the experimental testing of laboratory specimens and comparison of different existing methods for analyzing large deep beams. With the understanding of pier cap behavior gained from the experimental study and a suitable analysis method supported by the experimental results, the second part of the study could focus on methods for strengthening the reinforced concrete pier caps with externally bonded reinforcement. This second part entailed the use of a modified strut-and-tie analysis, supported by tests of laboratory specimens that were companions to those tested earlier but which had been retrofitted with externally bonded FRP composites.

Reinforced Concrete deep beams, such as pier caps, have a shear span over effective depth ratio less than two, which gives them the ability to carry load through arch action once some amount of diagonal cracking has occurred. It is the arch mechanism which determines the ultimate strength of the beam. The main factors that affect the strength of a reinforced concrete deep beam are its effective depth, shear span, longitudinal tension reinforcement, and the transverse shear reinforcement. The depth is of particular significance because there is a size effect associated with it. In this case, beams with a smaller depth have a higher capacity with respect to beams with large depths when normalized to account for differences in scale. Methods that might be suitable for the analysis and design of deep beams and their retrofits were also identified in Chapter 2; these methods are evaluated further in the context of the experimental program, particularly with regard to their ability to capture the dominant failure mode involving arch action.

The specimens for the experimental program were based on the pier caps for Bridge 085-0018 in Dawson County, Georgia. The variables which were examined with the specimens included the amount of longitudinal tension reinforcement, beam depth, and crack control reinforcement. Two longitudinal tension reinforcement ratios

were considered. The first was 0.65% which matched the reinforcement ratio of Bridge 085-0018, and the second was 1.3% which was simply double the first. The effect of beam depth was treated by scaling down full scale specimens with an approximate height of 36 inches to 18 inches using Bazant's Equation and the Buckingham Pi Theorem. Bazant's Equation was used for the scaling because it includes factors which account for size effect, such as the size of the largest coarse aggregate used in the concrete. The effects of crack control reinforcement were treated by comparing specimens with crack control reinforcement meeting the 2007 AASHTO LRFD Bridge Specification against specimens without crack control reinforcement. Eleven tests were performed and their results were analyzed with several different methods for determining the ultimate capacity of reinforced concrete deep beams. These methods included both the AASHTO and ACI strut and tie models with new procedures developed for the evaluation of existing structures, Bazant's Equation, Zararis's Method, and the new proposed Modified Zararis Method. The analysis methods were also compared using a larger database collected from literature.

A literature review on the strengthening of reinforced concrete members for shear with FRP was presented. The review was done by analyzing a database of beams strengthened externally with FRP. Of the 139 tests only 13 characterized the FRP material according to an ASTM Standard. In order to make comparisons between the materials used by different researchers the materials must be categorized according to ASTM Standards (ASTM D-3039 or D-638).

Finally the work presented in the previous chapters is synthesized into a method for externally strengthening reinforced concrete deep beams (pier caps). It begins by laying out a design strategy for specimens with longitudinal reinforcement ratios below the balanced point, defined as the point at which the Modified Zararis Method predicts that the longitudinal tension reinforcement yields at the same time as

the longitudinal compression zone in the concrete crushes. Reinforcement ratios below the balanced point were emphasized in this task because classic reinforced concrete design methodology has strongly encouraged that beam reinforcement be proportioned below the balanced point to improve their ductility, and pier caps showing distress are generally reinforced in this way. To increase the ultimate beam capacity, the amount of longitudinal tension reinforcement was increased. The calculation for the increase in capacity is done using the Modified Zararis Method.

8.2 Conclusions

Early in the experimental design, finite element models were used to determine the most highly stressed regions of the pier cap. These models showed that replacing the column with a steel plate to simplify specimen construction changed the stresses in the pier cap specimen. As a result, a stub column was cast on top of the specimens to maintain similitude between the specimen and the pier cap. The stub column was critical in modeling the behavior of the pier cap. It induced stress concentrations into the pier cap which dictated the failure mode in some cases, and it also affected the angle at which the principal compression strut formed. It shows the importance of the boundary conditions on the behavior of deep beams.

Increasing the longitudinal reinforcement caused an increase in the ultimate capacity of the specimen. The increase in capacity was due to an increase in the strength of the tension tie, and a change in the shape of the tied arch. The change in the shape of the tied arch decreased the effects of the stress concentration at the re-entrant corner of the beam-column. The change in the shape of the arch is shown by the change in the principal compression strut angle. Increasing the amount of reinforcement reduced the compression strut angle at ultimate. Without the change in the strut angle, increasing the tension tie would have had no benefit; this was shown in the comparison of the ultimate capacities of Specimens BL1 and Specimen AL1. Increasing the yield strength of the

tension tie increased its ultimate capacity, but not its stiffness. Without the change in stiffness, there was no change in the strut angle or the geometry of the tied arch which formed.

Two different ultimate limit states were observed. The first was yield of the tension tie. After the formation of the tied arch, the longitudinal tension tie reached its yield point. This limit state was generally a ductile one, and was a function of both the longitudinal reinforcement ratio and the yield stress of the steel. Generally the specimens with 0.65% longitudinal reinforcement had this limit state. The other limit state observed was splitting of the principal compression strut in the concrete arch. Splitting occurred due to the stress concentration introduced by the stub column. A splitting tension crack formed running from the corner of the column to the center of the nearest support. This failure mode was brittle. Generally the specimens with 1.3% longitudinal tension reinforcement had this limit state.

Crack control reinforcement in accordance with the 2007 AASHTO LRFD Bridge Design Specifications was added to specimens with 1.3% longitudinal reinforcement. The presence of the crack control reinforcement increased the beam capacity by reinforcing the splitting crack. In the specimens with crack control reinforcement, the splitting crack appeared and the specimen continued to carry increasing load. In specimens without crack control reinforcement, however, the splitting crack caused immediate failure. The crack control reinforcement only had a major effect on the splitting crack; it did not affect the point where other cracks developed.

The formation of diagonal cracks generally appeared at 40% of the ultimate capacity on average. The specimens still had the majority of their capacity left after the formation of diagonal cracks; the cracks do not indicate eminent failure.

Half scaled specimens were designed to investigate whether size effects might be significant. For specimens with 0.65% longitudinal reinforcement, no significant size effect was observed. However, a significant size effect was observed for specimens with 1.3% longitudinal reinforcement. In general, for specimens whose ultimate strength is governed by yield of the longitudinal reinforcement, there was no size effect. Conversely, for the specimens in which the ultimate strength was governed by splitting failure of the concrete there was a significant size effect.

The proposed Modified Zararis Method was chosen as the model that best represented the ultimate behavior of a reinforced concrete pier cap based on a comparison to both the results of the experimental program and a larger database. A small parametric study was performed using the proposed Modified Zararis Method. It showed that the most effective way to strengthen a beam reinforced below the balance point was to add additional longitudinal tension reinforcement. Increasing longitudinal tension reinforcement is not as effective in increasing the capacity of beams reinforced above the balance point. This method was adopted for the strengthening of reinforced concrete pier caps. Two tests were performed on specimens with 0.65% longitudinal reinforcement with externally bonded strengthening schemes. The results of the test agreed well with the predictions made using the Modified Zararis Method. This showed that increasing the strength of the longitudinal tension tie is an effective way to increase the strength of reinforced concrete deep beams reinforced below the balance point, and that the Modified Zararis Method is an effective way of determining the increase in capacity.

8.4 Recommendations for Design and Evaluation of Pier Caps

Measures should be taken to mitigate the stress concentration introduced by the column in the design of new pier caps. A simple way to accomplish this is to cast the pier caps with hammerhead columns. The hammerhead should be designed to transfer

the forces directly from the girders into the column. The strut and tie model and the Modified Zararis Method are both effective procedures for the design of new pier caps. The Modified Zararis Method has better correlation to the experimental results than either of the strut and tie models. The ultimate capacities calculated using the ACI strut and tie model had a better correlation to the experimental results than the AASHTO strut and tie model. The AASHTO strut and tie model can be improved by adopting the allowable strut stress parameters form the ACI model. The splitting failure of the concrete was shown to be a function of the stress concentration. When a column is present a splitting failure should be anticipated and crack control reinforcement provided.

The Modified Zararis Method should be used in the evaluation of existing structures. It eliminates the need for the extensive iteration required by the strut and tie model. The proposed Modified Zararis Method gives a simple procedure for determining the ultimate capacity of existing reinforced concrete deep beam.

8.4 Recommendations for Future Work

During the research a number of different lines of future inquiry were identified. The first major effort should be directed toward reducing the stress concentration at the interface of the beam and column, as it served as a crack starter in practically all of the tests in this research program and a related program (O'Malley, 2011). While stress concentrations are most commonly studied using a finite element analysis, the cracking in the reinforced concrete beam makes such an analysis problematic. In most FEA methods, the cracking of reinforced concrete is modeled as a reduction in stiffness, but the individual cracks themselves are not modeled. This method works when stiffness governs the behavior of the member and the discrete cracks play a minor role in structural behavior. In the case of reinforced concrete deep beams, however, diagonal cracking is essential for allowing a tied arch mechanism to

form, making the individual cracks important. When modeling a reinforced concrete deep beam with a FEA analysis, the nature of the cracking causes a singularity and ultimately causes the analysis to fail. A discrete element analysis (Lorig and Cundal, 1989) might provide a fruitful alternative to FEA in dealing with this issue numerically. Discrete element analyses have been employed successfully in geotechnical engineering, where they have been used to model movement in granular media and fracture in rock. This method of analysis allows for the formation of discrete cracks, which may make it a suitable method for modeling reinforced concrete pier caps and reinforced concrete in general. Reinforced concrete compression cylinders and flexural members have been successfully modeled using the discrete element method (Lorig and Cundal, 1989). With a properly calibrated discrete element model, parametric studies could be conducted on the stress concentration, factors which affect it, and practical approaches for its mitigation.

A deep beam is generally defined as having a shear span to depth (*a/d*) ratio less than 2.5, but not all deep beams exhibit the same behavior. All deep beams can be limited by their tension tie. Deep beams with an *a/d* ratio less than 2 can undergo arch action and fail due to crushing of the concrete in the arch. For beams with *a/d* ratios between 2 and 2.5, shear failure occurs by diagonal tension failure of the concrete in the compression zone. The research in this study only considers beams which fail due to crushing of the concrete in the arch. The effect of external strengthening schemes on beams with *a/d* ratios between 2 and 2.5 is still unknown.

There were no existing cracks in the strengthened specimens tested as part of this study. The concept used to strengthen the specimens dealt with using an increase in the longitudinal tension reinforcement ratio to effect a change in the shape of the tied arch which formed at ultimate. It may not be possible to change the shape of the tied arch if cracks are already present in the specimen.

The effects of adding external transverse reinforcement still needs to be studied. The experimental program focused on addition of longitudinal tension reinforcement because the Modified Zararis Method indicated that it would be the most effective way to increase the capacity of beams reinforced below the balanced point. It is important to determine what effect external transverse reinforcement has on deep beams. It may be an effective strengthening scheme for beams reinforced over the balanced point, or transverse and longitudinal reinforcement may successfully be used together.

The external reinforcement was a unidirectional composite. This was done to avoid the addition of variables which would complicate observations. The main advantage of composites are that through the use of lamination and different molding and shaping techniques a part can be designed with almost any required shape and mechanical property. It may be possible to design a FRP strengthening scheme specifically for the rehabilitation of reinforced concrete pier caps.

APPENDIX A

BAR DEVELOPMENT FORCES

The load cells were placed on the end of the longitudinal reinforcement to provide anchorage. It was hoped that since the bars had short development lengths (less than 12 in.), the bars would debond and the load cells would directly measure the force in the bar. This force could then be used to calculate the angle of the principal compression strut. What was found is that the equations for development length in the AASHTO 2007 LRFD Specifications are very conservative.

The equations for development length are based on the work of Orangun et al. (1977). This work is an empirical analysis of several different experimental programs on development length. It takes into account the effect of bar coating, size, and spacing; as well as the inclusion of transverse reinforcement and the amount of concrete cast under the bar. It was determined how these parameters affect the average bond stress of the bar defined as in Eq. A.1.

$$u = \frac{f_s d_b}{4 l_d} \tag{A.1}$$

u = average bond stress (psi)
f_s = maximum stress in bar (psi)
d_b = diameter of bar (in)
l_b = development length (in)

Equation A.1 was solved for l_d. This resulted in the equation for development length show in Section 5.11.2.1 of the AASHTO 2007 LRFD Design Specifications which is shown as Eq. A.2. Equation A.2 is for #11 bars and smaller. Other equations are listed for larger bars, but since none were used in the experimental program they are not included.

$$l_d = \frac{1.25 A_b f_y}{\sqrt{f'_c}} \geq 0.4 d_b f_y \qquad \text{(A.2)}$$

l_d= development length (in)

A_b= area of bar (in^2)

f_y= yield strength of bar (ksi)

f'_c= compression strength of concrete (ksi)

d_b= diameter of bar (in)

Knowing that the development lengths are based on average stress allows the development lengths required for full development of the bar calculated using Eqs. A.2 to be converted back into average bond stress using Eq. A.1. This is the average bond stress used to calculate the development length required by the code (u_{req}). Equation A.3 shows how the required average bond stress was calculated.

$$u_{req} = \frac{f_y d_b}{4 l_d} \qquad \text{(A.3)}$$

u_{req}= maximum average bond stress allowed by code (ksi)

$f_{y=}$ yield stress of longitudinal reinforcement (ksi)

d_b= diameter of bar (in)

l_b= development length as calculated by Eq. 4.3 (in)

It is also possible to calculate the average bond stress for the longitudinal bars in each specimen. Equation A.4 shows how the average bond stress (u_{test}) was

calculated using the data collected during the experiment. In Eq. A.4 l_b is the length of the bearing. At a crack the average development stress is equal to zero (Orangun, 1977). From the many pictures showing the cracks in the specimens, it can be seen that in general cracks develop at the corner of the bearing plate. This limits the development length of the bars to the area over the support. By subtracting the force measured by the load cells (F_{LC}) from the force calculated using the strains in the bar (F_ε) the force carried by the interaction of the bar and the concrete can be calculated.

$$u_{test} = \frac{(F_\varepsilon - F_{LC})d_b}{A_b 4 l_b} \qquad \text{(A.4)}$$

u_{test}= average bond stress (ksi)

F_{ε}= force in bar calculated from measured strains (kips)

F_{LC}= force measured by load cells at end of bars (kips)

d_b= diameter of bar (in)

A_b= area of bar (in^2)

l_b= bearing length (in)

Figure A.1 shows the development force measured by the load cells on the end of the bars vs. both the force in the bar and the vertical force for Specimen AL1. Due to symmetry, the vertical force is the applied load divided by two. The development force for other specimens is very similar to that measured for Specimen AL1. There is a nonlinear relationship between the development force and both the force in the bar and the vertical force. This means that there is not a point where the bars fully debond and the force in the bar was carried only by the anchorage.

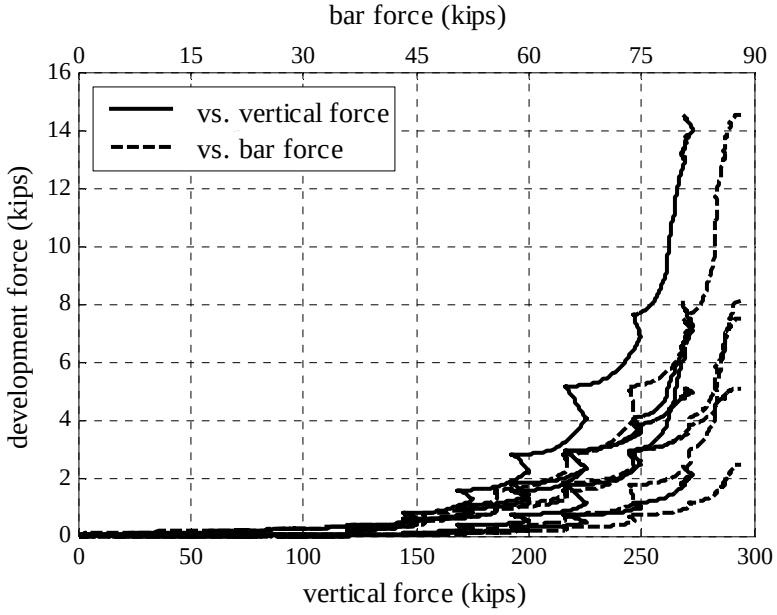

Figure A.1 Development force at end of bar vs. applied load and bar force for Specimen AL1

The inability of the longitudinal reinforcement to fully debond is a function of the confinement provided by the bearing plate and the principal compression strut which forms once arch action becomes the main load carrying mechanism. Figure A.2 shows the state of equilibrium at the support when arch action is the load carrying mechanism. The force from the strut (F_{strut}) has both a vertical and horizontal component. The vertical component of the strut force is in equilibrium with the vertical reaction force (F_{vert}) while the horizontal component is in equilibrium with the force in the bar (F_{bar}). The force in the bar is developed by the average bond stress (u) and the force in the bearing load cell (F_{LC}). Due to the vertical equilibrium there is also an average bearing stress (u_b). This stress serves to confine the concrete around the bar and increase the average bond stress (u) which can develop.

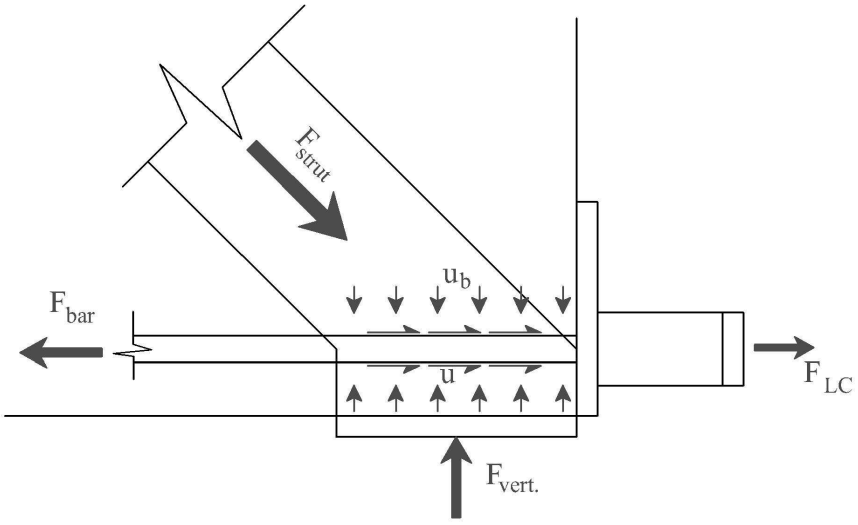

Figure A.2- Equilibrium at support during arch action

With this concept in mind the data for individual bar types was collected from specimens which had no crack control reinforcement and only one row of bars. The data from Specimens AL1 and BL1 were used to make conclusions about #10 bars, Specimens AS1 and AS2 were used to make conclusions about #5 bars, and Specimens AS3 and AS4 were used to make conclusions about #9 bars. Figure A.3 shows a plot of the average bond stress from the test (u_{test}) normalized by the required average bond stress (u_{req}) vs. the confining bearing stress (u_b) after the transition to arch action for #10 bars. Average bearing stress is, again, the vertical force divided by the bearing area. The plot of the data points has a linear trend. A linear regression is shown in the figure with the equation for the line as well as the coefficient of determination (R^2 value). Since the coefficient of determination is very close to one (0.95) the linear regression is a good fit.

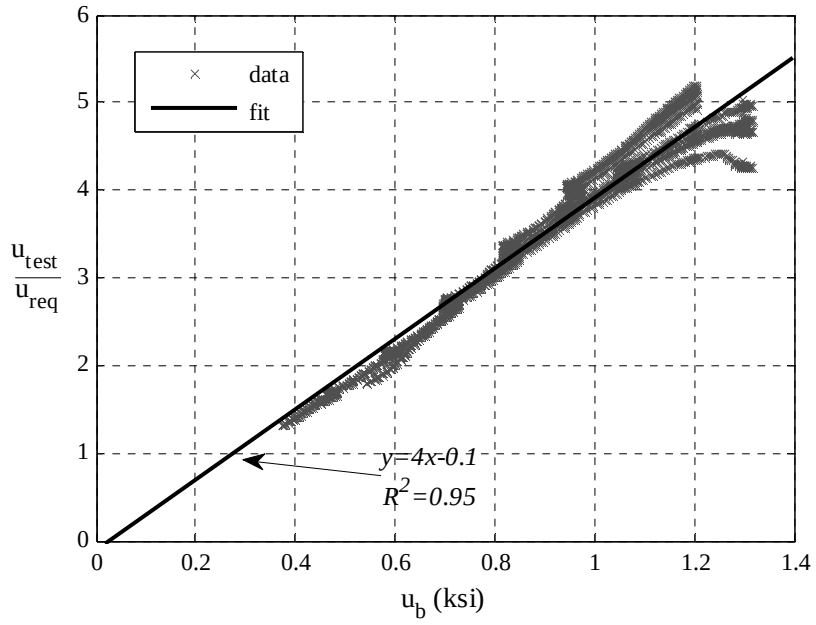

Figure A.3- Normalized average bond stress vs. bearing stress for #10 bars

Figures A.4 and A.5 show the same normalized plots for both #5 and #9 bars. The linear regression for the #9 bars was not as successful as that for the #10 and #5 bars; it had a coefficient of determination of 0.86.

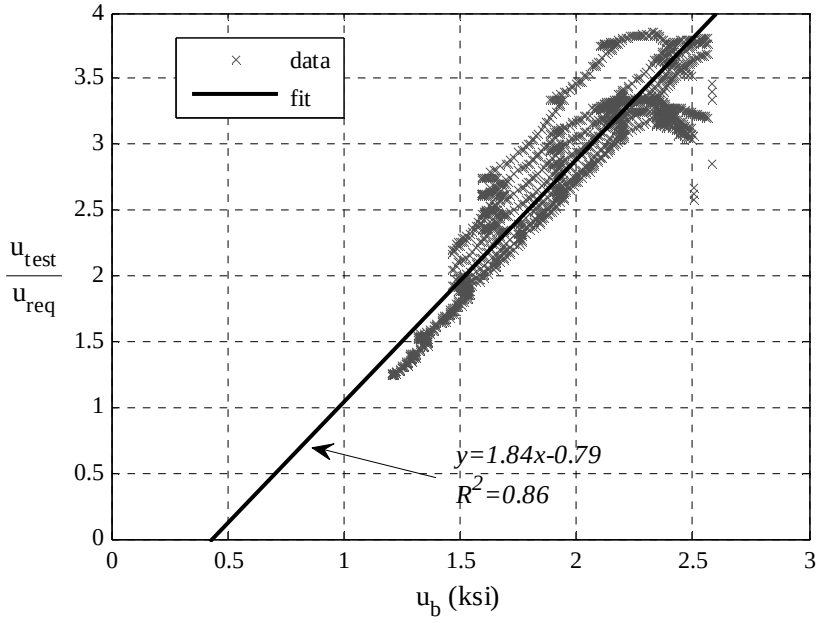

Figure A.4- Normalized average bond stress vs. bearing stress for #9 bars

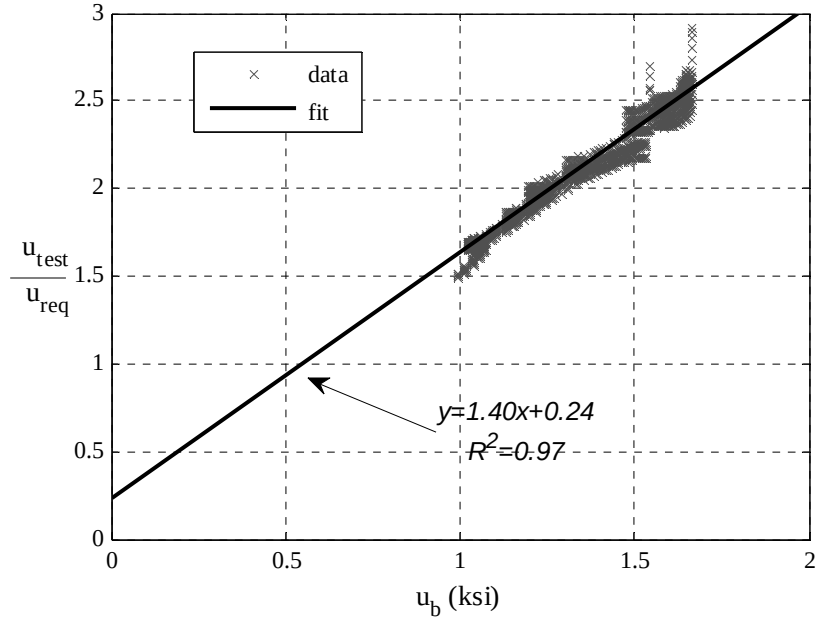

Figure A.5- Normalized average bond stress vs. bearing stress for #5 bars

With the results of the linear regression it is possible to develop equations which relate the development length calculated from the code using Eq. A.1 and what was seen in the experiments. The equations are not intended to be design equations. They are meant for the evaluation of existing structures when arch action is the primary load carrying mechanism. They remove the excess conservatism in the code and give an engineer a way of determining if a bar has sufficient development length if it does not meet the requirements of the current code. Each of the three bar types has a different equation which is a function of the average bearing stress (u_b) and the required development length (l_{dr}). Average bearing stress is the vertical reaction force divided by the bearing area, and the required development length is calculated through Eq. 4.3. If the development lengths calculated with Eqs. A.5, A.6 and A.7 are longer than the bearing length, the length can be converted back into a stress using Eq. A.2. This stress can be converted into a force by multiplying by the circumference of the bar and the bearing length. This force can be subtracted from the force required to yield the bar, and the remaining force can be input into Eq. A.1 to calculate the additional required development length.

#10 bar

$$l_{dt} = \frac{l_{dr}}{4u_b - 0.1} \leq l_{dr} \qquad \text{(A.5)}$$

#9 bar

$$l_{dt} = \frac{l_{dr}}{1.84u_b - 0.79} \leq l_{dr} \qquad \text{(A.6)}$$

#5 bar

$$l_{dt} = \frac{l_{dr}}{1.4u_b + 0.24} \leq l_{dr} \qquad \text{(A.7)}$$

l_{dt}= development length from test (in)

l_{dr}= development length from code Eq. 4.3 (in)

u_b= average bearing stress (ksi)

APPENDIX B

SAMPLE CALCULATIONS FOR ULTIMAE CAPACITY

In this Appendix each type of ultimate capacity calculation discussed in Chapter 5 will be demonstrated. To do this an example calculation will be performed using Specimen AL2 to illustrate the intricacies of each method. Specimen AL2 was chosen because it is a full depth specimen which underwent a brittle failure; this is considered a more dangerous failure mode. Figure 5.1 shows the reinforcement details for Specimen AL2, and on the day of testing the concrete that made up the beam had a compressive strength of 3651 psi, and the longitudinal steel had a yield stress of 65 ksi. Specimen AL2 reached its ultimate capacity at an applied load of 660 kips.

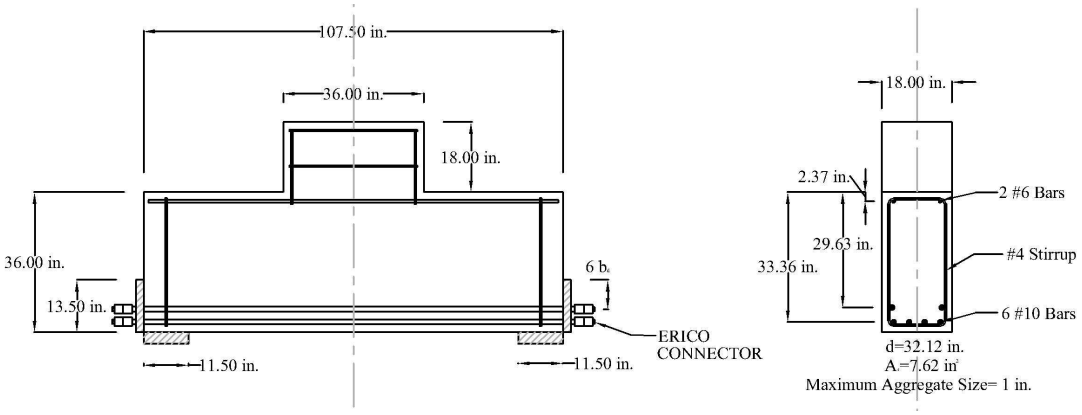

Figure B.1- Specimen AL2

B.1 AASHTO Simplified Method for Nonprestressesd Beams

The AASHTO Simplified Method for Nonprestressed Beams is based on the truss model, and it is shown in Eq. 2.3. In the equation, V_c is the shear contribution from concrete and V_s is the shear contribution from the transverse steel reinforcement. Since Specimen AL2 does not have any transverse steel in the shear span, the V_s can be ignored. This simplifies the calculations to:

$$V_n = V_c$$
$$V_c = 2(0.0316)\sqrt{f'_c}\, b_v d_v$$
$$f'_c = 3.651 \text{ ksi}$$
$$b_v = 18 \text{ in}$$
$$d_v = 32.12 \text{ in}$$
$$V_c = 2(0.0316)\sqrt{3.651}\,(18)(32.12)$$
$$V_n = V_c = 70 \text{ kips}$$

Specimen AL2 was loaded symmetrically; this makes the total calculated applied load equal two times the nominal shear.

$$P = 2V_n$$
$$P = 2(70) = 140 \text{ kips}$$

B.2 Strut and Tie Model

The first step in developing a strut and tie model according to the method developed in Chapter 5 is to determine the smallest bearing width.When looking at Specimen AL2, the smallest bearing width for a single strut is 11.5 inches. This corresponds to the bottom bearing plate. The available bearing width provided by the column is 36 inches. This means that l_b is equal to 11.5 inches. The known values for Specimen AL2 are:

A_s= 7.62 in^2

E_s= 29,000 ksi

f_y= 65 ksi

f'_c=3.651 ksi

b_v= 18 in

d= 32.16 in

a= 48 in

$l_{b\ comp}$= 36 in

l_b= 11.5 in

The first attempt at the solution will assume that the steel yields (ε_s=0.0022); which is simply calculated by f_y/E_s. The solution to the problem is as follows:

$$h_a = \frac{A_s E_S \varepsilon_s}{0.75 f'_c b_v} \tag{5.1}$$

$$h_a = \frac{(7.62)(29{,}000)(0.0022)}{0.75(3.651)(18)}$$

$$h_a = 9.86\,\text{in}$$

$$\theta_s = \tan^{-1}\left(\frac{d - \frac{1}{2}\frac{A_s E_s \varepsilon_s}{0.75 f'_c b_v}}{a - \frac{T_{bw}}{2} + \frac{l_b}{2}}\right) \tag{5.2}$$

$$\theta_s = \tan^{-1}\left(\frac{32.16 - \frac{1}{2}\frac{(7.62)(29{,}000)(0.0022)}{0.75(3.651)(18)}}{48 - \frac{36}{2} + \frac{11.5}{2}}\right)$$

$$\theta_s = 37.3°$$

$$w_s = l_b \sin(\theta_s) + h_a \cos(\theta_s) \quad (5.3)$$

$$w_s = 11.5 \sin(37.3) + 9.86 \cos(37.3)$$

$$w_s = 14.79 \text{ in}$$

$$f_n = \frac{A_s E_s \varepsilon_s}{w_s b_v \cos(\theta_s)} \quad (5.4)$$

$$f_n = \frac{(7.62)(29{,}000)(0.0022)}{(14.79)(18)\cos(37.3)}$$

$$f_n = 2.3 \text{ ksi}$$

$$\varepsilon_1 = \varepsilon_s + (\varepsilon_s + 0.002)\cot^2(\alpha_s) \quad (5.5b)$$

$$\varepsilon_1 = 0.0022 + (0.0022 + 0.002)\cot^2(37.3)$$

$$\varepsilon_1 = 0.0094$$

$$f_{cu} = \frac{f'_c}{0.8 + 170\varepsilon_1} \le 0.85 f'_c \quad (5.5a)$$

$$f_{cu} = \frac{3.651}{0.8 + 170(0.0094)} \le 0.85(3.651)$$

$$f_{cu} = \frac{3.651}{0.8 + 170(0.0094)} \le 0.85(3.651)$$

$$f_{cu} = 1.52 \text{ ksi} \le 3.10 \text{ ksi}$$

$$f_n > f_{cu} \rightarrow \text{try again}$$

The nominal strut stress is greater than the allowable strut stress. The whole calculation needs to be repeated assuming a smaller strain in the longitudinal steel. This is the point where having the whole process programmed becomes most helpful. The results of the computer analysis are as follows:

$\varepsilon_s = 0.001475$

$h_s = 6.61\,\text{in}$

$\theta_s = 39.2°$

$w_s = 12.40\,\text{in}$

$f_n = 1.89\,\text{ksi}$

$f_{cu} = 1.89\,\text{ksi}$

The only check that is required is that the stress on the limiting bearing is not too great. The ultimate load can be simply calculated based on the force in the longitudinal reinforcement; for Specimen AL2 this is:

$$P = 2A_s E_S \varepsilon_s \tan(\theta_s)$$
$$P = 2(7.62)(29{,}000)(0.001475)\tan(39.2)$$
$$P = 532.4\,\text{kips}$$

The limiting stress on the vertical bearing is given by $0.75f'_c$, and for Specimen AL2 is 2.73 ksi. The bearing stress at the ultimate load of 532.4 kips is 1.29 ksi. and is within the limit. This indicates that an acceptable strut and tie model has been established.

The American Concrete Institute has its own set of procedures for performing a strut and tie analysis. The main difference between the AASHTO and the ACI approach are the limit on the crushing stress of the concrete in the compression strut. In the ACI approach there is no Eq. 5.2. The allowable crushing stress in the strut is simply taken as:

$$f_{ce} = 0.85\beta_s f'_c \qquad (5.6)$$

f_{ce}= effective strut compressive strength (psi)

f'_c=compressive strength of concrete (psi)

β=*1.0* if strut is prismatic

β=*0.6* if strut is a bottle strut

β=*0.75* if strut if adequate reinforcement is provided

Adequate reinforcement is defined as:

$$\sum \frac{A_{si}}{b_s s_i} \sin(\alpha_i) \geq 0.003$$

A_{si}= total area of surface reinforcement (in^2)

b_s= width of beam (in)

s_i= spacing of reinforcement (in)

α_s= angle between reinforcement and axis of the strut (degrees)

Taking the nominal strut stress from the first iteration of the AASHTO strut and tie model it is compared to the allowable strut stress according to the ACI code.

$$f_{ce} = 0.85\beta_s f'_c \qquad (5.6)$$

β=*0.6* no reinforcement

$$f_{ce} = 0.85(0.6)(3651)$$

$$f_{ce} = 1862 \text{ psi} \rightarrow 1.862 \text{ ksi}$$

$$f_n = 2.3 \text{ ksi}$$

$$f_n > f_{cu} \rightarrow \text{Try Again}$$

Again the computer is turned to and the results of the analysis are:

$$\varepsilon_s = 0.001442$$

$$h_s = 6.47 \text{ in}$$

$$\theta_s = 39.3°$$

$$w_s = 12.29 \text{ in}$$

$$f_n = 1.862 \text{ ksi}$$

$$f_{cu} = 1.862 \text{ ksi}$$

The ultimate capacity based on the ACI procedures is:

$$P = 2A_s E_S \varepsilon_s \tan(\theta_s)$$
$$P = 2(7.62)(29{,}000)(0.001442)\tan(39.3)$$
$$P = 522 \text{ kips}$$

Again, performing the bearing checks shows that the stress on the vertical face of is 1.26 ksi which is within the limit of 2.73 ksi. This is an acceptable strut and tie model.

B.3 Zararis's Method

Zararis's Method is described in Chapter 2. Equations 2.11 to 2.13 are used to calculate the ultimate shear capacity of a reinforced concrete deep beam. The calculation of the ultimate capacity of Specimen AL2 with Zararis's Method is as follows:

$$\left(\frac{c}{d}\right)^2 + 87{,}000\frac{\rho}{f'_c}\left(\frac{c}{d}\right) - 87{,}000\frac{\rho}{f'_c} = 0 \qquad (2.11)$$

$$\left(\frac{c}{d}\right)^2 + 87{,}000\frac{0.0131}{3651}\left(\frac{c}{d}\right) - 87{,}000\frac{0.0131}{3651} = 0$$

$$\left(\frac{c}{d}\right)^2 + 0.312\left(\frac{c}{d}\right) - 0.312 = 0$$

$$\left(\frac{c}{d}\right) = \frac{-0.312 + \sqrt{0.312^2 - 4(1)(-0.312)}}{2(1)}$$

$$\frac{c}{d} = 0.424$$

$$R = 1 + (\rho_v / \rho)(a/d)^2 \qquad (2.12b)$$

$$R = 1 + (0/0.0131)(48/32.12)^2$$

$$R = 1$$

$$\frac{c_s}{d} = \frac{1 + 0.27R(a/d)^2}{1 + R(a/d)^2}\frac{c}{d} \qquad (2.12a)$$

$$\frac{c_s}{d} = \frac{1 + 0.27(1)(48/32.12)^2}{1 + (1)(48/32.12)^2}(0.424)$$

$$\frac{c_s}{d} = 0.210$$

$$V_u = \frac{bd}{a/d}\left[\frac{c_s}{d}\left(1-0.5\frac{c_s}{d}\right)f'_c + 0.5\rho_v f_{yv}\left(1-\frac{c_s}{d}\right)^2\left(\frac{a}{d}\right)^2\right] \qquad (2.13)$$

$$V_u = \frac{(18)(32.12)}{(48/32.12)}\left[0.210(1-0.5(0.210))(3651)\right]$$

$$V_u = 265{,}500 \text{ lbs} \rightarrow 265.5 \text{ kips}$$

Again, due to symmetry the ultimate capacity is twice the shear capacity.

$$P = 2V_u$$
$$P = 2(265.5) = 531.0 \text{ kips}$$

B.4 Proposed Modified Zararis Method

The Modified Zararis Method was developed in Chapter 5. Based on the observations made during the experimental program, it improves upon some of the assumptions which Zararis's made while developing his method. The calculations for the ultimate capacity of Specimen AL2 with the Modified Zararis Method are shown.

$$\left(\frac{c}{d}\right)^2 + 153{,}520\frac{\rho}{f'_c}\left(\frac{c}{d}\right) - 153{,}520\frac{\rho}{f'_c} = 0 \qquad (5.7a)$$

$$\left(\frac{c}{d}\right)^2 + 153{,}520\frac{0.0131}{3651}\left(\frac{c}{d}\right) - 153{,}520\frac{0.0131}{3651} = 0$$

$$\left(\frac{c}{d}\right)^2 + 0.551\left(\frac{c}{d}\right) - 0.551 = 0$$

$$\left(\frac{c}{d}\right) = \frac{-0.551 + \sqrt{0.551^2 - 4(1)(-0.551)}}{2(1)}$$

$$\frac{c}{d} = 0.516$$

$$c = 0.516 * 32.12 = 16.57 \text{ in}$$

$$C = \frac{2}{3} bc(0.85) f'_c \quad (5.9)$$

$$C = \frac{2}{3}(18)(16.57)(0.85)(3651)$$

$$C = 617.0 \text{ kips}$$

$$T = A_s f_y \quad (5.10)$$

$$T = (7.62)(65)$$

$$T = 495.3 \text{ kips}$$

$C > T$ therefore $\varepsilon_s > \varepsilon_y$

$$\frac{c}{d} = \frac{3A_s f_y}{2(0.85) f'_c bd} \quad (5.7b)$$

$$\frac{c}{d} = \frac{3(7.62)(65)}{2(0.85)(3.651)(18)(32.12)}$$

$$\frac{c}{d} = 0.414$$

$$a / d_{effective} \approx \frac{a - \frac{T_{bw}}{2} + \frac{l_b}{2}}{d\left(1 - \frac{3}{8}\left(\frac{c}{d}\right)\right)} \quad (5.8)$$

$$a / d_{effective} \approx \frac{48 - \frac{36}{2} + \frac{11.5}{2}}{32.12(1 - \frac{3}{8}(0.414))}$$

$$a / d_{effective} \approx 1.31$$

$$R = 1 + (\rho_v / \rho)(a / d_{effective})^2 \quad (5.11b)$$

$$R = 1 + (0 / 0.0131)(1.31)^2$$

$$R = 1$$

$$\frac{c_s}{d} = \frac{1 + 0.27R(a / d_{effective})^2}{1 + R(a / d_{effective})^2} \frac{c}{d} \quad (5.11a)$$

$$\frac{c_s}{d} = \frac{1+0.27(1)(1.31)^2}{1+(1)(1.31)^2}(0.414)$$

$$\frac{c_s}{d} = 0.223$$

$$V_u = \frac{bd}{a/d_{effective}}\left[\frac{c_s}{d}\left(1-0.5\frac{c_s}{d}\right)f'_c + 0.5\rho_v f_{yv}\left(1-\frac{c_s}{d}\right)^2\left(\frac{a}{d}_{effective}\right)^2\right] \quad (5.12)$$

$$V_u = \frac{(18)(32.12)}{(1.31)}\left[0.223(1-0.5(0.223))(3651)\right]$$

$$V_u = 319{,}300 \text{ lbs} \rightarrow 319.3 \text{ kips}$$

$$P = 2V_u$$

$$P = 2(326.6) = 638.6 \text{ kips}$$

B.5- Bazant's Equation

Bazant's equation is based on a regression analysis, and it takes the form of Eq. 2.2; it is solved in a straight forward manor.

ρ_o=400{1+tanh[2(1.49-2.8)]}= 4.22 (2.2b)

$$V_c = [\sqrt{3651} + 3000\sqrt{\frac{0.0131}{(48/32.12)^5}}] * \frac{6.5(0.0131)^{(1/3)}(1+\sqrt{0.2/1})}{\sqrt{1+\frac{32.12}{25(1)(1+\frac{0}{4.22})}}}](18)(32.12) \quad (2.2a)$$

$V_c = 158.3 \text{ kip}$ $P = 2(158.3) = 316.6 \text{ kips}$

APPENDIX C

REINFORCED CONCRETE DEEP BEAM DATABASE

Specimen	Loading	Column	a (in)	d (in)	a/d	b (in)	As (in^2)	Asv (in^2)	Agg. (in)	T_{bw} (in)	B_{bw} (in)	f'_c (psi)	f_y (ksi)	f_{yv} (ksi)	$P_{exp.}$ (kips)
Clark 1951															
B1-1	4 pt.	No	30.00	15.40	1.95	8.00	3.81	0.89	1.00	3.50	3.50	3388	46.5	48.0	125.4
B1-2	4 pt.	No	30.00	15.40	1.95	8.00	3.81	0.89	1.00	3.50	3.50	3680	46.5	48.0	115.4
B1-3	4 pt.	No	30.00	15.40	1.95	8.00	3.81	0.89	1.00	3.50	3.50	3435	46.5	48.0	128.1
B1-4	4 pt.	No	30.00	15.40	1.95	8.00	3.81	0.89	1.00	3.50	3.50	3380	46.5	48.0	120.6
B1-5	4 pt.	No	30.00	15.40	1.95	8.00	3.81	0.89	1.00	3.50	3.50	3570	46.5	48.0	108.6
B2-1	4 pt.	No	30.00	15.40	1.95	8.00	3.81	1.78	1.00	3.50	3.50	3370	46.5	48.0	135.4
B2-2	4 pt.	No	30.00	15.40	1.95	8.00	3.81	1.78	1.00	3.50	3.50	3820	46.5	48.0	144.9
B2-3	4 pt.	No	30.00	15.40	1.95	8.00	3.81	1.78	1.00	3.50	3.50	3615	46.5	48.0	150.6
B6-1	4 pt.	No	30.00	15.40	1.95	8.00	3.81	0.89	1.00	3.50	3.50	6110	46.5	48.0	170.6
C1-1	4 pt.	No	24.00	15.30	1.57	8.00	2.54	0.67	1.00	3.50	3.50	3720	46.5	48.0	124.9
C1-2	4 pt.	No	24.00	15.30	1.57	8.00	2.54	0.67	1.00	3.50	3.50	3820	46.5	48.0	139.9
C1-3	4 pt.	No	24.00	15.30	1.57	8.00	2.54	0.67	1.00	3.50	3.50	3475	46.5	48.0	110.6
C1-4	4 pt.	No	24.00	15.30	1.57	8.00	2.54	0.67	1.00	3.50	3.50	4210	46.5	48.0	128.6
C2-1	4 pt.	No	24.00	15.30	1.57	8.00	2.54	1.33	1.00	3.50	3.50	3430	46.5	48.0	130.4
C2-2	4 pt.	No	24.00	15.30	1.57	8.00	2.54	1.33	1.00	3.50	3.50	3625	46.5	48.0	135.4
C2-3	4 pt.	No	24.00	15.30	1.57	8.00	2.54	1.33	1.00	3.50	3.50	3500	46.5	48.0	145.6
C2-4	4 pt.	No	24.00	15.30	1.57	8.00	2.54	1.33	1.00	3.50	3.50	3910	46.5	48.0	129.6
C3-1	4 pt.	No	24.00	15.30	1.57	8.00	2.54	0.67	1.00	3.50	3.50	2040	46.5	48.0	100.5
C3-2	4 pt.	No	24.00	15.30	1.57	8.00	2.54	0.67	1.00	3.50	3.50	2000	46.5	48.0	90.1
C3-3	4 pt.	No	24.00	15.30	1.57	8.00	2.54	0.67	1.00	3.50	3.50	2020	46.5	48.0	84.6
C4-1	4 pt.	No	24.00	15.40	1.56	8.00	3.81	0.67	1.00	3.50	3.50	3550	46.5	48.0	139.0
C6-2	4 pt.	No	24.00	15.40	1.56	8.00	3.81	0.67	1.00	3.50	3.50	6560	46.5	48.0	190.6
C6-3	4 pt.	No	24.00	15.40	1.56	8.00	3.81	0.67	1.00	3.50	3.50	6480	46.5	48.0	195.6
C6-4	4 pt.	No	24.00	15.40	1.56	8.00	3.81	0.67	1.00	3.50	3.50	6900	46.5	48.0	192.7
D1-1	4 pt.	No	18.00	15.50	1.16	8.00	2.02	0.67	1.00	3.50	3.50	3800	48.6	48.0	135.4
D1-2	4 pt.	No	18.00	15.50	1.16	8.00	2.02	0.67	1.00	3.50	3.50	3790	48.6	48.0	160.4
D1-3	4 pt.	No	18.00	15.50	1.16	8.00	2.02	0.67	1.00	3.50	3.50	3560	48.6	48.0	115.4
D2-1	4 pt.	No	18.00	15.50	1.16	8.00	2.02	0.89	1.00	3.50	3.50	3480	48.6	48.0	130.4
D2-2	4 pt.	No	18.00	15.50	1.16	8.00	2.02	0.89	1.00	3.50	3.50	3755	48.6	48.0	140.4

Specimen	Loading	Column	a (in)	d (in)	a/d	b (in)	As (in^2)	Asv (in^2)	Agg. (in)	T_{bw} (in)	B_{bw} (in)	f'_c (psi)	f_y (ksi)	f_{yv} (ksi)	$P_{exp.}$ (kips)
Clark 1951 Continued															
D2-3	4 pt.	No	18.00	15.50	1.16	8.00	2.02	0.89	1.00	3.50	3.50	3595	48.6	48.0	150.4
D2-4	4 pt.	No	18.00	15.50	1.16	8.00	2.02	0.89	1.00	3.50	3.50	3550	48.6	48.0	150.6
D3-1	4 pt.	No	18.00	15.50	1.16	8.00	3.04	1.33	1.00	3.50	3.50	4090	48.6	48.0	177.6
D4-1	4 pt.	No	18.00	15.50	1.16	8.00	2.02	1.78	1.00	3.50	3.50	3350	48.6	48.0	140.4
D1-6	4 pt.	No	24.00	12.40	1.94	6.00	2.54	0.67	1.00	3.50	3.50	4010	48.6	48.0	78.6
D1-7	4 pt.	No	24.00	12.40	1.94	6.00	2.54	0.67	1.00	3.50	3.50	4060	48.6	48.0	80.6
D1-8	4 pt.	No	24.00	12.40	1.94	6.00	2.54	0.67	1.00	3.50	3.50	4030	48.6	48.0	83.6
B0-1	4 pt.	No	30.00	15.30	1.96	8.00	1.20	0.00	1.00	3.50	3.50	3420	53.7	0.0	54.4
B0-2	4 pt.	No	30.00	15.30	1.96	8.00	1.20	0.00	1.00	3.50	3.50	3468	53.7	0.0	42.4
B0-3	4 pt.	No	30.00	15.30	1.96	8.00	1.20	0.00	1.00	3.50	3.50	3410	53.7	0.0	57.6
C0-1	4 pt.	No	24.00	15.30	1.57	8.00	1.20	0.00	1.00	3.50	3.50	3580	53.7	0.0	78.4
C0-2	4 pt.	No	24.00	15.30	1.57	8.00	1.20	0.00	1.00	3.50	3.50	3405	53.7	0.0	79.9
C0-3	4 pt.	No	24.00	15.30	1.57	8.00	1.20	0.00	1.00	3.50	3.50	3420	53.7	0.0	75.1
D0-1	4 pt.	No	18.00	15.30	1.18	8.00	1.20	0.00	1.00	3.50	3.50	3750	53.7	0.0	99.6
D0-2	4 pt.	No	18.00	15.30	1.18	8.00	1.20	0.00	1.00	3.50	3.50	3800	53.7	0.0	116.9
D0-3	4 pt.	No	18.00	15.30	1.18	8.00	1.20	0.00	1.00	3.50	3.50	3765	53.7	0.0	100.4
Moody et al. 1954															
24 a	4 pt.	No	32.00	21.00	1.52	7.00	4.00	0.00	1.00	8.00	8.00	2580	45.7	0.0	133.0
24 b	4 pt.	No	32.00	21.00	1.52	7.00	4.00	0.00	1.00	8.00	8.00	2990	45.7	0.0	136.0
25 a	4 pt.	No	32.00	21.00	1.52	7.00	5.09	0.00	1.00	8.00	8.00	3530	45.4	0.0	120.0
25 b	4 pt.	No	32.00	21.00	1.52	7.00	5.09	0.00	1.00	8.00	8.00	2500	45.4	0.0	130.0
26 a	4 pt.	No	32.00	21.00	1.52	7.00	6.25	0.00	1.00	8.00	8.00	3140	43.8	0.0	189.0
26 b	4 pt.	No	32.00	21.00	1.52	7.00	6.25	0.00	1.00	8.00	8.00	2990	43.8	0.0	178.0
27 a	4 pt.	No	32.00	21.00	1.52	7.00	4.00	0.00	1.00	8.00	8.00	3100	45.7	0.0	156.0
27 b	4 pt.	No	32.00	21.00	1.52	7.00	4.00	0.00	1.00	8.00	8.00	3320	45.7	0.0	160.0
28 a	4 pt.	No	32.00	21.00	1.52	7.00	5.09	0.00	1.00	8.00	8.00	3380	45.4	0.0	136.0
28 b	4 pt.	No	32.00	21.00	1.52	7.00	5.09	0.00	1.00	8.00	8.00	3250	45.4	0.0	153.0
29 a	4 pt.	No	32.00	21.00	1.52	7.00	6.25	0.00	1.00	8.00	8.00	3150	43.8	0.0	175.0
29 b	4 pt.	No	32.00	21.00	1.52	7.00	6.25	0.00	1.00	8.00	8.00	3620	43.8	0.0	196.0

Specimen	Loading	Column	a (in)	d (in)	a/d	b (in)	As (in^2)	Asv (in^2)	Agg. (in)	T_{bw} (in)	B_{bw} (in)	f'_c (psi)	f_y (ksi)	f_{yv} (ksi)	$P_{exp.}$ (kips)
Moody et al. 1954 Continued															
30	4 pt.	No	32.00	21.00	1.52	7.00	6.25	0.76	1.00	8.00	8.00	3680	43.8	47.3	215.0
31	4 pt.	No	32.00	21.00	1.52	7.00	6.25	1.40	1.00	8.00	8.00	3250	43.8	44.0	228.0
Rogowsky 1984															
BM1/1.0 T1	3 pt.	Yes	39.40	37.40	1.05	7.87	2.79	0.17	0.40	11.81	7.87	3785	55.1	43.1	270.7
BM1/1.0 T2	3 pt.	Yes	39.40	37.40	1.05	7.87	2.79	0.00	0.40	11.81	7.87	3785	55.1	43.1	314.3
BM2/1.0 T1	3 pt.	Yes	39.40	37.40	1.05	7.87	2.79	0.17	0.40	11.81	7.87	3886	55.1	43.1	337.2
BM1/1.5 T1	3 pt.	Yes	39.40	21.06	1.87	7.87	1.86	0.00	0.40	11.81	7.87	6148	66.0	43.1	136.2
BM1/1.5 T2	3 pt.	Yes	39.40	21.06	1.87	7.87	1.86	0.21	0.40	11.81	7.87	6148	66.0	43.1	159.2
BM2/1.5 T1	3 pt.	Yes	39.40	21.06	1.87	7.87	1.86	0.21	0.40	11.81	7.87	6148	66.0	43.1	101.6
BM2/1.5 T2	3 pt.	Yes	39.40	21.06	1.87	7.87	1.86	0.21	0.40	11.81	7.87	6148	66.0	43.1	156.5
Foster and Gilbert 1998															
B2.0-1	3 pt.	Yes	32.40	24.62	1.32	4.92	2.92	0.39	0.40	9.84	9.84	12035	63.8	85.6	357.5
B2.0-2	3 pt.	Yes	32.40	24.62	1.32	4.92	2.92	0.39	0.40	9.84	9.84	17400	63.8	85.6	370.9
B2.0-3	3 pt.	Yes	32.40	24.62	1.32	4.92	2.92	0.39	0.40	9.84	9.84	11310	63.8	85.6	314.7
B2.0B-5	3 pt.	Yes	32.40	24.62	1.32	4.92	2.92	0.00	0.40	9.84	9.84	12905	63.8	85.6	263.0
B2.0C-6	3 pt.	Yes	32.40	24.62	1.32	4.92	2.92	0.54	0.40	9.84	9.84	13485	63.8	85.6	328.2
B2.0D-7	3 pt.	Yes	32.40	24.62	1.32	4.92	2.92	0.39	0.40	9.84	9.84	15080	63.8	85.6	323.7
B3.0-1	3 pt.	Yes	46.30	24.62	1.88	4.92	2.92	0.64	0.40	9.84	9.84	11600	63.8	85.6	229.3
B3.0-2	3 pt.	Yes	46.30	24.62	1.88	4.92	2.92	0.64	0.40	9.84	9.84	17400	63.8	85.6	236.1
B3.0-3	3 pt.	Yes	46.30	24.62	1.88	4.92	2.92	0.64	0.40	9.84	9.84	11165	63.8	85.6	236.1
B3.0A-4	4 pt.	No	36.40	24.62	1.48	4.92	2.92	0.59	0.40	9.84	9.84	12760	63.8	85.6	348.5
B3.0B-5	3 pt.	Yes	46.30	24.62	1.88	4.92	2.92	0.00	0.40	9.84	9.84	12905	63.8	85.6	195.6
Aguilar et al. 2002															
ACI-I	4 pt.	No	36.00	31.13	1.16	12.00	4.74	1.32	1.00	12.00	12.00	4750	61.0	65.0	610.0
STM-I	4 pt.	No	36.00	28.25	1.27	12.00	4.74	1.32	1.00	12.00	12.00	4750	61.0	65.0	510.0
STM-H	4 pt.	No	36.00	31.50	1.14	12.00	4.74	1.32	1.00	12.00	12.00	4130	61.0	65.0	578.0
STM-M	4 pt.	No	36.00	31.50	1.14	12.00	4.74	0.44	1.00	12.00	12.00	4130	61.0	65.0	574.0

Specimen	Loading	Column	a (in)	d (in)	a/d	b (in)	As (in^2)	Asv (in^2)	Agg. (in)	T_{bw} (in)	B_{bw} (in)	f'_c (psi)	f_y (ksi)	f_{yv} (ksi)	$P_{exp.}$ (kips)
Bechtel 2011															
AL1	3 pt.	Yes	48.00	32.80	1.46	18.00	3.81	0.00	1.00	36.00	11.50	3473	65.0	0.0	545.0
AS1	3 pt.	Yes	24.00	16.40	1.46	9.00	0.93	0.00	0.50	18.00	5.75	4123	79.0	0.0	170.0
AS2	3 pt.	Yes	24.00	16.40	1.46	9.00	0.93	0.00	0.50	18.00	5.75	4226	79.0	0.0	160.0
AL2	3 pt.	Yes	48.00	32.12	1.49	18.00	7.62	0.00	1.00	36.00	11.50	3651	65.0	0.0	660.0
AS3	3 pt.	Yes	24.00	16.06	1.49	9.00	2.00	0.00	0.50	18.00	5.75	4036	76.0	0.0	260.0
AS4	3 pt.	Yes	24.00	16.06	1.49	9.00	2.00	0.00	0.50	18.00	5.75	4650	85.0	0.0	252.0
BL1	3 pt.	Yes	48.00	32.80	1.46	18.00	3.81	0.00	1.00	36.00	11.50	3352	80.0	85.0	498.8
BL2	3 pt.	Yes	48.00	32.12	1.49	18.00	7.62	0.00	1.00	36.00	11.50	3352	80.0	85.0	630.8
BL3	3 pt.	Yes	48.00	32.12	1.49	18.00	7.62	2.40	1.00	36.00	11.50	3966	80.0	85.0	739.5
BL4	3 pt.	Yes	48.00	32.12	1.49	18.00	7.62	2.40	1.00	36.00	11.50	3873	80.0	85.0	859.0
BL5	3 pt.	Yes	48.00	32.12	1.49	18.00	7.62	2.40	1.00	36.00	11.50	3672	80.0	85.0	871.0

APPENDIX D

DATABASE OF SHEAR STRENGTHENING WITH EXTERNAL FRP REINFORCEMENT

Ref.	Specimen	Beam Geometry	H (in)	a/d	ρ_L	Fiber Type	Fiber Angle	Ratio t_{frp}	Wrap	ρ_w	ASTM for FRP	V_{ult} (kips)	$V_{control}$ (kips)	Increase
C-95	A1	T-Beam	7.5	2.1	2.10%	Aramid	0/90	1	U-C	0.00%	no	8.7	4.2	107%
C-95	A2	T-Beam	7.5	2.1	2.10%	Aramid	0/90	1	U-C	0.00%	no	6.8	4.2	61%
C-95	E1	T-Beam	7.5	2.1	2.10%	Glass	0/90	1	U-C	0.00%	no	8.3	4.2	96%
C-95	E2	T-Beam	7.5	2.1	2.10%	Glass	0/90	1	U-C	0.00%	no	7.6	4.2	81%
C-95	G1	T-Beam	7.5	2.1	2.10%	Carbon	0/90	1	U-C	0.00%	no	8.0	4.2	90%
C-95	G2	T-Beam	7.5	2.1	2.10%	Carbon	0/90	1	U-C	0.00%	no	8.2	4.2	95%
C-95	45G1	T-Beam	7.5	2.1	2.10%	Glass	45/135	1	U-C	0.00%	no	8.5	4.2	101%
C-95	45G2	T-Beam	7.5	2.1	2.10%	Glass	45/135	1	U-C	0.00%	no	10.7	4.2	154%
T-97	BS4	Rectangular	17.7	2.8	2.00%	Carbon	90	1	U-S	0.19%	yes	56.7	30.7	85%
T-97	BS5	Rectangular	17.7	2.8	2.00%	Carbon	90	1	U-S	0.19%	yes	38.2	30.7	24%
T-97	BS6	Rectangular	17.7	2.8	2.00%	Carbon	90	1	U-S	0.19%	yes	37.5	30.7	22%
T-97	BS7	Rectangular	17.7	2.8	2.00%	Carbon	90	1	U-S	0.19%	yes	52.9	30.7	72%
T-97	BS2	Rectangular	17.7	2.8	2.00%	Carbon	90	1	U-S	0.31%	yes	55.6	46.4	20%
A-97	CF-045	Rectangular	15.7	3.0	2.30%	Carbon	90	1	Full-S	0.19%	no	53.1	45.2	17%
A-97	CF-064	Rectangular	15.7	3.0	2.30%	Carbon	90	1	Full-S	0.19%	no	58.9	45.2	30%
A-97	CF-097	Rectangular	15.7	3.0	2.30%	Carbon	90	1	Full-S	0.19%	no	69.0	45.2	53%
A-97	CF-131	Rectangular	15.7	3.0	2.30%	Carbon	90	1	Full-S	0.19%	no	80.5	45.2	78%
A-97	CF-243	Rectangular	15.7	3.0	2.30%	Carbon	90	1	Full-S	0.19%	no	91.5	45.2	102%
A-97	AF-060	Rectangular	15.7	3.0	2.30%	Aramid	90	1	Full-S	0.19%	no	53.3	45.2	18%
A-97	AF-090	Rectangular	15.7	3.0	2.30%	Aramid	90	1	Full-S	0.19%	no	58.2	45.2	29%
A-97	AF-120	Rectangular	15.7	3.0	2.30%	Aramid	90	1	Full-S	0.19%	no	70.1	45.2	55%
K-97	No. 2	Rectangular	15.7	2.0	2.28%	Carbon	90	1	Full-S	0.00%	no	64.1	40.7	58%
K-97	No. 3	Rectangular	15.7	2.0	2.28%	Aramid	90	1	Full-S	0.00%	no	53.1	40.7	30%
K-97	No. 4	Rectangular	15.7	2.0	2.28%	Carbon	90	1	Full-S	0.00%	no	41.3	40.7	2%
K-97	No. 5	Rectangular	15.7	2.0	2.28%	Aramid	90	1	Full-S	0.00%	no	40.7	40.7	0%
K-97	No. 7	Rectangular	23.6	2.0	1.43%	Carbon	90	1	Full-S	0.00%	no	127.9	66.3	93%
K-97	No. 8	Rectangular	23.6	2.0	1.43%	Aramid	90	1	Full-S	0.00%	no	119.1	66.3	80%

C-95= Chajes et al. (1995), T-97= Taerwe et al. (1995), A-97= Araki et al. (1997), Kamiharako et al. (1997), U= wrapped on 3 sides, Full= wrapped on 4 sides, S= strips, C= continuous

ef.	Specimen	Beam Geometry	h (in)	a/d	ρ_L	Fiber Type	Fiber Angle	Ratio t_{frp}	Wrap	ρ_w	ASTM for FRP	V_{ult} (kips)	$V_{control}$ (kips)	Increase
S-97	No.2	T-Beam	11.8	2.0	3.28%	Carbon	90	1	U-C-A	0.35%	no	50.1	44.7	12%
S-97	No.3	T-Beam	11.8	2.0	3.28%	Carbon	90	1	U-C-A	0.35%	no	59.3	44.7	33%
C-98	RS90-1	Rectangular	9.8	NG	1.40%	Carbon	90	1	Side-S	0.45%	no	19.7	12.0	64%
C-98	RS90-2	Rectangular	9.8	NG	1.40%	Carbon	90	1	Side-S	0.45%	no	21.4	12.0	78%
C-98	RS135-1	Rectangular	9.8	NG	1.40%	Carbon	45	1	Side-S	0.45%	no	21.1	12.0	76%
C-98	RS135-2	Rectangular	9.8	NG	1.40%	Carbon	45	1	Side-S	0.45%	no	22.4	12.0	86%
K-00	BT2	T-Beam	15.9	3	1.50%	Carbon	90	1	U-C	0.00%	no	34.8	20.2	73%
K-00	BT3	T-Beam	15.9	3	1.50%	Carbon	90/0	2	U-C	0.00%	no	35.4	20.2	75%
K-00	BT4	T-Beam	15.9	3	1.50%	Carbon	90	1	U-S	0.00%	no	36.4	20.2	80%
K-00	BT5	T-Beam	15.9	3	1.50%	Carbon	90	1	Side-S	0.00%	no	27.3	20.2	35%
K-00	BT6	T-Beam	15.9	3	1.50%	Carbon	90	1	U-C-A	0.00%	no	49.7	20.2	146%
D-01	T6NS-C45	T-Beam	23.6	2.5	1.73%	Carbon	45	1	U-S	0.00%	yes	48.0	24.8	94%
D-01	T6S4-C90	T-Beam	23.6	2.5	1.73%	Carbon	90	1	U-S	0.24%	yes	61.3	42.2	45%
D-01	T6S4-G90	T-Beam	23.6	2.5	1.73%	Glass	90	1	U-C	0.24%	yes	66.9	42.2	58%
D-01	T6S4-Tri	T-Beam	23.6	2.5	1.73%	Glass	0/+-60	1	U-C	0.24%	no	71.2	42.2	69%
D-01	T6S2-C90	T-Beam	23.6	2.5	1.73%	Carbon	90	1	U-C	0.47%	yes	69.6	80.2	-13%
P-02	TR30C2	Rectangular	11.8	3	NG	Carbon	90	1	Side-C	0.00%	no	27.0	16.8	61%
P-02	TR30C3	Rectangular	11.8	3	NG	Carbon	90	3	Side-C	0.00%	no	25.4	16.8	51%
P-02	TR30C4	Rectangular	11.8	3	NG	Carbon	90	3	Side-C	0.00%	no	31.5	16.8	88%
P-02	TR30D10	Rectangular	11.8	3	NG	Carbon	90	2	Side-C	0.34%	no	43.4	36.3	20%
P-02	TR30D2	Rectangular	11.8	3	NG	Carbon	90	3	Side-C	0.34%	no	48.0	36.3	32%
P-02	TR30D20	Rectangular	11.8	3	NG	Carbon	90	3	Side-C	0.34%	no	55.6	36.3	53%
P-02	TR30D3	Rectangular	11.8	3	NG	Carbon	90	1	Side-C	0.34%	no	36.3	36.3	0%
P-02	TR30D4	Rectangular	11.8	3	NG	Carbon	90	2	Side-C	0.34%	no	46.9	36.3	29%
P-02	TR30D40	Rectangular	11.8	3	NG	Carbon	90	2	Side-C	0.34%	no	47.7	36.3	31%

S-97= Sato et al. (1997), C-98= Chaallal et al. (1998), K-00= Khalifa and Nanni (2000), D-01= Deniaud and Cheng (2001), P-02= Pellegrino and Modena (2002), Side= bonded on 2 sides, U= wrapped on 3 sides, Full= wrapped on 4 sides, S= strips, C= continuous, A= anchored, NG= not given

Ref.	Specimen	Beam Geometry	h (in)	a/d	ρ_L	Fiber Type	Fiber Angle	Ratio t_{frp}	Wrap	ρ_w	ASTM for FRP	V_{ult} (kips)	$V_{control}$ (kips)	Increase
K-02	SW3-2	Rectangular	12	3	3.50%	Carbon	90/0	2	U-C	2.00%	no	39.8	28.4	40%
K-02	SW4-2	Rectangular	12	4	3.50%	Carbon	90/0	2	U-C	2.00%	no	40.6	22.5	80%
K-02	SO3-2	Rectangular	12	3	3.50%	Carbon	90	1	U-S	0.00%	no	29.4	17.3	70%
K-02	SO3-3	Rectangular	12	3	3.50%	Carbon	90	1	U-S	0.00%	no	29.9	17.3	73%
K-02	SO3-4	Rectangular	12	3	3.50%	Carbon	90	1	U-C	0.00%	no	32.5	17.3	88%
K-02	SO3-5	Rectangular	12	3	3.50%	Carbon	90/0	2	U-C	0.00%	no	38.1	17.3	120%
K-02	SO4-2	Rectangular	12	4	3.50%	Carbon	90	1	U-S	0.00%	no	28.7	14.6	96%
K-02	SO4-3	Rectangular	12	4	3.50%	Carbon	90	1	U-C	0.00%	no	34.8	14.6	139%
D-03	T4S2-C45	T-Beam	15.7	2.6	1.10%	Carbon	45	1	U-S	0.60%	yes	49.2	45.2	9%
D-03	T4S4-G90	T-Beam	15.7	2.6	1.10%	Glass	90	1	U-C	0.30%	yes	46.2	35.3	31%
D-03	T4NS-G90	T-Beam	15.7	2.6	1.10%	Glass	90	1	U-C	0.00%	yes	35.7	26.0	37%
D-03	T4S2-G90	T-Beam	15.7	2.6	1.10%	Glass	90	1	U-C	0.60%	yes	50.7	45.2	12%
D-03	T4S2-Tri	T-Beam	15.7	2.6	1.10%	Glass	0/+-60	1	U-C	0.60%	no	54.5	45.2	21%
Z-04	Z11-S0	Rectangular	9	1.7	2.20%	Carbon	0	1	Side-S	0.00%	no	11.1	10.7	4%
Z-04	Z11-S90	Rectangular	9	1.7	2.20%	Carbon	90	1	Side-S	0.00%	no	19.1	10.7	78%
Z-04	Z11-S45	Rectangular	9	1.7	2.20%	Carbon	45	1	Side-S	0.00%	no	21.8	10.7	104%
Z-04	Z22-S0	Rectangular	9	1.1	2.20%	Carbon	0	1	Side-S	0.00%	no	23.4	16.4	42%
Z-04	Z22-S90	Rectangular	9	1.1	2.20%	Carbon	90	1	Side-S	0.00%	no	23.5	16.4	43%
Z-04	Z22-S45	Rectangular	9	1.1	2.20%	Carbon	45	1	Side-S	0.00%	no	27.3	16.4	66%
Z-04	Z31-F90	Rectangular	9	1.7	2.20%	Carbon	90	1	Side-C	0.00%	no	17.4	9.7	79%
Z-04	Z31-FD	Rectangular	9	1.7	2.20%	Carbon	0/90	1	Side-C	0.00%	no	19.8	9.7	104%
Z-04	Z31-FU	Rectangular	9	1.7	2.20%	Carbon	0	1	U-C	0.00%	no	21.6	9.7	123%
Z-04	Z42-F90	Rectangular	9	1.1	2.20%	Carbon	90	1	Side-C	0.00%	no	29.0	19.7	47%
Z-04	Z42-FD	Rectangular	9	1.1	2.20%	Carbon	0/90	1	Side-C	0.00%	no	30.0	19.7	52%
Z-04	Z42-FU	Rectangular	9	1.1	2.20%	Carbon	90	1	U-C	0.00%	no	28.7	19.7	46%

K-02= Khalifa and Nanni (2002), D-03= Deniaud and Cheng (2003), Z-04= Zhang et al. (2004), U= wrapped on 3 sides, Full= wrapped on 4 sides, Side= bonded on 2 sides, S= strips, C= continuous

Ref.	Specimen	Beam Geometry	h (in)	a/d	ρ_L	Fiber Type	Fiber Angle	Ratio t_{frp}	Wrap	ρ_w	ASTM for FRP	V_{ult} (kips)	$V_{control}$ (kips)	Increase
B-06	DB-S0-0.5L	T-Beam	16	1.3	2.00%	Carbon	0/90	1	U-C	0.00%	no	60.3	40	51%
B-06	DB-S0-1L	T-Beam	16	1.3	2.00%	Carbon	0/90	2	U-C	0.00%	no	64.2	40	60%
B-06	DB-S0-2L	T-Beam	16	1.3	2.00%	Carbon	0/90	4	U-C	0.00%	no	65.0	40	62%
B-06	DB-S1-0.5L	T-Beam	16	1.3	2.00%	Carbon	0/90	1	U-C	0.56%	no	69.8	72.7	-4%
B-06	DB-S1-1L	T-Beam	16	1.3	2.00%	Carbon	0/90	2	U-C	0.56%	no	79.9	72.7	10%
B-06	DB-S1-2L	T-Beam	16	1.3	2.00%	Carbon	0/90	4	U-C	0.56%	no	80.4	72.7	11%
B-06	DB-S2-1L	T-Beam	16	1.3	2.00%	Carbon	0/90	2	U-C	1.12%	no	87.6	74.6	17%
B-06	DB-S2-2L	T-Beam	16	1.3	2.00%	Carbon	0/90	4	U-C	1.12%	no	91.0	74.6	22%
B-06	SB-S0-0.5L	T-Beam	16	2.6	2.00%	Carbon	0/90	1	U-C	0.00%	no	23.0	18.3	26%
B-06	SB-S0-1L	T-Beam	16	2.6	2.00%	Carbon	0/90	2	U-C	0.00%	no	27.0	18.3	47%
B-06	SB-S0-2L	T-Beam	16	2.6	2.00%	Carbon	0/90	4	U-C	0.00%	no	27.4	18.3	50%
B-06	SB-S1-0.5L	T-Beam	16	2.6	2.00%	Carbon	0/90	1	U-C	1.13%	no	63.4	59.1	7%
B-06	SB-S1-1L	T-Beam	16	2.6	2.00%	Carbon	0/90	2	U-C	1.13%	no	57.3	59.1	-3%
B-06	SB-S1-2L	T-Beam	16	2.6	2.00%	Carbon	0/90	4	U-C	1.13%	no	60.1	59.1	2%
B-06	SB-S2-1L	T-Beam	16	2.6	2.00%	Carbon	0/90	2	U-C	2.26%	no	69.6	66.3	5%
B-06	SB-S2-2L	T-Beam	16	2.6	2.00%	Carbon	0/90	4	U-C	2.26%	no	66.8	66.3	1%
P-06	A-U1-C-17	Rectangular	11.8	3	7.50%	Carbon	90	1	U-C	0.39%	no	53.5	41.6	29%
P-06	A-U1-C-20	Rectangular	11.8	3	7.50%	Carbon	90	1	U-C	0.34%	no	50.6	38	33%
P-06	A-U1-S-17	Rectangular	11.8	3	7.50%	Carbon	90	1	U-C	0.39%	no	55.6	44.5	25%
P-06	A-U1-S-20	Rectangular	11.8	3	7.50%	Carbon	90	1	U-C	0.34%	no	52.9	45.7	16%
P-06	A-U2-C-17	Rectangular	11.8	3	7.50%	Carbon	90	2	U-C	0.39%	no	54.6	41.6	31%
P-06	A-U2-C-20	Rectangular	11.8	3	7.50%	Carbon	90	2	U-C	0.34%	no	51.6	38	36%
P-06	A-U2-S-17	Rectangular	11.8	3	7.50%	Carbon	90	2	U-C	0.39%	no	49.2	44.5	11%
P-06	A-U2-S-20	Rectangular	11.8	3	7.50%	Carbon	90	2	U-C	0.34%	no	46.6	45.7	2%

B-06= Bousselham and Chaallal (2006), P-06= Pellegrino and Modena (2006), U= wrapped on 3 sides, C= continuous

Ref.	Specimen	Beam Geometry	h (in)	a/d	ρ_L	Fiber Type	Fiber Angle	Ratio t_{frp}	Wrap	ρ_w	ASTM for FRP	V_{ult} (kips)	$V_{control}$ (kips)	Increase
C-05	145	Rectangular	19.7	2.5	2.68%	Carbon	45	1	Side-C	0.00%	no	55.5	28.3	96%
C-05	20	Rectangular	19.7	2.5	2.68%	Carbon	0	1.6	Side-C	0.00%	no	34.6	28.3	22%
C-05	245a	Rectangular	19.7	2.5	2.68%	Carbon	45	1.6	Side-C	0.00%	no	57.8	28.3	104%
C-05	245b	Rectangular	19.7	2.5	2.68%	Carbon	45	1.6	Side-C	0.00%	no	68.6	28.3	142%
C-05	245W	Rectangular	19.7	2.5	2.68%	Carbon	45	1.6	Full-C	0.00%	no	76.0	28.3	168%
C-05	245Ra*	Rectangular	19.7	2.5	2.68%	Carbon	45	1.6	Side-C	0.00%	no	68.8	28.3	143%
C-05	245Rb*	Rectangular	19.7	2.5	2.68%	Carbon	45	1.6	Side-C	0.00%	no	56.4	28.3	99%
C-05	290a	Rectangular	19.7	2.5	2.68%	Carbon	90	1.6	Side-C	0.00%	no	57.6	28.3	103%
C-05	290b	Rectangular	19.7	2.5	2.68%	Carbon	90	1.6	Side-C	0.00%	no	67.0	28.3	137%
C-05	290W	Rectangular	19.7	2.5	2.68%	Carbon	90	1.6	Full-C	0.00%	no	82.5	28.3	192%
C-05	290WR*	Rectangular	19.7	2.5	2.68%	Carbon	90	1.6	Full-C	0.00%	no	87.2	28.3	208%
C-05	345	Rectangular	19.7	2.5	2.68%	Carbon	45	2.4	Side-C	0.00%	no	75.1	28.3	165%
C-05	290	Rectangular	19.7	2.5	3.35%	Carbon	90	1.6	Side-C	0.39%	no	67.0	53.3	26%
C-05	390	Rectangular	19.7	2.5	3.35%	Carbon	90	2.4	Side-C	0.39%	no	67.0	53.3	26%
L-07	SB-U1	Rectangular	6	2.9	4.00%	Carbon	90	1	U-S	0.28%	no	14.6	9.2	59%
L-07	SB-U2	Rectangular	6	2.9	4.00%	Carbon	90	1	U-S	0.28%	no	10.3	9.2	12%
L-07	SB-F1	Rectangular	6	2.9	4.00%	Carbon	90	1	Full-S	0.28%	no	14.9	9.2	62%
L-07	SB-F2	Rectangular	6	2.9	4.00%	Carbon	90	1	Full-S	0.28%	no	15.0	9.2	63%
L-07	MB-U1	Rectangular	12	3.0	4.00%	Carbon	90	2	U-S	0.28%	no	34.8	33.7	3%
L-07	MB-U2	Rectangular	12	3.0	4.00%	Carbon	90	2	U-S	0.28%	no	35.9	33.7	7%
L-07	MB-F1	Rectangular	12	3.0	4.00%	Carbon	90	2	Full-S	0.28%	no	53.1	33.7	58%
L-07	MB-F2	Rectangular	12	3.0	4.00%	Carbon	90	2	Full-S	0.28%	no	56.3	33.7	67%
L-07	LB-U1	Rectangular	26	2.7	4.00%	Carbon	90	4	U-S	0.28%	no	126.7	121.0	5%
L-07	LB-U2	Rectangular	26	2.7	4.00%	Carbon	90	4	U-S	0.28%	no	125.8	121.0	4%
L-07	LB-F1	Rectangular	26	2.7	4.00%	Carbon	90	4	Full-S	0.28%	no	195.9	121.0	62%
L-07	LB-F2	Rectangular	26	2.7	4.00%	Carbon	90	4	Full-S	0.28%	no	198.1	121.0	64%

C-05= Carolin and Taljsten (2005), L-07= Leung et al. (2007), U= wrapped on 3 sides, Full= wrapped on 4 sides, Side= bonded on 2 sides, S= strips, C= continuous, *= repaired specimen

Ref.	Specimen	Beam Geometry	h (in)	a/d	ρ_L	Fiber Type	Fiber Angle	Ratio t_{frp}	Wrap	ρ_w	ASTM for FRP	V_{ult} (kips)	$V_{control}$ (kips)	Increase
B-08	ED1-S0-0.5L	T-Beam	16	3.0	2.00%	Carbon	0/90	1	U-C	0.00%	no	22.9	18.2	26%
B-08	ED1-S0-1L	T-Beam	16	3.0	2.00%	Carbon	0/90	2	U-C	0.00%	no	27.0	18.2	48%
B-08	ED1-S0-2L	T-Beam	16	3.0	2.00%	Carbon	0/90	4	U-C	0.00%	no	27.4	18.2	51%
B-08	ED1-S1-0.5L	T-Beam	16	3.0	2.00%	Carbon	0/90	1	U-C	1.13%	no	63.4	59.1	7%
B-08	ED1-S1-1L	T-Beam	16	3.0	2.00%	Carbon	0/90	2	U-C	1.13%	no	57.3	59.1	-3%
B-08	ED1-S1-2L	T-Beam	16	3.0	2.00%	Carbon	0/90	4	U-C	1.13%	no	60.0	59.1	2%
B-08	ED1-S2-1L	T-Beam	16	3.0	2.00%	Carbon	0/90	2	U-C	2.26%	no	69.5	66.3	5%
B-08	ED1-S2-2L	T-Beam	16	3.0	2.00%	Carbon	0/90	4	U-C	2.26%	no	66.8	66.3	1%
B-08	ED2-S0-1L	T-Beam	8.7	3.0	1.70%	Carbon	0/90	2	U-C	0.00%	no	13.3	8.1	64%
B-08	ED2-S0-2L	T-Beam	8.7	3.0	1.70%	Carbon	0/90	4	U-C	0.00%	no	15.3	8.1	89%
B-08	ED2-S1-1L	T-Beam	8.7	3.0	1.70%	Carbon	0/90	2	U-C	1.30%	no	21.6	20.9	3%
B-08	ED2-S1-2L	T-Beam	8.7	3.0	1.70%	Carbon	0/90	4	U-C	1.30%	no	23.6	20.9	13%

B-08= Bousselham and Chaallal (2008), U= wrapped on 3 sides, C= continuous

REFERENCES

AASHTO. (2008). *Manual for Bride Evaluation 1st Edition,* Washington, D.C.

AASHTO. (2007). *LRFD Design Specifications 4th Edition,* Washington, D.C.

ABAQUS (2009). *ABAQUS 6.9 Documentation.* Dassault Systems Simula Corp, Providence RI

ACI Committee 318. (2008). *Building Code Requirements for Structural Concrete and Commentary,* Farmington Hills, MI

Aguilar G., Matamoros, A., Parra-Montesinos, G., Ramirez, J., Wight, J. (2002) "Experimental Evaluation of Design Procedures for Shear Strength of Deep Reinforced Concrete Beams." *ACI Structural Journal,* 99(4), 539-548

ASCE. (2009). *Report Card for America's Infrastructure,* http://www.infrastructurereportcard.org/fact-sheet/bridges (June 19, 2009)

ASTM C-39. (2010). *Standard Test Method for Compressive Strength of Cylindrical Concrete Specimens,* Conshohocken PA

ASTM C-469. (2002). *Standard Test Method for Static Modulus of Elasticity and Poisson's Ratio of Concrete in Compression,* Conshohocken PA

ASTM C-496. (2004). *Standard Test Method for Splitting Tensile Strength of Cylindrical Concrete Specimens,* Conshohocken PA

ASTM D-3039. (2008). *Standard Test for the Tensile Properties of Polymer Matrix Composite Materials,* Conshohocken PA

Bazant, Z., and Sun, H. (1987) "Size Effect in Diagonal Shear Failure: Influence of Aggregate Size and Stirrups." *ACI Materials Journal*, 259-272

Bazant, Z., Pijaudier-Cabot, G. (1989). "Measurement of Characteristic Length of NonLocal Continuum." *Journal of Engineering Mechanics.* 115(4) 755- 767

Bazant, Z. Kim, J. (1984) "Size Effect in Shear Failure of Longitudinally Reinforced Beams." *ACI Journal.* 465- 468

Bousselham, A., and Chaallal, O. (2004) "Shear Strengthening Reinforced Concrete Beams with Fiber-Reinforced Polymer: Assessment of Influencing Parameters and Required Research." *ACI Structural Journal* 101(2), 219-227

Bousselham, A. and, Chaallal, O. (2006) "Behavior of Reinforced Concrete T-Beams Strengthened in Shear with CFRP- An Experimental Study." *ACI Structural Journal* 103(3), 339-347.

Bousselham, A., and Chaallal, O. (2008). "Mechanisms of Shear Resistance of Concrete Beams Strengthened in Shear with Externally Bonded FRP." *Journal of Composites for Construction.* 12(5), 499-512

Brown, M., and Bayrak, O. (2005) "Design for Shear in Reinforced Concrete Using Strut and Tie Models: A Summary." *Project Summary Report 0-4371-S,* Austin, TX

Carolin, A., and Taljsten, B. (2005). "Experimental Study of Strengthening for Increased Shear Bearing Capacity." *Journal of Composites for Construction.* 9(6) 488- 496

Carolin, A., and Taljsten, B. (2005). "Theoretical Study of Strengthening for Increased Shear Bearing Capacity." *Journal of Composites for Construction.* 9(6), 497-506

Chajes, M., Januszka, T., Mertz, D., Thomson, T., Finch, W. (1995). "Shear Strengthening of Reinforced Concrete Beams Using Externally Applied Composite Fabrics." *ACI Structural Journal.* 92(3), 295- 303

Challal ,O., Nollet, M., Perraton, D. (1998). "Shear Strengthening of RC Beams by Externally Bonded Side CFRP Strips." *Journal of Composites for Construction*. 2(2), 111- 113

Chen, J., and Teng, J. (2003). "Shear Capacity of Fiber-Reinforced Polymer-Strengthened Reinforced Concrete Beams: Fiber Reinforced Polymer Rupture." *Journal of Structural Engineering* 125(5), 615- 625

Choi, K., Park, H., Wight, J. (2007). "Unified Shear Strength Model for Reinforced Concrete Beams- Part I: Development." *ACI Structural Journal* 104(2), 142-152

Clarck, A. (1951). "Diagonal Tension in Reinforced Concrete Beams" *Journal of the American Concrete Institute.* 48(11), 145-156

Collins, M. (1978) “Towards a Rational Theory for RC Members in Shear” *Journal of the Structural Division*, 104(4), 649-666

Deniaud, C., and Cheng, J. (2001). “Shear Behavior of Reinforced Concrete T-Beams with Externally Bonded FRP Sheets” *ACI Structural Journal.* 98(3), 386-394

Deniaud, C., and Cheng, J. (2003) “Reinforced Concrete T-Beams Strengthened in Shear with FRP Sheets” *Journal of Composites for Construction* 7(4) 302-310

Deniaud, C., and Cheng, J. (2004) “Simplified Shear Design Method for Concrete Beams Strengthened with Fiber Reinforced Polymer Sheets.” *Journal of Composites for Construction.* 8(5) 425- 433

Fenwick, R., and Paulay, T. (1968). “Mechanisms of Shear Resistance of Concrete Beams” *Journal of the Structural Division*. 94(10), 2325- 2350

Foster, S., and Gilbert, R. (1998). “Experimental Studies on High-Strength Concrete Deep Beams.” *ACI Structural Journal*, 95(4), 382-390

Georgakakos, A. CEE 6231 Probability and Statistics. Georgia Institute of Technology, Atlanta GA. Fall, 2009.

Hawkins, Neil M. Kuchima, Daniel A. Mast, Robert F. Marshi, M. Lee. Reineck, Karl-Heinz. NCHRP Report 549. Transportation Research Board Washington D.C. 2005

Hsu, T. (1988). “Softened Truss Model for Shear and Torsion.” *ACI Structural Journal* 85(6), 624- 635

Kani, G. (1964). “The Riddle of Shear Failure and Its Solution” *Journal of the American Concrete Institute* 61(4) 441- 467

Kani, G. (1967). “How Safe Are Our Large Reinforced Concrete Beams” *ACI Journal*. 64(3) 128- 141

Khalifa, A., Gold, W., Nanni, A., Aziz, A. (1998). “Contribution of Externally Bonded FRP to Shear Capacity of RC Flexural Members.” *Journal of Composites for Construction.* 2(4), 195- 202

Khalifa, A., and Nanni, A. (2000). “Improving Shear Capacity of Existing RC T-section Beams Using CFRP Composites.” *Cement and Concrete Composites.* 22, 165-174

Khalifa, A., and Nanni, A. (2002). “Rehabilitation of Rectangular Simply Supported RC Beams with Shear Deficiencies Using CFRP Composites.” *Construction and Building Materials.* 16, 135- 136

Lampert, P., and Thurlimann B. (1968) “Torsion Tests of Reinforced Concrete Beams” (Torsionsversuche an Stahlbetonbalken) *Bericht* 6506(2) Institut fur Baustatik, ETH Zurich

Leung, C., Chen, Z., Lee, S., Ng, M., Xu, M., Tang, J. (2007). “Effect of Size on the Failure of Geometrically Similar Concrete Beams Strengthened in Shear with FRP Strips” *Journal of Composites for Construction*. 11(5), 487- 496

Li, A., Assih, J., Delmas, Y. (2001). “Shear Strengthening of RC Beams with Externally Bonded CFRP Sheets.” *Journal of Structural Engineering.* 127(4), 374- 380

Loov, R. (1988) “Review of A23.3-94 simplified method of shear design and comparison with results using shear friction.” *Canadian Journal of Civil Engineering* 25 437-450

Lorig, L., and Cundal, P. (1989) “Modeling of Reinforced Concrete Using the Distinct Element Method.” *Fracture of Concrete and Rock* 17(19) 276-287

MacGregor et al. (1965). “Strength of Rrestressed Concrete Beams with Web Reinforcement.” *Journal of the American Concrete Institute.* 62(12), 1503-1518

MacGregor, J. (1997) *Reinforced Concrete: Mechanics and Design Third Edition.* Prentice Hall, New Jersey.

Mallick, P. (1993) *Fiber Reinforced Composites: Materials, Manufacturing, and Design 2nd Edition.* Marcel Dekker New York.

Mattock et al. (1961). “Rectangular Concrete Stress Distribution in Ultimate Strength Design.” *Journal of the American Concrete Institute.* 57(43), 875-928

Mau, S., Hsu, T. (1987) “Shear Strength for Deep Beams with Web Reinforcement.” *ACI Structural Journal.* 84(6) 513- 523

Moody et al. (1954). “Shear Strength of Reinforced Concrete Beams.” *Journal of the American Concrete Institute.* 51(15), 317-392

Monti, G., and Liotta, M. (2007). “Tests and design equations for FRP-strengthening in shear” *Construction and Building Materials.* 21, 799- 809

O’Malley, Curtis. *Assessment of Bridge Pier Cap Shear Capacity Analysis and Retrofit Techniques*. A Thesis Proposal Presented to the Academic Faculty of the Georgia Institute of Technology. June 17, 2008

Orangun, C. (1977). “A Reevaluation of Test Data on Development Length and Splices” *ACI Journal* 114-122

Park, S., and Aboutaha, R. (2009). “Strut-and Tie Method for CFRP Strengthened Deep RC Members.” *Journal of Strutctural Engineering.* 135(6), 632-643

Pellegrino, C., and Modena, C. (2002). “FRP Shear Strengthening of Reinforced Concrete Beams with Transverse Steel Reinforcement.” *Journal of Composites for Construction.* 6(2), 104- 111

Pellegrino, C., and Modena, C. (2006). “FRP Shear Strengthening of Reinforced Concrete Beams: Experimental Study and Analytical Modeling” *ACI Structural Journal* 103(5). 720- 728

Pellegrino, C., Tinazzi, D., Modena, C. (2008). “Experimental Study on Bond Behavior between Concrete and FRP Reinforcement.” *Journal of Composites for Construction*. 12(2) 180- 189

Richart, F. (1927) “An Investigation of Web Stresses in Reinforced Concrete Beams,” *Bulletin No. 166, University of Illinois Engineering Experiment Station.* Urbana, IL

Rogowski, D., MacGregor, J. Ong, S. (1984). “Tests of Reinforced Concrete Deep Beams.” *ACI Journal.* 83(55), 614-623

Sabnis, G., Harris, H. (1983). *Structural Modeling and Experimental Techniques*. Prentice Hall, NJ

Sato, Y., Ueda, T., Kakuta, Y., Ono, S. (1997). “Ultimate Shear Capacity of Reinforced Concrete Beams with Carbon Fiber Sheet.” *Non-Metallic (FRP) Reinforcement for Concrete Structures: Proceedings of the Third International Symposium.* 1 499- 506

Senturk, A. and Higgins, C. (2010). "Evaluation of Reinforced Concrete Girder Bridge Bent Caps with 1950s Vintage Details: Analytical Methods." *ACI Structural Journal.* 105(5), 544-553

Schlaich, J., Schafer, K., Jennewein, M. (1987) "Toward a Consistent Design of Structural Concrete." *PCI Journal,* 3. 74- 151

Sherwood, E., Bentz, E., Collins, M. (2007) "Effect of Aggregate Size on Beam Shear Strength of Thick Slabs." *ACI Structural Journal* 104(2), 180- 190

Stamenkovic, Hrista. *Innovative Shear Design.* Spon Press New York 2002

Taerwe, L., Khalil, H., Matthys, S. (1997). "Behavior of RC Beams Strengthened in Shear by External CFRP Sheets" *Non-Metallic (FRP) Reinforcement for Concrete Structures: Proceedings of the Third International Symposium.* 1, 483- 490

Taylor, H. (1970). "Investigation of Forces Carried across Cracks in Reinforced Concrete Beams by Interlock of Aggregates." *TRA 42.447 Cement and Concrete Association* London

Timoshenko, S., and Young, D. (1968). Elements *of Strength of Materials 5th Edition.* D. Van Nostrad Company, New York

Triantafillou, C. (1998). " Shear Strengthening of Reinforced Concrete Beams Using Epoxy Bonded FRP Composites." *ACI Structural Journal.* 95(2), 107- 115

Triantafillou, T., and Antonopoulos, C. (2000). "Design of Concrete Flexural Members Strengthened in Shear with FRP." *Journal of Composites for Construction.* 4(4), 198-205

Vecchio, F. Collins, M. "The Modified Compression-Field Theory for Reinforced Concrete Elements Subjected to Shear" *Journal of the American Concrete Institute* 83(2), 219- 235

Walraven, J., and Lehwalter, N. "Size Effect of Short Beams Loaded in Shear." *ACI Structural Journal* 91(5), 585- 593

Zararis, P. (1997). "Aggregate Interlock and Steel Shear Forces in the Analysis of RC Membrane Elements" *ACI Structural Journal* 94(2), 1-12

Zararis, P. (2003). "Shear Compression Failure in Reinforced Concrete Deep Beams" *Journal of Structural Engineering* 129(4), 544- 553

Zhang Z., Hsu, T., Moren, J. (2004). “Shear Strengthening of Reinforced Concrete Deep Beams Using Carbon Fiber Reinforced Polymer Laminates.” *Journal of Composites for Construction.* 8(5), 403-414

Zsutty, T. (1971). “Shear Strength Prediction for Separate Categories of Simple Beam Tests.” *ACI Journal.* 68(2) 138- 143

Zureick, A., Ellingwood, B., Nowak, A., Mertz, D., Triantafillou, T. (2010). *NCHRP 655: Guide Specifications for the Design of Bonded FRP Systems for Repair and Strengthening of Concrete Bridge Elements* Washington D.C.